DEVELOPMENT OF FISSION-PRODUCTS TRANSPORT MODEL IN SEVERE-ACCIDENT SCENARIOS FOR SCDAP/RELAP5

By

EDUARDO HENRIQUE RANGEL HONAISER

A DISSERTATION PRESENTED TO THE GRADUATE SCHOOL
OF THE UNIVERSITY OF FLORIDA IN PARTIAL FULFILLMENT
OF THE REQUIREMENTS FOR THE DEGREE OF
DOCTOR OF PHILOSOPHY

UNIVERSITY OF FLORIDA

2003

Copyright 2003

by

Eduardo Henrique Rangel Honaiser

ACKNOWLEDGMENTS

Nuclear engineering is a complex science that includes knowledge in the fields of quantum mechanics, chemical engineering, statistics, mechanical engineering, physics and mathematics. Therefore, the learning process is not easy, especially for foreign students without background in the area. The University's professors make extraordinary efforts to overcome the complexity of the nuclear field, making our task easier. Therefore, I would like to recognize and thank Dr. Dugan, Dr. Vernetson, Dr. Anghaie, Dr. Jacobs, Dr. Hahighat and Professor Tulenko.

Dr. Anghaie, as my advisor, was remarkably supportive, encouraging and kind. With his theoretical and practical experience, he came up with the best solutions and orientations when doubts have appeared.

Also remarkable was the help of Richard Wagner and Dr. Chris Allison, from Idaho Falls. Richard Wagner was the responsible and great teacher of my first steps as a computer programmer. Dr. Allison's patience with me on my visits to Idaho Falls, and his willingness to return my consults were fantastic.

The most important person of this accomplishment was my wife, Valeria. Her supportive attitude during the times of hard studying, when we lost our leisure time, and she took care of our home and our sons gave me the force and balance to achieve my goal.

TABLE OF CONTENTS

Page

ACKNOWLEDGMENTS iii

LIST OF TABLES vii

LIST OF FIGURES x

ABSTRACT xvi

CHAPTER

1 INTRODUCTION 1

- Overview 1
- Research Background 2
- Objectives 8

2 CHARACTERISTICS OF THE MODEL 10

- Light Water Reactors 11
  - Boiling Water Reactor 13
  - Pressurized Water Reactor 16
- Severe Accident 19
  - Severe-Accident Phenomena 19
  - Severe-Accident Scenarios 21
  - Thermal-Hydraulic Behavior of Severe Accidents 24
  - Thermal-Hydraulic Parameters of Severe Accidents 28
- The Relap/Scdap Code 30
  - The Relap5 Code 30
  - The Scdap Code 32
  - The Scdap/Relap Code 35
- Fission-Products Behavior 37
  - Initial Inventory of Fission Products 39
  - Importance of Fission Products 42
  - Fission Products and Non-Radioactive Material Release 45
    - Release from intact fuel 47
    - Release from debris 51
    - Release from molten pool 52
    - Release from control rods and structural materials 52
  - Chemistry 56

Radioactive decay 56
Chemical reactions 57
Fission-Products Transport...66
Characteristics of the Fission Products-Transport Model 68

3 DEVELOPMENT OF THE MODEL..70

Physical-Mathematical Model Development 70
Derivation of the Fission Products-Transport Analytical Equations...................70
Derivation of the Fission Products-Transport Numerical Equations 76
The convective term 76
The radius treatment and integral terms...80
Selection of the Numerical Method...86
Imposed Constraints 97
Physical constraint...97
Problem constraint...100
Optimization constraint 100
Phenomenological Model Development...101
Hydrodynamics Review 102
Vapor Phenomena 112
Adsorption 113
Condensation onto structural surfaces...117
Vapor-Aerosol Phenomena 120
Composition and structure of nuclear aerosols 122
Critical radius 126
Homogeneous nucleation 129
Condensation onto aerosol surfaces (Heterogeneous nucleation).............135
Aerosol Phenomena...140
Aerosol hydrodynamics...149
Aerosol deposition...152
Re-suspension...184
Agglomeration...193
Vapor Species Properties...209
Comparison with Other Models...210

4 IMPLEMENTATION AND VERIFICATION 213

Programming Features of Scdap/Relap 5 213
Implementation..222
Input/Output Design 225
Calculation Implementation 227
Verification 233
Input File Description...234
First Verification 242
Second Verification 248
Global mass error 250
Stability 251

5 PRELIMINARY ASSESSMENT....................271

Adjustment and Validation Matrix....................271
Phebus Experimental Program....................274
Phebus Test Facility....................276
Geometry and material....................276
Instrumentation....................283
Test Conduct and Bundle Degradation....................294
Lessons Learned from Phebus FPT-01 Experiment....................302
Remarks on the Fission Product Results of Phebus FPT-01 Experiment....................303
Modeling the Phebus Experiment with Relap/Scdap....................312
Elaboration of Nodalization Diagram....................312
Comparison of Experimental and Calculated Results....................326

6 CONCLUSIONS....................362

APPENDIX

A FISSION PRODUCTS-VAPOR PROPERTIES....................377

B SYNERGISMS OF AEROSOL INTERACTIONS IN SEVERE-ACCIDENT ENVIRONMENTS FOR LIGHT WATER REACTORS....................384

Agglomeration....................76
Deposition....................39271

LIST OF REFERENCES....................396

BIOGRAPHICAL SKETCH....................408

LIST OF TABLES

Table page

2-1. Typical parameters for a large BWR 15

2-2. Typical parameters for a PWR 18

2-3. Symbols adopted in severe accident scenarios 22

2-4. Thermal-hydraulic parameters for the most important severe accident sequences 28

2-5. Simplified fission-product inventory for end-of-life fuel PWR 3412 MW....................43

2-6. Importance of major fission-product elements....................45

2-7. Environment conditions for the fission-products transport....................68

2-8. Phenomenological assessment of the fission-products transport 69

3-1. Range of decay constants for the fission product transport phenomena: (a) vapor phenomena; (b) aerosol phenomena 93

3-2. Equivalent equations and parameters for different transferring processes....................111

3-3. Summary of deposition velocities for adsorption interactions (m/s)....................115

3-4. Nucleation physical properties for different species 123

3-5. Best estimative of initial masses and released masses for potential aerosol sources in the Phebus FPT-01 experiment....................124

3-6. Release fractions of each phase in Phebus FPT-01 (%) 125

3-7. Various aerosol shapes investigated in the literature....................143

3-8. Chi-square values for several models for several experiments 162

3-9. Comparison of different approaches for thermophoretic deposition efficiency for Montassier experiment....................168

3-10. Comparison of different approaches for thermophoretic deposition efficiency for TUBA experiment....................169

3-11. Coefficients of the re-suspension rate (Equation 3-181) 188

3-12. Comparison of mathematical developments of different codes 211

3-13. Comparison of vapor phenomenological treatment of different codes 211

3-14. Comparison of aerosol phenomenological treatment of different codes 212

4-1. Phenomenological chosen equations 223

4-2. Auxiliary quantities of the fission product transport 224

4-3. Input quantities of fission product transport module 226

4-4. Input cards of fission product transport module 227

4-5. Function of sub-routines called by fpmdlk..229

4-6. Function of sub-routines called in Fpgedr structure 231

4-7. Major settings of the first verification model: (a) initial conditions; (b) geometric settings 245

4-8. Flow inlet conditions for the sets used in the sensitivity studies...............................260

4-9. Ranges and typical values of the reciprocal time-constants for fission-products transport phenomena...261

5-1. Fission-products integral effects experiments 274

5-2. Fuel bundle geometrical parameters..280

5-3. Geometrical characteristics of the experimental circuit 283

5-4. Axial power profiles $F_d(z)$ during the bundle degradation phase 297

5-5. Radial power profile during the bundle degradation phase.......................................297

5-6. Global mass balance for Phebus FPT-01 experiment (% of initial inventory).........310

5-7. Release time characteristics for the several release groups.......................................311

5-8. Relative releases for the fission product groups...312

5-9. Elements of the core region in Phebus test train 315

5-10. Elements of the experimental circuit in the Phebus FPT1 experiment...................317

5-11. Speciation used in the Phebus FPT-01 Relap/Scdap experiment model 325

5-12. Release rates for element considered in the modeling of FPT-1 experiment.........325

5-13. Singularities in the Phebus experimental circuit...326

5-14. Release rates and speciation after preliminary run analysis...................................335

5.15- Experimental fractional deposition (% of released mass).....................................336

5-16. Comparison of log-normal distribution parameters from predicted and experimental data for Ag weight as function of particle diameter...354

6-1. Future-work matrix for the fission products-transport model.................................376

6-2. Future-work matrix for the fission products-behavior model..................................376

A-1. Lennard-Jones parameters for more important species..379

A-2. Concentration equilibrium for CsI...382

A-1. Most significant phenomena synergisms for different particle interactions............385

LIST OF FIGURES

Figure page

2-1. The fission process in U235 isotope 11

2-2. Boiling Water Reactor major components 14

2-3. Reactor composition of a BWR 15

2-4. Pressurized water reactor loops 17

2-5. Pressurized water reactor plant scheme 17

2-6. Final core condition of TMI-2 accident 21

2-7. Major thermal-hydraulic parameters of LOFT FP-2 experiment 28

2-8. Typical average thermal-hydraulic behaviors for S_2D sequence 29

2-9. Phenomena in the fuel liquefaction process 34

2-10. Primary circuit nodalization diagram 36

2-11- Typical nodalization diagram for the pressure vessel 36

2-12. Fission products-behavior modules and their inter-linkages among themselves and with other calculation modules 38

2-13. Fission-product spectrum 40

2-14. Decay chain for mass number 135 41

2-15. The release from the fuel to the coolant channel processes 46

2-16. Physical processes and states for release from intact fuel (a) schematic (b) physical representation 50

2-17. Migration processes for bubbles in molten pools 52

2-18. The OLAM signal for Phebus FPT-1 experiment 56

2-19. Parametric study of the Cs-I-O-H quaternary system in NUREG-0772 63

2-20. Barium standard Gibbs free energy for several species 64

2-21. Vapor pressure for barium species 65

2-22. Physical processes during fission-products transport (a) schematic (b) physical representation 68

3-1. Schematic of the states and physical processes in fission products transport 71

3-2. The process of heat and momentum transfer in a turbulent flow 107

3-3. Velocity profiles: (a) exact solution for laminar flow; (b) average velocity for turbulent flow 108

3-4. Transport process steps for vapor to piping wall phenomena 113

3-5. Sophie approach to solve the adsorption/desorption of nuclear vapors over structural surfaces of the primary circuit 117

3-6. Layering composition of nuclear aerosol particle in Phebus experiments by X-ray photoelectric spectroscopy analysis 124

3-7. Homogeneous nucleation process 127

3-8. Comparison classical/kinetic/discrete models for Θ=19 , S=200 134

3-9. Particles formation by heterogeneous condensation 139

3-10. Most common aerosol shapes: (a) oblate (plaquette), (b) oblate (fiber), (c) spherical, (d) agglomerated 142

3-11. Scanning electron micrographs of material on filters from effluent samples of SFD-4 experiment 144

3-12. Scanning electron micrograph of Phebus FPT-01 circuit filters: (a) cold leg filter substrate; (b) spotted particle on cold leg; (c) spotted particle on hot leg. 145

3-13. Interactions of aerosol particles: (a) without hydraulic interactions; (b) with interactions 148

3-14. Comparison of theories and Liu and Agarwal experiments 159

3-15. Penetration of 20 μm aerosol particles through a 102mm vertical tube 161

3-16. Aerosol particle movement under a temperature gradient.....................................163

3-17. Particles distribution and trajectories: (a) in a horizontal tube; (b) downstream of a 90-degree following the a horizontal tube; (c) particle trajectories in a bend (dashed line represent penetrating particle)...172

3-18. Laminar flow field in a vertical bend 173

3-19. Normalized system of coordinates for a curved tube 175

3-20. Typical 90-degrees bend of nuclear power plant....................176

3-21. Radial iso-velocity contours and secondary streamlines for increasing Dean number 177

3-22. Comparison of Cheng and Wang theoretical curves for intermediate Dean numbers and flow Reynolds number of 1,000 and Pui et al. experimental data 178

3-23. Streamlines in a 90-degree contraction 179

3-24. Up-comer cyclone-type steam separator 182

3-25. Steam drier....................183

3-26. Turbulent bursts continuously crushing the boundary layer 184

3-27. Aerosol re-suspension rates obtained from several experiments....................187

3-28- Polar-coordinate system for two particle Brownian coagulation 195

3-29. Boundary conditions for the Brownian agglomeration calculation....................195

3-30. Agglomeration process due to different gravitational deposition velocities 199

3-31. Simplified model for differential-gravitational deposition model....................199

3-32. Realistic model for differential-gravitational model: (a) streamlines and particle trajectories; (b) impaction area 200

3-33. Coordinate system for the Stokes flow field 202

4-1. Top-level structure for Scdap/Relap5....................218

4-2. First level below fptran....................228

4-3. The fpmdlk routine and its sub-routines....................229

4-4. Solution process for the ODE system in Hindmarsh package....................230

4-5. Fpgedr sub-routines structure 231

4-6. Simplified scheme of fission product transport modular organization....................232

4-7. Geometrical settings of Relap: (a) references for azimuthal and inclination angle; (b) volume face numbers 236

4-8. Nodalization diagram for the firs model used in the verification 243

4-9. Thermal-hydraulic parameters for the first verification model: (a) fluid velocity and system pressure; (b) maximum fluid temperature 246

4-10. Nodalization diagram of the second verification model 250

4-11. Sectional analysis for control volume 10-02: (a) number of particles distribution for diferent number of sections; (b) location of the volume 10-02; (c) total number of particles for different number of sections 253

4-12. Sectional analysis for control volume 11-01: (a) number of particles distribution for diferent number of sections; (b) location of the volume 11-01; (c) total number of particles for different number of sections 254

4-13. Sectional analysis for control volume 11-10: (a) number of particles distribution for diferent number of sections; (b) location of the volume 11-10; (c) total number of particles for different number of sections 255

4-14. Comparison of silver mass distribution (Kg) for the 20 and 40 volumes models in volume 11-10 and 496.5 seconds transient time of the basic model (logarithmic scale) 258

4-15. Comparative CPU times for different iterative methods with the case of no fission product for the input decks of the first and second verification, using a 1.2 GHz CPU, an 256 Mbytes of RAM. 262

4-16. Variation of CPU time with the number of sections for second verification model: (a) bars representations; (b) best-fit expression for the variation 263

4-17. Comparison of the CPU time of the basic model (20 volumes) and the re-nodalized model (40 volumes) 264

4-18. Agglomeration phenomenological maps: (a) laminar; (b) turbulent (Re=5869); (c) turbulent (Re=79,550) 266

4-19. Deposition phenomenological maps: (a) vertical and laminar conditions; (b) vertical and turbulent conditions; (c) horizontal and laminar conditions; (d) horizontal and turbulent conditions 268

5-1. Phebus experimental facility 276

5-2. Driver core of Phebus Test Facility 277

5-3. Radial Cross Section of the test bundle 281

5-4. Axial cross-section of the test bundle 282

5-5. Location of thermocouples in the bundle: (a) radial; (b) axial 287

5-6. Instrumentation in the experimental circuit 293

5-7. Boundary conditions of the FPT-01 experiment 298

5-8. Phebus FPT-01 parameters and major events....................302

5-9. On-line aerosol monitor signal for Phebus FPT-01 experiment....................307

5-10. Aerosol composition for several transient times for the cold leg 308

5-11. On-Line Monitor signal function for Phebus experiment 312

5-12. Nodalization diagram: (a) test bundle region; (b) experimental circuit 314

5-13. Recommended axial power profile for Phebus experiment 320

5-14. Comparison of outside cladding temperature at the fresh fuel, at 650 mm elevation....................328

5-15. Hydrogen parameters: (a) production rate; (b) total hydrogen produced 329

5-16. Comparison of experimental circuit temperatures: (a) cold leg; (b) hot leg 331

5-17. Comparison of predicted and experimental deposition fractions (%) for the nucleating group along the experimental circuit: (a) silver; (b) rhenium 338

5-18. Comparison of calculated and experimental deposition fractions (%) for the structural materials group along the experimental circuit: (a) indium; (b) cadmium; (c) tin 342

5-19. Comparison of calculated and experimental deposition fractions (%) for the first fission product group along the experimental circuit: (a) cesium; (b) molybdenum....................344

5-20. Comparison of calculated and experimental deposition fractions (%) for the second fission product group along the experimental circuit: (a) tellurium; (b) iodine 347

5-21. Aerosol composition: (a) calculated; (b) experimental 350

5-22. Silver weight distribution function comparison of calculated and experimental data....................355

5-23. Dynamics of the deposition in the experimental circuit for several species 356

5-24. Activity of Ag^{110m}, obtained by γ spectroscopy 357

6-1. Comparison of different regulatory containment source terms with the experimental data and calculated values for the Phebus FPT-01 experiment 364

A-1. Typical vapor diffusivities....................380

A-2. Equilibrium concentrations using Scdap approach....383

B-1. Spherical polar coordinate system adopted....386

B-2. Relative increase of agglomeration kernel for gravitational-diffusive synergy....390

B-3. Directions of the themphoretic and gravitational deposition velocities in a horizontal pipe, according to the particle position....393

Abstract of Dissertation Presented to the Graduate School
of the University of Florida in Partial Fulfillment of the
Requirements for the Degree of Doctor of Philosophy

DEVELOPMENT OF FISSION-PRODUCTS TRANSPORT MODEL IN SEVERE-ACCIDENT SCENARIOS FOR SCDAP/RELAP5

By

Eduardo Henrique Rangel Honaiser

December 2003

Chairman: Samim Anghaie
Major Department: Nuclear and Radiological Engineering

The understanding and estimation of the release of fission products during a severe accident became one of the priorities of the nuclear community after 1980, with the events of the Three-mile Island unit 2 (TMI-2), in 1979, and Chernobyl accidents, in 1986. Since this time, theoretical developments and experiments have shown that the primary circuit systems of light water reactors (LWR) have the potential to attenuate the release of fission products, a fact that had been neglected before.

An advanced tool, compatible with nuclear thermal-hydraulics integral codes, is developed to predict the retention and physical evolution of the fission products in the primary circuit of LWRs, without considering the chemistry effects. The tool embodies the state-of-the-art models for the involved phenomena as well as develops new models.

The capabilities acquired after the implementation of this tool in the Scdap/Relap5 code can be used to increase the accuracy of probability safety assessment (PSA) level 2, enhance the reactor accident management procedures and design new emergency safety features.

CHAPTER 1
INTRODUCTION

Overview

Nuclear power plants design is based on the principle of “defense in depth,” which is translated in multiple barriers to the release of fission products to the environment. The first barrier is the fuel cladding (metallic tubes housing the fuel elements). The second, and third barriers are provided, respectively, by the primary circuit and the containment. During a severe accident, the first barrier is partially or totally lost.

Accordingly, the fission products source term of a severe accident is estimated by dividing the calculation into two separate calculations, which are the release of fission products from the primary circuit to the reactor containment and the release from the containment to the external environment. This difference is made as a consequence of the distinctions existent on the thermal-hydraulic conditions, and phenomena affecting the fission products. This research focuses on the first calculation.

The research of the release of fission products from the primary circuit to the reactor containment is divided into three major fields. The first is the release from the fuel to the coolant channel. The second is their transport through the primary circuit via convection, where the fission products can assume the form of vapor or aerosol, depositing onto the structures of the primary circuit, or being transported to the containment. The third is the chemistry field, which studies the chemical reactions between fission products and bulk materials, and among themselves, in the fuel and primary circuit regions, as well as the effects of radioactive decay in the evolution of the fission products. Inside these fields, several phenomena occur, caused by different mechanisms. The aerosol deposition over the primary circuit structural walls, for instance, can be caused by diffusion, turbulence and temperature gradient.

This research comprises the second field (transport of fission products in the primary circuit), which provides, ultimately, the containment-source term. A containment-source term complete description comprises the amount of fission products released to the containment, their release-time behavior, and their chemical and physical form, i.e., the chemical species under which the fission products present, and whether the fission product is in vapor or aerosol form. The calculation involves a set of time-dependent equations, which performs mass balances among pre-defined states, coupled to transport terms.

Research Background

Before the TMI-2 accident (1979), two studies were used as the basis on fission products release and transport in support of reactor-accident analysis of source terms. Both the TID-14844 (1) and the 1975 Reactor Safety Study (WASH-1400) (2) use extremely simplified models, based on poor models and unrealistic assumptions.

The low radioactive release that occurred in the TMI-2 accident led to significant international efforts to reassess the technical basis for estimating LWRs source terms from severe accidents. It became evident from these assessments that phenomena associated with primary system fission products release and transport, including fission products vapor and aerosol retention on the walls of the primary circuit and vapor-aerosol chemistry, which had been ignored in the past, have major roles in realistic estimations of accident source terms (3). Knowledge about these phenomena needed to be enhanced.

Improvements in understanding and modeling of fission-products behavior have occurred through three major activities. The first activity was the realization of separate effects experiments and theoretical model developments to study each field and specific phenomena in the field. The development and validation of theoretical or empirical models for aerosol deposition caused by temperature gradient are examples of such activity. The development and selection of mathematical models are treated in Chapter 3.

The second activity was to integrate the solution of the problem, i.e., how to couple the fields and even in each field how to provide a feasible mathematical basis for the coupling of several phenomena. This was achieved through the development of the fission product transport equations, which is also treated in Chapter 3.

Finally, there is the activity of coupling an integrated fission products model with a thermal-hydraulic calculation code. This activity is completed through the performance of large-scale experiments to investigate integrated phenomena and evaluate computer code performance. The coupling of the thermal-hydraulic code Scdap/Relap5 and the developed fission products transport model is treated in Chapter 4, and the modeling of a large-scale experiment to perform the preliminary assessment of the model is performed in Chapter 5. In the next paragraphs, a historic description of the research on the behavior of fission product in light water reactors is performed, highlighting the most important model developments and experimental programs.

The fission-products codes and experiments are divided in several categories. The separate-effect experiments are the ones treating only a unique phenomenon, and normally are used to evaluate correlations and theoretical models of that phenomenon.

The Tuba experiment, for instance, is a separate effect experiment used to assess the thermophoretic deposition of the aerosol on structural surfaces.

The field-integrated models or field-integrated experiments deal with the phenomena in a specific field. The fission products transport code developed in this research is an example of such a field-integrated model, because it involves all the phenomena of the fission products transport field.

The integrated fission products behavior code or experiment is the one modeling or with occurrence of phenomena in the three major fields, and the integral codes or experiments are the ones having thermal hydraulic/severe accident calculations or events coupled with fission product behavior modules or measurements.

The release of fission products from the fuel was first modeled in the early eighties using a highly empirical approach. Under this guideline, the Nuclear Regulatory Commission (NRC) funded a series of experiments at the Battelle Columbus Laboratories (BCL), which led to the BMI-2104 series of reports (4), and the purely empirical release model Corsor. This model was later refined by the Oak Ridge National Laboratory (ORNL), using the BCL experiments to obtain diffusion coefficients for the Booth (5) diffusive model, generating the Corsor-Booth model (6) (1989), a semi-mechanistic model. Later (1993), the Argonne National Laboratory (ANL) developed Fastgrass (7), a highly mechanistic model, considering other processes than diffusion.

Experiments that have been used to assess and develop models of the release from fuel to coolant channels are the Organization of Economic and Culture Development (OECD) Loss of Fluid Test (LOFT) FP1 (8) and FP2 (9) tests, performed at the Idaho National Engineering and Environmental Laboratory (INEEL), the ORNL HI (10) and VI

(11) tests, the Severe Fuel Damage (SFD) tests (INEEL) (12) and Annular Core Research Reactor (ACRR) tests at Sandia National Laboratories (13). Assessments of these experiments using the described models and the comparison of experimental data to the calculated values showed that the Fastgrass mechanistic model better predicted the release from the fuel (3).

The transport of fission products in the primary circuit system is modeled based on the state of the fission product and the transformation between states. Aerosol, vapor and structural surfaces are the used states. The research in this area involved the development of models and realization of separate-effect experiments of the processes by which the fission products change from one state to the other, as well as integrated equations solution and experiments. In these integrated codes and experiments, the several processes of state modification are considered simultaneously. The separate-phenomena experiments and modeling review is presented in Chapter 3. Thus, the following review is restricted to the integrated transport codes and experiments.

Two developments of the early eighties were used as the basis for the integrated transport field code developments. The Reactor Aerosol Formation and Transport (RAFT) code was developed (14) by the ANL under sponsorship of the Electrical Power Research Institute (EPRI). Simultaneously, the BCL developed the Trapmelt (15). These two basic models were used in all transport programs developed afterwards. These models were repeatedly improved or replaced and tested against experimental data, resulting in the current state-of-the-art models, such as the Japan Atomic Energy Research Institute (JAERI) Aerosol Retention-Transport (ART), and the French Institut de Protection et de Surete Nucleaire (ISPN) Sophie (16) and Aerosim B2 (17), which were merged in the Sophaeros code (18). These codes also contain new processes modeling, such as aerosol re-suspension and nucleation.

In the experimental area of fission products transport in primary circuits, the major transport integral experiments were the Markiven Test, a multi-nationality financed program in Sweden, the Large Aerosol-Containment Experiment (LACE) and the Aerosol Transport Test (ATT) experiments (ORNL), all described in the work of Wright et al. (19). The previously mentioned LOFT and SFD can also be used to assess fission products transport, as well as the currently-under-development Phebus (20) series of tests.

The chemistry field is the less understood, modeled and assessed field in the fission products behavior. The large number of materials and elements, the lack of thermo-chemical data, and difficulty in the chemical conditions reproduction in small-scale experiments contribute to the difficulty of the task. Furthermore, both heterogeneous and homogeneous reactions occur in the fuel and bulk region. Reactions of the fission products with structural materials can also be important.

Regarding the activity of mathematically solving the problem, in the three fields the mathematical representation of the physics is achieved through mass conservation equations, yielding systems of first order differential equations, most of the time non-linear. In the mechanistic release model, mass is balanced in the granular regions, whereas in the transport field, the mass is balanced between the aerosol, vapor and surface states. The aerosol conservation equation is particularly troublesome due to the intra-state phenomenon of agglomeration and the dependency on the particle size. Several published works were devoted to the numerical treatment of this equation. Charm (21) and Maeros (22) are finite-difference particle size discretization based methods, whereas Lemmon and Marwill (23) developed a discrete-ordinate based method. Besides the aerosol equations, usual numerical difficulties, such as non-linearity, stiffness, and convergence, are encountered.

Integral fission products behavior codes are the Source Term Package Code (STPC) and Victoria. The STPC, which joins the Corsor release model with the Trapmelt transport code, was developed by the BCL (24). Victoria (25) is a highly mechanistic code, using Fastgrass/Corsor-Booth in the release and Charm and Trapmelt models in the transport calculation. It was developed by the ANL. In addition, Victoria has a mechanistic chemical calculation.

Integral codes are the codes that integrate the fission products behavior with thermal-hydraulic and severe-accident phenomena calculations. The United States integral codes are the Melcor, Scdap/Relap5 and Maap. Melcor (26) was developed at SNL and has extended capability to the containment. Scdap/Relap5 (27) was developed at the INEEL, and will be extensively analyzed in the next chapter. Maap (28) was developed by the Nuclear Industry, and sponsored by the EPRI. From other countries, the Escadre (29) is the most important fission products behavior code, and works coupled to the Cathare/Ichare code. The EPRI also developed the Siam (30) code, which is the merger of Cormlt (a core degradation code), Psaac (a thermal hydraulic code) and RAFT.

Integral experiments were conducted at the INEEL and were mentioned before (the LOFT and SFD). Under execution is the most important fission products experiment, the Phebus, in Cadarache, France. The experiment is a reactor in scale, with a primary circuit and containment, with several state-of-the-art measurement devices.

Objectives

The goal of this research is to develop a tool capable of calculating the fission products transport into the primary circuit of LWRs under severe accident conditions, implement in Scdap/Relap5, and testing it. This goal is achieved by defining the characteristics of the model, developing the numerical transport equations, selecting or developing models for the physical phenomenon involved, implementing and verifying the implemented model, and performing a preliminary assessment of the model.

The first step to reach the goals is to understand the problem and establish the characteristics the model should have. The characteristics of the model comprise the definition of environmental conditions and the scope of the model. This step included the understanding of light water reactors operation under normal and severe accident conditions, the understanding of the numerical and mathematical methods employed in the thermal-hydraulic nuclear codes (also known as best-estimate codes), the understanding of severe accident phenomena and evolution, and the comprehension of the scope of each field of fission products behavior (release, transport and chemistry). Chapter 2 treats these issues in the research perspective.

Chapter 3 starts from the physical states of the fission products and derives the analytical equations. Departing from these equations, the numerical form of them is derived. Then, the mathematical solver of the system is described, as well as the necessary constraints to make the mathematical solution consistent with the physics of the problem.

Then, Chapter 3 promotes a survey of the existent models describing the physical processes taking place in the transport of fission products. A literature research is performed and selective criteria are used to define the models. New models are also developed, when necessary.

Chapter 4 describes the programming features of Scdap/Relap5 and the modular structure of the fission-product transport package. The used routines are rapidly described. The developed code is then tested about the more important aspects, such as discretization in space and aerosol size, negative masses and mass conservation. A new model is developed in Appendix B to take into account the synergisms in the aerosol processes, based on a sensitive analysis established in this chapter.

In the Chapter 5, a survey of the more important experiments that can be used to assess the models and the code is performed, establishing a validation matrix. The performance of the code is assessed against the experimental data of the Phebus FP-1 experiment.

During the development, weaknesses of the model and necessities are identified, to establish a consistent orientated basis for future works needed for improvement of the developed model, as well as to obtain an integral fission products code coupled to Scdap/Relap5. The achievements of the research and the future work are presented in Chapter 6.

CHAPTER 2
CHARACTERISTICS OF THE MODEL

This chapter is dedicated to the determination of the physical and mathematical conditions imposed by a severe accident in light water reactors and the program Scdap/Relap5 respectively, in order to establish characteristics the developed model must have in terms of environmental and numerical conditions. Still in this chapter, the scope of the model referring to physical processes is clearly defined.

In order to reach the first purpose, a basic description of light water reactors (LWR), focusing on the major components and engineered safety features, is necessary, laying down a fundamental understanding of the operation of LWR and identifying the possible pathways for the release of fission products from fuel to the containment. Next, severe-accident scenarios and phenomena are described, in order to identify the thermal-hydraulic behavior and parameters during the most probable sequences. Following that, there is a description of the major features and mathematical methods of the Relap/Scdap5 program.

The transport of fission products in the primary circuit of a commercial nuclear reactor is preceded by the release from the fuel. The released quantities have direct dependency on the previous irradiation history, compiled by the fission products initial inventory. During the release and the transport, fission products can change their chemical nature decaying or reacting chemically. To reach the second purpose of the chapter, the release, transport and chemistry processes are introduced and its inter-linkages are defined, isolating what constitutes the scope of the here developed transport model.

Light Water Reactors

Commercial reactors base their operation on the fission process, an interaction between a neutron and a fissile or fissionable nucleus, producing as a result an average number of neutrons and two or more fission products, as shown in Equation 2-1 and represented in Figure 2-1 (32). The interaction is exothermal, and the energy is carried by the fission products, the resultant neutrons, gamma rays and neutrinos.

$$n + U^{235} \longrightarrow FP_1 + FP_2 + \nu n + \gamma + \underline{\nu} \quad \text{(Equation 2.1)}$$

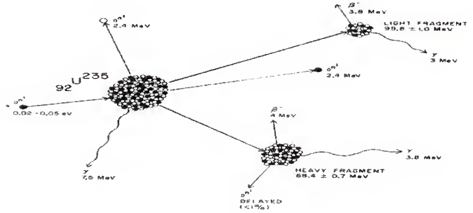

Figure 2-1. The fission process in U235 isotope (32)

Knowing that the parameter ν is greater than one, one may infer that the interaction can sustain itself. In order to sustain a reactor's operation, each neutron must generate, on average, one neutron in the reactor. Under this condition, the reactor is called critical. The conduction of a nuclear reactor can be summarized as based on the maintenance of criticality and control of the power by neutrons population control.

The fission interaction is much more likely to occur in the thermal energy range (up to 1.86 eV). In order to take advantage of this property, most reactors reduce the neutrons' energy by moderation (neutrons from fission are released with energy in the order of magnitude of MeVs), accomplished by scattering with light elements, resulting in a higher average energy loss. Hydrogen is, therefore, an ideal moderating element. Light water reactors use water as the moderator because of its hydrogen content, its capacity as a coolant, and its other characteristics. Nuclear fuels are in the form of ceramic UO_2, with up to 4.2% being U^{235} (enriched uranium).

Nuclear fuel exists in several shapes, but the cylindrical shape is the one used in LWRs. The fuel is fabricated in pellets with 9 to 12mm of diameter and height of typically 15mm. These pellets are put together vertically and housed in a thin tube made of zircaloy (0.5 to 0.8 mm thick), called cladding. The set is commonly referred to as pin, and they are arranged in square lattices called assemblies. Mechanical resistance of the assemblies is obtained through spacer grids. The assemblies are arranged in the center of a cylindrical vessel, the pressure vessel, and the location where they stay is the reactor core. Outside the reactor, the primary circuit is responsible for the water circulation and is composed of a piping system and several equipments. The region surrounding the rods is called the coolant channels and the center-to-center distance between two adjacent channels is called pitch (typically 15mm).

In the next sections, the two types of light water reactor are described, and their major components and engineered safety features are identified. This information, together with the typical thermal-hydraulic parameters, provides the basis of understanding the severe-accident progression in the next section. Furthermore, the pathway and the materials in contact with fission products are identified.

The principle of operating a LWR is to heat water, thereby changing it into steam that is used to generate electricity in a steam turbine. Two designs currently are in use in the industry: the boiling water reactor (BWR) and the pressurized water reactor (PWR). The basic components of a LWR are the reactor, the reactor coolant pump, the pipes, the turbine, the condenser, and the emergency safety features. In a PWR, in addition to the foregoing, the pressurizer, the main feed water pump and the steam generator are found.

Water in the core is heated by the heating of the fuel material, mainly by the deposition of fission products energy in the fuel. Other mechanisms are the fast neutrons' newly born kinetic energy and gamma ray energy released at the time of fission. Another important mechanism, responsible for six percent of the deposited energy, is the decay energy of the fission products that occurs in the fuel and structural materials. This decay energy is particularly important because it cannot be stopped, whereas the fission process and all deposition mechanisms associated with it can be stopped, through the insertion of neutron-absorbing materials (commonly boron, indium or cadmium) in the form of control rods. The control rods, therefore, constitute the major engineered safety feature in a LWR.

Boiling Water Reactor

The boiling water reactor (BWR) has the simplest configuration, having only one cycle or circuit. As shown in Figure 2-2 (33), the water is heated in the core and exits from the coolant channels as a steam-water mixture. The steam is separated and dried in the steam separators and the driers, respectively, which are in the upper part of the core (see Figure 2-3). After leaving the driers, the steam goes directly to the turbine, where part of it is changed into work and used to generate electricity. The exiting fluid condenses in the condenser and is pumped into the reactor again. This water is mixed with the water flowing downwards from the separators and the driers, and the re-circulation pumps force the combined flow into the lower plenum.

The pathway for fission products released from the fuel passes through the upper plenum, the separators and the pipes. Most of the escaping fission products would also pass through the drier assembly, although there is a small bypass path around the drier. It is estimated that ten percent of the steam bypasses the drier. Also, the re-circulation piping is a pathway for fission products. Typical parameters, under normal operation, of a large BWR are shown in Table 2-1.

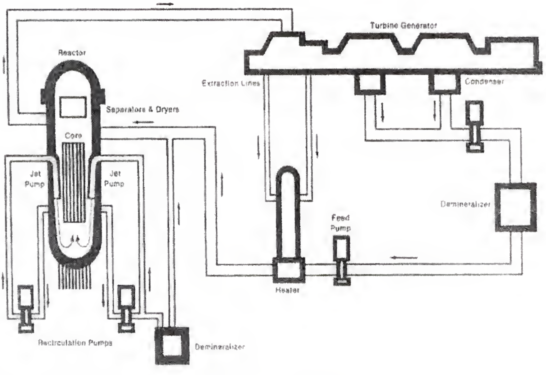

Figure 2-2. Boiling water reactor major components (33)

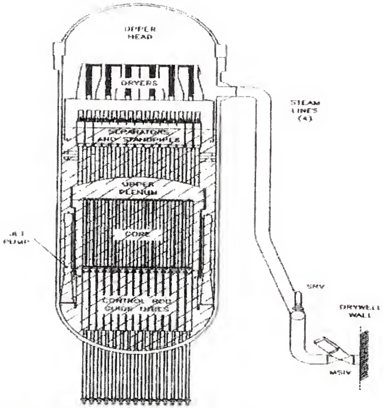

Figure 2-3. Reactor composition of a BWR (33)

Table 2-1. Typical parameters for a large BWR (34)

I. Thermal Hydraulic	
Thermal power	3579 MW
No of loops	2
Pressure	7.17 MPa
Steam Mass flow rate	13,100 Kg/s
Core Mass Flow Rate	153,000 Kg/s
Aver. Inlet temperature	278 C
Aver. outlet temperature	288 C
Linear gen. heat	19 KW/m (average)
Power density	54.1 Kw/l
II. Geometric	
II.a Core	
Fuel rods (pin)	12.27mm (d)x 4.1m (H)
Cladding thickness	0.813 mm (zircaloy)
Rod Pitch	16.2 mm
Assembly Arrangement	8 x 8
II.b Primary System	
Re-circulation pipe diameter	0.5 m (Stainless Steel)
Steam line pipe	0.7 m (Stainless Steel)

The BWR has four separate engineered safety systems (32): the high-pressure core spray system (HPCS), the automatic depressurization system (ADS), the low-pressure core spray system (LPCS), and the low-pressure coolant injection system (LPCI). If the HPCS cannot maintain water level or if it fails, reactor pressure can be reduced by independent actuation of the ADS so that flow from the LPCI and LPCS systems provides sufficient cooling. The ADS employs safety relief valves (SRV) for discharging steam to the pressure-suppression pool.

Pressurized Water Reactor

The pressurized water reactor (PWR) operates with two circuits or systems. The primary coolant system consists of a multi-loop arrangement. Depending on the design, a PWR can have two or four loops. A loop consists of the coupling of a steam generator and a reactor coolant pump, as can be seen in Figure 2-4 (33), which represents a four-loop configuration. The pipe that leaves the reactor vessel and enters the steam generator is called the hot leg, whereas the pipe exiting the steam generator is called the cold leg. A pressurizer is situated in one of the hot legs. It is designed to maintain the pressure of the flow into the primary system at the desired level.

In the PWR, the secondary system is identical to that of the BWR, but the steam generator instead of the reactor supplies the heat. The steam flows through a turbine, a condenser and a feed-water pump. The scheme of a PWR is shown in Figure 2-5 (34). Auxiliary systems, such as the emergency safety systems components are located in the auxiliary building.

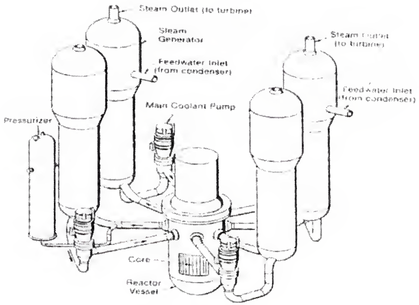
Steam Outlet (to turbine)
Steam Generator
Feedwater Inlet (from condenser)
Steam Outlet (to turbine)
Feedwater Inlet (from condenser)
Main Coolant Pump
Pressurizer
Core
Reactor Vessel

Figure 2-4. Pressurized water reactor loops (33)

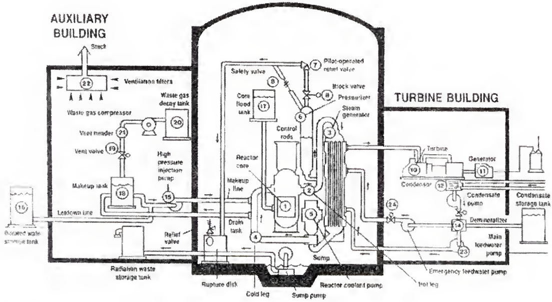

Figure 2-5. Pressurized water reactor plant scheme (34)

From Figures 2-4 and 2-5 the pathway for fission products may be inferred. The fuel-released fission products flow through the coolant channels, pipes, bends, contractions and singularities of the primary system, and through the steam generator.

The pathway depends on scenario conditions, such as the location of a pipe break. Typical parameters for a PWR are shown in Table 2-2.

Table 2-2. Typical parameters for a PWR (34)

I. Thermal Hydraulic	
Thermal power	3411 MW
No of loops	4
Pressure	15.5 MPa
Mass flow rate	17,400 Kg/s
Aver. Inlet temperature	286 C
Aver. outlet temperature	324 C
Linear gen. heat	17.8 KW/m (average)
Power density	105 Kw/l
II. Geometric	
II.a Core	
Fuel pellet	8.2 mm (D)x 13.5 mm (H)
Fuel rods (pin)	9.5mm (d)x 4.0m (H)
Cladding thickness	0.57 mm
Rod Pitch	12.6 mm
Assembly Arrangement	17 x 17
Equivalent diameter	3.37 m
II.b Primary System	
Hot leg	0.79 m
Cold leg diameter	0.74 m
II.c Steam Generator	
Number of tubes	4,674
Tube length	1.7 m
Shell Diameter	3.35 m
Tube diameter	1.9 cm

In the event of a loss of coolant from the primary circuit, a series of components inject enough water to prevent excessive overheating of the fuel. To ensure that the system is adequately reliable, it usually consists of three or four identical but completely independent sub-systems; sufficient water would be provided by only two of the four sub-systems. The systems are either active (activated by the operator or by control systems) or passive. An active system is composed of a low-flow, high-pressure pump-injection system (HPIS) and a low-pressure, high-flow pump-injection system (LPIS). A passive system consists of a tank, filled with borated water pressurized to 3 MPa by a nitrogen overpressure and released into the primary circuit via a non-return valve.

Severe Accident

A severe accident in a LWR is a sequence of abnormal events in the operation of the reactor, leading to the loss of the original geometry of the core elements. Currently, severe accidents are not considered in the licensing of commercial reactors; accidents used for licensing purposes are the design-basis accidents (DBA). Severe accidents, on the other hand, are among the beyond design-basis accidents (BDBA).

The interest of this research is to establish ranges and typical parameters for the most probable scenarios, in order to validate assumptions made during the next chapter. The quantities of interest are the transport time of the fission products, the Reynolds number and the fluid velocity throughout the fission-products pathway, the fluid composition, and the temperatures of the fuel and the fluid. The purpose of this section is accomplished providing a general description of the severe-accident phenomena and phases.

Severe-Accident Phenomena

Severe-accident researchers usually divide severe-accident phenomena into the early phase phenomena, the late phase phenomena, and pressure-vessel failure, occurring at the lower plenum. Early-phase characteristics are the initial heating and melting of core structures, with the original rod-like geometry remaining identifiable. During this phase, zircaloy oxidation at high temperatures is the most important process, due to the great amount of zircaloy in the core, the reaction's exothermal character, and hydrogen release, which is hazardous because of its explosive nature. The net results of the reaction are a general increase of the core temperature at the spots where the reaction is occurring, the formation of zirconium oxide, which has low thermal conductivity, and the release of hydrogen, which affects the bulk-gas composition and, thus, the thermal-hydraulic solution. As the reaction rate increases exponentially with the temperature, the energy released in the oxidation can increase rapidly.

Other phenomena in the early phase are the ballooning and the rupture of the cladding. Normally, depressurization of the reactor leads to a greater difference between the internal rod and the coolant channel pressures, deforming the shape of the cladding, which tends to acquire a “sausage” shape. The process intensifies until the time the cladding ruptures. The higher temperature and the formation of zirconium oxide affect the mechanical properties of zircaloy, acting as a secondary factor.

In the late phase, melt relocation occurs. The formation of zirconium oxide is important because it has a high melting point and low thermal conductivity, leading to the melting of the zirconium in the inner layers and its interaction with the fuel matrix (UO_2), forming a Zr-U-O mixture. The result of this interaction is a lower melting point of the UO_2 in its new form. The fuel therefore liquefies; eventually the cladding breaches, and the fuel slumps down in the form of drops.

Similarly, the control rod stainless steel cladding swells and contacts with zircaloy guide tube, forming a Fe-Zr eutectic mixture, which melts at low temperature. This mixture ends up resulting in the breach of the control rod and release of the melted material (the Ag-In-Cd alloy has a low melting point). This molten material can penetrate the fuel cladding, forming a new mixture with uranium, oxides and zirconium.

The destruction of the zircaloy in some regions leaves the upper part of the cladding, which does not experience such a harsh environment, without any structural support, resulting in debris formation. On the other hand, molten material can accumulate, forming pools that slump into the lower head. This molten pool heats the pressure vessel at the lower plenum, eventually causing creep failure of the pressure vessel. The final stage of the TMI-2 core, shown in Figure 2-6, confirms this evolutionary scenario, where a large molten pool formed and debris was deposited above it. The pressure vessel did not fail in the accident, once no significant molten material slumps into the lower plenum.

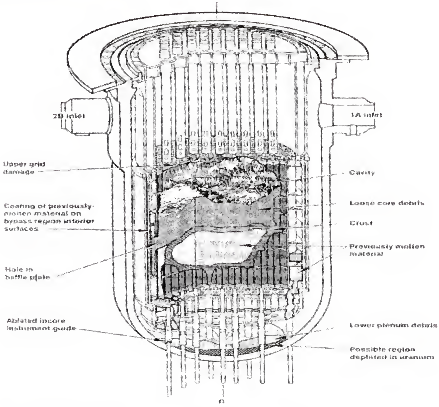
2B inlet
1A inlet
Upper grid damage
Cavity
Coating of previously-molten material on bypass region interior surfaces
Loose core debris
Crust
Previously molten material
Hole in baffle plate
Ablated incore instrument guide
Lower plenum debris
Possible region depleted in uranium

Figure 2-6.Final core condition of TMI-2 accident

Severe-Accident Scenarios

A scenario that leads to a severe accident is composed of two or more simultaneous events, and the results of the severe accident are strongly dependent upon its duration and timing. Therefore, a great number of combinations are possible. In order to fully address the problem, various sequences should be identified and their probabilities evaluated.

The activity of scenarios' identification was addressed by the BMI, under the sponsorship of the NRC (35). The BMI series of reports provides the possible sequences and explains their descriptive symbols. In Table 2-3 below, a summary of the major symbols used in sequence-descriptions is provided. The NUREG 1150 study (36) addressed the probability of several sequences' occurrence.

Table 2-3. Symbols adopted in severe accident scenarios (35)

Symbol	Event
A	Intermediate to large loss-of-coolant accident (LOCA)
B	Failure of electric powered to engineered safety features
S	Small Break LOCA
SGTR	Steam generator tube rupture
D	Failure of ECC system
LOSP	Loss of Offsite Power
T	Transient event (Reactor trip)
M	Failure of secondary system steam relief valves and the power conversion system
L	Failure of the auxiliary feed-water system
B'	Failure to recover either on-site or off-site electric power within 1-3h following the LOSP
V sequence	Failure and leakage of the valves of the LPIS
ATWS	Anticipated transient without scram

The dominant BWR severe-accident sequences are station blackout and Anticipated Transient without Scram (ATWS). However, there are two forms of station blackout (37). Long-term station blackout (LTSB) implies maintenance of reactor vessel-injection capability by means of steam-turbine-driven systems until exhaustion of the plant batteries (six to eight hours after scram), whereas short-term station blackout (STSB) implies independent failure of the steam-turbine-driven injection, leading to a more rapid progression of core damage. An assessment from Peach Bottom (38) shows that about 30% of the risk associated with BWR is assigned to STSB.

A loss of all offsite power prohibits the re-circulation pumps from working. As a result, the reactor is shut down and the main steam isolation valve (see Figure 2-3) is closed. Since no such accidents have ever happened in a BWR, the behavior of the major parameters is evaluated by code simulation. Several references describe the sequences and provide some calculations. What follows depends on the operational procedure of each plant, but the objective is to try to maintain the coolability of the core.

During an ATWS sequence in a BWR, the reactor's safety system fails to trip the reactor. The closure of the MSIV in conjunction with the start of the transient causes a pressure surge in the reactor, tripping the re-circulation pumps. The procedure is to manually insert the control rods and depressurize the reactor, in order to activate the ECCS, providing coolability to the core.

For the PWR configuration, the LOSP and the LOCA are the most probable design basis accidents. The most probable severe accidents are sequences under which this two accidents are accompanied by additional failures that leads to a sever accident occurrence.

The TMLB' is a well-studied scenario presenting the loss of offsite power, accompanied by a failure of the secondary relief valves, the power-conversion systems and the auxiliary feed-water. Coolant discharge initially is intermittent because of cyclic operation of the valves between open and closed set-points. As a result, initial core uncovery, heat-up and melting occur at high pressure, as opposed to the LOCA scenarios, as will be seen later.

The most well-analyzed and comprehended scenario is the LOCA, on which an extensive literature is available. Among the several LOCA severe-accident scenarios studied, much attention has been focused on two. The S_2D is the most extensively considered in LOCA simulations, whereas the V sequence is considered due to the possibility of containment bypass. The S_2D sequences typically result from leakage at a small-to-intermediate rate from the primary system, accompanied by a failure in the ECCS. The V sequence is caused by the failure of the valves isolating the low-pressure injection system from the primary loop. The coolant rapidly discharges through the valves and bypasses the containment, flowing toward the auxiliary building through long, small-diameter piping. During the transient, the loss of coolant results in reduction of the pressure and temperatures' increase. The pressure reduction gradually activates the ECCS that is designed to compensate this loss, by injecting additional coolant. Hence, severe accident in these scenarios should imply deviation from the designed condition, i.e., failure of the ECCS or design failure.

Thermal-Hydraulic Behavior of Severe Accidents

The behavior of most of the scenarios, except for the BWR station blackout, ends up being similar, because they imply in a depressurization, which is not possible without leaking the steam from the primary system through valves. Therefore, some time is spent going through the major events and thermal hydraulic behavior observed in experiments and calculations for these scenarios where depressurization of the primary coolant system happens. The events and behavior is essentially the same for all scenarios, varying the intensity of each phenomenon and duration of the phases, according to the timing and intensity of the failure, and the accident management procedure. Hence, as one should expect, the rate of coolant loss, management measures and thermal-hydraulic characteristics of the plant are decisive for the timing of the following described phases and events, as well as thermal hydraulic response.

The thermal-hydraulic conditions of a severe accident can be summarized, initially, by the energy source, composed of the stored energy of the fuel and by the decay heat, and the reduction of the system's cooling capacity through the loss of coolant or pumping power. Later on, the energy from zircaloy oxidation is added, gradually becoming the major energy source. As mentioned before, the ATWS sequence initially has a super-critical power, but it is reduced to the same source when the control rods are inserted.

The plant's response depends, therefore, on the intensity of the source and the degree of degradation of core coolability. Generally, the response can be divided into the blow-down, heat-up and the re-flood phases.

Depressurization of the primary system, due to the operational procedures or a leak, characterizes the blow-down phase. Two sub-phases are the sub-cooled depressurization and the saturated depressurization. Immediately following the start of depressurization, the pressure rapidly drops to the highest local fluid-saturation pressure, due to sub-cooled depressurization. After the coolant pressure has reached or fallen below the local saturation pressure, boiling starts, and, as a result, depressurization continues at a considerably reduced rate.

During this phase, the fluid temperature tends to decrease because the pressure decreases, and, consequently, so too does its saturation temperature. As the latent heat of vaporization represents a large amount of energy, this phase extends for a relatively long time and ends with the uncovery of the core. As a consequence of the sudden loss of heat from the fuel rods, the large amount of heat stored within the fuel redistributes, leading to an equalization of the internal temperature-distribution tendency. This in turn causes the cladding temperature to rise. Nevertheless, the average core temperature slightly decreases at this phase. During depressurization, several engineered safety features are activated; the progression of the accident depends on which of the ECCS are activated and whether they fail or not.

After the core becomes uncovered, the heat-up phase start; the average core temperature starts to rise rapidly, leading to the initiation of the core's melting and subsequent relocation. This rapid increase is due mainly to zircaloy oxidation and the complete change of the coolant liquid phase into gaseous phase (the latent heat of vaporization has already been "used"). During the heat-up period, damage of the core occurs. The damage extent is determined by the dynamics of the accident related to the action of the ECCS.

The ECCS water begins filling the lower plenum. The re-flood period begins when the water level begins to rise in the reactor, and, as it rises, it gradually reduces the cladding temperature and thus deprives the oxidation of its energy source (that is, zircaloy oxidation is highly dependent upon the cladding temperature), mitigating the accident. Depending on the temperature of the zircaloy, a sharp increase in the temperature has been observed during re-flood in some experiments. This sharp increase was associated with the cracking of the cladding, caused by thermal stresses induced by the great difference between the temperatures of the cladding and of the re-flood fluid, allowing additional zircaloy to be exposed to steam.

Obviously, the evolution of the accident and its consequences are determined by the depressurization rate and the evolution and the intensity of the re-flood. The cladding ruptures only after the uncovery of the core; therefore, for the purposes of the fission-products transport study, the behaviors after core-uncovery are more important than those beforehand.

Under designed conditions, i.e., event sequences considered during the plant design, the uncovery of the core should not happen, or, if it happens, should not be so intense to cause fuel damage. Core uncovery is, therefore, an event present in severe accidents that results in the flowing of only steam in the primary coolant system (single-phase regime).

Figure 2-7 presents the major thermal-hydraulic parameters for the LOFT-LP FP-2 Experiment (10). The experiment is an in pile representation of a PWR in scale 1/500 of a commercial reactor. The experiment set-up is to represent a V sequence, and the depressurization phase can be identified as finishing at 800s transient time, when the cladding temperature starts to increase. This phase extends up to about 1700 s, when the temperature decreases due to the re-flood. The system pressure has a sharp drop of its value, characterizing the sub-cooled depressurization and then starts to fall in a continuously lower rate up to the end of the transient.

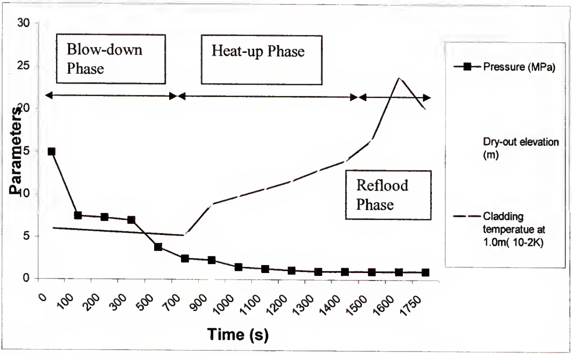

Figure 2-7. LOFT LP FP2 major thermal-hydraulic parameters

Thermal-Hydraulic Parameters of Severe Accidents

Extensive results of severe accident calculations of thermal hydraulic behavior are available in the literature. A compilation of the significant thermal hydraulic parameters for the most important sequences is provided below, based on data of the NUREG 6193 (3) and NUREG 1150 (36). The transient time range corresponds to the uncovery core average time in its minimum time and pressure vessel failure in the maximum time.

Table 2-4. Thermal-hydraulic parameters for the most important severe accident sequences

Parameter	BWR ATWS	PWR TMLB'	PWR S_2D
Pressure (MPa)	7.2-0.1	14.7 14.7-0.2	14.7-0.2
Transient time (min)	40-297	90-295	38-238
Flow regime	Laminar/Turbulent	Laminar/Turbulent	Laminar/Turbulent
Flow velocity (m/s)	1.0-0.001	1.0-0.001	1.0-0.001
Average/Maximum core temperature (K)	667/730- 2123-3000	647-670 2240-2990	580-585 2200-3000
Fluid core temp. (K)	550-1700	550-1400	550-1550

The behavior of the thermal-hydraulic parameters for a S_2D sequence is presented in Figure 2-8. This plot was obtained by Warman et al. (39) as part of the preparations for the Phebus experiment. Notice that the mass flow rate decreases from the start of the transient, whereas the hydrogen mass flow rate increases. When the core collapses, the dislocation of hot materials to the bottom enhances water vaporization, increasing the flow rates.

Average parameters were added in Figure 2-8, from Warman et. al (39), to provide a more complete picture of the thermal-hydraulic conditions during a severe accident. This plotted parametric behavior was obtained from simulation used as basis for the PHEBUS experiment conduction setup.

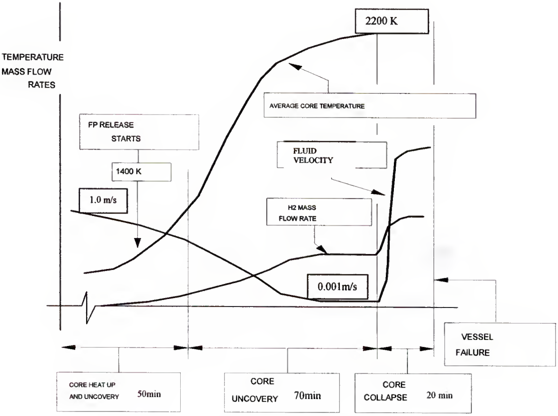

Figure 2-8. Typical average thermal-hydraulic behaviors for S_2D sequence (39)

The Relap/Scdap Code

The Relap5 Code

The Light Water Reactor (LWR) transient analysis code, Reactor Excursion and Leakage Package (Relap5), was developed at the INEEL for the United States Nuclear Regulatory Commission (NRC). Code uses include analyses required to support rulemaking and licensing, audit calculations, evaluation of accident-mitigation strategies, evaluation of operator guidelines, and experiment-planning analysis. Relap5 has also been used as the basis of a nuclear plant analyzer. Specific applications have included simulations of transients in LWR systems such as loss of coolant, ATWS, and operational transients such as loss of feed-water, loss of offsite power, station blackout, and turbine trip.

Relap5 is a highly generic code that, in addition to calculating the behavior of a reactor's coolant system during a transient, can be used to simulate a wide variety of hydraulic and thermal transients in both nuclear and non-nuclear systems involving mixtures of steam, water, non-condensable, and solute. Under this philosophy, Relap allows best estimates of thermal hydraulic results than old methods applied in the nuclear field, which were excessively conservative. Therefore, they can be used conveniently for licensing optimization. Nevertheless, the code cannot be applied for detailed thermal-hydraulic behavior studies, but can be used to obtain boundary conditions for these calculations. As mentioned before, because of the code nature, the Relap code is considered a best-estimate code.

The latest version of Relap5 code is based on a non-homogeneous and non-equilibrium model for the two-phase system that is solved by a fast, partially-implicit numerical scheme, permitting economical calculation of system transients. The objective of the Relap5 development effort from the outset was to produce a code that included important first-order effects necessary for accurate prediction of system transients, but that was sufficiently simple and cost-effective to make possible parametric or sensitivity studies.

The development of the models and code versions that constitute Relap5 has spanned approximately 17 years from the early stages of Relap5's numerical-scheme development to the present. Relap5 represents the aggregate accumulation of experience in modeling reactor-core behavior during severe accidents, two-phase flow processes, and LWR systems. The code's development has benefited from extensive application and comparison to experimental data in the LOFT, PBF, Semiscale, ACRR, NRU, and other experimental programs.

The Relap5 hydrodynamic model is a one-dimensional, transient, two-fluid model of the flow of a two-phase steam-water mixture, that can handle non-condensable components in the steam phase and a soluble component in the water phase (which commonly is boron). The model contains several options, which can be used independently or in combination for invoking simpler hydrodynamic models, including homogeneous-flow, thermal-equilibrium, and frictionless-flow models. The two-fluid equations of motion that are used as the basis for the Relap5 hydrodynamic model are formulated in terms of the volume and the time-averaged parameters of the flow. Phenomena that depend upon transverse gradients, such as friction and heat transfer, are formulated in terms of the bulk properties using empirical transfer-coefficient formulations. In situations where transverse gradients cannot be represented within the framework of empirical-transfer coefficients, such as sub-cooled boiling, an additional model developed especially for the particular situation is employed.

The system model is solved numerically using a semi-implicit, central finite-difference technique. The semi-implicit numerical solution-scheme uses a direct sparse matrix-solution technique for time-step advancement. The user can select an option for solving the system model using a nearly implicit, finite-difference technique, which allows violation of the material Courant limit. This option is suitable for steady-state calculations and for slowly varying, quasi-steady transient calculations.

The Relap5 thermal-hydraulic model solves six differential equations (mass continuity and momentum- and energy-conservation for the liquid and the gas phases) for six primary dependent variables. The primary dependent variables are pressure, phase-specific internal energies, vapor-volume fraction (void fraction), and phasic velocities. The independent variables are time and distance. The model is defined as one-dimensional, two-phase, and non-equilibrium.

The Scdap Code

The Severe Core Damage Package (Scdap) is a package of models and extensions of the Relap5 models, designed to improve the capabilities of Relap5 (40) through the modeling of the severe-accident phenomena and the calculation of their products and the effects of the thermo-hydraulic variables.

The Scdap code models the behavior of the core elements and the evolution of core damage during severe accidents. Treatment of the core elements includes fuel-rod heat-up, ballooning and rupture, fission-products release and transport, and cladding oxidation and embrittlement. Regarding core-damage progression, the code treats zircaloy melting,

UO_2 dissolution, ZrO_2 breach, the flow and the freezing of molten fuel and cladding, and debris-formation behaviors.

Heat conduction in the fuel rods is treated in two dimensions (axial, radial), and the treatment of radiative heat transfer is improved because the higher temperatures of the core make it more important. The zircaloy-oxidation model calculates the hydrogen mass generated, the oxidation energy released, and the thickness of the resultant oxide layer, using an Arrenhius-type correlation with experimentally obtained coefficients.

The Scdap/Relap5 code uses a mechanistic model to calculate the elastic-plastic deformation that can occur in fuel rods during a severe accident. Anisotropic plastic deformation is calculated using the theory of Hill (41) and the Prandtl-Reuss equations that does not take into account circumferential variations in cladding temperature. Cladding failure is predicted by comparing the tangential component of true stress to burst stress, which is obtained experimentally.

The Liquefaction-flow-Solidification (LIQSOL) model calculates the change in fuel-rod configuration due to meltdown, and also calculates the oxidation and the heat transfer occurring at the locations of a fuel rod where liquefied cladding slumps. Fuel-rod meltdown may have a significant impact on the subsequent damage progression that occurs in a reactor core. In some cases, meltdown may result in decreased oxidation of the reactor core, from cladding that slumps to a cooler location. In other cases, meltdown may block the coolant flow, thereby inhibiting oxidation in the reactor core. With the processes it calculates shown in Figure 2-9, the LIQSOL model is designed to calculate these important stages in damage progression. First, it calculates the rate of dissolution of the fuel by the cladding. Then, the model determines the times when and the locations in the fuel rod where liquefied fuel and cladding breach the cladding-oxide shell. Last, the model calculates the downward movement of the mixture from gravity, the configuration and the rate of oxidation of the liquefied mixture while it slumps, and also the same after it has stopped slumping (after solidifying).

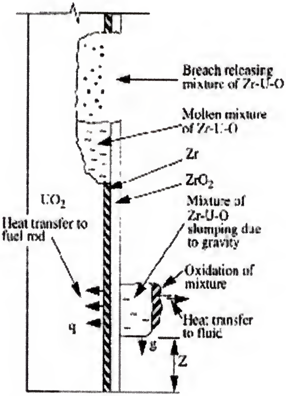
Breach releasing mixture of Zr-U-O
Molten mixture of Zr-U-O
Zr
ZrO2
UO2
Mixture of Zr-U-O slumping due to gravity
Heat transfer to fuel rod
Oxidation of mixture
Heat transfer to fluid
q
g
Z

Figure 2-9. Phenomena in the fuel liquefaction process (40)

Scdap has a creep model to calculate the pressure-vessel stresses and to establish when the pressure vessel fails at the lower head, and a special model to represent the upper plenum structure. There are also Scdap/Relap models, which are extensions of the Relap models: the radiation, the reactor-kinetics, and the nuclear heat power models.

The Scdap/Relap Code

The Scdap/Relap5 is the result of merging the Relap5/MOD3 and Scdap models. The Relap5 models calculate overall RCS thermal-hydraulics, control-system interactions, reactor kinetics, and transport of non-condensable gases.

The Scdap/Relap5 code is capable of modeling a wide range of system configurations from single pipes to various experimental facilities to full-scale reactor systems. The configurations can be modeled using an arbitrary number of fluid-control volumes and connecting junctions, heat structures, core components, and system components. Flow areas, volumes, and flow resistances can vary with time through either user control or models that describe the changes in geometry associated with damage in the core. System structures can be modeled with Relap5 heat structures, Scdap core components, or Scdap debris models.

The method applied in order to model nuclear power plants (NPP) is to divide the NPP or the thermal-hydraulic structure being modeled into coarse regions or nodes. Inside these nodes, heat structures and fuel and control rods can be defined. To link these nodes, the Eulerian approach is used for the hydraulic approach and the integral approach is used to be consistent with the coarse nodalization, applying averaged and macroscopic properties. A sketch of the discretized system is called a nodalization diagram; one for the primary circuit and another for the pressure vessel are presented below (in Figure 2-10 and Figure 2-11, respectively) (44).

Some effort was made by Lemmon and Marwill (23) to model fission products-transport, but these models were never completely implemented or used. These early developments are used along the development in the next chapter, but they suffer significant changes to make the model feasible to be used by the code. Furthermore, the phenomenological modeling is completely new. For these reasons, the research as a whole can be considered a new development where the important work of Lemmon and Marwill is used.

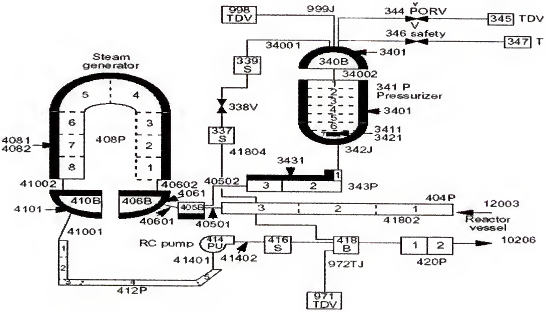

Figure 2-10. Primary circuit nodalization diagram (42)

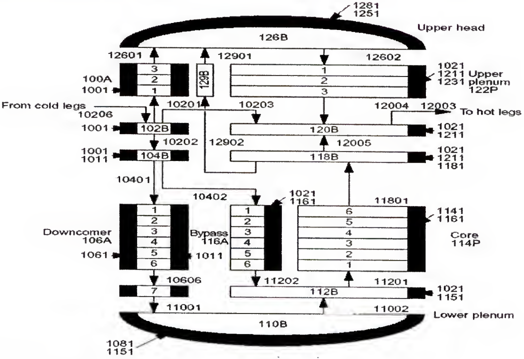

Figure 2-11- Typical nodalization diagram for the pressure vessel (42)

The diagrams above show that special elements are available in Scdap/Relap5 in order to model NPP components, such as pumps and valves. Also, in Figure 2-11, one can see that the core has about ten nodes. Each node, therefore, is 0.4 m long. Typical time-steps are on the order of 0.1 s for the phase when the early phase of a severe accident and one or two orders of magnitude less for the late phase.

Hence, Scdap/Relap5 is a thermal-hydraulic code designed to perform transient and steady-state NPP calculations. In order to achieve this goal, the code employs a coarse spatial discretization of the system, a one-dimensional solution of the basic conservation equations for the two phases, and a semi-implicit time-advancement scheme. Additional models were added to account for severe-accident phenomena. By the end of this research new capability will be available.

Fission-Products Behavior

The fission-products transport problem solution has dependencies on phenomenological occurrences and on the thermal-hydraulic conditions of the severe accident, and, therefore, on the severe-accident phenomena calculation. A whole picture of the calculation, and the major inter-linkages of the study fields are provided in Figure 2-12 below. The dependencies of the transport on thermal-hydraulic parameters are obvious, because the fission products are transported with the fluid velocity and flow conditions and temperatures as well as material surface temperatures affect the transport phenomena. The thermal-hydraulic parameters are directly affected by severe-accident phenomena and, hence, indirectly affect the transport. In addition, the release of fission products affects the fluid composition, changing its properties.

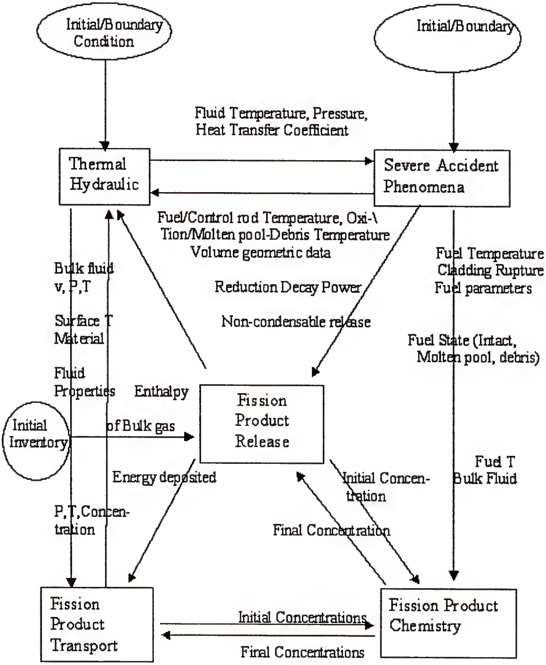
Initial/Boundary Condition
Initial/Boundary
Fluid Temperature, Pressure, Heat Transfer Coefficient
Thermal Hydraulic
Severe Accident Phenomena
Fuel/Control rod Temperature, Oxi-\ Tion/Molten pool-Debris Temperature Volume geometric data
Fuel Temperature Cladding Rupture Fuel parameters
Bulk fluid v, P,T
Surface T Material
Reduction Decay Power
Non-condensable release
Fuel State (Intact, Molten pool, debris)
Fluid Properties
Enthalpy of Bulk gas
Fission Product Release
Initial Inventory
Energy deposited
Initial Concen-tration
Fuel T Bulk Fluid
P, T, Concen-tration
Final Concentration
Fission Product Transport
Initial Concentrations
Final Concentrations
Fission Product Chemistry

Figure 2-12. Fission-products behavior modules and their inter-linkages among themselves and with other calculation modules

In this Section, the focus is on the fission-products behavior understanding and inter-linkages determination, in order to clearly define the scope of the development and provide a general view of the field, introducing its nomenclature and peculiarities. Researchers have divided the study of fission-products behavior in three major fields, as mentioned in Chapter 1, and shown in Figure 2-12. The fission-products release is related to the behavior of the fission products while in the fuel region, and has as initial condition the initial inventory of fission products. The fission-products transport takes care of the fission-products behavior once released from the fuel into the bulk fluid region. Processes that are common to both regions were differentiated, given its implementation complexity. These processes are called inter-species processes, and comprise the chemical inter-species reactions and radioactive decay. The release and transport, on the other hand, are known as intra-species processes, because they do not imply changes in the speciation. In the next sub-sections, a basic theoretical review of these fields is provided. Other vital aspect for fission-products calculation is the importance of each chemical element for the transport calculation.

Initial Inventory of Fission Products

Fission products have excess neutrons, i.e., a high neutron-proton ratio. Hence, the fission products decay through β^- decay and γ^- associated radiation, retaining their original mass number. Another distinguishable feature is that fuel can stay for up to three years in the reactor. Therefore, from the birth of the fission product to the time that the transient (that is, the severe accident) begins, two processes can take place. The fission products can decay or a neutron can capture it. A comprehensive treatment of the fission-products initial inventory, therefore, involves two phases: first, the birth of the fission product, and second, the processes from the birth to the onset of the calculation time.

The fission product's birth is the fission process. Therefore, birth depends on the reaction rate of the fission together with the spectrum of the fission, which is the probability-distribution function of each isotope per fission-event. The fission reaction rate is calculated by reactor physics means, whereas the fission spectrum is shown below, in Figure 2-13.

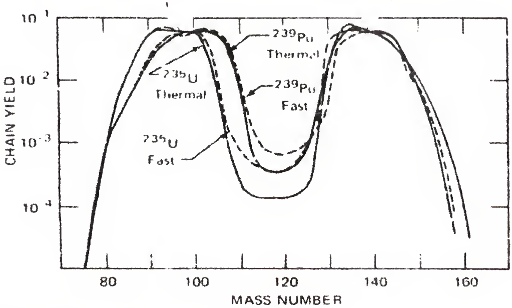

Figure 2-13. Fission-product spectrum (43)

Figure 2-13 shows the fission-product spectrum, which illustrates that the probability of the release of the fission products of a given mass number is a function of the fissile isotope and the neutron energy. For plutonium and fast fissions the curve tends to be flatter. Because of the build-up of plutonium from uranium transmutation, there is a shift into the spectrum as the fuel is burned during the time it stays in the reactor. Also, the amount of fission due to fast neutrons is important. Therefore, the spectrum has a moderate dependence upon reactor physics. After the birth of the fission product, it undergoes several decay processes up to the stable form because it is highly unbalanced in its neutron-proton ratio. The scheme of this decay process through to the stable form is called the decay chain, which is identified by its mass number. A typical decay chain for the mass number 135 is presented below.

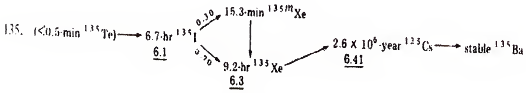

Figure 2-14. Decay chain for mass number 135 (43)

The half-lives of radioisotopes vary from days (short-lived isotopes) to years (long-lived isotopes). Another competing process for isotopes is the capture of a neutron by the fission product. The dynamics of the problem are complex. Fission products are constantly being generated, and they decay in long decay chains. The time can range from hours (trace-irradiated fuel) to years. The fission-products inventory, therefore, is dependent upon reactor physics, fission rate and fission energy-distribution and depletion conditions (inventory of fissile actinides), and irradiation time.

The mathematical solution of the problem is a set of ordinary differential equations where the coefficients represent the physical processes involving the isotopes. The system is advanced up to the desired time. Then, the elemental isotopes are merged to determine the elemental initial mass. Other simplified approach exists that uses decay rates analysis, resulting simple linear dependence on the burn-up, which is called elemental yield. In Scdap/Relap5, initial inventory can be user input or the code calculates initial inventories using the elemental yield technique that means, based on the specified fuel burn-up.

Table 2-5 presents a typical initial inventory for a PWR 3412 MW end-of-life, three-cycle fuel, presented in the NUREG-4467 (44). The Table was reduced from 60 to

43 most significant elements. This initial inventory was obtained using the ORIGEN code (45), the program more used for this purpose. Actually, the ORIGEN code calculates 500 nuclides from 89 elements. However, estimative of the inventory of activation products from control-rod materials is not of interest to this study and was eliminated.

In the first column of Table 2-5, the 43 isotopes of 25 elements that could be important for the transport are presented. The two subsequent columns present the inventories of these radionuclides (atomic gram). In the next columns, the half-life of each nuclide and the fractional release rate at 1800 C are presented. The half-lives are obtained from the Chart of Nuclides (46). The fission product release rates are obtained from the NUREG-0772 (47).

Importance of Fission Products

Nuclear fission of uranium in the core of a reactor produces a variety of radioactive materials (more than 800 isotopes). In addition to the large number of fission-produced nuclides, there are radioactive products from activating the control rods materials, from the structural materials and the bulk fluid, from transmutation because of neutron capture, from various decay reactions, and from transformation of uranium into other actinides. The characteristics of radioactive fission products are of interest in the modeling of their release and transport. The actinides' transmutations and the characteristics of radioactive fission products are important for the determination of the fission-products initial inventory. The structural materials are important because they nucleate aerosols and these aerosols play an important role in the fission product containment-release modeling.

Table 2-5. Simplified fission-product inventory for end-of-life fuel PWR 3412 MW (45)

Nuclide	Mass (at-g)	Half-life (s)	FR (1/min)
Co-60	9.95 E 00	1.66E8(5.26 y)	5E-5
Kr-85	1.99 E -01	3.38E8(10.7y)	5E-2
Kr-87	2.30 E -02	4.56E3(1.26h)	5E-2
Kr-88	6.87 E -02	1.02E4(2.83h)	5E-2
Sr-89	3.81 E +01	4.36E6(0.14y)	3E-4
Sr-90	4.06 E +02	9.15E8(26y)	3E-4
Sr-91	3.74 E -01	3.43E4(9.52h)	3E-4
Sr-92	1.12 E -01	9.76E3(2.71h)	3E-4
Y-90	1.10 E -01	2.30E5(63.9h)	8E-5
Y-91	5.27 E +01	5.06E6(0.16y)	8E-5
Y-92	1.46 E –01	1.27E4(3.53h)	8E-5
Zr-95	7.32 E +01	5.53E6(0.17y)	8E-5
Zr-97	8.36 E –01	6.05E4(1.68h)	8E-5
Nb-95	3.71 E +01	3.02E6(0.09y)	1E-5
Mo-99	3.48 E +01	2.38E5(66.1h)	8E-3
Ru-103	3.77 E +01	3.40E6(0.10y)	1E-5
Ru-106	8.19 E +01	3.18E7(0.9y)	1E-5
Rh-105	6.32 E –01	1.28E5(35.5h)	8E-5
Sb-127	2.25 E –01	3.28E5(91.1h)	4E-3
Sb-129	3.76 E –02	1.58E4(4.38h)	4E-3
Te-127	2.23 E –02	3.38E4(9.39h)	1E-2
Te-129	9.49 E –03	4.2E3(1.17h)	1E-2
Te-129m	1.71 E +00	2.89E6(0.08y)	1E-2
Te-131m	1.23 E –01	1.08E5(30h)	1E-2
Te-132	3.15 E 00	2.81E5(78.1h)	1E-2
I-131	5.38 E 00	6.95E5(8.04d)	5E-2
I-133	1.22 E 00	7.49E4(20.8h)	5E-2
I-134	5.64 E –02	3.16E3(0.87h)	5E-2
I-135	3.64 E –01	2.37E4(6.58h)	5E-2
Xe-133	7.46 E 00	4.54E5(5.25d)	5E-2
Xe-135	1.11 E –01	3.27E4(9.08h)	5E-2
Cs-134	7.27 E +01	6.50E7(2.06y)	5E-2
Cs-136	3.89 E –01	1.13E6(14.6d)	5E-2
Cs-137	5.50 E +02	9.51E8(27.06y)	5E-2
Ba-139	7.54 E –02	4.99E3(1.39h)	1E-3
Ba-140	1.65 E +01	1.11E6(11.57d)	1E-3
La-140	2.20 E 00	1.45E5(1.68d)	3E-4
La-142	7.47 E –02	5.72E3(1.59h)	3E-4
Ce-141	3.80 E +01	2.81E6(29.2d)	1E-4
Ce-143	1.56 E 00	1.19E5(1.38d)	1E-4
Ce-144	1.99 E +02	2.46E7(0.78y)	1E-4
Pr-143	1.51 E +01	1.17E6(13.54d)	1E-4
Np-239	3.33 E +01	2.03E5(2.35d)	1E-4

The most abundant fission products and actinides represent about 30 different chemical elements and can be classified into four major groups: noble gases (Xe and Kr), volatile species (I, Cs, Br, Rb), semi-volatile species (Te, Mo, Tc, Sb, Sn), and low-volatile species (Ba, Ru, Sr, Ag, Y, Zr, Nb, Pd, La, Ce, Pr, Nd, Pm, Sm, Eu, U, Np, Pu, Am). The noble gases do not chemically react and do not condense at operational or accident-condition temperatures. The volatile elements are generally regarded as being released in a manner similar to the noble gases. However, they differ from the noble gases in that they can form less volatile compounds. The semi-volatile category includes elements that are not significantly volatile at moderate temperatures in their elemental form, but can become volatile at higher temperatures or as oxides or other compounds. The less-volatile elements tend either to remain in solid solution or to form stable compounds with high melting temperatures.

A coarse estimation of the most important elements can be obtained by applying the fission product release rate to the initial inventory on Table 2-5. Assuming the total transient time of 180 minutes, obtained from the previous chapter, and an average temperature of 1800 C, the release quantities are calculated, neglecting radioactive decay during this period. The relative amounts are then calculated and presented in Table 2-6 below.

The results of this coarse calculation show cesium, iodine, xenon and tellurium as more important elements. Then, ruthenium, barium, molybdenum, krypton, strontium, and antimony appear in a second group and finally lanthanum and cerium in a third group. This result agrees with the common sense established by researchers in the literature about the most important elements, and is also in concordance with the volatility of each element, that is, for more volatile elements the importance is greater.

Table 2-6. Importance of major fission-product elements

Element	Mass(%)	Element	Mass(%)
Co	0.016	Te	5.344
Kr	0.208	I	1.869
Sr	1.358	Xe	11.567
Y	0.016	Cs	43.139
Nb	0.011	Ba	0.506
Mo	4.3	La	0.061
Tc	0.000	Ce	0.012
Ru	0.251	Pr	0.005
Rb	0.002	Np	0.010
Sb	0.028		

Fission Products and Non-Radioactive Material Release

Oxide fuel is fabricated by sintering pellets of pressed powdered UO_2 at high temperature (typically 1700 C) for a certain period of time. By controlling the sintering conditions, material of any desired density between 80% and 98% may be obtained. Typical LWR fuel densities are, theoretically, 90% to 95%. Therefore, the LWR-fuel morphology is characterized by a fine-grained, polycrystalline structure. A typical grain-equivalent diameter is on the order of 10 μm, with porosity defined as the volume of the pores divided by the total fuel volume.

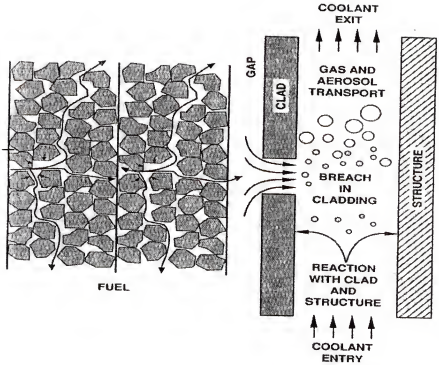

Figure 2-15. The release from the fuel to the coolant channel processes (7)

The release process can be understood as a three-requirements process, as shown in the Figure above. First, the fission product must migrate from the fuel to the gap. Second, the cladding must rupture to allow the fission product to be released to the coolant channel or bulk fluid region and third, the fission product must be transported from the gap to the coolant channel. This section just addresses the first requirement. The conditions for the cladding rupture were previously discussed. The transport in the gap is commonly neglected in the release calculation. Even though the technical basis for this procedure is not presented, the several tools used for calculation of fission product release commonly accept it.

In a severe accident, the fuel can be present in intact state, or as debris or liquid (molten pool, fuel liquefaction). Different mechanisms prevail, according to the fuel's state. In the following sections, the major mechanisms corresponding to each state are described, as well as their second-order effects.

Release from intact fuel

Fission products are considered released from the fuel when they reach any space that is connected to the free volume in a fuel element. This free volume or gas-collection zone can be the gap between the fuel and the cladding or the open porosity, that is, the porosity that communicates directly with the gap; cracks, bubbles, inter-linkages and pores communicating to the fuel cladding are the most important types of open porosity. For practical purposes, fission products have the capacity to dislocate only when in gaseous form.

Concern with the behavior of fission-produced gases (43) started at the late 1950s. By that time, release from the fuel was treated by classical solid diffusion theory, in which the gases diffuse as atoms from the fuel matrix move to a surface that communicates with the gap. It soon became obvious that the diffusion medium could not be the entire fuel pellet, and to account for this discrepancy the fuel was considered as being composed of many small spheres, with spaces in between large enough to permit easy escape of the gas. The size of the equivalent sphere was adjusted to produce agreement with experimental data. This equivalent size showed consistency with the grain-boundary size, showing that the grain boundary serves as a pathway for the fission-gas release, and that the release process is intimately related to the fuel's microstructure.

However, closer examination of experimental results still showed significant departures from ordinary diffusion theory. Experimental fuel examination demonstrated that fission products become trapped in fuel-matrix defects. The "defects" in a solid that can act as trapping centers can be divided into natural defects and radiation-produced defects. The natural defects are grain boundaries, dislocation lines, closed pores in the as-fabricated fuel, and impurities in the solid. The radiation-produced defects are fission-gas bubbles and solid fission-product precipitates. Current models consider only grain boundaries and bubbles as trapping centers.

Actually, bubbles have dislocation capability, but their mobility is significantly less than the gas-diffusion mobility, especially at lower temperatures. For higher temperatures the bubble movement should be considered. Also, as stated before, the bubbles at the grain boundary gradually form an inter-linkage tunnel, which serves as a pathway to vent the gas atoms from the inter-granular bubble to the open porosity. Therefore, bubble-trapping most of the time serves to retard gas release, but eventually it can result in a bubble inter-linkage, which facilitates release.

The physical processes of "entrapment" are nucleation and coalescence. Nucleation is produced by the chance encounters of wandering atoms; coalescence is the atomic capture by existing bubbles, which yields the bubble's growth. Other physical processes are the migration of bubbles and of gas atoms to the grain boundary.

Further investigation revealed that gas-atom and bubble migration is caused by diffusion (called random migration), but the steep temperature gradient also provides a significant driving force for bubbles and gas atoms, in so-called biased migration. Also, it was realized that the traps could be destroyed by natural thermal annealing or by fission fragments (i.e., fission-induced), a physical process called atom re-solution.

In analyses made up to the present, grain boundaries were assumed stationary. Nevertheless, it is known that at temperatures of approximately 2000 K grain boundaries move and grains grow. Small gas bubbles in the path of a moving boundary are swept along with it, whereas large bubbles, because of their higher drag force, detach from the grain boundary and are absorbed into the grain.

Two other mechanisms can be responsible for the release of fission gas, but, in the presence of high temperatures (above 1300 K) and steep temperature gradients, they are negligible: direct flight from the fission product (recoil) or a collision cascade with a stationary gas atom near the surface (knockout). Considering that the fission products are released isotropically, and given the range of fission products, the amount of fission gas released by these mechanisms is quite small.

The importance of each mechanism was summarized by Olander (43). At low temperatures (less than 1300 K), the mobility of fission-gas atoms is too low to permit atomic movement, and the fission gases freeze into the fuel matrix. In this condition, recoil and knockout are the only active mechanisms, but, again, the volume of gases released is quite small. At temperatures between 1300 and 1900 K, atomic migration, immobilization of gas atoms by defects, and re-solution become important, but in any event the bubbles do not have enough mobility to migrate considerable distances. All of the physical processes can happen, however, at temperatures greater than 1900 K.

A representation of the possible states of the fission products conveniently shows the various physical processes that accelerate or slow their release, in which we are most interested. Figure 2-16 below shows the states and the physical processes involved in the release from intact fuel.

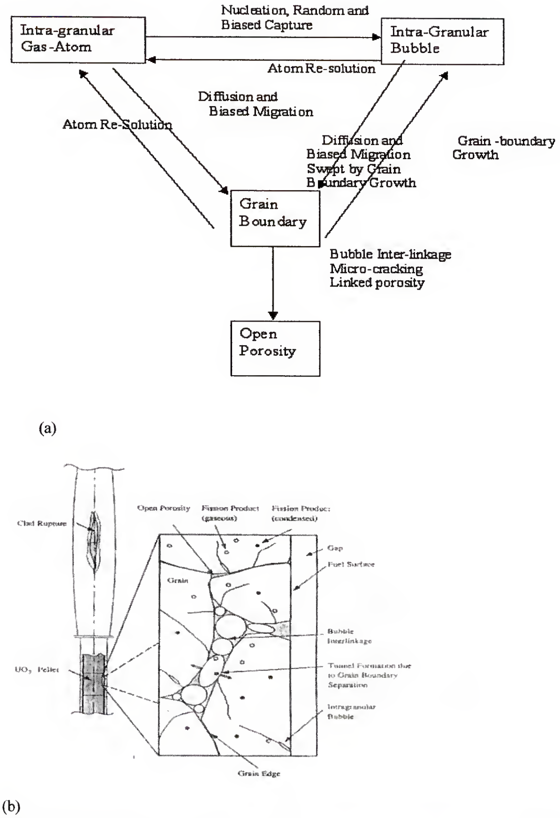

Figure 2-16. Physical processes and states for release from intact fuel (a) schematic (b) physical representation (7)

As stated before, fission products must be gaseous in order to have significant mobility. Hence, the capacity to exist in gaseous form, the volatility, is an important property of fission products. The physical property associated with volatility is saturation vapor pressure, which is dependent upon the temperature: the greater the temperature, the greater the saturation vapor pressure; and the greater the saturation vapor pressure, the more easily it can remain in vapor. As mentioned before, because of the importance of volatility in the release process, the most abundant fission products are classified according to their volatility.

An important second-order effect is the hyperstoichiometry of the UO_2. The uranium dioxide fuel may become oxidized to varying degrees during normal irradiation or during severe-accident conditions. This hyperstoichiometry is caused by fission, which liberates the oxygen atoms, thereby increasing the oxygen-to-metal ratio. The net result of this hyperstoichiometry is increased diffusion coefficients and also, consequently, higher release rates for many fission products.

Release from debris

As mentioned before, a debris bed can form during a severe accident when structural support is lost or when the zircaloy embrittles during the re-flood phase. In debris beds formed by any of these mechanisms, the mean particle size is about 1 mm and is related to the cracking pattern within the fuel caused by power changes associated with reactor start-ups and shutdowns. This particle size is two orders of magnitude larger than the fuel grain. As a consequence, the release of noble gases and volatile fission products from a debris bed should not vary significantly from those released from intact fuel.

Release from molten pool

In the molten pools as well as in the regions of fuel dissolved by α-Zr(O) contact, examinations of the TMI-2 and SFD cores showed that bubble dynamics dominate the release of fission gases and volatile fission products. The dominant mechanism of bubble rise in a molten pool, for bubbles with diameter less than 0.3 μm, is volume diffusion, whereas for bubbles larger than 1 μm in diameter, viscous rise is the dominant mechanism (shown in Figure 2-17 (7)).

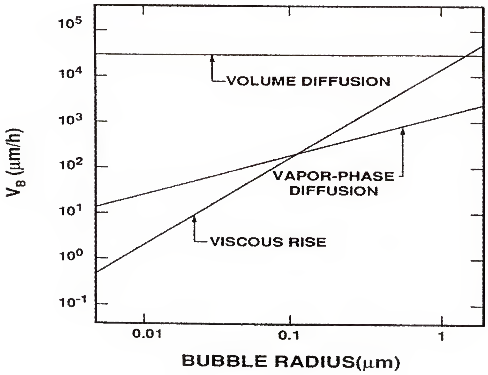

Figure 2-17. Migration processes for bubbles in molten pools (7)

Release from control rods and structural materials

The materials of the control rods, fuel and the structural components have unique features that make them very important in the progression of fission-products transport: non-radioactive nature and low vapor pressure. The structural materials are especially important because after their release, most of them will rapidly nucleate into aerosols, and, as will be seen later, the aerosol particles provide important surface areas for vapor condensation.

Control rods normally are enclosed in a stainless-steel (Fe, Ni and Cr) cladding. Other structural materials are the zircaloy (98.5% Zr and 1.5% Sn) fuel cladding and the inconel spacer grids. Pressurized water reactors use Ag-In-Cd control rods in stainless steel cladding (80% Ag, 15% In and 5% Cd) that are housed in zircaloy guide tubes, whereas BWR use a boron-carbide material (B_4C). The vapor-release process depends upon the material's vaporization, but the kinetic barriers to the process are not understood; it is known, however, that it is dependent on temperature and system pressure. In PWR, it has been observed in experiments that control rods fail at about 1500 K at low pressures and at 1700 K at high pressures. These materials constituted 45% of the non-fission materials of the SFD-4 experiment, distributed in the following manner: 40% of Cd, 3% of Ag and 2% of In. Notice that Cd is the most abundant element, even though it is present in smaller amounts in the PWR control rod, because of its higher vapor pressure. However, the major aerosol source in severe accidents is the Ag, due to its lower vapor pressure and surface tension, as explained in the Chapter 3. These materials represent a significant portion of the non-fission products released. Regarding the fuel cladding, the vapor pressure of tin is much higher than of zirconium, having superior released masses than zirconium, even tough the initial inventory of tin is more than one order of magnitude lower than the zirconium initial inventory.

Uranium was also identified as a potential aerosol source, mainly due to the enormous presence of uranium dioxide in the reactor core. Uranium was identified in the

SFD and Phebus experiments, in the form of aerosol U_3O_8, which is chemically more stable than UO_2.

In Chapter 1, the major release models were described, ranging from mechanistic to empirical models. Empirical evidence has shown that the Fastgrass model is better. Scdap/Relap5 uses Paragrass, which is a simplification of the Fastgrass. A review of these simplifications is a recommended future work as a part, together with this research, of an effort to improve the fission product behavior model. In Chapter 5 (preliminary assessment) known released inventories are used to avoid relying on the current release model.

Also important is the review of the control rods and structural release models currently under usage in Scdap/Relap5. The current model is based on the empirical observations of the Severe Fuel Damage test. Therefore, is based on scarce data and no evaluation of the procedure never existed. Again, known inventories are used in Chapter 5, to avoid carrying errors from the release to the transport.

Release profile

The variation of the released mass with time is an important feature to be known because it has influence in the fission products source term of the containment. The behavior following presented is a general description, but differences in the timing exists according to the element, as will be seen in Chapter 5.

The release of fission products to the cooling channels starts with the cladding rupture, but not significant amount is released by this time due to the low level of fuel temperatures. The first strong release of fission products happens in the first oxidation peak, i.e., the oxidation of zirconium becomes auto-catalytic, leading to a temperature escalation at the hot spots up to the zirconium consumption, when the temperatures decrease. The fission-products release has a steep increase, following the temperature behavior.

Following the severe accident progression, material is re-located to the bottom in the debris or molten pool form. This phase is longer and normally is associated to higher releases (for most species). A second oxidation peak exists, because of the intact fuel fallen in the lower plenum of the reactor. Therefore, the release of nuclear materials vapors to the cooling channels is divided into three phases, the first oxidation phase, the main release phase (molten pool formation phase) and the second oxidation phase. This description is correspondent to a complete accident, where both oxidation and molten pool formation occur.

This behavior can be seen in Figure 2-18 below (48), which is the On-line Aerosol Monitor (OLAM) signal for the Phebus FPT-01 experiment. The OLAM signal is based on the attenuation of the light by aerosol particles, i.e., the signal decreases as the aerosol concentration increases. As most of the fission products are present in the aerosol, their presence can be roughly estimated using the OLAM signal. Figure 2-18 shows that the first strong peak in the transient represents the first oxidation process, then a less steep region corresponds to the molten pool formation release that ends in a second peak (second oxidation).

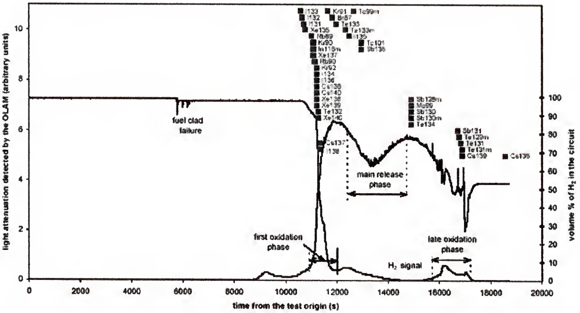

Figure 2-18. The OLAM signal for Phebus FPT-1 experiment (48)

Chemistry

The inter-species processes, radioactive decay and chemical reaction are here referred as chemistry. They are following briefly described, referring their importance, methods, and difficulties.

Radioactive decay

Once the radioactive isotope is involved in release or transport, the radioactive fission products undergo decay in their decay chains. The problem, when modeling radioactive decay, is that for the other modules of the fission-products calculation the isotopes are treated as elements, but an accurate radioactive decay model should consider each different elemental isotope. This approach increases significantly the number of species to be tracked, increasing the computational time. Fortunately, the half-life of the more present isotopes for each element is in the order of days or years. Since the transport time is in the range between one and three hours, it can be assumed that the radioactive decay will not affect significantly the calculation if neglected. This is an expected behavior since as long as the isotopes start to decay, they tend to accumulate in the long-lived isotopes in its chain. The only case when the short-lived isotopes will be significant is the case of trace-irradiated fuel. However, it is highly unlikely to occur accidents with trace-irradiated fuel, and, if it happens, the fission product inventories are small.

Chemical reactions

The thermodynamic conditions in the fuel and in the primary circuit, especially the high temperature and the variety of materials present, make these regions highly susceptible to chemical reactions. The several isotopes in the fuel and in the fluid have the tendency to combine among themselves and with the bulk materials, forming compounds or species. For fission products researchers, species can represent either element in the atomic or the molecular form or in compounds. Distinction is also made between the gaseous and the condensate states of the species. The major property used in the chemistry calculations is chemical potential, which measures the potential of the species to be formed. The species' chemical potential is a function of temperature and of pressure. Also reaction-kinetics parameters, such as reaction constants, can be important, but chemical calculations under usage in codes assume thermodynamic equilibrium. In the next two sections, the major qualitative aspects of the chemistry in the fuel region and in the primary circuit are discussed.

Chemistry plays an important role in calculating the behavior of the fission products. The major effect is change in volatility: when the element changes from one species to another, the average volatility of the element changes; volatility is a major property for both release and transport. In addition, certain important properties (such as the diffusion coefficients) vary from species to species.

Chemical reactions in the fuel region

The environment in the fuel region is characterized by the highest temperature in the core and the solid UO_2 matrix as predominant chemical species. Furthermore, oxygen potential develops because of the degree of hyperstoichiometry of the UO_{2+x}. This stoichiometric variation is caused by an increase in the oxygen-to-metal (O/M) ratio during irradiation, due to the different oxidation states of the fission products and the fuel. This deviation from stoichiometry directly impacts speciation.

This analysis considers only the major elements in terms of release, which are Xe, Kr, I, Cs, Te, Ba, Sr, Sb and Mo. Most of these elements are inert with respect to the fuel matrix. Cesium is an element having more affinity with UO_2; it tends to form urinates and molybdates. Tellurium is considered non-reactive with the fuel, and the alkaline earth elements tend to form oxides. Under normal circumstances, and if the opportunity occurs, iodine prefers to exist predominantly as the stable species CsI or as some other iodine species, rather than as the atom I or as the molecule I_2.

The observations set forth above support the dominant reactions encountered within the fuel:

$$2Cs(g)+UO_2(c)+O_2(g) \rightarrow Cs_2UO_4(c)$$

$$2Cs(g)+Mo(c)+2O_2(g) \rightarrow Cs_2MoO_4(c)$$

$$Cs(g)+I(g) \longrightarrow CsI\ (c)$$

$$CsI\ (c) \longrightarrow CsI\ (g)$$

$$Sr(s)+1/2\ O_2(g) \rightarrow SrO(c)$$

$BaO(c) + UO_2(c) + 1/2\ O_2(g) \longrightarrow BaUO_4(c)$

$Ba(s) + 1/2\ O_2(g) \longrightarrow BaO(c)$

$BaO\ (c) \longrightarrow BaO\ (g)$

$SrO\ (c) \longrightarrow SrO\ (g)$

Notice that in the first two reactions, the cesium changed from gas to condensate. This reaction, therefore, reduces the amount of cesium released. For the alkaline earth elements Ba and Sr, their oxide forms also have lower equilibrium vapor pressures.

Chemical reactions during transport

The transport environment constitutes a more difficult problem for analysis, because the predominant environment varies in its composition. In addition, the large number of species resulting from fuel and control-rod release and from chemical reactions yields a very complex environment, and a rational and feasible treatment of the problem is a very intricate issue, in which one should analyze chemical properties, molar concentrations, chemical reactions kinetics and equilibrium calculation processes. The development of this consistent model constitutes the major future challenge. The difficulties and scarceness in experimental observation, absence of chemical data and mathematical difficulties of the composed problem are the main difficulties of the development. In the next paragraphs, the qualitative aspects of the major interactions and their effect in the fission products behavior are discussed.

Fission-products codes approaches range from mechanistic codes, such as the Victoria code, to fixed species, using simplified assumptions and procedures to form the fixed species. Scdap/Relap5 uses this last approach. The species considered are CsI, CsOH, TeH_2, I_2, Ba, Sr, Te, Mo, Cd, Sn, Ag, In, Zr, U, Ru and Sb. Iodine is assumed in the form of cesium iodide after release and the exceeding cesium assumes the form of CsOH.

The mechanistic solution of the chemistry in the bulk region is the result of balancing the chemical potentials of the several species present in the environment, in order to minimize the Gibbs free energy of the system. In addition, the constraint of closed systems and non-negativity masses are applied. Reaction rates also can be considered, but thermodynamic equilibrium is reportedly (7) feasible to be assumed. Smith and Missen (49) describe mathematical methods of solution of this problem, which results in a set of non-linear ordinary differential equations.

Chemical potential is a measure of the tendency to react: the higher the chemical potential, the greater is the tendency to react. The first term of chemical potential, presented in Equations 2-1 and 2-2, is the standard Gibbs free energy, which is measured for a thermodynamic standard state and for each species. The second term accounts for the amount of the species present in the environment; obviously, the greater the amount, the higher is the probability of reaction. Therefore, the higher the chemical potential, the greater is the probability of reducing its amount, whereas the opposite is valid for lower potentials.

$$\mu_i = \mu_i^0(P_0,T) + RT\ln(P_i / P_0) \quad if \quad i \in g(gas) \qquad \text{(Equation 2-2)}$$

$$\mu_i = \mu_i^0(P_0,T) + RT\ln(c_i V / n_c) \quad if \quad i \in c(condensate) \qquad \text{(Equation 2-3)}$$

$$n_c = \sum_{i \in c} n_i \qquad \text{(Equation 2-4)}$$

Where:

μ_i^0 : standard Gibbs free energy of the pure i th species;
P_i: partial pressure of species i;
c_i: concentration of species i;

$n_{c/i}$: number of moles in condensate phase/of species i in condensate phase.

One simple manner of approaching the problem, which provides some insight in the qualitative behavior of the fission products speciation, is to consider a quaternary system for the major elements (Cs, I, H, O) and to perform separate thermodynamic analysis for the other elements, in order to estimate the predominant species for that element.

Following, a summary of the major aspects and conclusions of the NUREG-0772 (47), which has performed the quaternary study, is done. Later, a thermodynamic analysis for Ba is performed and the possible predominant species for other elements are cited. Thermodynamic data for the species were obtained by Barin (50), Chase (51), Ball (52) and Powers (53). In the light of these two preliminary approximated analyses, the principal points regarding the chemical behavior of the species in the RCS are explained.

In the NUREG-0772 study, temperatures ranged from 600 to 2300 C, pressures from 1 to 150 Bars, hydrogen-to-oxygen ratios from 1.5 to 30, and iodine-to-water ratios (I(moles)/H_2O(moles)) from $2x10^{-7}$ to $2x10^{-1}$, and the cesium-to-iodine ratio was 10. Three major iodine species were I, CsI and HI, whereas the major cesium species were CsOH and Cs.

A qualitative description of the effects of changing the system parameters: temperature, pressure and fission-products concentration on the presence of the species is provided below.

Recall that chemical equilibrium has a dynamic, not static, nature: molecules continually dissociate to atoms, and atoms continually combine to form molecules; equilibrium is attained when the rates of dissociation and of recombination are equal. The probability of dissociation is greater at higher temperatures, but the probability of recombination is not. As a result, equilibrium will be established at a low concentration. For this reason, an increase in I or HI and Cs (or all) was observed at high temperatures, whereas a decrease in CsI was observed.

On the other hand, the potential to combine is sensitive to temperature and the probability of collision, which itself is greatly affected by pressure and concentration. As a result, a greater quantity of CsI was observed when pressure and concentration increased. CsOH was little affected by pressure and concentration (not shown); the cesium atom was always close to hydrogen- and oxygen-containing species. CsOH was affected by the H/O ratio, as the excess amount of hydrogen diluted the oxygen concentration, reducing the probability that oxygen atoms were nearby.

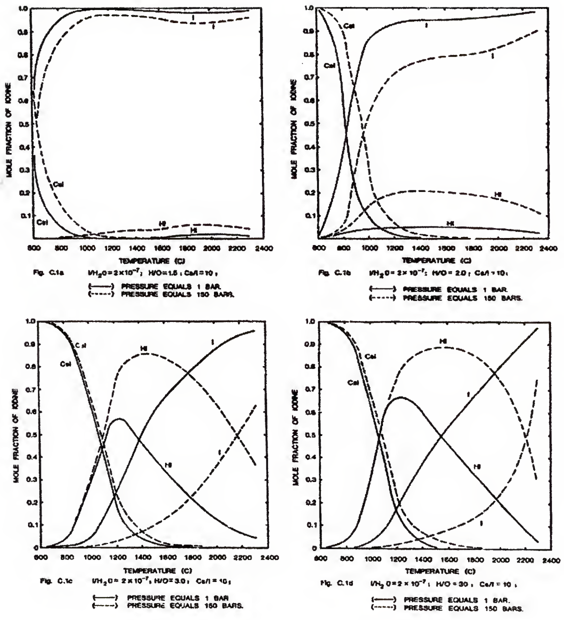

Figure 2-19. Parametric study of the Cs-I-O-H quaternary system in NUREG-0772 (47)

The effect of the increasing H/O ratio is a greater stability temperature of CsI. For instance, for I/H$_2$O ratio of 2x10^{-7} at an H/O ratio of 1.5 (oxidizing), about 50% of the iodine is present as CsI, for a system at 550 C. As the H/O ratio increases to two, the temperature for the same condition is 820 C, and for an H/O of three, the temperature rises to 1150 C. The effect of increasing the H/O ratio is to make CsI more stable. This can be seen in Figure 2-19 above. The same effect is observed by increasing the I/H_2O.

Barium's and strontium's behaviors are very similar. Recalling that these elements are released as oxides, analysis of the free energies showed that BaI_2 is the most stable species, as shown in Figure 2-20, but it is very rare due to its combination probability. Hence, it is consistent to assume that the oxides (SrO and BaO) are the predominant forms of these elements. The formation of these elements has a devastating effect on their volatility, as shown in Figure 2-21, leading to the inference that significant amounts of these elements will be retained in the primary coolant system. For this reason, these elements are considered low volatile elements.

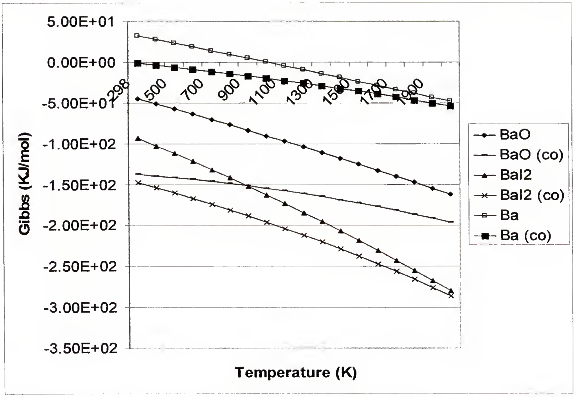

Figure 2-20. Barium standard Gibbs free energy for several species

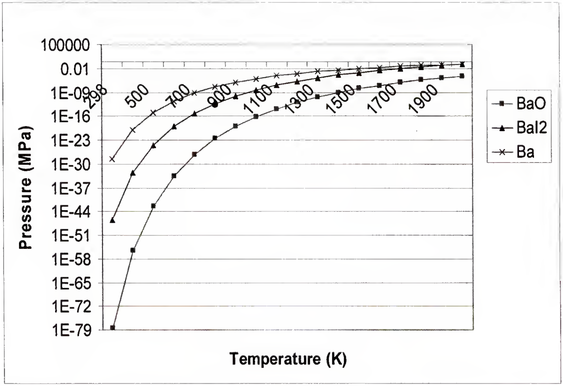

Figure 2-21. Vapor pressure for barium species

Similar analysis can be performed for other elements. For Tellurium, the predominant species are the TeH_2 for reducing environments, or TeO for oxidizing environments. For antimony (Sb), molybdenum (Mo), and ruthenium (Ru), the preferable species possibly are SbOH, MoO_2 and RuO_3, respectively.

For silver, the probable predominant species are Ag_2O_2 or Ag_2O, but no major effect on the volatility results from this change. The probable predominant species of cadmium and tin, however, affect significantly those elements' behaviors. The observation of their free-energy data shows that for both elements, the iodides (SnI, CdI) are more stable, but, due to their combination probabilities, the oxides (CdO, SnO) can be more probable. The effects of speciation are opposed from one species to the other, whereas cadmium's volatility is decreased and tin's is increased. In the oxide form, they have almost the same vapor pressure. For Uranium, both thermodynamic analysis, as well as experimental evidence shows that U_3O_8 is the predominant specie.

The NUREG-0772 results showed that speciation can vary significantly with different environmental conditions, such as temperature and gas composition. Qualitative analysis can indicate predominant species, but, since speciation showed to be dependent upon the environmental conditions, these predominant species cannot be confirmed without strong empirical evidence. Mechanistic calculations, on the other hand, are computational expensive, and thermo-chemical data is scarce. Therefore, as pointed out earlier, speciation is very important for the fission products calculation, and constitutes a major challenge for the future.

Fission-Products Transport

A general picture of the problem was provided until this point, describing the thermal-hydraulic and chemical conditions under which the model must operate and the fission products processes that provide some kind of boundary to the transport (the release and chemistry). In this section, the transport competitive phenomena are listed, to support the definition of the scope of the research.

After leaving the fuel rod, the fission products face a completely different environment, encountering a convective medium with velocities ranging from 0.001 to 1.0 m/s, composed of steam and hydrogen, and having a chemical composition ranging from oxidizing to reducing. The pressure of the primary circuit can range from operational pressure to atmospheric. Also, fluid temperatures range from high values of 1500 K to 450 K, and the fission products will be transported in coolant channels, pipes, singularities (bends, contractions, separators, etc.), contacting different materials, notably, zircaloy, stainless steel and inconel.

Several physical processes can take place during fission-products transport through the primary circuit. First, vapors can settle in the walls of the pipe or the zircaloy-clad coolant-channel walls, by adsorption or condensation. Also, vapor can condense on the aerosol surfaces and, under super-saturation conditions, aerosol nucleation can happen. On the other hand, condensate can re-vaporize and aerosol can be re-suspended.

Fission products in aerosol state can be deposited onto the materials' surfaces by several processes, which can be related to diffusive, field or centrifugal forces. Also, the aerosols can agglomerate among themselves, which is an important process because deposition processes are dependent upon the aerosol size. Settled aerosols can be re-suspended into the bulk flow.

Analogous to what was given for the release process, a representation of the possible states of the fission products and the physical processes from one state to the other, is presented in Figure 2-22. Figure 2-22 (a) is a schematic, whereas 2-22 (b) is a physical representation.

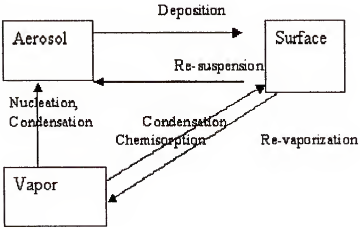

(a)

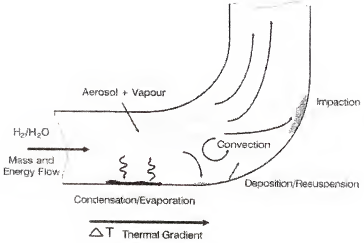

(b)
Figure 2-22. Physical processes during fission-products transport (a) schematic (b) physical representation

Characteristics of the Fission-Products Transport Model

The environment of the problem and typical calculation parameters were defined in the first section of this chapter. The important information for the development of the model is summarized in the Table 2-7 below.

Table 2-7. Environment conditions for the fission-products transport

Parameter	Range
CORE	
1. Structural Materials	Zircaloy, Inconel
2. Fluid Temperatures	600-1800 K
PRIMARY CIRCUIT	
1. Structural Materials	Stainless Steel
2. Fluid Temperatures	500-1500K
3. Structural Temperatures	450-1350K
4. Flow Regime	Laminar or turbulent
5. Fluid Velocity	0.001-1.0 m/s
6. System Pressure	0.1-15.5 MPa
7. Chemical environment	Oxidizing-Reducing
CALCULATION	
1. Nodes	0.01- 1.0 m^3 (Typical 0.4 m^3)
2. Time step	0.1- 0.001 s

In the second part of the chapter, the fission-products behavior modules were defined, and qualitatively described, setting up the inter-linkage of the several modules. In addition, the phenomena corresponding to the transport module are represented in Figure 2-21. Hence, the clear scope of the research can be defined using Figure 2-21 (a). The aerosol agglomeration process is not represented in the Figure 2-21, but it is an important process, as will be seen in next chapter.

Table 2-8. Phenomenological assessment of the fission-products transport

Initial State	Phenomenon	Final State
Vapor	Condensation	Structural Surfaces
Vapor	Adsorption	Structural Surfaces
Vapor	Condensation	Aerosol
Vapor	Nucleation	Aerosol
Structural Surface	Re-vaporization	Vapor
Aerosol	Agglomeration	Aerosol
Aerosol	Deposition	Structural Surface
Structural Surface	Re-suspension	Aerosol

The fission products-transport model is here characterized. The boundary conditions under which the model must operate and the physical phenomena considered by the model are summarized, respectively, in Tables 2-7 and 2-8.

CHAPTER 3
DEVELOPMENT OF THE MODEL

In the previous chapter, the requirements of the model in terms of environmental and calculation conditions, and the scope of the model were defined. In this chapter, that information is used in the development of a mathematical model that represents the fission products transport problem for thermal-hydraulic and severe accident best-estimate nuclear codes. The development was divided into two major activities. First, is the mathematical representation of the problem, departing from the analytical equations to the numerical optimal and feasible form. The second activity is the optimization of the phenomenological modeling of the processes involved in the problem, presented in Table 2-7, providing the coefficients for the equations.

Physical-Mathematical Model Development

Derivation of the Fission Products-Transport Analytical Equations

Recalling that the purpose of the model is to determine fission-products masses released to the containment, the problem can be seen as a mass transport problem, i.e., a mass conservation equation, with a convective term. This kind of equation is known to be a first-order, partial differential equation, with a time derivative term and a convective spatial-dependent term. Hence, the problem is solved by defining the transferences of mass that affect the overall released mass to the containment. These processes were defined in the previous chapter.

A more complete diagrammatic of the processes is provided below, in Figure 3-1, accounting for the agglomeration process. Aerosol particles in typical nuclear concentrations agglomerate, forming a new, larger particle. The aerosol deposition process is dependent on the size distribution of the particle. Hence, the agglomeration process should be accounted for, because it indirectly affects the aerosol deposition and the mass of fission products deposited on the structural surfaces. In addition, the condensation of vapors onto aerosol surfaces is also responsible for aerosol growth. The aerosol behavior modeling introduces a new dependence, the size of the particle.

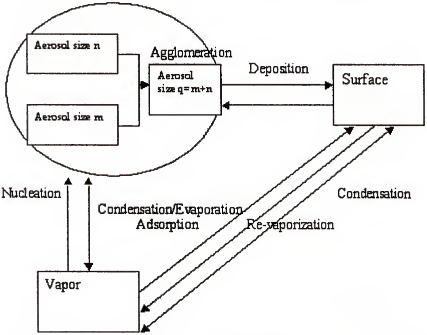

Figure 3-1. Schematic of the states and physical processes in fission products transport

The mass transport equations are defined by the quantities of interest and the rate of physical processes in Figure 3-1, respecting the direction of the process. The surface mass is obviously important because it is the retained mass. The vapor and aerosol masses are important because there are processes whereby they go from one state to the other, and once this happens, the fission product deposits at a different rate. Therefore, the determination of the vapor and aerosol masses is necessary. Furthermore, the kinematics of the movement of the vapor and aerosol need to be modeled. In the surface state, the mass can deposit by adsorption, condensation and aerosol deposition. These states are computed to provide the user of the model with the capability of executing sensitive studies.

In addition to the processes in Figure 3-1, in the vapor and aerosol equations there is the streaming or transport term through convection: as molecules and aerosols have little mass, they follow the movement of the bulk gas (steam-hydrogen mixture).

The vapor transport equation is given by:

$$\frac{\partial m_i(x,t)}{\partial t} = \frac{\partial(\vec{v}\, A_c C_i(x,t))}{\partial x} - \sum_{j=1}^{N} k_{sc,j} A_{sd,j} (C_i(x,t) - C_{eq_i}) - \int_0^{r_{max}} k_{car} A_{ard} (C_i(x,t) - C_{eq_i}) dr$$

$$- \sum_{j=1}^{N} k_{ad,i,j} A_{sd,j} C_i(x,t) + \sum_{j=1}^{N} k_{rev,i,j} A_{sd,j} C_{c,i,j}(x,t) + S_{i,che} + S_{i,rad} + S_{i,ind} - J_i$$

$$(Equation\ \ 3-1)$$

Where:

Ac: Cross-sectional area (m^2)
m_i: Mass of vapor species i (Kg)
v: Fluid velocity (m/s)
C_i: Concentration of vapor species i in the cell (Kg/m^3)
$A_{sd,j}$: Surface deposition area for surface j (m^2)
$k_{sc/e,j}$: Condensation surface deposition velocity for surface j (m/s)
A_{ard}: Surface deposition area for aerosol of r radius (m^2)
k_{acr}: Condensation deposition velocity for aerosol of radius r (m/s)
C_{eqi}: Equivalent vapor concentration (Kg/m^3)
$K_{ad,j}$: Adsorption surface deposition velocity for surface j (m/s)
$k_{rev,i,j}$: Re-vaporization velocity for species i at surface j (m/s)
$C_{c,i,j}$: Concentration of condensate species i at surface j (Kg/m^3)
$S_{i,che}$: Chemistry external source for species i (Kg/s)
$S_{i,rad}$: Radioactive decay external source for species i (Kg/s)
$S_{i,ind}$: Independent external source for species i (Kg/s)
J_i: Rate of aerosol nucleation of species i (Kg/s)

The first term on the right-hand side represents the transport or streaming term. The second and third terms represent the loss of vapor mass due to condensation on the walls of the structural materials, assuming N different surfaces, and on aerosol surfaces. The fourth and fifth terms are, respectively, the loss by adsorption of the vapor species on the surfaces and the gain by re-vaporization. The last three terms are representative of chemistry, radioactive decay, and the independent source. Notice that the first two come from the chemistry and the decay calculations, and can be positive or negative. The independent source is the coupling of the release and the transport processes. These three source terms are here represented to show the external nature of these sources. Aerosol nucleation is represented in the last term. Because condensation onto aerosol surfaces is size-dependent, the loss of vapor mass through this process is integrated across the range of particle sizes.

Additional complications arise when considering the aerosol-transport equation. The first is related to additional dependence upon the size of the particle. The second is the agglomeration process, presented below:

$$\frac{\partial m_i(r,x,t)}{\partial t} = \frac{\partial(\vec{v} A_c C_i(r,x,t))}{\partial x} + \int_0^{r_{\max}} k_{c/ear' \to r}[\ C_i(r',x,t)\ ]dr' - k_{c/ear}[\ C_i(r,x,t)\ ]$$

$$+\frac{1}{2}\int_0^{r} dr' k_{agg}(r',r-r')N(r',x,t)C_i(r-r',x,t) - C_i(r,x,t)\int_0^{\infty} k_{agg}(r',r)N(r',x,t)dr'$$

$$-\sum_{j=1}^{N} k_{dep,i,j} A_{sd,j} C_i(r,x,t) + \sum_{j=1}^{N} k_{res,j} A_{sd,j} C_{d,i,j}(r,x,t) + S_{i,che} + S_{i,rad} + J_i$$

$(Equation\ 3-2)$

Where:

A_c: Cross-sectional area of the cell (m^2)
m_i: Mass of aerosol species i (Kg)
v: Fluid velocity (m/s)
C_i: Concentration of aerosol species i in the cell (Kg/m^3)
$A_{ar'd}$: Surface deposition area for aerosol of radius r' (m^2)
$k_{c/er' \to r}$: Condensation/evaporation aerosol velocity from aerosol of radius r' to r (m/s)
A_{ard}: Surface deposition area for aerosol of $\underline{r}$ radius (m^2)
$k_{c/ear}$: Condensation\evaporation velocity for aerosol of radius r (m/s)
k_{agg}: Agglomeration coefficient for two different particles (m^3/s)
$k_{dep,j}$: Surface deposition velocity for aerosol with radius r on surface j (m/s)
$k_{res,i,j}$: Re-suspension velocity for species i at surface j (m/s)
$A_{sd,j}$: Surface deposition area for surface j (m^2)

$C_{d,i,j}$:	Concentration of aerosol species i at surface j (Kg/m^3)
$S_{i,che}$:	Chemistry external source for species i (Kg/s)
$S_{i,rad}$:	Radioactive decay external source for species i (Kg/s)
$S_{i,ind}$:	Independent external source for species i (Kg/s)
N:	Number of particles in the cell

The first term on the left-hand side of the equation is the transport term. The second is the gain by condensation of vapor species onto aerosols of other sizes, resulting in the size of interest. Notice that the coefficient implies a summation over all of the vapor species, including the species of interest. Therefore, there should be a summation over all of the species, which couples the species equations. In this equation, this summation is not explicitly expressed, but will become clear later, when the condensation coefficient $k_{c/er'\rightarrow r}$ is expressed. In the same manner, the mass of the species of interest in the aerosol size of interest is eliminated from that size by condensation. Notice also that condensation or evaporation couples the vapor equation with the aerosol-transport equation.

The fourth and the fifth terms are related to the agglomeration of two aerosol particles of sizes less than or equal to the size of interest, creating a particle of the size of interest with its respective aggregate mass of the species of interest, and the loss of mass of the species of interest of particle-size of interest, by agglomeration with other particles. The one-half coefficient in front of the agglomeration term accounts for the double counting of the particle-to-particle interactions. The sixth and seventh terms are related, respectively, to deposition and re-suspension of particles. The last three terms are the independent source terms and the nucleation term.

In addition, the deposited mass of vapor (by condensation or adsorption) and aerosol of each species on structural are also quantities of interest. Notice that the condensed and aerosol deposited masses need to be computed, because the re-vaporization and re-suspension model use these quantities. Therefore the three equations below complement the description of the problem.

$$\frac{dm_{chem,i}(x,t)}{dt}=\sum_{j=1}^{N} k_{ch,i,j}A_{sd,j}C_{i}(x,t)-\sum_{j=1}^{N} k_{rev,i,j}A_{sd,j}C_{c,i,j}(x,t) \quad (Equation \;\; 3-3)$$

$$\frac{dm_{cond,i}(x,t)}{dt}=\sum_{j=1}^{N} k_{sc/e,j}A_{sd,j}(C_{i}(x,t)-C_{eq_i})-\sum_{j=1}^{N} k_{rev,i,j}A_{sd,j}C_{c,i,j}(x,t) \quad (Equation \;\; 3-4)$$

$$\frac{dm_{dep,i}(r,x,t)}{dt}=\sum_{j=1}^{N} k_{dep,i,j}A_{sd,j}C_{i}(r,x,t)-\sum_{j=1}^{N} k_{res,j}A_{sd,j}C_{d,i,j}(r,x,t) \quad (Equation \;\; 3-5)$$

Where:

$m_{dep,i}$: Mass of aerosol species i deposited on the structural surfaces (Kg)
$m_{cond,i}$: Mass of vapor species i condensed on the structural surfaces (Kg)
$m_{chem,i}$: Mass of vapor species i chemisorbed on the structural surfaces (Kg)

The equations presented above already consider the code one-dimensional characteristic and take the well-mixed assumption, i.e., the concentrations are assumed as homogeneous inside the cell, and the coefficients are assumed as average coefficients or use average cell properties to be calculated. Besides these, four additional assumptions are implicit in these equations. First, particles are characterized by only their size; that is, particles can have a shape factor, which is a function of size, but particles of the same size must have the same shape factor, which is a good assumption, since the known expressions for shape factors are basically dependent on the aerosol size. Second, transverse gradient effects deposition are not treated in detail. This assumption is consistent with the code's logic, as it is one-dimensional with transverse phenomena treated instead by empirical or special models. Third, particles do not break up into smaller particles. The fourth assumption is that ternary and upper-order collisions may be neglected, which is to be expected because the probability of ternary collision is significantly lower than that of binary collision.

Derivation of the Fission Products-Transport Numerical Equations

It is not feasible to solve analytically the system of equations previously derived, because of their integro-differential nature. In addition, discretization in time and space are determined from the Scdap;Relap5 thermal-hydraulic modeling, having typical cell size and time steps determined in the previous chapter. Hence, a numerical treatment is necessary for the equations. In order to be able to derive the final numerical form of the equations, two preliminary issues need to be treated, which are the convective term and the particle size-dependence of the aerosol-related terms in the equations and their integral terms. In the next sections, these issues are discussed, before the presentation of the final form of the equations.

The convective term

The numerical procedure chosen to treat the convective term is the first-order-accurate, donored-cell-differences approach, presented in Equation 3-6, to be consistent with the numerical treatment to the convective term in other modules of the code.

$$\frac{\partial}{\partial x}(vc_{v/ai}A_{gz})dx = A_{n+}v_{n+}\left[c_{v/ain-1}f_{n+} + c_{v/ain+1}g_{n+}\right] - A_{n-}v_{n-}\left[c_{v/ain+1}f_{m-} + c_{v/ain-1}g_{n-}\right] \qquad \text{(Equation 3-6)}$$

This equation corresponds to the first term in equations 3-1 and 3-2. The terms f and g correspond to the functions determining the volume from which the species of interest is convected into the cell of interest, and the cell into which goes the species convected from the cell of interest. According to the fluid's velocity, the directions from and to cells are inverted. The terms in Equation 3-6 are:

$c_{v/ai}$: Concentration of species i in the form of vapor or aerosol (Kg/m^3)
$c_{v/ain\pm1}$: Concentration of species i in the form of vapor or aerosol from and to cell of interest n, depending on the direction of velocity (Kg/m^3)
A_{n+}: Area of junction connecting the donor cell to the interest cell (m^2)
dt: Time step (s)
v_{n+}: Velocity of junction connecting the donor cell to the interest cell (m/s)
A_{n-}: Area of junction connecting the receptor cell to the interest cell (m^2)
v_{n-}: Velocity of junction connecting the donor cell to the interest cell (m/s)

The donor-cell parameters are defined in Equation 3-7 as:

$$f_{m\pm} = \left\{ \begin{matrix} 1 \ \ if \ \ v_{\pm} \geq 0 \\ \\ 0 \ \ if \ \ v_{\pm} \leq 0 \end{matrix} \right\} and \quad g_{m\pm} = 1 - f_{m\pm} \qquad \text{(Equation 3-7)}$$

The transport term is the only one that shows dependence upon the adjacent cells. Its decoupling from the equation, therefore, can rather simplify the calculation. The possibility of decoupling the transport term can be evaluated through the comparison of time constants of the convection with the other time constants. The maximum transport velocity is close to 1.0 m/s, as seen in Chapter 2. Assuming an accident length (characteristic length) of 10 m, the time constant of the convection of the fission product from the site of the release to the leakage to-containment location is of 10 s. Typical deposition velocity, as seen later, are of the order of 10^0 to 10^{-3} m/s, but the faster terms always dominate the solution, and an average velocity of 10^{-1} m/s can be assumed, based on observation of the results in the next chapter. The characteristic length of the deposition is given by the cell radius, which has a typical value of 0.3 m. The time constant under this conditions will be 3 s. The convection time constant is 3 times larger than the other processes, given the compared conditions. Therefore, time constant analysis cannot support completely the idea of decoupling the convective term without significant impact on the calculation.

Analysis of Equation 3-6 shows that the convective term is the result of the difference between the velocities multiplied by the cell area and species concentration in the cell of interest and the previous cell, according to the flow direction. The impact of decoupling the convective term deserves a closer examination, aided by the nature of the code numerical solution.

Considering that the convective term is being applied first (before the deposition calculation), the impact would be that a fraction of the fission products that should compete with the other processes in one cell would compete in the next. Hence, it is important to know the order of magnitude of this fraction, and the thermal-hydraulic conditions differences between adjacent cells.

The fraction of transported mass can be estimated considering a typical cell length of 0.5 m, and a maximum and an average flow velocity of 0.5 and 0.05 m/s, respectively. Also, a typical time step, by the time the release occurs can be assumed as 0.005 s (time-step tend to reduce by one order of magnitude during the solution of the fuel damage part of the transient, when the release occurs). Under these circumstances, the transported fraction would be a maximum of 0.5 and typically 0.05 %.

On the other hand, in general terms, fluid and structural surfaces decrease their temperatures as long as they advance in the primary circuit. This difference normally is not very significant, and the effect is that deposition tends to increase progressively along the primary circuit, and the rate of mass deposition increases. Therefore, a compensatory process happens. The transport is advanced, but this advanced mass deposits more quickly.

Since the transported fraction is rather small, the thermal-hydraulic differences between adjacent cells is not significant; and there is a compensatory effect in the transport-deposition process in the decoupling of the convective term, the effects of decoupling probably would not harm the solution. In addition, other codes, such as Victoria and Melcor, already use this decoupling simplification.

Even though there is some evidence supporting the idea of simply decoupling the convective term, it is still not quantitatively proved that the decoupling is completely reasonable. However, the coupling of the convective term is extremely expensive. A solution is achieved by applying the fractional-step method.

Fractional step methods separate the generator of an evolution operator into parts and build a solution over each time step out of fractional steps that resolve the different parts separately. This method has been used with relative intensity in the solution of thermal-hydraulics problems. It had originally been developed by Yanenko (54), who defined and surveyed the several existent techniques.

Two major types of fractional steps methods exist. The time-splitting method entails fractional step methods in which each part, or factor of the evolution operator, appears in one fractional step only. There exist numerous realizations of time splitting in finite-differences applications. Stabilizing correction methods may, on the contrary, involve part of the operator differenced by one technique and other by another technique. The nature of our problem resulted in the selection of the time-splitting method.

The time-step is equally divided. First, the species are transported from cell to cell in their original form. Second, a system of ordinary differential equations is solved for each cell and each species for each time-step. Equation 3-6 provides the transport part of the solution.

The radius treatment and integral terms

The integral terms in Equations 3-1 and 3-2 stem from the radius dependence of some processes. In order to reduce these terms to summation terms and to provide a computer-feasible form of the equations, numerical methods are used. The procedures are basically divided into finite-elements and finite-differences. MAEROS (22) and CHARM (23) are finite-element derivations, and are used in Melcor and Victoria, respectively. Marwil (23) developed an independent discrete ordinates method.

The first two approaches divide the range of particle sizes into several sections or bins, applying a logarithmic scale, given the wide range of possible particle sizes. Particles from agglomeration and condensation are moved accordingly among the several sections. An average radius is then calculated, and used to obtain the coefficients, which are size-dependent. Numerical integration methods, such as the trapezoidal rule, are applied so to replace the integral terms.

In the Marwill approach, the sizes are fixed, according to the number of sections defined. Then the mass of size-changed particles is divided between the adjacent bins, according to an appropriate transfer function. This approach never was used in a nuclear code, but it has a clear advantage for future simplifications. The size of particle is fixed, and, as the particle change-size processes are predominantly dependent on particle size, the coefficients calculation, which takes considerable computational time, can be simplified, resulting in a more efficient model. In addition, the adoption of this new approach is important for determining, in the future, the differences between the various approaches in terms of performance. These two arguments, together with the fact that the method is already partially implemented in the code, support the decision to use the Marwill approach.

The Marwill approach is described next, following the steps to the transformation of the integral terms. Given that one wants to discretize the whole range of sizes into a certain number, N, of bins or sections, their width is given by Equation 3-8:

$$h = \left(\frac{R_{\max}}{R_{\min}} \right)^{1/N} \quad \text{(Equation 3-8)}$$

Where:
h : width factor of the section
Rmax: maximum radius considered
Rmin: minimum radius considered

The sections have the lower limit radius, the upper limit radius and the mean radius. The smaller and larger radii are related through Equation 3-9. In order to be consistent with the logarithmic discretization, the geometric mean is adopted as the mean radius. Beginning from the lower limit and marching towards the upper limit, it is possible to determine the geometric mean of each bin, using Equation 3-10.

$$\frac{R_{l+1}}{R_l} = h \quad \text{(Equation 3-9)}$$

$$\bar{r}_l = \sqrt{R_l R_{l+1}} \quad \text{(Equation 3-10)}$$

Where:
R_l: Radius of the lower limit of l section (m)
R_{l+1}: Radius of the upper limit of l section (m)
r_l: Geometric mean radius of section l (m)

Consider now the physical processes that are able to change the size of aerosols. First, consider the condensation/evaporation term. The Marwill model calculates the final volume of the particle after computing the condensation or evaporation of all of the species over all sections. Then, it locates the sections between which the new particle is located. After that, the procedure is to remove all mass of the considered species from that section and redistributes it among the sections receiving the mass. This operation is mathematically represented by the following operation:

$$\sum_{l'=1}^{B}\{\ f_{l'\to l}[\frac{M_{l',i}}{\Delta t}+k_{c/e,l',i}(C_{i,vap/con}-C_{eq,i})]\ \}-[\frac{M_{l,i}}{\Delta t}+k_{c/e,l,i}(C_{i,vap/con}-C_{eq,i})] \qquad \text{(Equation 3-11)}$$

Where:

$f_{l' \text{ to } l}$: Fraction of aerosol mass from l' section that goes to section l of interest after condensation/evaporation of all species
B: Number of bins (sections)
$M_{l',i}$: Mass of species i in section l' (Kg)
$M_{l,i}$: Mass of species i in section l (Kg)
Δt: Time step (s)
$k_{c/e,l',i}$: Condensation/evaporation coefficient for species i on the surface of aerosol in section l' (m^3/s)
$k_{c/e,l,i}$: Condensation/evaporation coefficient for species i on the surface of aerosol in section l (m^3/s)
$C_{i,vap/con}$: Vapor/condensate concentration in the bulk fluid or aerosol surface (Kg/m^3)
$C_{eq,i}$: Equivalent concentration of species i (Kg/m^3)

The fraction of aerosol mass transferred ($f_{l'tol}$) is calculated by Equation 3-12 below:

$$f_{l'\to l}=1-\frac{\bar{V}_{l+1}-(\bar{V}_{l'}+\sum_{i=1}^{S}k_{c/e,i,l'}(C_{vap/con,i}-C_{eq,i}))}{\bar{V}_{l+1}-\bar{V}_{l}} \qquad \text{(Equation 3-12)}$$

given:

$$\bar{V}_{l+1}\geq(\bar{V}_{l}'+\sum_{i=1}^{S}k_{c/e,i,l'}(C_{vap/con,i}-C_{eq,i})\geq\bar{V}_{l}$$

Where:

$\bar{V}_{l+1}$: Volume geometric mean of aerosol in section l+1

$\bar{V}_{l}$: Volume geometric mean of aerosol in section l

$k_{c/e,l',i}$: Condensation/evaporation coefficient for species i on the surface of aerosol in section l' (m^3/s)

$C_{i,vap/con}$: Vapor/condensate concentration in the bulk fluid or aerosol surface (Kg/m^3)

$C_{eq,i}$: Equivalent concentration of species i (Kg/m^3)

Agglomeration is the other physical process capable of changing aerosol size, which corresponds to the fifth and the sixth terms in Equation 3-2 (the integral terms). In the discrete-ordinate approach, these terms are represented by the following expressions:

$$0.5\sum_{m=1}^{l}\sum_{k=l-1}^{l} f_{mk\rightarrow l}k_{agg,m,k}N_m(x,t)C_{k,i}(x,t)-\sum_{m=1}^{B}k_{agg,m,l}N_mC_{l,i}(x,t) \quad \text{(Equation 3-13)}$$

Where:

$f_{mk\rightarrow l}$: Fraction of particles in section m agglomerating with particle in section k, resulting in a particle in size of interest l

N_m: Number of particles in section m

$k_{agg,m,k}$: Agglomeration coefficient for particles in section m with particles in section k (m^3/s)

$C_{k,i}$: Concentration of species i in section k (kg/m^3)

$k_{agg,m,l}$: Agglomeration coefficient for particles in section m with particles in section l (m^3/s)

$C_{l,i}$: Concentration of species i in section l of interest (kg/m^3)

B: Number of bins

The first term in Equation 3-13 corresponds to the species of interest in other sections going into the section of interest. The second term corresponds to the removal of the species of interest from the section of interest by the agglomeration of particles in the section of interest with particles of other sections.

The fraction of particles that go into section l (the section of interest) from the agglomeration of particles of section m ($m \leq k$) with a particle in section k ($k=l-1$) is given by Equation 3-14 (54):

$$f_{mk \to l} = \frac{\bar{V}_l - (\bar{V}_m + \bar{V}_k)}{\bar{V}_l - \bar{V}_k} \qquad \text{(Equation 3-14)}$$

In this expression, $\bar{V}$ represents the volume geometric mean, and the subscripts correspond to the numbers of the sections where the aerosol is located. An important issue of aerosol treatment is the overspill bin, i.e., the particles that become larger than the upper size range limit. The treatment here used is the overspill deposition. The argument used to justify this is, the aerosols become so heavy that gravitational deposition will dominate their behavior (they will have a very fast gravitational deposition velocity). The theoretical basis for this assumption is provided in the next chapter. Actually, as will be seen in the second part of this chapter, the process is reversed; that is, the upper-size-limit range is determined by estimating the particle size when the deposition velocity is considerably higher than convective velocity.

The evaporation process is not considered in the model, because since the fission product is released in the vapor form, and it is transported to colder regions, condensation is the natural trend. Evaporation during the transport is feasible only under special circumstances, where: (1) The mass is already in the condensed form; (2) A surge in the temperature makes the heat-up rate increase extremely faster than the transport velocity. The combination of these two conditions is extremely rare in severe accident conditions. Hence, neglecting the evaporation process is computationally advantageous (it reduces the problem size) and viable.

The equations, in their final numerical form, are presented next:

$$\frac{dm_{i,vap,z}}{dt}=-\sum_{j=1}^{N} k_{sc,j}A_{sd,j}(C_{i,vap/can}-C_{eq_i,j})-\sum_{l'=1}^{B}k_{c,l',i}A_{a,l'}N_{l'}(C_{i,vap/can}-C_{eq,i})$$

$$-\sum_{j=1}^{N} k_{ch,i,j}A_{sd,j}C_i+\sum_{j=1}^{N} k_{rev,i,j}A_{sd,j}C_{c,i,j}-J_i \qquad (Equation\ \ 3-15)$$

$$\frac{dm_{i,ch,z}}{dt}=\sum_{j=1}^{N} k_{ch,i,j}A_{sd,j}C_{i,vap}-\sum_{j=1}^{N} k_{rev,i,j}A_{sd,j}C_{ch,i,j} \qquad \text{(Equation 3-16)}$$

$$\frac{dm_{i,c,sf,z}}{dt}=\sum_{j=1}^{N} k_{sc,j}A_{sd,j}(C_{i,vap/can}-C_{eq,j})-\sum_{j=1}^{N} k_{rev,i,j}A_{sd,j}C_{c,i,j} \qquad \text{(Equation 3-17)}$$

$$\frac{dm_{i,l,z}}{dt}=\sum_{l'=1}^{B}\{\ f_{l'\to l}[\frac{M_{l',i}}{\Delta t}+k_{c,l',i}A_{l'}N_{l'}(C_{i,vap/con}-C_{eq,i})]\ \}-[\frac{M_{l,i}}{\Delta t}+k_{c,l,i}A_lN_l(C_{i,vap/con}-C_{eq,i})]$$

$$+0.5\sum_{m=1}^{l}\sum_{k=l-1}^{l}f_{mk\to l}k_{agg,m,k}N_mC_{k,i}-\sum_{m=1}^{B}k_{agg,m,l}N_mC_{l,i}-\sum_{j=1}^{N} k_{dep,i,j}A_{sd,j}C_{i,l}+\sum_{j=1}^{N} k_{res,j}A_{sd,j}C_{d,i,j,l}+J_i$$

(Equation 3-18)

$$\frac{dm_{i,sf,z}}{dt}=\sum_{j=1}^{N} k_{dep,i,j}A_{sd,j}C_i-\sum_{j=1}^{N} k_{res,j}A_{sd,j}C_{d,i,j}$$

(Equation 3-19)

The subscript z is used to represent the position, and the subscript l in the equations represents the aerosol's section. For simplicity, these terms were omitted from the parameters in the equations. The meaning of all of the terms was laid down previously. Another important observation to be drawn from the equation is that the agglomeration terms in the aerosol equation (Equation 3-18) represent the number of particles in the equation.

The represented numerical equations were presented disregarding the re-vaporization process and considering the aerosol nucleation process having a fixed born-size. As will be shown later (Chapter 5), there is not enough knowledge about the re-vaporization process to allow a consistent modeling. The nucleation was chosen to give birth to a fixed particle-size, rather than a log-normal distribution, as a simplification. The external source terms were also removed from the equations. They make up part of the model, but they are not part of the research. Hence, these equations are the very representation of the problem comprised by this research.

Selection of the Numerical Method

Given that the problem was transformed into a system of ordinary differential equations (ODE), a method to solve this system needs to be selected. The selection of the method is guided by the characterization of the problem, i.e., the definition of the features of the system and the identification of the method more appropriate for the problem. In order to define these features, the position of the fission product module inside the code structure is briefly discussed, the main types of ODE and its systems are defined, the problem type is defined, and the available solution methods are presented, displaying their features. After that, the solution method is selected accordingly.

The fission product transport model is called, in the code structure, after perform the thermal-hydraulic solution. Therefore, the time-step size is already defined when the solution is executed. At each time-step, for each volume in the nodalization the number of equations is defined by Equation 3-20.

$N_{eq}=(N_s+1+3N_{surf})N_{species}$ (Equation 3-20)

Where:

N_{eq} : Number of equations
N_s : Number of sections
N_{surf} : Number of structural surfaces
$N_{species}$: Number of species

The number of equations, or number of states, accounted for in the above equation, is the number of sections plus the vapor state, added to the three defined surface states (condensed, adsorbed or aerosol deposited mass). Hence, a typical calculation, involving 20 sections, one surface and 10 species, leads to an overall number of equations of 240 equations per volume.

The solution of an ordinary differential equation, as well as a system of ordinary differential equations, is performed numerically by discretizing the independent variable, in this case time, and defining an approach of estimating the time by the end of the step. For simplicity, the equations presented following have a single equation format. In the case of a system of equations, the equations merely acquire a matricial format. The simplest of the existing methods is the Euler method, which uses the slope, i.e., the derivative at the first known point (initial condition) to estimate the function at the end-point, as shown in Equation 3-21.

$y_{i+1} = y_i + f(y_i, t_i)\Delta t$ (Equation 3-21)

The Euler method is extremely simple, but it has two disadvantages. First, it is a first-order method, and, therefore, highly inaccurate. Second, it is an explicit method, i.e., using only old information in its computation. Explicit methods have the disadvantage of instability for certain problems.

The accuracy problem is solved using higher order accurate methods. The best-known and most used family of higher order accurate methods is the Runge-Kutta (55). Runge-Kutta methods achieve the accuracy of a Taylor series approach without requiring the calculation of higher order derivatives. Many variations exist, but all can be cast in the generalized form:

$y_{i+1} = y_i + \phi(t_i, y_i, h)h$ (Equation 3-22)

Where ϕ is called increment function,

$\phi = a_1k_1 + a_2k_2 + \dots\dots\dots + a_nk_n$ (Equation 3-23)

Various types of Runge-Kutta methods can be devised by employing different numbers of terms in the increment function as specified by n. Note that the first-order Runge–Kutta method is, in fact, Euler's method. Once n is chosen, the values of a and k are obtained setting Equation 3-23 equal to the terms in the Taylor series expansion. The Euler and Runge-Kutta methods are, in fact, part of a broader class called one-step methods, i.e., those that use only one step information, without iterations.

The above class of solutions uses information of the initial point to obtain the estimative of the function in the final point. Another approach is to use the average slope considering the first and final point. The initial slope is used to estimate the final point and then the average slope is used to correct the final point, as shown in the Equations below:

$$y_{i+1}^{0} = y_i + f(t_i, y_i)h$$
$$y_{i+1} = y_i + \frac{f(t_i, y_i) + f(t_{i+1}, y_{i+1}^{0})}{2}h \qquad \text{(Equation 3-24)}$$

This class of solution is called the predictor-corrector approach, and has the advantage of allowing an iterative procedure. This iteration allows a local evaluation of the convergence ability of the method. This method has an inconvenience, which is that the predictor (first equation) is first order accurate, whereas the corrector is second order accurate. A remedy is applied using the last step information to make the predictor also second order, as shown in the Equation below:

$$y_{i+1}^{0} = y_{i-1} + f(t_i, y_i)2h \qquad \text{(Equation 3-25)}$$

The importance of the step size, or time-step in our case, can now be realized. In regions where the curvature of the solution is low, larger time-steps can be taken; whereas in regions where the larger curvatures are found, smaller time steps must be taken. Hence, the idea of adaptive time steps, except for very simple applications, is a concept of the numerical strategies incorporated so to solve the problem. The quantification of the variable step size is possible by the estimation of the local truncation error, i.e., the error consequent of the numerical treatment, considering the initial value as the exact solution. Various strategies can be used to estimate the local error, such as step-halving and Runge-Kutta. Felhberg presented different strategies for error estimation applied to Runge Kutta methods.

Another concept in Equation 3-25 is the multi-step concept. Notice that in this approach, the previous step value is involved. The class of solutions using more than one step is called the multi-step methods. From a computational point of view, these methods require the storage of previous data, but they have the advantage of yielding the truncation error estimates that can be used to improve the adaptive size control. They are also referred to as non-self-starting methods, which means that they cannot start independently, but only by using the initial value.

The multi-step methods are based on the insight that, once the computation has begun, valuable information from previous points is available and are exploited by these methods to obtain the trajectory of the solution. A third order accurate method was presented in Equation 3-25. Higher order integration formulas can be used as predictors and/or correctors in multi-step methods. The two most widely used methods are Newton's and Adams'. Since the different methods have a similar feature in terms of computational effort and stability, only the Adams-Moulton approach is presented.

The Adams-Moulton method is derived by approximating the derivative by a n^{th}-order polynomial, obtained through the usage of the backward Taylor series around the desired end of time-step t_{i+1}. Then, the difference is used to approximate the n-1th derivative. This difference is used in the original equation. Collecting terms in these equations, the nth-order Adams-Moulton method can be written generally as:

$$y_{i+1} = y_i + h\sum_{k=0}^{n-1} \beta_k f_{i+1-k} \qquad \text{(Equation 3-26)}$$

The methods presented previously work fine for problems considered non-stiff. There is another class of ODEs or system of ODEs for which the previous method is inefficient due to stability problems. This class of problem constitutes the stiffness problems.

A stiff equation or system is one involving rapidly changing components together with slowly changing ones. In many cases, the rapidly varying components are ephemeral transients that die away quickly, after which the solution becomes dominated by the slowly varying components. The rapidly varying component requires a very small time step to obtain stability and even smaller time-steps to obtain accuracy. Superficially, one might suppose that adaptive step-size can resolve the problem, by using small time steps during the rapid transients, and large time steps otherwise. However, this is not the case, because the stability requirement will still necessitate very small steps throughout the entire solution.

Rather than using explicit approaches, implicit methods offer an alternative remedy. These approaches are called implicit because the unknown appears on both sides of the equation. An implicit form of Euler's method can be developed by evaluation of the derivative at a future time:

$$y_{i+1} = y_i + \frac{dy_{i+1}}{dt}h \qquad \text{(Equation 3-27)}$$

When considering the application of the implicit method for a system of equations, the problem will consist of a set of simultaneous equations. The solution becomes more difficult because it requires the solution of a system of simultaneous equations. Thus, although stability is gained through implicit approaches, a price is paid in the form of added solution complexity.

The implicit Euler method is unconditionally stable and only first-order accurate. It is also possible to develop in a similar manner a second order accurate implicit rule integration scheme for stiff systems. It is usually desirable to have higher-order methods. The Adams-Moulton formulas described earlier can also be used to devise higher order implicit methods. However, the stability limits of such approaches are very limited, when applied to stiff systems.

Gear (56) developed a special series of schemes that have much larger stability limits based on backward difference formulas. The backwards-differential formula (BDF) method is the most popular currently used for stiff problems. Differently from other methods, which have to use small step-size throughout the solution, the BDF method may have to use small time-steps in regions where the most rapid exponentials are active. However, outside these regions, which usually are small relative to the integration interval, larger step sizes may be used. The equation of the Gear method is given by:

$$y_{i+1} = \sum_{j=1}^{q} \alpha_j y_{i-j} + h\beta_0 \frac{dy_{i+1}}{dt} \qquad \text{(Equation 3-28)}$$

Notice, from Equations 3-26 and 3-28, that both Adams-Moulton and the BDF method have dependencies on the future point, and, as mentioned earlier, can be used to devise implicit methods. Nevertheless, these implicit equations are computationally extremely expensive, and not feasible for a large number of equations problems. The scheme normally used is the corrector-predictor approach, which is stable by some extent, but has a considerably smaller computational burden. Under this scheme, the Gear method proved to be much more stable than Adams-Moulton.

Important issues in the selection of a solution to solve a system of the ODE are the type of the problem (stiff or not), the number of equations, and the accuracy of the problem. Hence, it is important to establish the nature of the problem we are solving. Since a typical problem involves a larger number of time steps (10^4 to 10^6), accuracy should be considered in the highest level as possible, to avoid a large global error. Also, control of local truncation error is important. Therefore, the Euler method (first order method) and lower order methods should not be used. Considering the number of equations, we saw that a typical number would be 240 per volume, and this number could reach into the thousands under ordinary circumstances. Implicit methods, hence, would make the computational cost prohibitive.

Regarding the stiffness of the system of equations, an idea of the variation in the orders of magnitude of the fission products-transport phenomena is provided in Table 3-1. The phenomena were divided into vapor phenomena and aerosol phenomena. The vapor phenomena are condensation over structural and aerosol surfaces, and adsorption. Aerosol nucleation is considered later. For the aerosol phenomena, aerosol growth by condensation, agglomeration and aerosol deposition over structural surfaces were considered.

These reciprocal time-constants were obtained from sample problems used in the verification process in the next chapter. Notice the extremely wide range of variation of the order of magnitude of the condensation and agglomeration. This variation is due to the dependency of those coefficients on the number of particles concentration, as shown in Equations 3-15 and 3-18. Since the number of particles progressively increases during the solution, ranging from 10^1 to 10^{14} particles/m^3, the coefficients have this wide range. Table 3-1 shows that the problem is widely stiff, because the processes have this wide variance; certainly the exact solution has terms presenting this wide variation in the decay (or time) constants. The analysis is completed when we compare the time constant with the currently used time-step. The minimum time step would be of the order of 0.001s, and the minimum time constant is of the same order. Therefore, for these conditions, the time step does not need additional reduction, i.e., the problem cannot be considered stiff. However, it is not guaranteed that the thermal-hydraulic time step will always make the problem non-stiff, but most of the time the problem will not be stiff. To be conservative, the problem is here assumed as a stiff problem for the selection of the method of solution for the ODE system.

Table 3-1. Range of decay constants for the fission product transport phenomena: (a) vapor phenomena; (b) aerosol phenomena

Vapor phenomena	Order of Magnitude (s^{-1})
Aerosol condensation	10^{-6} to 10^{3}
Structure condensation	10^{-3} to 10^{-1}
Adsorption	10^{-6} to 10^{-3}

(a)

Aerosol phenomena	Order of Magnitude (s^{-1})
Vapor condensation	10^{-6} to 10^{3}
Agglomeration	10^{-6} to 10^{-1}
Deposition	10^{-6} to 10^{0}

(b)

Given that the problem is considered stiff, needs a high order of accuracy and is large, the BDF method is the best alternative to fulfill the requirements of the problem. A predictor-corrector method with time step control was chosen, given its speed compared to a completely implicit method. The Hindmarsh LSODE package (57) was chosen to be implemented, because it contains the BDF method as an option in its settings and was already coded in another section of the code. Therefore, the subroutines were adapted to the set of equations and the settings were re-defined. LSODE is a computational package that developed the best techniques in the optimization of the application of the multi-step methods. Among these techniques are the matrix operations optimization, through the use of the Nordseick's history matrix (58), the development of a fast step-size and order selection technique and the use of different iterative techniques to correct the predicted value, according to the user definition.

Stability characteristics limit the order of the BDF method to 5 (56). The employed strategy to solve the problem is to first obtain the predicted value of the function and the quantities $h_n \dot{\underline{Y}}_n$ and $\underline{e}_n$, applying Equation 3-29, 3-30 and 3-31:

$$\underline{Y}_n^{[0]} = \sum_{j=1}^{q} \alpha_j^* \underline{Y}_{n-j} + h_n \beta_1^* \dot{\underline{Y}}_{n-1} \qquad \text{(Equation 3-29)}$$

$$h_n \dot{\underline{Y}}_n^{[0]} = \frac{\underline{Y}_n^{[0]} - \sum_{j=1}^{q} \alpha_j \underline{Y}_{n-j}}{\beta_0} \qquad \text{(Equation 3-30)}$$

$$\underline{e}_n^{[0]} = 0 \qquad \text{(Equation 3-31)}$$

Where:

$\underline{Y}_n = (Y_{1,n}, \ldots\ldots, Y_{N,n})^T$

The coefficients $\{\alpha_j^*\}$ and β_1^* are selected such that Equation 3-29 will be exact if the solution of the problem is a polynomial function of order q. The superscript T means "transpose" and the subscript n represents the end of the current step, whereas j represents other, previous steps. The coefficients α_j and β_0 were derived by Gear (56). The second and third quantities above are auxiliary quantities used in the errors estimation and to aid the advancement of the solution.

After the prediction step, a series of algebraic and matrix operations were performed by Hindmarsh (57) to obtain a convenient form of the corrector, which is presented below:

$$\underline{g}(\underline{Y}_n^{[m]}) = h_n \underline{f}(\underline{Y}_n^{[m]}) - h_n \dot{\underline{Y}}^{[m]} \qquad \text{(Equation 3-32)}$$

$$\underline{Y}_n^{[m+1]} = \underline{Y}_n^{[m]} + \beta_0 P^{-1} \underline{g}(\underline{Y}_n^{[m]}) \qquad \text{(Equation 3-33)}$$

$$h_n \dot{\underline{Y}}^{[m+1]} = h_n \dot{\underline{Y}}^{[m]} + P^{-1} \underline{g}(\underline{Y}_n^{[m]}) \qquad \text{(Equation 3-34)}$$

$$\underline{e}_n^{[m+1]} = \underline{e}_n^{[m]} + P^{-1} \underline{g}(\underline{Y}_n^{[m]}) \qquad \text{(Equation 3-35)}$$

The vector function g is an auxiliary function defined to optimize the calculation. All quantities needed to compute the new value in Equation 3-33 are available in the equations previously presented. The usage of the last equation is related to the convergence and accuracy tests executed by the package. The only term that is not yet explained is the P matrix. The P matrix has different compositions, according to the iterative method.

Two iterative methods are available in the Hindmarsh package. The first one is the functional iteration, which can be compared to the single point iteration used to solve numerically equations. This method employs only the function to obtain the future point estimative. This method is very simple, but it has, as disadvantage, a low rate of convergence. On the other hand, the Newton-Raphson iteration technique utilizes the Jacobian of the system or the partial derivatives to point the solution. It is a more laborious technique, but converges faster. For both techniques the vector P is presented next.

$P = I$ (Equation 3-35)

$P = I - h_n\beta_0 J$ (Equation 3-36)

In these equations, I is the identity matrix, and J is the Jacobian matrix. Since the problem is apparently stiff, convergence is probably difficult at sometimes during the calculation. Considering this, the Newton-Raphson iterative method was first chosen. This choice implies the necessity of definition of the Jacobian. A sensitive study performed in the next chapter showed that the functional iteration technique is actually more efficient.

After performing the correction of the predicted value, the convergence is tested through the following test:

$$\varepsilon_m = \sqrt{\frac{1}{N}\sum_{i=1}^{N}\left(\frac{\delta_{i,n}^{[m]}}{EWT_{i,n}}\right)^2} \le \frac{\tau(q,q)}{2(q+2)} \qquad \text{(Equation 3-37)}$$

The arguments that led to this test are presented by Hindmarsh (57). In this expression:

$$\delta_n^{[m]} = h_n \dot{\underline{Y}}_n^{[m]} - h_n \dot{\underline{Y}}_n^{[m-1]} \qquad \text{(Equation 3-38)}$$

$$EWT = RTOL_i\left|Y_{i,n-1}\right| + ATOL_i \qquad \text{(Equation 3-39)}$$

$$\tau(q,q) = \frac{1}{C_{q+1}q!l_q} \qquad \text{(Equation 3-40)}$$

$$C_{q+1} = \frac{1}{q+1} \qquad \text{(Equation 3-41)}$$

The q stands for the order of the method, and the l_q was tabulated by Gear. The RTOL and ATOL are respectively the relative tolerance and absolute tolerance, which are user-defined.

After passing in the convergence test, the local truncation error test is performed, in accordance with Equation 3-42. Moreover, the result of this test is used to adjust the time –step and the method order. The method and iterative technique are the same throughout the calculation.

$$\sqrt{\frac{1}{N}\sum_{i=1}^{N}\left(\frac{e_{i,n}}{EWT_{i,n}}\right)^2} \leq \tau(q,q) \qquad \text{(Equation 3-42)}$$

Imposed Constraints

At this point the problem is completely defined in terms of mathematical modeling. The problem was defined as a set of ordinary differential equations, and a numerical method was chosen to solve this set of equations. Nevertheless, constraints need be imposed, due to the physical limitations and peculiarities of the problem. Some constraints are also imposed by the limitations of the method or motivated by calculation optimization. Next, these constraints are described, in accordance with the reason of the constraint.

Physical constraint

The solution method employs a polynomial function of the method order to obtain the set of coefficients used by the method. It is correct to assume that the function used to estimate the new point is of this type. For this reason, negative masses are possible to appear in the solution. However, negative masses are not physically possible. Hence, constraints need to be imposed to the solution to avoid these negative masses. Actually, negative masses can have a devastating effect, because the negative sign can propagate along the solution.

Two approaches were initially considered. The first to be considered was to make an iterative process, where the coefficients were corrected after the computation. Second, correcting the coefficients before the computation was considered, taking account of the derivative (slope) at the initial point.

During the implementation, the first approach showed to be computational expensive, because of the elevated number of iterations, in some calculations. Consequently, the second approach was chosen.

The procedure of this second approach is to test if the total or single process removing mass in a state is capable of removing all the initial mass, considering the removal rate at the beginning of the time-step. If the mass removing rate is capable of remove more than the initial mass, the coefficients are re-evaluated to make the initial mass matches zero at the end of time step, assuming a linear rate. This procedure could be thought inconsistent with the solution method, since the method uses a higher order polynomial approach, rather than a first order, as this procedure uses. Nevertheless, the non-negativity is guaranteed since it is known that the exact solution has an exponential behavior, and, therefore, the coefficients' correction lead to a conservative set of coefficients, because the tendency is to have smaller slopes after the initial point. A linear extrapolation will lead to a smaller value than a polynomial, following a negative exponential. Therefore, forcing a linear extrapolation to zero will lead to a greater-than-zero estimative using a higher order method.

For the vapor state, each process (adsorption, structural-surface condensation, and condensation on aerosol surfaces) is limited by the amount of vapor available. Also the net change, i.e., the summation of all these effects, should be less than the available mass of vapor.

The constraints for vapor processes are represented below:

$$\sum_{j=1}^{N} k_{ch,i,j} A_{sd,j} C_i \leq C_i V / \Delta t$$

(Equation 3-43)

$$\sum_{j=1}^{N} k_{sc,j} A_{sd,j} (C_{i,vap} - C_{eq_i,j}) \leq C_i V / \Delta t$$

(Equation 3-44)

$$\sum_{l'=1}^{B} k_{c,l',i} A_{a,l'} N_{l'} (C_{i,vap} - C_{eq,i}) \leq C_i V / \Delta t$$

(Equation 3-45)

In the equations above, the constraints for each phenomenon are present. The V represents the cell volume, and the Δt represents time-step. In the case of a violation of the physical constraint, the term is substituted with the right-hand-side term of the inequality. For the case of condensation on an aerosol surface, the right-hand amount is re-distributed proportionally to the sectional coefficient (the product of the condensation velocity multiplied by the aerosol surface-area). Equation 3-46 presents the condition for the entire equation, i.e., all three processes summed cannot remove more than the available mass.

$$\sum_{j=1}^{N} k_{sc,j} A_{sd,j} (C_{i,vap} - C_{eq_i,j}) + \sum_{l'=1}^{B} k_{ca,l',i} A_{a,l'} N_{l'} (C_{i,vap} - C_{eq,i}) + \sum_{j=1}^{N} k_{ch,i,j} A_{sd,j} C_i \leq C_i V / \Delta t$$

(Equation 3-46)

In the case of a violation of the constraint, the mass (the RHS of the inequality) is distributed among the terms proportionally to their intensities. The sectional condensed-masses are redistributed among the several sections in accordance with the condensation coefficients.

Analyzing now the aerosol state, two processes can remove the available species-mass from a section: deposition, and agglomeration. The two constraints are imposed separately and together and are expressed below:

$$\sum_{m=1}^{B} k_{agg,m,l} N_m C_{l,i} (1 - f_{ml \to l}) \le C_{l,i} V / \Delta t$$

$$\sum_{j=1}^{N} k_{dep,i,j} A_{sd,j} C_{i,l} \le C_{l,i} V / \Delta t$$

(Equation 3-47 and 3-48)

$$\sum_{m=1}^{B} k_{agg,m,l} N_m C_{l,i} (1 - f_{ml \to l}) + \sum_{j=1}^{N} k_{dep,i,j} A_{sd,j} C_{i,l} \le C_{l,i} V / \Delta t$$

(Equation 3-49)

Problem constraint

A wide range of variation exists in the decay constants of the several phenomena, as shown in Table 3-1. It is convenient to reduce the computational effort and the stiffness of the system, neglecting processes that are extremely slow. These processes were defined as those having imposed negligible losses to the mass state, considering a computation through the entire transient. In other words, processes with time constants significantly higher than the transient time. As shown in Chapter 2, maximum transient times are of the order of 300 minutes, or 10^5s. Given that information, it is assumed that phenomenon with decay constants less than 10^{-7}s^{-1} should be neglected.

Optimization constraint

The procedure of size calculation of agglomerated particle is to add the volumes of the particles and then look for the new size into the size distribution, to determine which sections will share the mass of that particle. Then, the fractions correspondents to each section are calculated. This search procedure can be eliminated if the number of sections is fewer than 50. It could be easily proven that for a number of sections lower than 50 the agglomerated particle will have the size of that between the current section and the upper section. This limitation is adopted in the developed model for the sake of computational economy and because the computational time is very large for this number of sections (the usual value adopted is 20).

Along the calculation, very small masses appear, mostly in the sections due to the particles' growth by condensation and agglomeration. These small masses, if left in the calculation, propagate even smaller masses, causing unnecessary calculations. Therefore, masses of less than 10^{-19} Kg were neglected.

Phenomenological Model Development

In the first part of the chapter, a consistent package of mathematical treatment, methods, procedures and techniques were chosen or developed, so to arrive at the more appropriate tool to model the fission product transport in the Scdap/Relap code. In this second part of the chapter, mathematical models for the several phenomena presented in Figure 3-1 are chosen or developed. These models are realized, in the transport equations, through the coefficients of the equations, represented by the $\underline{k}$ terms.

The criteria adopted to select the appropriate model are based upon three basic principles. Simplicity is the first one, and is always an engineering-desired characteristic of the model. The simplicity of the model is important because it means less computation and allows the understanding of the dependences of the phenomena on the several parameters governing its behavior. Consistency with the code's philosophy is another requirement of the model. Two major issues need to be considered in this principle: (1) the code used the concept of well-mixed cells, i.e., the cells are homogeneous in terms of chemical composition and thermal-hydraulic properties, and (2) transverse phenomena are modeled empirically or by special models, such as boundary-layer theory. The third principle is accuracy, which was addressed through the survey of experimental validation of the model and through the comparison of the model's performance with the results of more accurate and elaborated methods.

This part of the chapter opens with a hydrodynamics review, due to the importance of the issue for the understanding of the models. Then the development is divided into vapor, vapor-aerosol (terms that couple aerosol and vapor behavior), and aerosol phenomena. Finally, in the last item the current development is compared to developments of fission product transport in other codes.

Hydrodynamics Review

Since most of the phenomenon involve the mass transfer under laminar or turbulent flow conditions, it is convenient to provide a summarized description of the hydrodynamics field equations, methods and tools, since it has strong impact in the mass transfer modeling. The most important hydrodynamic equation, the Navier-Stokes equation, is derived from the linear Boltzman transport equation for the continuum region, assuming the momentum as the arbitrary function. The steady-state Navier-Stokes for incompressible fluid, neglecting external forces and the body force, can be expressed (59) as:

$$\left(\vec{V}\nabla\right)\vec{V} = -\frac{1}{\rho}\nabla P + \nu\left(\nabla^2\vec{V}\right) \qquad \text{(Equation 3-50)}$$

Where:

$\vec{V}$: Flow velocity (m/s)
ν: Kinematics viscosity (m^2/s)
P: Pressure (Pa)
ρ: Fluid density (Kg/m^3)

The Navier-Stokes equation, or momentum conservation equation, has its importance related to the calculation of the drag forces imposed by the tube wall, among others. The solution can be completed through the calculation of the flux of momentum transfer, known as Newton's Law, represented by the expression:

$$\tau = -\mu \nabla \vec{V} \qquad \text{(Equation 3-51)}$$

Where:
μ: Dynamic viscosity (kg/m-s)
τ : Shear tension or momentum flux rate (Pa)

Dimensional analysis and similarity theory have been applied widely to hydrodynamics and related subjects, including heat transfer and mass transfer processes. Characteristic dimensions are combined with others to obtain a certain quantity based purely on the dimensional analysis and physical understanding of the problem. The similarity theory uses dimensionless parameters to establish similarities between different flow conditions. This similarity can be used to establish expressions from experimental data. Equation 3-50 can be expressed in terms of dimensionless parameters.

$$\left(\vec{V}_{\dim} \nabla\right)\vec{V}_{\dim} = -\nabla p + \frac{1}{\mathrm{Re}}\left(\nabla^2 \vec{V}_{\dim}\right) \qquad \text{(Equation 3-52)}$$

Where:

$$\mathrm{Re} = \frac{V_0 d_h}{\nu} \text{ (a)} \quad \vec{V}_{\dim} = \frac{\vec{V}}{V_0} \text{ (b)} \quad p = \frac{P}{\rho V_0^2} \text{ (c) (Equation 3-53: (a) , (b) and (c))}$$

The coordinate system is also expressed as dimensionless quantity, by dividing the coordinate components by the characteristic length, the tube diameter (d_h). In Cartesian coordinates this transformation is expressed by:

$$X = \frac{x}{d_h}; Y = \frac{y}{d_h}; Z = \frac{z}{d_h} \qquad \text{(Equation 3-54)}$$

The Reynolds number, therefore, is the dimensionless parameter affecting the momentum transfer. For a high Reynolds number (>>1), the last term in Equation 3-52 can be neglected. In this case, the viscosity, or viscous forces, was neglected, and the fluid is termed an ideal fluid. This simplification leads to Euler and Bernoulli's equations. Another consequence of this simplification was described by the D'Alembert paradox. This paradox states that the drag force on a solid body in steady motion through an ideal fluid is zero, which is an absurdity. This absurdity is a consequence of the fact that the ideal fluid approximation is unsatisfactory for describing fluid motion near phase interfaces, such as pipe walls and gas-liquid interfaces.

Thus, near the surface of the pipe there must be a thin zone in which the tangential component of fluid velocity undergoes a very abrupt change, from a high value at the outer border of the zone to zero at the wall surface. The thin zone is the boundary layer. This explanation is founded on both theoretical and experimental base.

Another important issue in hydrodynamics is the classification of the single-phase flow into laminar flow and turbulent flow. In the fully developed laminar flow, the flow is separated into layers, where viscous forces prevail. At a certain value of the Reynolds number, steady laminar flow gives way to distinctly unsteady, chaotic motion in which only on the average there is net flow in a particular direction.

Studies of the transition to the turbulent regime have shown that it is related to the inherent instability of the flow at Reynolds number in excess of some critical value Re_{cr}, i. e., at $Re< Re_{cr}$, disturbances that occur in the fluid are rapidly damped. When $Re>Re_{cr}$, disturbances are not damped, but rather they reinforce each other. A quantitative theory of turbulence has not been perfected, but qualitative and semi-quantitative theories have evolved. The generally accepted Re_{cr} is 2300, for vapor and aerosol phenomenological modeling. Some variations are found in the literature. Some of them present 2500, and other authors define a transition regime, for the Reynolds variation from 2300 to 4000, but these variations are normally considered in the frictional losses determination. Throughout the modeling of this research, the value of 2300 was assumed.

If one observes the trajectory of a particular mass of fluid in turbulent flow, he finds it highly complex. Random eddies are superposed on the basic motion. The tendency toward a systematic advance can only be described in terms of averages. The trajectory, in this case, is somewhat similar to the motion of a gas molecule in a stream of gas, indicating that the theory of turbulence must be statistical in nature.

Eddy velocities of varied magnitudes are superposed upon the average motion of a fluid having a velocity (V). Turbulence eddies are characterized by their velocities, and by the distances over which these velocities change significantly, which are the eddies' scale of motion. The largest scale of turbulence is equal to the diameter of the tube. These largest eddies have the major change in the average velocity over the scale of motion (ΔV), and such large eddies contain the main part of the kinetic energy of turbulent motion. The eddy has its own Reynolds number defined by:

$$\mathrm{Re}_\lambda = \frac{V_\lambda \lambda}{\nu} \qquad \text{(Equation 3-55)}$$

Where:
V_λ: Eddy velocity (m/s)
λ: Length scale (m)

Together with these large scale eddies, turbulent flow also includes eddies of smaller scale, with smaller eddy velocities. Although the number of such small eddies is very large, they represent only a small part of the kinetic energy of the stream. Large eddies, with scale motion of the order of the tube diameter (d_h), have a very large Reynolds number, and, therefore, viscous forces have no effect, and such motion takes place without energy dissipation and momentum transfer. Nevertheless, the superposition of large-scale eddies on each other creates small-scale eddies, for which the Reynolds numbers rapidly decrease with the decreasing λ. At a determined value of the scale of motion λ_0, where its Reynolds number is approximately the unity (micro-scale turbulence), viscous forces begin to have a noticeable effect in the motion of the fluid. Eddy motion of a scale λ_0 is accompanied by dissipation of energy.

With a large quantity of small-scale motion, there is a considerable dissipation of energy, which is transformed in heat. This energy is continually drawn by small-scale motion from the large-scale motion, i.e., large-scale eddies are continually superposed, generating small eddies, until these small-scale eddies reach the micro-scale region, when they dissipate energy. For steady-state fluid flow, the process of energy transfer is also steady. Eddies of a given scale receive as much energy from larger-scale eddies as they pass to small-scale eddies. Thus, although turbulent motion occurs only at relatively high Reynolds numbers, it is accompanied by considerable dissipation of energy. From this standpoint, it is possible to define a certain effective "eddy viscosity" μ_{turb}, appropriate to turbulent flow. This "eddy viscosity" expresses energy losses occurring in the flow, per second, per unit volume:

$$\varepsilon = -\frac{dE}{dt} = \mu_{turb}\left(\frac{\Delta V}{d_h}\right)^2 \qquad \text{(Equation 3-56)}$$

The effective eddy viscosity is very large in comparison with the ordinary viscosity. Therefore, the heat and momentum transfer is much higher for turbulent flows. Dimensional analysis can provide an idea of the magnitude of the kinematics viscosity, as shown below:

$\nu_{turb} = \Delta V d_h$ (Equation 3-57)

The process of momentum and energy transfer in a turbulent flow is represented below, in Figure 3-2. Assuming that a single irregularity generates a large eddy, this eddy will successively transfer its kinetic energy to smaller eddies until the energy reaches the micro-scale region, where momentum and energy transfer are viscous, such as in laminar flows.

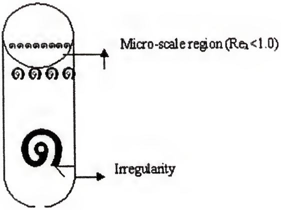

Figure 3-2. The process of heat and momentum transfer in a turbulent flow

The velocity profile for the laminar flow is calculated exactly, and is presented in Figure 3-2. On the other hand, for the turbulent flow, only the average flow velocity can be found. Contemporary hydrodynamics do not offer any singular point of view regarding the velocity distribution in the viscous sub-layer. Two hypotheses have been suggested: (1) Prandtl's hypothesis states that in the region $y<\delta_0$ (boundary layer thickness), the fluid motion is entirely laminar. In the outer region, a turbulent flow prevails. (2) Von Karman proposed a theory in which the flow is divided into three regions: (a) a region of turbulent flow, (b) a buffer layer and (c) a laminar sub layer. According to Van Karman, the turbulent flow in the buffer layer is gradually damped as it approaches the solid wall. Applying the second approach, a better equation (better agreement with experimental data) for the boundary layer was obtained by Lifshitz (59). This Equation was obtained based on dimensional analysis and momentum conservation equation, and its derivation is not here presented.

$$\frac{V}{V_0} = y_* \quad 0 \le y_* \le 5$$

$$\frac{V}{V_0} = 10 arctg(0.1 y_*) + 1.2 \quad 5 \le y_* \le 30 \qquad \text{(Equation 3-58)}$$

$$\frac{V}{V_0} = 5.5 + 2.5 \ln y_* \quad y_* > 30$$

Where:

U: Average velocity of the region (m/s)
u_0: Characteristic velocity of the flow (m/s)
y_*: Dimensionless radial distance given by y/R

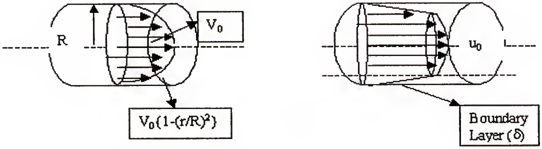

(a) (b)

Figure 3-3. Velocity profiles: (a) exact solution for laminar flow; (b) average velocity for turbulent flow

So far, the physical understanding of the momentum and energy transfer under laminar and turbulent flows, the flow velocity behavior, and the basic hydrodynamics equations have been presented. Next, the basic energy and mass conservation and flux equations are presented. Similarity among these equations and the hydrodynamics equations are presented. The dimensionless steady-state energy and mass continuity are expressed below:

$$(\vec{V}\nabla)C = \frac{1}{Pe}\nabla^2 C; \quad Pe = \frac{d_h V_0}{D} \qquad \text{(Equation 3-59)}$$

$$(\vec{V}\nabla)T = \frac{1}{Pe_{th}}\nabla^2 T; \quad Pe_{th} = \frac{d_h V_0}{\alpha} \qquad \text{(Equation 3-60)}$$

Where:

Pe: Peclet Number
Pe_{th} : Thermal Peclet Number
d_h: Hydraulic diameter (m)
V_0: Fluid characteristic velocity (m/s)
D: Molecular diffusivity coefficient (m^2/s)
α: Thermal diffusivity (m^2/s)

The thermal diffusivity and the dimensionless parameters are given by:

$$\alpha = \frac{k}{\rho c_p}; \quad C = \frac{c}{c_\infty} \quad \vec{V}_{\dim} = \frac{\vec{V}}{V_0} \qquad \text{(Equation 3-61)}$$

Where:

k: Fluid thermal conductivity (W/m-K)
c_p: Specific heat (J/Kg-K)
ρ : Density (Kg/m^3)

Notice that these equations are similar to the momentum conservation equation of the boundary layer, which is Equation 3-52 without the pressure gradient term. Similarity can also be observed in the flux equations, i. e., momentum flux equation (3-51), and the energy and mass flux equations, presented in Equations 3-62 and 3-63 below.

$$J_D = -D\nabla c \qquad \text{(First Fick's Law)} \qquad \text{(Equation 3-62)}$$

$$J_Q = -k\nabla T \qquad \text{(Fourier's Law)} \qquad \text{(Equation 3-63)}$$

Considering that the equations are similar, and the boundary layer thickness calculation is performed based on the shear stress, Equation (3-51), complete analogy exists between the velocity field, the concentration field and the temperatures field, as well as the laminar, thermal and concentration boundary layer thickness. In order to perform this analogy, the quantities need to be comparable, which is possible using the quantities ν (kinematics viscosity or "momentum diffusivity"), α (thermal diffusivity) and D (mass diffusivity). The manners these parameters compare define the relative order of magnitude of the boundary layer thickness. Two dimensionless parameters are used to define the boundary layer behavior:

$$\mathrm{Pr} = \frac{\alpha}{\nu} \qquad \text{(Equation 3-64)}$$

$$Sc = \frac{D}{\nu} \qquad \text{(Equation 3-65)}$$

Where:
Pr: Prandtl Number
Sc: Schimidt Number

Notice that the Peclet and the thermal Peclet number are, respectively, the multiplication of the Reynolds number by the Schimidt and Prandtl number. Also important in thermal heat transfer is the convective heat transfer coefficient, obtained from the determination of the heat flux through the wall, and the correspondent dimensionless parameter Nusselt:

$$hA(T_b - T_w) = k\frac{dT}{dy}\ )_{wall} \qquad \text{(Equation 3-66)}$$

$$Nu = \frac{hd_h}{k} \qquad \text{(Equation 3-67)}$$

Where:
h: Convective heat transfer coefficient (W/m^2K)
T_b: Bulk gas temperature (K)
T_w: Wall temperature (K)

Equation 3-67 shows that experiments using only measurements of temperatures are capable of providing the Nusselt number. The equivalent dimensionless number related to the mass transfer process is the Sherwood number expressed below. Nusselt and Sherwood numbers present the relation of the convective transfer to non-convective heat transfer. In the case of non-convection, the thermal process is conduction, and the mass transfer process is molecular diffusion.

$$Sh = \frac{V_d d_h}{D} \qquad \text{(Equation 3-68)}$$

For gaseous fluid, the diffusivities for several transfer processes are of the same order of magnitude; i.e., the Prandtl and Schimidt number are close to one, meaning that the analogy can be applied. The equivalent parameters and equations are present in Table 3-2.

Table 3-2. Equivalent equations and parameters for different transferring processes

	Energy	Momentum	Mass
Flux equation	Fourier's Law	Newton's Law	Fick'sLaw
Boundary layer dimensionless	Prandtl		Schimidt
Boundary layer parameter	α ($k/\rho c_p$)	ν (μ/ρ)	D
Convective/Non conv. dimensionless	Nusselt		Sherwood

Even though numerical methods, aided by the computers, allowed the solution of the Navier-Stokes equations in arbitrary geometries for laminar flows or with simple models of turbulence, this approach is not convenient, because the problem is more complex than a simple mass transfer problem, involving simultaneity of several other processes, which are not compatible with these numerical approaches. In addition, the discretization required by these methods is much more refined than the discretization used in the code. Hence, is more appropriate to use the development in boundary layer theory and statistical treatment of the turbulence to obtain the model of the phenomena, applying analogy between mass transfer and energy (heat) and momentum transfer to obtain the models.

Vapor Phenomena

The purely vapor phenomena of interest are restricted to the vapor-structure phenomena. The transport of vapor molecules to the surface of structural materials, in the specific case of this research, to the piping walls, occur by two major processes, according to the process driving force. Adsorption is a process governed by chemical affinity of the vapor species with the structural materials present in the problem (zircaloy or stainless steel). Condensation is governed by the difference between the partial pressure and the equilibrium vapor pressure of the species at the structural surface temperature.

Vapor-surface processes involve several steps. The first step is the transfer of the molecules to the reacting surface. The second involves the kinetics of the interaction, which, in the case of adsorption, is represented by the reaction kinetics, and in the condensation case, represented by aspects such as solubility and wet-ability. The third step involves the transfer of the reaction products away from the reaction site and its sequential behavior. These steps are represented in Figure 3-4.

The rate of the process as a whole is determined by the combined effect of separate stages. However, the rate of the entire process is governed by the slowest step if one step is significantly slower than the others. In those cases where the slowest step is the mass transfer to the surface, the processes is diffusion controlled, and if the chemical transformation constitutes the slowest step, the rate of the process is governed by the kinetics of this transformation.

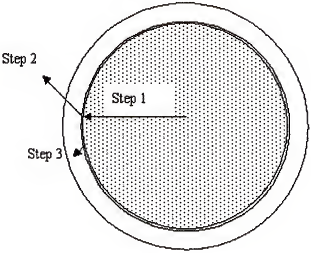

Figure 3-4. Transport process steps for vapor to piping wall phenomena

Adsorption

Adsorption refers to heterogeneous reactions of vapors and the solid surface material surrounding it. Two types of adsorption exist, physisorption and chemisorption.

A weak bond between the surface material and the gaseous molecule characterizes physisorption. In contrast to physisorption, chemisorption involves the formation of strong chemical bonds between adsorbate molecules and specific surface locations known as chemically active sites.

Physisorption is the most common type of adsorption. Physisorbed molecules are fairly free to move around the surface of the structural material. As more gas molecules are introduced into the system, the adsorbate molecules tend to form a thin layer that covers the entire adsorbent surface. Continued addition of gas molecules beyond monolayer formation leads to the gradual stacking of multiple layers (or multi-layers) on top of each other. The formation of multi-layers occurs in parallel to condensation.

The opposite process of adsorption is desorption. Desorption refers to gas molecules that were somehow linked to the surface material and are released from the same. Normally, desorption is more common to physisorbed molecules.

Table 3-1 shows, by comparing the condensation decay rate to the adsorption decay rate, that the adsorption velocity is significantly lower than the mass transfer process. Hence, the process is controlled by the kinetics of the reaction. Hence, at first glance, a first order kinetics theory, as presented in Equation 3-69 (a part of Equation 3-2) would be enough to represent the phenomenon.

$$\frac{dM_{ch,i}}{dt} = v_{d,i,j} A_{dep} C_{vap,i} \qquad \text{(Equation 3-69)}$$

Where:

$v_{d,i,j}$: Velocity of deposition of species i on material j (m/s)
A_{dep}: Deposition surface area (m^2)
$C_{vap,i}$: Concentration of vapor species i (Kg/m^3)

The deposition velocity was empirically determined for the most important species on stainless steel and zircaloy, by submitting metal samples to gaseous flow of the several species. Three different sites performed these adsorption experiments. They were the Sandia National Laboratories, with the results presented in a series of reports (60), (61), the Withfrin Laboratories (United Kingdom) (62), and the DEVAP program (France) (63).

The methodology used to obtain the deposition velocities is to assume an Arrenhius type behavior of the deposition velocity, and from the plotting, perform a best-fit procedure. The assumed form is presented below:

$$v_d = A_{i,j} e^{-B_{i,j}/RT_j} \qquad \text{(Equation 3-70)}$$

Where:

$A_{i,j}$ $B_{i,j}$: Kinetics constants, dependent on species material and surface material (A in m/s and B in J/mol)
T : Surface temperature (K)
R: Universal constant of gases (8.314 J/mol K)

A summary of the more important adsorption interactions, presenting their respective expression is presented below, in Table 3-3. The data is resultant of the mentioned experiments and references.

Table 3-3. Summary of deposition velocities for adsorption interactions (m/s)

Species	Stainless Steel	Zircaloy
CsI	2×10^{-7}	N/M
CsOH	0.139exp(-7177/T)	N/M
I_2	9e-10exp(4076/T)	1.2e-9exp(3955/T)
HI	5.5e-7exp(-2294/T)	N/M
Te	2×10^{-6}	$0.0739(\exp(-4000/T))/\exp(4200x^{1/2}/T)$
Ref.	(60),(61)	(60), (61) and (62)

Measurements of uncertainties of the expression are available in the literature for cesium hydroxide interaction with stainless steel, and can be assumed to be in the order of 50%. The explanation for such uncertainty derives from a closer examination of the kinetics of cesium hydroxide chemical behavior on stainless steel. The reaction involves a physisorption process followed by the slow diffusion of cesium into the metal oxides, along which insoluble and soluble species are formed. These new species have different thermo-chemical properties. As temperatures increase in the primary coolant system, these species can be released (desorption). Hence, desorption process tends to deviate the phenomenon behavior from the assumed first order approach.

Regarding the reactions with zircaloy, tellurium is by far the most reactive species. The extent of the Te-zircaloy reaction depends on the degree of zirconium oxidation. A rapid reaction occurs at the metal surface in the absence of a protective oxide film. The speciation of the reacted tellurium also varies in the presence of an oxide film. For oxide-free surfaces, Te_2 tends to be formed, whereas SnTe tend to be formed in the presence of an oxide layer. A correlation was obtained in the Withfrin Laboratories (61):

$$\ln(10^2 v_d) = \frac{(-4000 \pm 1000)}{T} - \frac{(4200 \pm 1200)x^{1/2}}{T} + (2 \pm 1.0) \quad \text{(Equation 3-71)}$$

In this equation, x is the fractional degree of oxidation, which is obtained by the mass fraction $m_{ZrO2}/(m_{ZrO2}+ m_{Zr})$, and T is the surface temperature. A high level of uncertainty is still present in this correlation. The reason for this uncertainty is related to the speciation of Te in the chemical or diffusive processes involved, and their respective desorption rates. Even with the consideration of an additional refinement in the Te-Zircaloy correlation, which is the zirconium oxide film presence, the uncertainty level is still very high.

In general terms, a high uncertainty level is encountered in the empirical correlations of Table 3-3. In general terms, this elevated uncertainty level is result of the simplifications implicit in the first order approach, in other words, is result of the fact that desorption and the correct kinetics were not modeled.

Sophie code has a more elaborated procedure, with different deposit layers, as shown in Figure 3-5. The solution is obtained by applying the deposition velocity for the first layer and then diffusively transfer to the second layer, where the specie changes into another one, and can be released by desorption.

In the last years, attention to the adsorption of fission product vapors with metallic aerosols has grown. The adsorption of tellurium by silver aerosols was identified as a possible important reaction and was discussed by Alonso (64), but an appropriate model for implementation is still not developed.

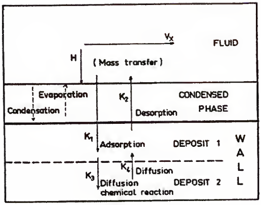

Figure 3-5. Sophie approach to solve the adsorption/desorption of nuclear vapors over structural surfaces of the primary circuit

The implementation of Sophie's approach has several difficulties. First, additional equations need to be set so to balance mass in the layers, increasing the size of the problem. Second, the diffusion coefficients between layers are not available (at least in the open literature), and third, the adsorption rates are not known.

Condensation onto structural surfaces

In the condensation of vapors onto structural surfaces mass transfer process dominates, oppose to the surface kinetics, as in the physisorption process. The surface kinetics, in this case, can be associated to surface effects as solubility and wet-ability of the surface. These processes are usually negligible and difficult to model. Although there is no documented proof that such aspects could be neglected, it is generally accepted in the nuclear community that these aspects can be neglected. Hence, the condensation process can be considered a diffusion-controlled process.

The condensation process has been modeled by the expression of Equation 3-72, which is part of the differential equations. Again, a first order approach is adopted. Equation 3-72 shows that the process is dependent on the condition that the vapor concentration or partial pressure is larger than the equilibrium concentration or vapor pressure. The vapor pressure is a vapor property, and is treated at Appendix A, remaining only the deposition velocity unknown.

$$\frac{dm_i(t)}{dt} = k_{s,i} A_{sd} (C_i(x,t) - C_{eq_i}) \quad \text{(Equation 3-72)}$$

Where:

m_i: Mass of vapor species i (Kg)
C_i: Concentration of vapor species i in the cell (Kg/m^3)
$A_{sd,j}$: Surface deposition area for surface (m^2)
$k_{sc,i}$: Condensation surface deposition velocity for species i on surface (m/s)
C_{eqi}: Equivalent vapor concentration (Kg/m^3)

The convective-diffusion process, as pointed out earlier, is analogous to the momentum transfer and heat transfer processes. Therefore, they have dependence on the flow regime and can use similarities with these processes to obtain mathematical formulas capable to reproduce the physical behavior. Steady-state convective-diffusive process is expressed by Equation 3-59, and is re-written here in one-dimensional cylindrical coordinates:

$$u\frac{\partial c}{\partial x} = \frac{1}{Pe}\frac{1}{r}\frac{\partial}{\partial r}\left(r\frac{\partial c}{\partial r}\right) \qquad \text{(Equation 3-73)}$$

For the laminar flow, the exact flow velocity can be used in Equation 3-73. Assuming a fully developed laminar flow, Gormley and Kennedy (65) solved this equation applying the separation of variables and eigen-function expansion techniques. They arrived at the following expression for the deposition efficiency, aided by the mass flux equation.

$$\frac{C}{C_0} = 0.8191e^{-7.314h} + 0.0975e^{-44.6h} + 0.0325e^{-114h} \quad \text{(Equation 3-74)}$$

Since, in the differential equations, physical processes are presented as deposition velocities, the conversion to laminar diffusion velocity is performed through Equation 3-75 below:

$$v_{dL} = \left(1 - \frac{C}{C_0}\right)\frac{d_h}{L_n}V_{fluid} \qquad \text{(Equation 3-75)}$$

The term h is a measurement of the diffusive-to-convective transport and is determined from:

$$h = \frac{L_n D}{r_h^2 V_{fluid}} \qquad \text{(Equation 3-76)}$$

Where:
L_n: Length of the pipe or cell (m)

A simpler expression was obtained by Lifshitz (59), presented in Equation 3-77 below:

$$\frac{C}{C_0} = 1 - 4.07h^{2/3} \qquad \text{(Equation 3-77)}$$

Equation 3-74 is actually a truncation of an expansion. Typical parameters applied to this equation showed that more terms were necessary to converge. Since it converges slowly, and Equation 3-77 showed consistency with the solution obtained by expanding the series, Equation 3-77 was adopted.

Regarding the turbulent deposition velocity, the physical process responsible for the mass transport to the walls is analogous to the molecular diffusion. Because, under turbulent conditions, a chaotic fluid movement exists, the fluid constantly bounces around, and eventually fluid masses are thrown to the wall. Such process is considerably more efficient than laminar diffusion, and the theoretical treatment is analogous to the momentum transfer treatment, when an eddy viscosity is defined. Similarly, eddy diffusivity is established. Even though there are some models of the determination of these parameters on theoretical basis, they usually rely on improper assumptions or approximations. Hence, the use of empirical models is convenient.

In heat transfer, the Dittus-Boelter is the most extensively used empirical correlation to determine the Nusselt number. Gilliard (66), using similar dimensionless parameters, established and tested experimentally an equivalent expression for the Sherwood number, obtaining good results. Since then, this correlation has been used to obtain the deposition velocity under turbulent conditions. The correlation is presented below:

$$Sh = \mathrm{Re}^{0.83}\, Sc^{0.33} \qquad \text{(Equation 3-79)}$$

Notice that this equation differs from the heat transfer correlation in the last term. Rather than the Prandtl number, the Schimidt number is used, but they have the same meaning, which is how their boundary layer thickness compares to the hydrodynamic boundary layer. The expression shows a high level dependency on the Reynolds number, representing the turbulence mass transport, and a mild dependence on the Schimidt number, representing the boundary layer process, as expected. The model adopted employs Equation 3-68 to obtain the deposition velocity from the correlation of Equation 3-79.

Vapor-Aerosol Phenomena

A severe accident leads to the release of numerous different species, from different sources (fuel, control rod or structural elements) into the primary circuit. The amount and release timing profile is distinct for each species. After the release, the vaporized species migrate to cooler regions, where they can condense onto the structural surface wall, be adsorbed by this structure, or nucleate aerosols. Later, when aerosol particles are present in the environment, condensation onto pre-existing aerosols will also occur. The vapor-aerosol phenomena include the aerosol homogeneous nucleation and the condensation of vapor onto already existent aerosols, or heterogeneous nucleation.

A consistent and optimized model would consider all of the factors involved. The first factor involved is the composition and morphology of the nuclear aerosols, which provides valuable information on whether nuclear aerosols have a pattern (or not) and if existent, what is the composition pattern. More important is the determination of the seed particles, that is, the particles that first nucleate and serve as bases for the heterogeneous nucleation. Also important is the observation of the variation in the composition during the transport time, especially changes in the seed particles with the evolution of the accident.

Parallel to the observation of the typical aerosol composition, analysis of the species physical properties could be used to justify, on theoretical grounds, the observed composition, as well as raise some convenient questions. Once this analysis is performed, establishing the general strategy to deal consistently with the vapor-aerosol problem, the models to be used for the nucleation and condensation onto aerosol surfaces are considered. Another important issue of the vapor-aerosol process is the initial size to be regarded in the aerosol modeling. The existence of a critical size of aerosol, below which the particle "embryo" is unstable, will be shown later. The determination of this size is important in the determination of the lower limit of the range of particle sizes to be considered.

Aerosol behavior is a well-reported field due to its importance to other fields, such as environmental, health and climate researches. Consequently, extensive work is available, both in books and in technical journals, even though most of them are not nuclear-aerosol oriented. Hence, analyses of the applicability of modeling procedures need to be done to verify the applicability of the problem to nuclear aerosols. Three aerosol books have been used in this research: Hinds (68) provide a general understanding of the issue, whereas Fuchs (69) and Loyalka (34) provide a more detailed analysis.

Composition and structure of nuclear aerosols

As pointed out earlier, several aerosol sources exist in a LWR core during a severe reactor accident. They include silver, indium and cadmium vapors released from molten absorbed material, CsI and CsOH, the potential forms of cesium and iodine volatile fission products, tin released from hot cladding, and UO_2 from molten fuel.

Neglecting first the released inventories and time-release profile, an analysis is performed based purely on the examination of the material properties of these aerosol sources. This analysis suggests that silver, cadmium, cesium iodide, and uranium would bracket the nucleation behavior of vapors released in a severe accident. The material properties affecting homogeneous nucleation are the surface tension and the saturation ratio.

The term saturation is used to describe the physical state of a pure vapor. The saturation ratio is defined as the ratio of vapor pressure to the equilibrium vapor pressure. Hence, a vapor is saturated ($S=1$) when its vapor pressure is equal to its equilibrium vapor pressure, sub-saturated ($S<1$) when the vapor pressure is less than the equilibrium vapor pressure, or super-saturated ($S>1$) if the vapor pressure exceeds the equilibrium vapor pressure. The surface tension is a measurement of the intra-molecular force of species in the liquid state. The higher the surface tension, the greater is the difficulty to form droplets of the species. Therefore, higher saturation ratios (necessarily greater than one) and lower surface tensions benefit aerosol nucleation. The dependencies on these properties are shown later.

The surface tension and the equilibrium concentration (converted from vapor pressure expressions) for the most important species are presented in Table 3-4. Silver and uranium are low vapor pressure materials with a high surface tension. Cadmium is very volatile, but has a moderate surface tension. Since cesium iodide is a salt, it has a low surface tension and low vapor pressure. The surface tension and concentration equilibrium at 850 K at a system pressure of 0.2 MPa are presented below in Table 3-4.

Table 3-4. Nucleation physical properties for different species

	Surface Tension (N/m)	Equilibrium concentration (Kg/m^3)
CsI	0.073	0.0018
Cd	0.65	0.11
Ag	0.9	2.4×10^{-6}
U	0.9	

The other piece in the puzzle of the species' homogeneous nucleation analysis is the released masses, or the partial pressures of each species. The Phebus series experiment provided a typical initial inventory of all fission products, control rod and fuel elements under a severe accident scenarios. The masses of initial inventories as well as released masses of the Phebus FPT-01 experiment (48) are presented in Table 3-5 below.

The information of Tables 3-4 and 3-5 do not allow any definite conclusion about seed particles in nuclear aerosols. Cesium Iodide has a low surface tension, meaning that lower super-saturation ratios are necessary to the occurrence of nucleation. This fact led researchers, such as Petti (70), to wrongly infer that nucleation would occur onto cesium iodide particles. The fact that partial pressures will be lower than other species, and other species, such as Ag and U, have lower equilibrium vapor-pressure species do not allow any conclusion. In fact, uranium and mainly silver will have significantly higher saturation ratios.

Table 3-5. Best estimative of initial masses and released masses for potential aerosol sources in the Phebus FPT-01 experiment

Species	Initial Inventory (g)	Released Mass (g)
CsI	1.12	0.97
Cd	29.89	20.9
Ag	478	71.7
U	9163	11.0

X-ray photoelectron spectroscopy of nuclear aerosols in the Phebus series of experiments (20) shows that nuclear aerosols, in the presence of Ag-In-Cd control rods have the composition shown in Figure 3-6 below. This Figure shows that nuclear aerosols are composed of a seed particle over which several layers of different materials deposit.

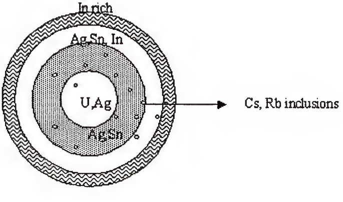

Figure 3-6. Layering composition of nuclear aerosol particle in Phebus experiments by X-ray photoelectric spectroscopy analysis

Figure 3-6 shows that typically silver and uranium are seed particles for a heterogeneous nucleation of other species over their surfaces. This condensation occurs in a layered form, except for the cesium and rubidium, which condense as inclusions.

Another factor that possibly can affect the aerosol composition is the release timing, because the heterogeneous nucleation depends on the existence of the seed particles. Hence, a synchrony in the release of seed particles vapors and other vapors must exist. In Chapter 2, it was shown that the release process of fuel, control rod and structural materials occurs according to the severe accident events, and the release phases are defined based on these events into first oxidation, main release, and second oxidation phases. The release fractions in each phase for above elements in the Phebus experiment FPT-01 are presented in Table 3-6 below.

Table 3-6. Release fractions of each phase in Phebus FPT-01 (%)

Element	First Oxidation	Main Release	Second Oxidation
Cs	19	48	33
Ag	9.5	15.6	74.9
U	0.0	16.4	83.6
Cd	14.3	54	31

Table 3.6 shows that more volatile elements, such as cesium and cadmium, tend to be released in a larger fraction in the first oxidation and main release phase, whereas silver and uranium tend to be released in the main release and second oxidation phases. The existence of silver throughout all phases shows that it will be the seed particle most of the time. Uranium's presence is significant only in the second oxidation phase.

The facts presented so far are sufficient to set up a simple and consistent general strategy to model the vapor-aerosol processes. The strategy is to calculate only homogeneous nucleation for silver and uranium and assume that the other species will nucleate heterogeneously over the silver and uranium seed particles. The silver presence is always guaranteed by the presence in Table 3-6 and by the large masses in the initial inventory, presented in Table 3-5. Hence, the procedure is simpler than considering homogeneous nucleation for all species. Subsequent steps would be to select models for homogeneous and heterogeneous nucleation. Before, the seed particle's initial size will be considered.

Critical radius

In the presence of its liquid or solid phases, a vapor will condense whenever it is supersaturated. However, in the absence of pre-existing nucleation sites, significant super-saturation is necessary before vapor condensation occurrence. In this case, a process of nucleation sites generation takes place.

A vapor is defined as a collection of monomers or single molecules in the gas phase. These monomers undergo collisions to form dimmers, trimers and other small clusters. The theoretical basis (70) used to explain these collisions is that these collisions cause a n-mer to either growth by condensation or shrink by evaporation. Under super-saturated conditions, a continuous growth of monomers takes place, leading to the formation of aerosol. It could be easily inferred that this process is faster and more intense for higher super saturation ratios. The nucleation process is shown in Figure 3-7 below.

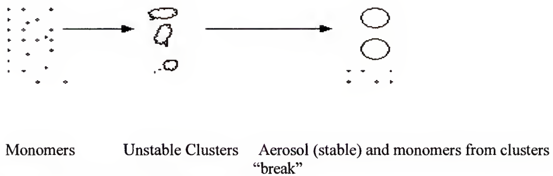

Figure 3-7. Homogeneous nucleation process

The cluster is considered an aerosol once the cluster becomes stable. There is a minimum molecular cluster size guaranteeing that a supersaturated condition yields condensation. Considering the shape of the particle as spherical, this size is called the critical radius. The critical radius is obtained when the free energy released in the condensation process over a particle of size r must overcome the surface energy required to form a droplet of size r. In other words, the free energy of formation of a cluster must be positive. The free energy of formation of a spherical molecular cluster of radius r is given by:

$$\Delta G_0 = 4\pi r^2 \sigma - \frac{4}{3}\pi r^3 \rho_l \frac{R}{M} T \ln S \qquad \text{(Equation 3-80)}$$

Where:

ΔG_0: Free energy of formation of molecular cluster of size r (J)
σ: Surface tension (J/m^2)
R: Universal constant of gases (J/mol-K)
M: Molecular weight (Kg/mol)
r: Molecular cluster radius (m)
S: Saturation ratio
T: Temperature (K)
ρ_l: Density of the liquid phase (Kg/m^3)

The first term in Equation 3-80 represents the surface energy required to form a droplet of size r, whereas the second term represents the energy released in the condensation process. The critical radius can, therefore, be obtained by making Equation 3-80 equals to zero. Performing this operation, the critical radius is given by:

$$r^* = \frac{3\sigma M}{\rho_l RT \ln S} \quad \text{(Equation 3-81)}$$

In the previous section, it was seen that the seed particles will preferably be silver and, late in the accident, uranium seed particles will add to the silver particles. Therefore, the size of the seed particles, which is the minimum limit of the size range of aerosol particles (to be set in Equation 3-8), can be estimated by applying Equation 3-81 to silver and uranium. Assuming an average temperature of 850 K and an average super-saturation ratio of 20, sizes of seed particles in the order of $10^{-1}\mu m$ are obtained.

Numerous experiments were conducted at Winfrith Laboratories in England by Bowsher et al. (71) to study the behavior of control rods in severe reactor accident conditions. The primary particles originated from control rods have geometric mean diameter of 0.3 μm for argon environment and 1 μm for steam environment, with standard deviation of 1.6 and 1.8 μm, respectively. The empirical evidence is consistent with the estimative performed.

Because the estimative for silver yield an approximate primary particle of 0.5 μm, and silver is the main particle seed material, this size is adopted in the code. Therefore, all particles originated by homogeneous nucleation are set in the first section. Alternatively, a distribution could have been set, but the standard deviation is small compared to the range of particle sizes considered, resulting in small quantity of particles in sections other than the first.

Homogeneous nucleation

During the past 75 years, many researchers have studied the theory of homogeneous nucleation. The methods of modeling homogeneous nucleation that have been developed are based on analytical expressions or based on the solution of the dynamics equation for sub-critical particles. The second represents a tremendous computational work, which in our framework represent an additional equation to be coupled to the already existent equation. However, they result in a more accurate response than analytical methods. Because of the increase in the problem size, the analytical models are preferred in the solution of our equations. The analytical models are based on two different approaches, the classical nucleation theory and the kinetic theory.

The homogeneous nucleation theory for analytical models begins considering the net rate of a g-mer molecules:

$$J_g = \beta_{1,g-1} n_1 n_{g-1} - E_g n_g \qquad \text{(Equation 3-82)}$$

Where:

$\beta_{i,j}$: Collision frequency function for collisions between i-mers and j-mers (m^3/s)
n_g: Concentration of clusters size g ($\#/m^3$)
J_g: Rate of formation of a g-mer ($m^{-3}\ s^{-1}$)
E_g: Evaporation rate (s^{-1}), expressed by

$$E_g = \beta_{1,g-1} n_1^e \left(\frac{n_{g-1}^e}{n_g^e}\right) \qquad \text{(Equation 3-83)}$$

The superscript e denotes equilibrium concentrations. Typically, $\beta_{i,j}$ is known (e.g. from gas kinetic theory). Where the classical nucleation theory and the kinetic theory differ is over the choice of the equilibrium state. The classical theory considers equilibrium to mean metastable equilibrium that would exist for a vapor having the same super-saturation and temperature as the vapor in question. The kinetic theory considers equilibrium to mean stable equilibrium of a saturated vapor as the same temperature as the vapor in question.

Both theories proceed by the same sequence of arguments to derive a nucleation rate that can be written as:

$$J = N\frac{\beta_{1,1}n_1}{12}\sqrt{\frac{\Theta}{2\pi}}\exp\left[-\frac{4\Theta^3}{27(\ln S)^2}\right] \qquad \text{(Equation 3-83)}$$

Where:

J: Nucleation rate (# aerosols/m^3 s^1)
N: Normalization constant (m^{-3})
$\beta_{1,1}$: Collision frequency function of monomers (m^3/s), obtained by kinetic theory means by Friedlander (72):

$$\beta_{1,1} = \left(\frac{3V_l}{4\pi}\right)^{1/6}\sqrt{\frac{6kT}{\rho_l}} \qquad \text{(Equation 3-84)}$$

V$_1$: Monomer volume (m^3)
ρ_l: Density of the species liquid phase (Kg/ m^3)
Θ: Dimensionless surface tension, given by:

$$\Theta = \frac{\sigma S_1}{kT} \qquad \text{(Equation 3-85)}$$

S$_1$: Surface area of a monomer (m^2)

Thus, both nucleation rates are indeed identical except for a possible difference in the normalization constant N. In both approaches, this constant is the same as appears in the Boltzmann distribution for the cluster population at equilibrium:

$$n_e^g = N\exp\left[\frac{-\Delta G(g)}{kT}\right] \qquad \text{(Equation 3-86)}$$

where ΔG is the Gibbs free energy of n-mer.

In the classical theory, the monomers concentration will be given equally by the equilibrium concentration as a result of its assumption. This is equivalent to saying that N is equal to the equilibrium concentration, or equal to the monomers concentration, as expressed in Equation 3-87.

$$N_{classical} = n_1^e = n_1 \qquad \text{(Equation 3-87)}$$

The application of this normalization constant to Equation 3-83, together with the application of some algebra, yields the classical Becker-Doring expression for homogeneous nucleation, represented below:

$$J = n_1^2 \left(\frac{2\sigma m}{\pi} \right)^{0.5} \frac{S^2}{\rho_l} \exp\left(-\frac{4\pi}{3} \frac{\sigma r^{*2}}{kT} \right) \qquad \text{(Equation 3-88)}$$

In their kinetic derivation, Katz and Donohue (73) assumed that for a saturated vapor in equilibrium, the free energy of a cluster is given by:

$$\Delta G(n) = \sigma s(g) = \sigma s_1 g^{2/3} \qquad \text{(Equation 3-89)}$$

So that the equilibrium concentration distribution for monomers n can be written:

$$n_g^e = N \exp(-\Theta g^{2/3}) \qquad \text{(Equation 3-90)}$$

Later, Girshick et al. (74) suggested that the kinetic normalization constant can be evaluated simply by requiring that Equation 3-89 should be satisfied for monomers, yielding:

$$N_{kinetic} = n_1^e \exp\Theta \qquad \text{(Equation 3-91)}$$

Performing an interpretation of these results, Girshink et al. (74) concluded that nucleation rates from the two theories are related by:

$$J_{kinetic} = \frac{\exp\Theta}{S} J_{classical} \qquad \text{(Equation 3-92)}$$

The basic assumptions inherent in the analytical models derivation are: (1) The free energy of formation of a cluster is comprised of the free energy change due to condensation and the surface tension energy of the drop formed; (2) Particles are spherical and charge neutral; (3) Surface tension is size-independent (capillarity approximation); (4) Initially the system consists of particle-free vapor; (5) Steady-state process.

Lothe and Pound (74) suggested that important statistical mechanical contributions to the free energy of formation of clusters were neglected in the analytical approach. They add three additional terms to the free energy of formation of clusters: the free energy of separating a group of g molecules from a larger ensemble, the translational free energy, and the rotational free energy. However, the Lothe and Pound predictions for cloud chambers disagree with the experimental data. The compilation of results from cloud chambers showed that the considerations of Lothe and Pound should not be used, because, actually, the predictions without Lothe and Pound's terms were better than their predictions.

Aerosol particles nucleated from condensation normally are spherical and the assumed seed particle (Ag) is charge-neutral. What could have been pointed out is that ion-induced nucleation will compete with homogeneous nucleation. Actually, there is a great concentration of ions in the fluid under a severe accident, most of them from water ionization by radiation. Petti (70) plotted aerosol maps that show the importance of each process according to the saturation ratio and temperature. These maps showed that the importance of the ion-induced nucleation is limited to a small range of conditions.

The third assumptions referred to the surface tension. The surface tension, especially for fission products, is not a well-understood property. Obtaining reliable data and good understanding of the surface tension property for fission products, especially the seed particles is an important improvement for the field. Hence, as the fission products surface tension data-base is limited, the capillarity consideration is not possible.

The assumption of particle-free vapor has two important aspects. First, it is consistent with the general assumption that no cross terms exits in the general equations, i.e., no physical synergisms takes place. In reality, homogeneous nucleation competes with wall condensation and heterogeneous nucleation, and these processes can affect each other. The mathematical coupling of these processes is treated by the general equations. Therefore, the treatment is consistent with the general equations, that is, the phenomena are treated separately, and their interaction is considered in the general equation.

Several authors (75) have investigated the steady state assumption. They have calculated the time constant for the nucleation process, and concluded that its order of magnitude is 10^{-7}s. This time constant is orders of magnitude less than typical time steps taken by the code. Thus, the steady-state assumption is consistent.

Girshick et al. (74) performed a comparison of calculations that applies their model coupled to the moments method to treat the stable aerosol, the classical Becker-Doring model coupled to the moments method, and a discrete model. The comparison was established based on the dimensionless time and concentration parameters shown below.

$$\tau = n_1 \beta_{1,1} t \qquad \text{(Equation 3-93)}$$

$$N^* = \frac{N}{n_0} \qquad \text{(Equation 3-94)}$$

The calculations were performed for different sets of dimensionless surface tension and saturation ratio. The two sets analyzed have: (1)$\Theta=19$, $S=200$; (2)$\Theta=8$, $S=6$.

The first one refers to situations where the vapor has high surface tension and high molar concentration or low equilibrium concentration, which coincides to the situation of the previously identified seed particles of silver and uranium. The second set is more consistent with water behavior.

Figure 3-8 shows the result for the first set of parameters. This set was chosen because it has more similarity with the identified seed particles. The figure shows that the kinetic/moments model has a quite good agreement with the discrete model, whereas classical/moments model presented predictions five to six orders of magnitude below the discrete predictions. Since discrete models tend to have better results, it is consistent to assume that the kinetic theory is a better approach to be applied. The same tendency was observed for the other set of parameters.

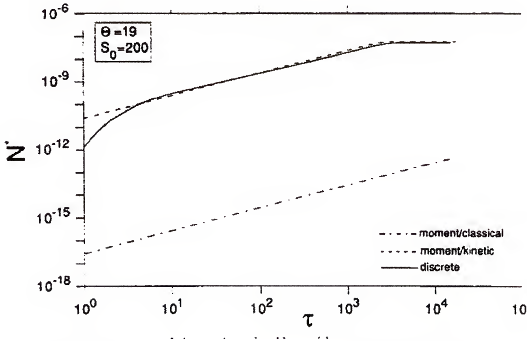

Figure 3-8. Comparison classical/kinetic/discrete models for Θ=19 , S=200 (73)

In several earlier experiments studies of dibutylphthalate (DBP) nucleation, the observed homogeneous nucleation rate was found to exceed the classical rate by a factor of six orders of magnitude, which is consistent with the Girshik study. These differences between the classical/moments and discrete and experimental results highlight a flaw in the derivation of classical nucleation. Namely, evaporation coefficients should be obtained by referring to a saturated vapor in equilibrium, and not a supersaturated vapor in constrained equilibrium.

Since the analytical approach was chosen due to its simplicity, the kinetic model presented a more consistent theoretical approach and better agreement with the experimental and discrete results. For these reasons, the Girshik model (73) was chosen. Martin, in his doctoral thesis (76), arrived at the same conclusion, performing a more detailed analysis.

Hence, the proposed vapor-aerosol solution strategy involves the following procedures: (1) Inclusion of the homogeneous nucleation in the solution of the equations only for silver and uranium, using the Girshik model; (2) Use of only heterogeneous nucleation for other species.

Condensation onto aerosol surfaces (Heterogeneous nucleation)

The particle-condensation solution could be performed by solving the steady-state molecular transport in the gas, according to Seinfeld (77). The mass condensation rate of vapor condensing on a sphere can be expressed as (34):

$$\dot{m}_v = 4\pi r_p^2 m_v (J_- - J_+) \qquad \text{(Equation 3-95)}$$

Where:

m_v: Mass of vapor monomer (Kg)

r_p: Aerosol radius (m)

J-: Current of vapor molecules directed towards the particle (#/m^{2}s)

J+: Current of vapor molecules directed outwards from particle (#/m^{2}s)

The current of vapor molecules reaching or leaving the particle is given by:

$$J_{\pm} = \int_{(c\bullet n_r)><0} dc|cn_r|f_v^{\pm}(r_p,c) \quad \text{(Equation 3-96)}$$

In Equation 3-96, r is the position vector, c is the molecular velocity, and f_v is the molecular distribution of the vapor. The subscripts + and – indicate the distributions of outgoing and incoming molecules, respectively. Note that n_r is a unit vector normal at r, directed from the sphere into the vapor-gas mixture.

For the outward current, assuming a diffusive reflection boundary condition, a simple maxwelian corresponding to the saturation concentration and the temperature, determines the molecular distribution, but for the incoming the Boltzmann transport equation (BTE) need be solved. The solution of the BTE is conveniently divided into three regions, according to the Knudsen vapor number, expressed in Equation 3-97 below:

$$Kn_v = \frac{\lambda_v}{r_p} \quad \text{(Equation 3-97)}$$

Where:

λ_v: Vapor molecular mean free path (m), given by:

$$\lambda_v = 2D_{v,bulk}(\frac{m_v}{2KT})^{0.5} \quad \text{(Equation 3-98)}$$

r_p: Particle radius (m)

$D_{v,bulk}$: Diffusivity of vapor in the bulk gas (m^2/s)

m_v: Vapor molecule mass (Kg)

For large Knudsen numbers (Kn>>1), the region is called the free molecular region, whereas for small Knudsen numbers (Kn<<1), the region is called the continuum region. The region between these two is called the transition region. The range of Knudsen numbers for our problem is in the continuum region for most of the particles sizes, but for small particles (r_p of the order of 10^{-6} and 10^{-7} m), the Knudsen number will fall into the region between the continuum and the transition region, called the near continuum regium (Kn close to 1). For the continuum region, the deposition rate can be obtained by solving Equation 3-59 for a quiescent medium (u=0) in spherical coordinates:

$$\frac{1}{r^2}\frac{d}{dr}\left(r^2\frac{d}{dr}\right)C(r)=0 \qquad \text{(Equation 3-99)}$$

With the boundary conditions:

$$C(r)=C_s \quad \text{for } r=r_p \qquad \text{(Equation 3-100)}$$

$$\lim_{r\to\infty}(C(r))=C_\infty \qquad \text{(Equation 3-101)}$$

The solution of this problem yields:

$$k_{dep}=4\pi D_{v,bulk}r_p(C_\iota-C_{eq}) \qquad \text{(Equation 3-102)}$$

The meanings of all of the terms were determined beforehand. The transition regime has been the focus of research, and various models and methods, relying, most of the time in numerical approaches (depending on the application, an analytical result can be obtained). However, fairly accurate results can be obtained for near continuum regions using approximations. According to Park's (78) analysis, the Fuchs and Stugin (79) model is the most used and assessed approximation for the near continuum region. Furthermore, this formulation, presented below, is extremely simple and converges to the continuum formulation when approaching small Knudsen numbers, and has a maximum error of 13.4% (69).

$$\dot{m}_v=4\pi D_{\iota,bulk}r_pN(C_\iota-C_{eq})\left[\frac{1+Kn_v}{1+1.71Kn_v+1.333Kn_v^{\,2}}\right] \qquad \text{(Equation 3-102)}$$

Therefore, the continuum expression for the aerosol condensation previous shown, corrected by the Fuchs-Stuggin factor is used in the implemented model. Notice that the number of the particles was added in the expression (N). Recall that the expression was derived for one particle, it being necessary to multiply it by the number of particles. The derivation of this expression is based on the following assumptions: (1) The medium is quiescent; (2) Kelvin effect can be neglected; (3) Solute effect can be neglected; (4) Spherical particles; (5) Mass and energy transfer equations can be decoupled.

The derivation of these models is based on a quiescent medium. It has been speculated that turbulent flow conditions could lead to a significant enhancement of the transport rates, and such effects should be accounted for. Kress analysis (80) determined that enhancement is not significant and need not be accounted for.

Saturation vapor pressures are defined and measured for a plane (flat) surface at a given temperature. If the liquid surface is sharply curved, such as with aerosol surfaces, Kelvin pointed out that the partial pressure required to maintain equilibrium is higher than that for a flat surface. It is a consensus among aerosol researchers that Kelvin effect can be neglected for particles larger than 0.1 μm. Once the aerosol minimum size determined is 0.5 μm, neglecting the Kelvin effect is consistent.

The solute effect takes into account the differences in solubility between the vapor and the aerosol species, or the effects of the chemical compositions of the aerosol and the vapor. Accordingly, most soluble aerosols are activated preferentially, or have a higher utilization. The aerosol or nuclei to be condensed are classified into soluble and insoluble nuclei. With insoluble nuclei, surface characteristics are important, for once the nucleus is coated with liquid, it behaves in a manner similar to a drop of pure liquid.

Solubility is considered in the condensation onto aerosol surfaces through adjustment of the equilibrium concentration. With soluble nuclei, vapor changes the properties of the nucleus, forming a solution. In general, the equilibrium solvent vapor pressure over a solution surface is lower than that over a pure solvent surface. Therefore, condensation on soluble nuclei can happen effectively at super-saturation ratios less than one. On the other hand, insoluble nuclei require saturation ratios greater than one. Figure 3-9 presents the alternative of the condensation onto aerosol surface process.

Soluble or Insoluble Nuclei

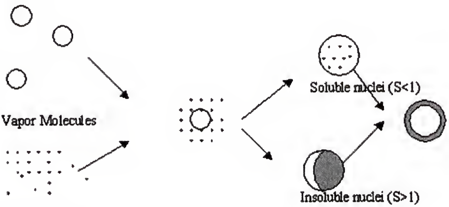

Figure 3-9. Particles formation by heterogeneous condensation

Actually, Figure 3-9 shows that the kinetics of the vapor-aerosol condensation is the same as the vapor-structure kinetics, that is, the process takes place in three steps, transport of vapor molecules to the surface, kinetics of the interaction with the surface of the aerosol, which has the influence of the solubility, and transport away from the reaction site, when important changes can take place. The chosen model actually neglects aspects of the second and third phases. There are no elements or researches to support such an assumption. Thus, this constitutes a limitation of the currently used model, but no model has ever been presented to solve this limitation.

Another assumption of the model is that the aerosol is spherical. Actually, it is known that condensation rates depend on aerosol shape, and aerosol shape varies according to composition and thermal-hydraulic conditions. This issue is detailed in the next section. Available shape factors models show that difference in the condensation rates of up to 25 % can be found when neglecting the aerosol shape.

The solution of the condensation of vapors onto aerosol particles should include energy- and mass-balancing equations for a closed system of aerosol and condensable vapor, as pointed out by Gelbard (70). They need to be coupled because the gas thermal variation in time is dependent on the condensation rate. On the other hand, equilibrium concentration depends on temperature. Notice that this development is for a closed system. Considering a severe accident, the heat source resulting from the condensation can be neglected, and the temperature of the mixture is not dependent on concentration variation. Now, considering that the time-steps used in the solution are small (10^{-2} to 10^{-3}s), no significant thermal variation will occur in a time-step, thus do not affecting significantly the mass transport solution. Thus, decoupling the mass and energy transfer solutions is entirely consistent.

Aerosol Phenomena

It was pointed out earlier that aerosol behavior plays an important role in a severe-accident source term. Purely aerosol processes important for the source term are the aerosol deposition onto structural surfaces, the agglomeration of two particles, and the re-suspension of aerosols onto the surface by turbulence. In this and the following sections, the important aspects related to the hydrodynamics of the aerosol, and the process of each phenomenon are addressed, highlighting assumptions, identifying models and selecting the more appropriate one.

The entire theory of aerosol available is developed based on the assumption of aerosol spherical shape. However, most of the time aerosols are not spherical. The procedure adopted is to correct the spherical-derived expression by an appropriate factor, the so-called shape factor. Because the shape of aerosols affect differently the several phenomena involved in the aerosol, different shape factors are defined for vapor condensation (condensation shape factor), for aerosol hydrodynamics (dynamic shape factor) and for aerosol agglomeration (collision shape factor).

A consistent consideration of the aerosol shape would involve two steps. First, a consistent model addressing the nuclear aerosol shape needs to be established (shape selection model). Second, models need to be selected or developed to obtain the shape factors for the shape selection model.

Aerosol shape is strongly influenced by the process that leads to their initial creation. Coarse particles (> 2μm) are generally created by mechanical processes, such as friction, rarely leading to spherical particles. Most of the time, these particles have irregular shapes. Fibers and elongated "plaquettes" are the most common shapes for aerosols created by mechanical processes, and are shown in Figure 3-10 (a). On the other hand, fine particles (< 2μm) are generated by combustion or gas-to-particle conversion (nucleation). Aerosols formed by vaporization, followed by condensation have initially spherical shapes, as shown in Figure 3-10 (b).

After the generating process, aerosols undergo other processes that decisively impact their shapes. Most of the aerosols, even if they are created as spheres, will coagulate and tend to be irregular aggregations, which can vary from "fluffy" balls to long dendritic or fractal forms. Another important process is condensation. If there is considerable condensation taking place, aerosols tend to develop a closed, packed form, resembling spheres. When it is not the case, it is necessary to develop a procedure for calculating the drag on and effective sizes of such agglomerates. On top of that, it has been argued that external forces, such as drag, can provoke distortion of the aerosol shape.

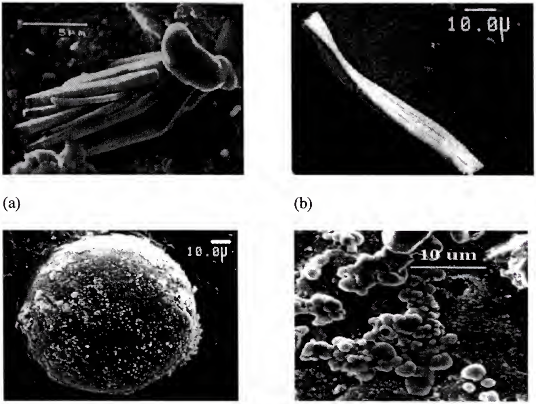

(a) (b)

(c) (d)

Figure 3-10. Most common aerosol shapes: (a) oblate (plaquette), (b) oblate (fiber), (c) spherical, (d) agglomerated

Nuclear aerosols associated with severe accidents are formed by gas-to-particle conversion and fragmentation of material, being only the first to be considered in our model. The way it evolves, in the nuclear primary circuit, poses formidable challenges in the task of a shape factor selection model. The determination of the shape of agglomerates and the dynamics of these shapes deserves a detailed analytical and experimental investigation.

Regarding the second step necessary to consider aerosol shape, there are several models in the literature for dynamic shape factors. The various shapes investigated in the literature are presented below, in Table 3-7.

Table 3-7. Various aerosol shapes investigated in the literature

Shape	Work
Spheroids and needles	Payne and Pell (82)
Toroids	Payne and Pell (82)
Bi-spherical Units	O'Neill (83)

Condensation shape factors were summarized by Williams (84) for oblate spheroids, bi-spherical and toroidal particles. Collisional shape factors for large spheroids and small spheres, large spheres and small spheroids, and large and small spheroids were derived by Booth (85). Therefore, a limited number of shape factors models are available.

Scanning electron microscope micrographs from sample filters of the SFD-4 experiment are presented in Figure 3-11. Both spherical and crystalline-like deposits are presented. The spheres of material are aerosol particles that were trapped by the filter, whereas the crystalline like material is representative of vapor deposition on the filter (70). Hence, the implicit assumption that the bulk of the aerosol formation occurs through gas-to-particle conversion, which results in spherical aerosols, is consistent with the experimental evidence of SFD-4. However, given that the length of the distance release site-filter is not known, and the fact that the filtered aerosol is not under the flow influence, it is not possible to conclude with complete certainty that spherical shape can be assumed, since the agglomeration influence and the flow influence are not taken in account.

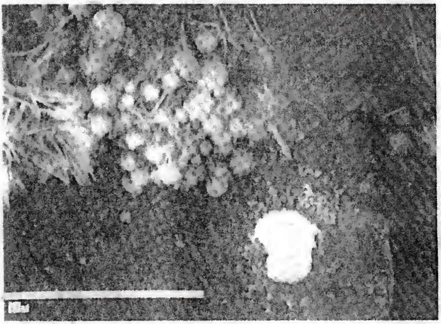

Figure 3-11. Scanning electron micrographs of material on filters from effluent samples of SFD-4 experiment (70)

Aerosols in the Phebus FP-01 experiment were identified as having 1.2 and 1.7 μm aerosol mean radius in the hot and cold leg respectively. These radiuses represent the agglomeration of 15 and 28 particles, respectively, neglecting the condensation onto aerosol surface, i.e., considering that only agglomeration is responsible for the aerosol growth.

Examination of circuit and filter deposits (Figure 3-12 (a)) indicated that the deposit was particulate with no notable morphology and was thick enough to hide the filter or impactor substrate. Pictures presented in Figure 3-12 show these features of an amorphous particle deposit apparently composed of very fine particles whose size would be about 0.5 μm in diameter both in the circuit hot leg, and in the cold leg. Observations showed that these very fine particles may be agglomerated to form particles of size up to 20 μm. Specific particles could be spotted during the SEM examination campaign such as

Ag/U-rich particles on point C samplings (a sample of a Ag/U-rich particle or solidified droplet is shown in Figure 3-12 (b)). These particles may reach sizes up to 20 μm. Some samples of Re-Ag-U, Re-Cs (rhenium from thermocouples) and Ag rich particles collected on point G impactor plates are displayed in Figure 3-12(c).

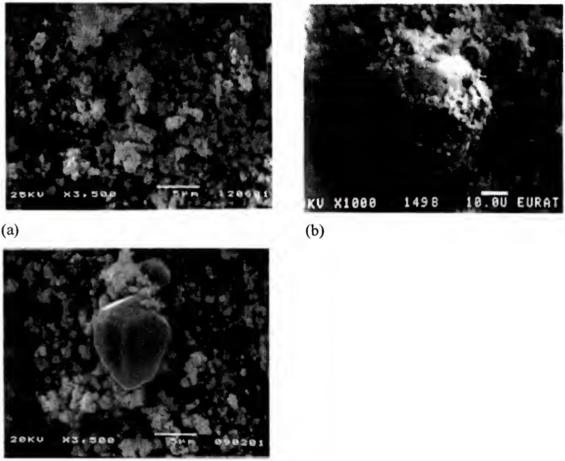

(a) (b)

(c)

Figure 3-12. Scanning electron micrograph of Phebus FPT-01 circuit filters: (a) cold leg filter substrate; (b) spotted particle on cold leg; (c) spotted particle on hot leg.

Empirical evidence of both the SFD-4 experiment and Phebus FP-01 showed that aerosol shape is close to spherical, even though agglomerates were identified. As pointed out earlier, agglomeration tends to deviate from the original spherical shape of the aerosol. However, condensation tends to transform the particles' shape into spherical. Thus, condensation may be intense enough to overcome the agglomerative tendency to deviate from spherical shape. Further investigation needs to be done to confirm this theory, which must be conducted both by gathering empirical evidence as well as by performing calculations to evaluate the comparison of the two processes. However, for now, it is accepted that spherical shape is a good assumption.

Another assumption used in the development of aerosol phenomena modeling for the nuclear field is the neglect of synergy effects. Synergy, in this work, is considered in two perspectives, the mathematical and physical aspects. These two aspects are considered below.

The deposition total velocity is considered the addition of the deposition velocity due to several deposition mechanisms. This is the mechanism employed in the modeling, represented in Equation 3-103:

$$V_{dep} = V_{T/L} + V_{Therm} + V_{grav} + V_{inertial} \qquad \text{(Equation 3-103)}$$

Where:

V_{dep}: Total deposition velocity (m/s)
$V_{T/L}$: Turbulent/Laminar deposition velocity (m/s) (convective-diffusive velocity)
V_{Therm}: Thermophoretic deposition velocity (m/s)
V_{grav}: Gravitational deposition velocity (m/s)
$V_{inertial}$: Inertial deposition velocity (m/s)

Actually, this procedure for obtaining the total deposition is not correct. The correct procedure would be the solution of the continuity equation considering only the deposition, expressed in Equation 3-104:

$$\frac{\partial C}{\partial t} + \nabla J = 0 \qquad \text{(Equation 3-104)}$$

Where:

$$J = J_{DT/L} + J_{Therm} + J_{grav} + J_{inertial} \qquad \text{(Equation 3-105)}$$

In these equations, the J is the particle current with the same subscripts of Equation 3-105, and C is the particle concentration. Equation 3-104 can be replaced by the steady-state solution, provided by:

$\nabla J = 0$ (Equation 3-106)

The problem in solving Equation 3-106 is the difficulty in obtaining a solution, and when it is achieved, an analytical solution. Most of the time, numerical integrations need to be performed, enhancing the computational work. Loyalka (34) and Fernandes (86) developed several works considering partial synergisms. On the other hand, Equation 3-105 is a good approximation to the true solution when there is a dominant term in the summation. The dominant mechanism depends on particle size, Reynolds number and thermal gradient. However, more calculations need to be done to confirm these preliminary observations.

Similarly to deposition, total agglomeration kernels can be calculated by the summation of the kernels of each phenomenon separately:

$K_T = K_B + K_{DG} + K_{Turb}$ (Equation 3-107)

Where:

K_T: Total agglomeration kernel (m^3/s)
K_B: Brownian agglomeration kernel (m^3/s)
K_{DG}: Differential gravitational agglomeration kernel (m^3/s)
K_{Turb}: Turbulent agglomeration kernel (m^3/s)

Using the same kind of argument, the agglomeration kernel considering both Brownian and gravitational mechanisms can be derived through the following equation:

$D\nabla^2 C - \vec{V}\nabla C = 0$ (Equation 3-108)

In this equation, the diffusion coefficient is the relative diffusion coefficient of two particles, and the velocity is the relative velocity of two particles. Loyalka (34) performed some work in solving general equations, such as Equation 3-108. The rationale behind the additive assumption is that, again, always there will be a dominant mechanism for agglomeration.

The additive assumption constitutes the basis of the mathematical aspect of the synergetic neglecting. The physical aspect of this neglecting is related to second order effects. The most recognizable is the flow field. Certainly, the flow field around one particle affects the flow over other particles and the trajectory of other particles. A possible example of interaction is shown in Figure 3-13 below, where particles farther apart have no hydraulic interactions and closer particles have hydrodynamic interaction, affecting the drag force.

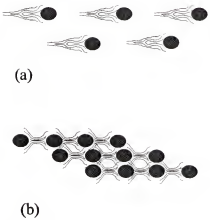

Figure 3-13. Interactions of aerosol particles: (a) without hydraulic interactions; (b) with interactions

The physical synergetic effects are sometimes taken into account and sometimes neglected. Along the model development, the hydrodynamic interactive effects are mentioned, when their effect is important.

Regarding the mathematical synergy, the procedure adopted was to consider valid the additive simplification, and then perform a sensitive study that confirms the validity of this simplification in the next chapter.

Aerosol hydrodynamics

The first one to contribute significantly to the understanding of aerosol dynamics was Stokes (87). He calculated the drag force of a spherical particle into a fluid in movement, making the following assumptions: (1) Flow is in the continuum region ($Kn<<1.0$); (2) Particle is in the viscous region ($Re_p<1.0$); (3) Aerosols are spherical and rigid; (4) No intra-particle hydrodynamic interaction. Under these conditions, the drag force is expressed by:

$$F = 6\pi\mu r_p V \qquad \text{(Equation 3-109)}$$

The last term in Equation 3-109 is the fluid velocity, and the other terms in this equation were previously defined. The particle Reynolds and Knudsen numbers are given by Equations 3-110 and 3-111 below:

$$\mathrm{Re}_p = \frac{2V\,r_p}{\nu} \qquad \text{(Equation 3-110)}$$

$$Kn_g = \frac{\lambda_g}{r_p} \qquad \text{(Equation 3-111)}$$

Where:

λ_g: Gas molecular mean free path to the particle radius (m), given by:

$$\lambda_g = \frac{3}{2}\mu_g\left[\frac{\pi}{2P\rho_g}\right]^{0.5} \qquad \text{(Equation 3-112)}$$

Regarding the first assumption, when the diameter of a particle is approaching the mean free path of the molecules in the medium, Cunnigham (88) and Milikan (89) showed that because the medium is no longer a "perfect" continuum, the resisting force offered to the particle should be smaller than that predicted by the Stokes Law. The difference in the dependence of resistance on particle diameter corresponds to the conditions prevailing at the two extremes of the particle ranges. For large particles, the primary source of resistance is the viscosity of the medium, whereas with small particles or with a highly rarefied medium, the predominant resisting mechanism is due to the inertia of gas molecules the particle encounters. This effect has significance for gas Knudsen numbers greater than 0.1, which typically occurs for particles less than 1.2 μm, i.e., the lower part of the particles size spectrum. The Cunningham corrective procedure is only convenient for Knudsen numbers close to one (for very large Knudsen numbers, another approach is needed), which is the case of our particles size spectrum and typical gas thermal-hydraulic conditions.

To correct this effect, a factor, commonly known as the Cunningham correction or slip factor is applied to the denominator of the Stokes expression, given by:

$$C_c = 1 + Kn_g\left[A + Q\exp\left(-\frac{b}{Kn_g}\right)\right] \qquad \text{(Equation 3-113)}$$

Where:
A,Q,b: Constants provided by Davies (90) (1.25,0.41,0.88)
C_c: Cunnigham correction factor

Regarding the second assumption, it is first necessary to set up the upper limit. This limit is established in the next section, and is 50 μm. For limiting thermal hydraulic conditions (higher flow velocity and smaller gas temperature), the maximum particle Reynolds number is 0.5. Hence, the viscous flow assumption is reasonable.

The third assumption is consistent with the assumption, still needing more assessment, of spherical particles. The fourth, nevertheless, needs proof, which is achieved by considering a typical maximum particle number concentration of 10^{14} particles/m^3 (from preliminary runs) and an average size of the particle of 1.7 μm, from the Phebus FPT-01 experiment. This data yields that the total particle volume represents a little more than 1% of the total volume, and the distance between particles will be in the order of 10 times larger than the particle diameter. This means that the particles are so distant that no hydrodynamic interactions between particles actually will occur with significance, even for the higher typical particle number concentration.

Small particles suspended in gas undergo random translational motion because they are buffeted by collisions with swiftly moving gas molecules. This phenomenon has been observed by Robert Brown, in 1828, and was called Brownian motion. The particles migrate by a diffusion process. Later, Einstein (91) demonstrated that the diffusion coefficient of this process is given by:

$$D_p = kTB_p \qquad \text{(Equation 3-114)}$$

Where:

D_p: Diffusivity of particle p in the bulk gas (m^2/s)
B_p: Mobility of particle p (m/Ns)

Also important in the derivation process is the appearance of the mobility concept. Notice that the mobility has units of velocity per unit force. This quantity actually can have its capability extended, since it represents the velocity of the particle, once submitted to any force. Therefore, once known any force acting on a particle, the resultant velocity can be obtained by multiplying it by its mobility. Still, from Einstein's derivation, the mobility is defined as the division of the drag force by the velocity. In our case, this operation yields the following expression for the mobility:

$$B_p = \frac{C_c}{6\pi\mu\, r_p} \qquad \text{(Equation 3-115)}$$

All derivations assumed that a steady-state condition exists, i.e., transient periods can be neglected. This is confirmed as a good assumption in several books, by observing that the relaxation time of the system particle-flow, given in Equation 3-116, is too small compared to the interest time, in our case the time step. Therefore, the transient effects can be neglected, and a steady-state condition can be assumed. Same behavior was observed in the other considered processes.

$$\tau = \frac{2C_c\rho_p r_p^2}{9\mu} \qquad \text{(Equation 3-116)}$$

Where:
ρ_p: Particle density (Kg/m^3)

Aerosol deposition

Aerosol deposition onto structural surfaces is a consequence of several different causes. Under the predominant conditions of a severe accident, the phenomena identified as causing deposition were gravitation, laminar/turbulent diffusion, thermophoresis and inertia of the particle when flowing through irregularities. The additive procedure was adopted (Equation 3-103), and each phenomenon is considered in the next sections.

An assumption of the aerosol deposition modeling is that all the particles stick at the piping walls. Exact sticking coefficients are very difficult to obtain. It has been observed experimentally that it could be a good assumption, which can be explained by the fact that nuclear aerosol particles are possibly liquid due to the effect of condensation. Tandom et al. (92) pointed out that rebound is not a characteristic of liquid particles.

Gravitational deposition

The gravitational deposition velocity is the result of the application of the mobility concept to gravitational force, yielding the following expression:

$$V_{dg} = m_p g B_p \cos\theta \qquad \text{(Equation 3-117)}$$

Where:

V_{dg}: Gravitational deposition velocity (m/s)
m_p: Particle mass (Kg)
g: Gravitational acceleration (9.81 m/s^2)
B_p: Particle mobility (m/N-s) (Equation 3-115)
θ : Angle of the deposition surface with the horizontal orientation

As long as the particle size increases, the gravitational force is increased and the mobility decreases. The deposition velocity increases with the square of the particle radius. For typical severe accident conditions, the gravitational deposition velocity becomes comparable to the flow velocity for particles of 50 μm. In addition, as mentioned earlier, the typical particle sizes of reactor aerosols in the primary circuit are of the order of 1.5 μm. Because the flow velocities and deposition (considering only the gravitational) are comparable at 50 μm, and few particles are going to reach this size, the upper limit of the size spectrum is set at this value. Particles that grow above this size are assumed to deposit in the volume as it happens.

Convective-diffusion deposition (laminar deposition)

The flow can be characterized, according to the flow velocity behavior, in laminar or turbulent flow, as pointed out in the hydrodynamics review. The process of mass transfer is modeled by the same equation used to solve the laminar-diffusive mass transfer for vapor molecules (Equation 3-73), which is the exact solution truncated to three terms is presented in Equation 3-74 (derived by Gormley and Kennedy).

Contrary to what happens in the vapor molecule case, the aerosol solution converges quickly, it being convenient and accurate to use Equation 3-75 for the laminar-diffusive deposition velocity, and Equation 3-74 to provide the concentration at the end of the cell. These equations are repeated here, with new numeration for the completeness of the work. Equation 3-118 is equivalent to Equation 3-73 and so on.

$$u\frac{\partial c}{\partial x}=\frac{1}{Pe}\frac{1}{r}\frac{\partial}{\partial r}\left(r\frac{\partial c}{\partial r}\right) \qquad \text{(Equation 3-118)}$$

$$\frac{C}{C_0}=0.8191e^{-7.314h}+0.0975e^{-44.6h}+0.0325e^{-114h} \qquad \text{(Equation 3-119)}$$

$$v_{dL}=\left(1-\frac{C}{C_0}\right)\frac{d_h}{L_n}V_{fluid} \qquad \text{(Equation 3-120)}$$

Turbulent deposition

Turbulent flow is a complex phenomenon and difficult to describe, and particle motion within turbulence is even more difficult because of inertia. Particle inertia is important in relation to particle motion within varying eddy sizes and frequencies. Owing to drag, a particle will be directed in the general path of the motion of the several eddies that pass across the particle. If a particle were to remain infinitely within a particular eddy, the particle would eventually obtain the same velocity as the eddy. Eddies are transient, however; consequently, the effect of turbulence on the particle's motion depends upon the integrated force on the particle while the particle is in each eddy.

Because there are insufficient data to describe the continuously-varying forces acting on a particle in turbulent flow, the ideal approach is to try to describe the statistical average of the particle's motion over a period of time that is long with respect to the time the particle remains in the eddy. The theoretical modeling of turbulent, however, historically is based on the concept of eddy diffusivity, associated with the deposition velocity definition, i.e., inertia is neglected:

$$V^+ = \left(\frac{D}{\nu} + \frac{\varepsilon}{\nu}\right)\frac{dC^+}{dy^+} \qquad \text{(Equation 3-121)}$$

Where:
V^+ : Dimensionless velocity, given by V/V_*
C^+ : Dimensionless concentration, given by C/C_0
y^+ : Dimensionless axial distance, given by $y\ V_*/\nu$
V_*: Frictional velocity (m/s)

The terms inside the parentheses are the dimensionless Brownian and eddy diffusivities. The eddy diffusivity expression was obtained by Lin et al. (93):

$$\frac{\varepsilon}{\nu} = \left(\frac{y^+}{14.5}\right)^3 \text{ for } y^+ \leq 5, \text{ and}$$

$$\frac{\varepsilon}{\nu} = \left(\frac{y+}{5}\right) - 0.959 \text{ for } \quad 5 \leq y^+ \leq 30 \qquad \text{(Equation 3-122)}$$

Diffusion for regions of $y^+ \geq 30$ is usually neglected since this region is often assumed to be a uniformly mixed turbulent core of concentration $C^+=1$. A concept introduced in the solution of Equation 3-121 is that of free-flight distance. According to the researchers that developed this theory, there is a distance from the wall where the inertia of the particle will be great enough to throw the particle onto the wall. Applying this concept to the equation and performing a separation of variables:

$$\frac{1}{V^+}\int_{C^+(S^+ + r^+)}^{1} dC^+ = \int_{S^+ + r^+}^{5} \frac{dy^+}{(D/\nu) + \left(y^+/14.5\right)^3} + \int_{5}^{30} \frac{dy^+}{(D/\nu) + (y^+/5) - 0.959} \qquad \text{(Equation 3-123)}$$

The lower limits of integration are evaluated at the distance $S^+ + r^+$. The term S^+ is the dimensionless distance a particle with initial velocity of v_0 will move horizontally through still fluid before coming to rest, or, in other words, the assumed radial velocity the particle possesses at the start of the free-flight distance. The term r^+ is the dimensionless radius of the particle. This integral is evaluated (93), yielding:

$$V^+ = \frac{1}{Int. + (1/\left[(V_0)^+\right]_{S^+ + r^+})} \qquad \text{(Equation 3-124)}$$

Where:

$$Int. = 14.5\left(\frac{\nu}{D}\right)^{2/3}\left\{\frac{1}{6}\ln\left[\frac{(1+\phi)^2}{(1-\phi)+\phi^2}\right] - \frac{1}{(3)^{1/2}}\tan^{-1}\left[\frac{2\phi-1}{(3)^{1/2}}\right]\right\}\Bigg|_{y^+=S^++r^+}^{y^+=5} + 5\ln\left[\frac{D}{\nu}+\frac{y^+}{5}-0.959\right]\Bigg|_{5}^{30} \qquad \text{(Equation 3-125)}$$

And:

$$\phi = \frac{y^+}{14.5}\left(\frac{\nu}{D}\right)^{1/3} \qquad \text{(Equation 3-126)}$$

The described theoretical procedure is based in the following assumptions: (1) The particle eddy diffusivity is equal to the fluid eddy diffusivity; (2) A free-flight mechanism is the final cause of deposition, and the velocity of the particle (v_0^+) is known at the start of the free-flight; (3) The surface is a perfect sink, i.e., it has a sticking coefficient of 1.0.

The diffusivity approach can be considered good for small particles, which effectively will follow eddies' movement and have insufficient inertia to leave the eddy. Loyalka (34) pointed out that for particles that are smaller by, at least, one order of magnitude than the length scale of small eddies it would be the small-scale motion that governs the motion of the aerosol. Since the micro-scale of turbulence, even with very energetic mixing, is of order 100-500 μm, and the particle spectrum selected is much smaller than this, it is clear that all particles will be fully entrained in the eddies. Hence, this can be considered a good assumption.

The theoretical models differ on about the velocity of the particle at the start of the free-flight. Friedlander and Johnstone (95) were the first to use the concept of free flight as the final mechanism of particle deposition. They neglected Brownian diffusion, and the velocity at the start of free flight was assumed constant:

$$V_0^+ = \frac{V_{dt}}{V^*} = 0.9 \qquad \text{(Equation 3-127)}$$

Where:
V_0+: Dimensionless velocity at the start of the free-flight
V*: Frictional velocity (m/s)

The Davies model (96) assumed that the velocity at the start of free-flight was given by the root mean square (rms) of the radial velocity of the fluid at the beginning of free-flight, obtained from Laufer's (97) expression. In the Beal's model (98), the free-flight velocity is taken to be one-half of the axial velocity of the fluid. Davies and Beal considered Brownian diffusion in his model.

Later on, Sehmel (93) developed a semi-empirical model. In his model, he used the theoretical formalism presented, but, considering a set of experiments, determined the effective eddy diffusion coefficient and the velocity at the start of the free-flight, resulting in the following expression:

$$v_{dT} = 1.47x10^{-16}\left[\frac{\rho_p}{1000.}\right]^{1.01} \bar{R}^{2.1} \mathrm{Re}^{3.02} V^* \qquad \text{(Equation 3-128)}$$

The term R is the ratio of the particle diameter in μm to the hydraulic diameter in cm, which yields:

$\bar{R} = (2r_p x10^4)/d_h$ (Equation 3-129)

A third class of models is based upon experimental data. These models explored already known dependencies of the turbulent deposition velocities to set experiments, and obtained correlations based upon the experimental result. The experimental data is presented in the form of dimensionless velocity as a function of dimensionless relaxation time:

$$V^+ = \frac{V}{V*}$$ (Equation 3-130)

Where:
V^+: Dimensionless deposition velocity
V : Fluid velocity (m/s)

$$\tau^+ = \frac{\tau V^{*2}}{\nu}$$ (Equation 3-131)

Where:
τ^+: Relaxation dimensionless time
τ: Relaxation time (s)

Liu and Agarwal (99) have obtained the following relationship between the dimensionless particle deposition velocity and the dimensionless relaxation time, using olive oil drops containing less than 10% by weight of uranine as a fluorescent tracer. The particles' diameters range from 1.4 to 21 μm, and are transported upwards in a vertical tube of 3.2 cm diameter:

$V^+ = (6x10^{-4})\tau_+^2$ for $30 > \tau^+ > 0.21$ (Equation 3-132)

The experiment range was:

$774 > \tau^+ > 0.21$ $50{,}000 > Re > 5{,}000$

Several theories were compared to the experimental data of Liu and Agarwal. The theories of Friedlander and Johnstone and Beal are seen to describe the experimental data very well below τ^+ of 20, whereas Davies description is not good at all, as shown in Figure 3-14. For τ^+ above 30 none of the theories predictions were good.

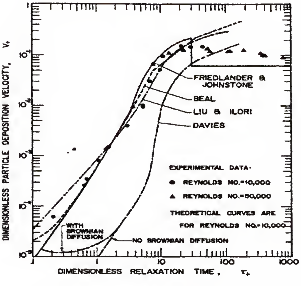

Figure 3-14. Comparison of theories and Liu and Agarwal experiments (99)

Some important observations can be made based on Figure 3-14. First, for very small τ^+, Brownian diffusion contributes to the deposition. This can be inferred comparing the Friedlander (without Brownian diffusion) model to the Beal (with Brownian diffusion). The Beal model prediction is above the Friedlander prediction, and closer to the experimental data for small τ^+. Second, for τ^+ greater than 20, none of the models used are good. The occurrence of large τ^+ is caused mainly by increasing particle size. Therefore, a possible cause of such disagreement can be, for larger particles, the first assumption, that the particle eddy diffusivity is equal to the fluid eddy diffusivity, meaning that the particle does not follow the eddy movement.

For typical particle's size (1.5 μm), and typical thermal-hydraulic conditions, the dimensionless relaxation time is below 20, and the first assumption can be considered good for our problem. Another important conclusion is that Brownian diffusion should be considered in the chosen model, because a very small dimensionless relaxation time is going to be part of the solution.

Muyshondt et al. (100) performed a series of experiments in large tubes (27, 55 and 102 mm diameter, 5.5 m long). During the experiment, a vibrating jet atomizer was used to generate a nearly mono-dispersed aerosol from a mixture of oleic acid, alcohol, and sodium fluorescein (analytical tracer). The range of particles size was 5 to 20 μm. The obtained correlation is presented below:

$$v_{dT} = 2.26x10^{-2} e^{-0.5\left(\frac{Re-4.03x10^4}{1.533x10^4}\right)} + 0.1394e^{-0.5\left(\frac{\ln \tau_+ - \ln 49}{1.136}\right)^2} V^* \quad \text{(Equation 3-133)}$$

The experiment range was:

$100 > \tau^+ > 0.1$ $\qquad$ $55{,}000 > Re > 5{,}000$

A comparison was made of Equation 3-133 to other models using Muyshondt data. A good agreement was achieved for all models for the tubes with smaller diameter, but for the largest tube (102 mm), the predictions of the aerosol penetration for 20 μm particles was over-predicted by Friedlander and Beal theories, as shown in Figure 3-15.

Muyshondt et al. pointed out that the turbulent diffusion effect cannot be taken into account by τ^+ alone, and suggested that the correlation must consider the dependence on the Reynolds number also, as shown in Equation 3-133. This dependency has not been considered in other empirical correlations. This impossibility is also used to justify the scatter they have obtained in their experimental data. Thus, the dependency on the

Reynolds number is an additional dependency that can help significantly in the matching of experimental data for empirical expressions.

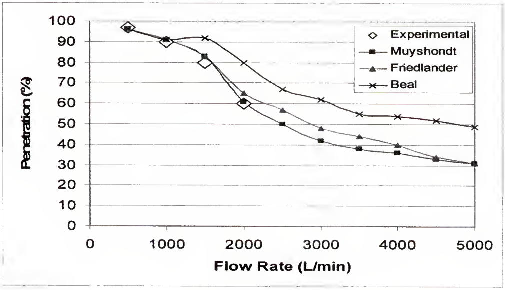

Figure 3-15. Penetration of 20 μm aerosol particles through a 102mm vertical tube (100)

Chiang (101) presented a new correlation based upon the experimental results of several authors and obtained a chi-squared value for several models based upon the compendium of all of those results. These chi-squared values represent the deviation of the predicted value for the several models from the experimental data. The correlation is presented below, and Table 3-8 presents the chi-square values of several models.

$$v_{dT} = 27.13\left(\frac{\rho_p}{\rho_b}\right)^{0.249}\left(\frac{d_p}{d_h}\right)^{2.223}\mathrm{Re}^{0.73}V^{*} \qquad \text{(Equation 3-134)}$$

The correlation validity range is:

$6{,}613 > \rho_p/\rho > 403$ $\qquad 61{,}000 > \mathrm{Re} > 5{,}000$

$6{,}613 > r_p/r_h > 403$

Table 3-8. Chi-square values for several models for several experiments

Model	Chi-Square
Friedlander (1957)	0.308
Sehmel (1970)	0.111
Davies (1966)	0.342
Liu and Agarwal (1974)	0.306
Chiang (1996)	0.039

Geometrical and thermal-hydraulic conditions, and the particle size spectrum of our problem impose the following features the selected model needs to attend:(1) Small values of τ^+, for which Brownian diffusion needs to be considered; (2) Wide range of Reynolds number. Under these conditions, dependency on the Reynolds number is important. Therefore, the Friedlander and Beal models (neglecting Brownian diffusion) can be eliminated. In addition, Davies' model's performance in the several experiments was not satisfactory. Thus, Davies' model was also eliminated from the selection process. Liu and Agarwal, on the other hand, did not considered the Reynolds effects in its expression.

The choice, therefore, should be among the Sehmel, Muyshondt and Chiang models. The preference was for the Sehmel model due its good performance in the comparison of prediction to experimental data in several experiments, as shown in Table 3-7. The Muyshondt and Chiang models are recent models with a small number of assessments, and, therefore, an evaluation its performance at this point would be premature. In addition, the range of Reynolds numbers where their correlation is valid is limited to 5,000 in the lower limit, whereas Sehmel is based on data that contains Reynolds number lower than 5,000.

Thermophoretic deposition

Thermophoresis is the term describing the phenomenon wherein aerosols, when suspended in a gas characterized by a temperature gradient, experience a force in the direction opposite to that of the temperature gradient (from higher to lower temperature).

The physical principle involved is that vapor molecules at higher temperatures have higher thermal energy, resulting in a more intense momentum transfer on the higher temperature side than the lower temperature side, as shown in Figure 3-16.

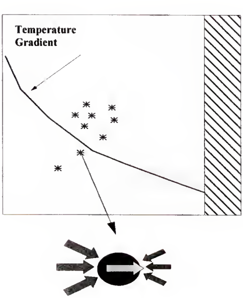

Figure 3-16. Aerosol particle movement under a temperature gradient

In the hydrodynamics section, it was shown that, for the particle size spectrum selected, the continuum region could be assumed for almost the entire range of particles. The following derivations assumed that the particle is in the continuum or slip-flow regime region.

The first one to model the thermophoretic phenomenon was Epstein (102), who derived an expression for the thermal force in the slip-flow regime based on the solution of the Navier-Stokes equations, yielding the expression in Equation 3-135 for the thermal force. Nevertheless, this expression disagreed with experimental results when the thermal conductivity of the particle was much higher than the gas-thermal conductivity.

$$F_T = 9\pi r_p \frac{\mu^2}{\rho T}\left(\frac{k_g}{2k_g + k_p}\right)\nabla T \qquad \text{(Equation 3-135)}$$

Where:

∇T: Temperature gradient (K)
kg: Gas thermal conductivity (W/mK)
kp: Particle thermal conductivity (W/mK)

Brock (103) identified two serious flaws in Epstein's derivation: (1) Appropriate boundary conditions have not been used for the slip flow regime; (2) The continuum energy equations have been solved neglecting the convective terms. He improved the Epstein approach by solving the equations based on the Navier-Stokes-Fourier theory, with slip-corrected boundary conditions.

For the purpose of his analysis, Brock concluded that he could assume that the contribution of thermal stresses to the thermal force is small. In addition, frictional losses were neglected. A physical system composed of a sphere surrounded by a gas under temperature gradient. Accordingly, the steady-state energy equations for the gas and particle regions in spherical coordinates (origin of the coordinates in center of suspended particle) can be written as:

$$\nabla^2 T_g = \frac{1}{\alpha}\left(\frac{V_\theta}{r}\frac{\partial T_g}{\partial \theta} + V_r \frac{\partial T_g}{\partial r}\right) \qquad \text{(Equation 3-136)}$$

$$\nabla^2 T_p = 0 \qquad \text{(Equation 3-137)}$$

The ϕ (axial) component of velocity is neglected, as is the dependence of T on ϕ. The following boundary conditions are applied to the above equations:

$$(T_g)_{r>>r_p} = T_o + (\nabla T) r \cos\theta \qquad \text{(Equation 3-138)}$$

$$T_p \ \text{is finite} \qquad \text{(Equation 3-139)}$$

The phenomenon of the temperature jump in rarefied gases is well known and confirmed by experiment. The temperature-jump boundary condition associated with the energy flux equation complete the problem boundary conditions.

$$T_g - T_p = C_t \lambda \left(\frac{\partial T_g}{\partial r} \right) \quad for \quad r = r_p \quad \text{(Equation 3-140)}$$

$$k_g \left(\frac{\partial T_g}{\partial r} \right) = k_p \left(\frac{\partial T_p}{\partial r} \right) \quad for \quad r = r_p \quad \text{(Equation 3-141)}$$

The Ct term is the temperature-jump correction-factor, which is used together with the temperature-jump boundary condition. This factor is obtained by kinetic-theory means. The mass and momentum equations have their usual form for the Stokes problem for the flow around a sphere:

$$\nabla^2 \vec{V} = \frac{1}{\mu} \nabla p \qquad \text{(Equation 3-142)}$$

$$\nabla \vec{V} = 0 \qquad \text{(Equation 3-143)}$$

It is assumed that the particle is sufficiently small relative to the extent of fluid that all mass averaged velocities vanish as r goes to infinity. Additionally, proper slip-flow boundary condition must be used for the motion of the fluid at the particle surface. At a gas-particle interface, the following conditions apply:

$$V_r = 0 \quad for \quad r = r_p \qquad \text{(Equation 3-144)}$$

$$V_\theta = C_m \lambda \left[r \frac{\partial}{\partial r} \left(\frac{V_\theta}{r} \right) + \frac{1}{r} \frac{\partial V_r}{\partial \theta} \right]_{r=r_p} + \frac{C_s \mu}{\rho T} \frac{1}{r_p} \left(\frac{\partial T_f}{\partial \theta} \right)_{r=r_p} \qquad \text{(Equation 3-145)}$$

The first term on the right hand side is the velocity slip-correction boundary condition, with C_m being the momentum exchange coefficient. The second term represents the contribution of thermal slip to the gas velocity at the surface of the sphere, being C_s the thermal slip coefficient. This term couples the temperature distributions in the gas and particle with the velocity field. It is from slip-flow boundary conditions that one obtains the principal contribution to thermal force. Epstein, in his analysis, has considered only the second term of Equation 3-145.

An exact analytical solution of Equations 3-136, 3-137, 3-142 and 3-143 has not been found. A perturbation solution was achieved by Brock. The derivation and solution details are not here presented, but can be found in Brock's work (103). In order to calculate the thermal force, Brock integrated the normal component of the pressure tensor over the surface of the particle. An expression of the thermophoretic deposition velocity can be derived using the mobility concept:

$$v_{dTr} = \frac{2C_s\left(\frac{k_g}{k_p}+C_t Kn(r_p)\right)C_c \nu \, \frac{\nabla T}{T_g \Delta_T}}{(1+3C_m Kn(r_p))\left(1+2\frac{k_g}{k_p}+2C_t Kn(r_p)\right)} \qquad \text{(Equation 3-146)}$$

Where:
C_s, C_m, C_t : Constants defined by Brock (1.14, 1.17 and 2.18)
Δ_T: Thermal boundary layer thickness (m), given by:

$$\Delta_T = \frac{d_h}{Nu} \qquad \text{(Equation 3-147)}$$

The values of slip coefficients C_s and C_m considered by Brock were 1.17 and 2.18, because they result in a better agreement with the Schadt and Cadle (104) empirical results for sodium chloride particles in air (particle sizes 0.22-0.35 μm). Talbot (105) pointed out that 1.14 is a more consistent value for the C_t, resulting in better experimental agreement and consistent with theoretical values, oppose to the value of 0.75 adopted by Brock. Thus, the value of 1.14 was adopted.

Springer (106) developed a model to cover all flow regimes (free molecular, transition and continuum) through the interpolation between the free molecular expression of Waldman (107) and the continuum solution, consummated in the following expression:

$$\frac{F}{F_{FM}} = \left[1 + \left(\frac{F_{FM}}{F_C}\right)\right]^{-1} \qquad \text{(Equation 3-148)}$$

Where:

F: Thermal force for the transition regime (N)
F_C: Thermal force in the continuum regime (N), given by Brock
F_{FM}: Thermal force in the free molecular regime (N), given by Waldmann:

$$F_{FM} = \frac{8r_p^2}{15}\left(\frac{2\pi}{RT}\right)^{0.5} k_g \nabla T \qquad \text{(Equation 3-149)}$$

In his model, Springer used a different expression for the continuum thermal force, using also different values for slip flow jump coefficients.

In the literature, the thermophoretic deposition velocity is usually expressed as in Equation 3-150 below. The term K is the thermophoretic deposition coefficient, which can be easily inferred from the Brock derived expression or another author's expression.

$$V_{dTr} = K\frac{\nu}{T}\nabla T \qquad \text{(Equation 3-150)}$$

Considerable experimental work has been done for thermophoretic deposition onto pipes surfaces under laminar flow conditions. Montassier et al. (108), Shimada et al. (109), Stratmann et al. (110) and Dumaz (111) performed experimental studies with particle sizes ranging from 0.38 μm to 0.02 μm. Their experimental data agreed reasonably well with theoretical models when the thermophoretic coefficient expression of Brock with Talbot correction was used for the thermal slip coefficient.

A convective-thermophoretic expression for deposition efficiency for the pipe case was derived by Bachelor and Chen (111). Dumaz (112) developed a new correlation for laminar deposition efficiency onto pipes, presented in Equation 3-151. He compared Brock with Talbot correction, referred to in the literature as the Talbot model, with the Springer coefficient expressions with the Motassier data and TUBA experiment data (113), using the Batchelor and Chen formula and his expression for the deposition efficiency. The results are presented below, in Tables 3-9 and 3-10.

$$\eta_{trL} = 1 - \exp(-0.91\tau) \qquad \text{(Equation 3-151)}$$

Where:

$$\tau = \Pr K \frac{\nabla T}{T_w} \qquad \text{(Equation 3-152)}$$

T_w: Wall temperature (K)

Table 3-9. Comparison of different approaches for thermophoretic deposition efficiency for Montassier experiment

D_p (μm)	Kn	$\eta_{Experimental}$	Talbot	Coefficient	Springer	Coefficient
			$\eta_{Batchelor}$	η_{Dumaz}	$\eta_{Batchelor}$	η_{Dumaz}
0.05	2.67	9.5-11.1	9.27	9.05	9.65	9.42
0.1	1.336	8-9.4	8.8	8.56	9.56	9.32
0.2	0.67	6.7-7.8	8.93	8.72	9.76	9.55
0.38	0.35	6.6-7.7	8.12	7.9	7.77	7.68
1.03	0.13	3.7-4.3	7.71	7.57	5.18	5.06
4.0	0.033	2.7-3.1	4.75	4.64	2.83	2.76

In the Montassier experiments, the inlet temperature was 373 K. The fluid was air, and the mass flow rate was 0.2 g/s. Notice that even for Knudsen numbers greater than one, the use of the Talbot coefficient yielded a good prediction of the deposition efficiency. Thus, for Knudsen numbers close to one, the use of Talbot, which was derived for the continuum region, is still possible. For the Montassier experiments (small thermal gradient), the choice of the coefficient and the correlation for the efficiency should not make much difference, since all predictions are close to the experimental value.

Table 3-10. Comparison of different approaches for thermophoretic deposition efficiency for TUBA experiment

T_{fluid}	Kn	$\eta_{Experimental}$	Talbot	Coefficient	Springer	Coefficient
			$\eta_{Batchelor}$	η_{Dumaz}	$\eta_{Batchelor}$	η_{Dumaz}
671	0.15	38	21.4	27.2	10.1	13.2
673	0.29	45	25.2	31.7	16.9	21.7
749	0.16	39	24.2	32.3	11.9	16.5
869	0.18	43	28.2	40.8	14.7	22.5

For the Tuba experiment, different inlet temperatures were taken, resulting in large temperature gradients. The fluid was air, and the mass flow rate was 0.04 g/s. The picture showed to be considerably different under the Tuba experiment conditions. Theoretical predictions stayed well below the experimental values, but a better agreement was obtained from the Dumaz correlation, using the Talbot coefficient.

Regarding the laminar deposition, some gain can be obtained by applying the efficiency expressions obtained by considering the simultaneity of convection, and thermophoresis, expressed through the deposition efficiencies.

In contrast to the laminar flow case, thermophoretic deposition under turbulent condition is not a well-understood issue. Analytical models are not available in the literature and the experimental data in this field is not extensive enough to develop consistent empirical expressions. Hence, the current procedure has been to add separately the turbulent diffusion deposition velocity to the thermophoretic velocity (addition approximation).

Since large temperature gradients may occur in the severe accident condition, the Dumaz correlation is preferable for use. Therefore, for the laminar deposition case, the deposition velocity will be given by:

$$v_{dTrL} = \eta_{Dumaz} \frac{d_h}{L_n} V_{fluid} \qquad \text{(Equation 3-153)}$$

In order to be consistent with the additive procedure assumed, the thermophoretic deposition velocity obtained by Brock, with Talbot coefficients is used. Nevertheless, the usage of the Dumaz efficiency is encouraged in the future for the laminar flow regime, if a strong synergetic effect exists.

Inertial deposition (singularities)

As particles travel along the primary-circuit system, they can encounter several different types of singularities, as mentioned in Chapter 2. These singularities were defined as bends, contractions, expansions, driers and steam separators.

Particles deviate from fluid streamlines whenever there is an acceleration of the stream caused by surfaces or obstacles. This deviation is not significant for particles that are small or when the flow speed is low (low inertia), but larger particles can deviate from the flow for appreciable periods such that their trajectories intercept a surface located in the flow. Inertial deposition is, thus, an important mean for collecting and sizing large particles.

The Stokes number is the dimensionless number used to describe the effect of curvilinear motion, and, therefore, of singularities that introduce curvilinear motion, such as bends and separators. Its derivation is based on the estimation of the stopping distance of a particle due to the radial velocity induced by the centrifugal force when traveling through a full 90-degree directional change. The stopping distance is, therefore, the relaxation time times the flow velocity. This stopping distance is compared with the problem characteristic length, in our case the pipe hydraulic diameter, yielding:

$$St = \frac{4C_c \rho_p r_p^2 V_{fluid}}{9\mu_b d_h} \qquad \text{(Equation 3-154)}$$

If the gravitational effect is neglected, the motion of a spherical particle, which follows the Stokes Law, is described by the following equation in dimensionless form (114):

$$\frac{d^2\vec{x}}{dt^2} = \frac{1}{St}(V_{\dim} - \frac{d\vec{x}}{dt}) \qquad \text{(Equation 3-155)}$$

Where:
$\vec{x}$: Dimensionless position vector (X/d_h)

The solution of the problem thus depends on the knowledge of the fluid motion and the particles' trajectories, which are derived from Equation 3-155, knowing an analytical expression for the fluid motion.

The aerosol deposition onto singularities is usually expressed in terms of deposition efficiency. The deposition efficiency is obtained though the following procedure: (1) Equation 3-155 is solved, and the critical trajectories which separate the particle depositing on the irregularity from the particles penetrating the bend are determined; (2) The initial positions of the deposited particles in the inlet cross-section are calculated; (3) The particle distribution at the inlet is calculated solving the equation of aerosol motion. Comparing the initial position distribution of the deposited particle trajectories to the initial particle distribution, it is possible to establish the fraction of the particles that will deposit, i.e., the deposition efficiency. Figure 3-17 shows the particle distribution profile in the inlet of a horizontal bend (3.17 (a)) and downstream of a 90-

degrees downward bend following a horizontal tube (3.17(b)) for Reynolds of 220 and R_0 of 3.1. The parameter R_0 is the curvature ratio of the bend. These profiles were obtained both experimentally, by Davies (115), and theoretically, by Cheng and Wang (116). Figure 3.17 (c) shows some trajectories projected on a cross section of a curved tube for Stokes of 0.4, Reynolds of 1000, and R_0 of 8.

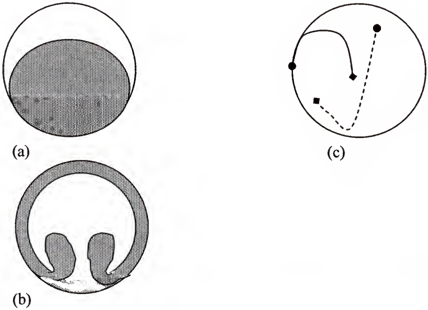

Figure 3-17. Particles distribution and trajectories: (a) in a horizontal tube; (b) downstream of a 90-degree following the a horizontal tube; (c) particle trajectories in a bend (dashed line represent penetrating particle)

Deposition in circular bends

The flow field in a bend is a complex matter. As it will be shown later, the flow field depends on the flow regime, which varies with the Reynolds number and the Dean number (relationship of the curvature and pipe radius). An analytical expression for the turbulent flow into pipes is not available, but some approaches have been used to calculate the laminar deposition efficiency. Hence, laminar and turbulent conditions are treated separately.

Even under laminar conditions, the actual flow field is very difficult to represent. The flow field is a three-dimensional flow composed of a core flow with a distorted parabolic flow in the direction of the outer edge, and a semi-circular secondary flow, as shown in Figure 3-18 (117).

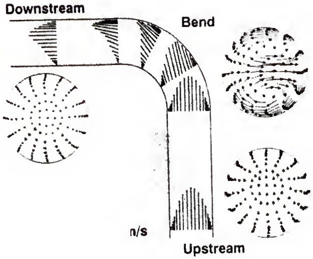

Figure 3-18. Laminar flow field in a vertical bend (117)

One important feature of the flow field under laminar conditions is that the secondary flow makes the flow more stable. Therefore, the transition Reynolds number from laminar to turbulent condition should be at higher Reynolds numbers. The agreement of theoretical predictions to experimental data registered by Pui et. al. (118) indicated that 5000 should be the transition Reynolds number for flow into a 90-degrees bend.

Several theoretical models have been developed, using different flow fields. Landahl and Hermann (119) assumed a parabolic flow without secondary motion. Cheng and Wang (114) developed a more complex solution and assumed a forced vortex flow, with the axis at the center of the curvature of the bend, and neglected the existence of any secondary flow. The Cheng flow is known as the idealized flow. Crane and Evans (120) were the first investigators that included in their calculations the effect of secondary flow. However, their results do not differ very much from those obtained by Cheng and Wang (114). Some years later, Cheng and Wang (116) developed a new theory using a three-dimensionally developed laminar flow developed by Mori and Nakayama (121), which includes the effect of secondary flow. The later model presented a considerably better agreement with Pui et al.'s (118) data, which is consistent with the higher degree of elaboration of its solution.

The Mori-Nakaya flow field consists of a core region and a boundary layer. The thickness of the boundary layer, normalized by the radius of the tube is given by:

$$\delta = 4.6311 Dn^{-0.5} - 0.7659 Dn^{-1} \qquad \text{(Equation 3-156)}$$

Where:
Dn: Dean Number, given by:

$$Dn = \left(\frac{\mathrm{Re}}{R_0^{0.5}} \right) \qquad \text{(Equation 3-157)}$$

$$R_0 = \frac{R_b}{r_h} \qquad \text{(Equation 3-158)}$$

R_b: Curvature Radius of the bend (m)

In the core region, the radial, circumferential and axial velocity components, normalized by the mean axial velocity, and in accordance with the system of coordinates in Figure 3-19, are given by:

$$V_r = \frac{2D}{\mathrm{Re}} \cos\psi \qquad \text{(Equation 3-159)}$$

$$V_\psi = -\frac{2D}{\mathrm{Re}} \sin\psi \qquad \text{(Equation 3-160)}$$

$$V_\theta = \frac{2}{\mathrm{Re}}\left(E + \frac{C}{D} r\cos\psi\right) \qquad \text{(Equation 3-161)}$$

Where:

$$C = \frac{4E}{\delta}; D = 0.9656Dn^{0.5} + 1.65; E = \left[1 - (2/3)\delta + (1/6)\delta^2\right]^{-1}$$

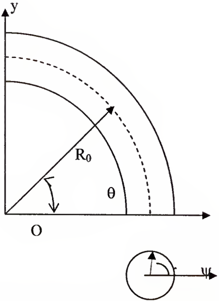

Figure 3-19. Normalized system of coordinates for a curved tube

In the boundary layer, the dimensionless velocity components are given by:

$$V_r = \frac{2D\cos\psi}{r\,\mathrm{Re}}\left[\left(\frac{12}{\delta} - 6\right)\frac{(1-r)^2}{2\delta} + \left(9 - \frac{24}{\delta}\right)\frac{(1-r)^3}{3\delta^2} + \left(-4 + \frac{12}{\delta}\right)\frac{(1-r)^4}{4\delta^3}\right] \qquad \text{(Equation 3-162)}$$

$$V_\psi = -\frac{2D\sin\psi}{\mathrm{Re}}\left[\left(-\frac{12}{\delta} + 6\right)\frac{(1-r)}{2\delta} + \left(\frac{24}{\delta} - 9\right)\frac{(1-r)^2}{3\delta^2} + \left(4 - \frac{12}{\delta}\right)\frac{(1-r)^3}{\delta^3}\right] \text{(Equation 3-163)}$$

$$V_\theta = \frac{2}{\mathrm{Re}}\left\{\left[E + \frac{C}{D}(1-\delta)\cos\psi\right]\left[2\frac{(1-r)}{\delta} - \frac{(1-r)^2}{\delta^2}\right] + \frac{\delta C}{D}\cos\psi\left[\frac{(1-r)}{\delta} - \frac{(1-r)^2}{\delta^2}\right]\right\}$$

(Equation 3-164)

Visual observation of the above equations shows that the parameters affecting the particle deposition over the bend's edges are the Stokes, the Reynolds and the Dean number. Examinations of the flow field under different parametric conditions allowed the establishment of a laminar flow characterization, according to the Dean number. Hence, the typical Dean numbers need to be established. A typical bend used in nuclear power plants is shown in Figure 3-20 below. For the geometry of Figure 3-20, and considering the maximum Reynolds number (5,000) and the approximated minimum Reynolds (based on minimum velocities) of 100, Dean numbers ranging from 59 to 2,900 are encountered.

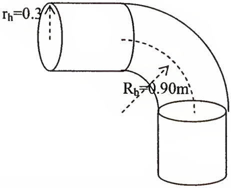

Figure 3-20. Typical 90-degrees bend of nuclear power plant

Researchers have defined three different flow regimes for the flow around circular bends. For small Dean numbers (De<17), a pair of counter-rotating helical vortices, placed symmetrically with respect to the plane of symmetry, are formed because of the centrifugally-induced pressure gradient that drives inward the slower moving fluid near the wall, while the faster moving fluid in the core is swept outward. The position of the maximum axial velocity moves toward the outer bend.

For intermediate Dean numbers (17<De<370), the flow pattern is the same as for the small, but with the peak velocity closer to the outer bend and a distortion of the secondary streamlines. For large Dean numbers (De>370), the centrifugal force creates increased axial velocity and draws more fluid into the boundary layer near the outer bend.

The axial and the radial profiles of the streamlines and the contours of the constant axial velocities, for small and intermediate Dean numbers are shown in Figure 3-21.

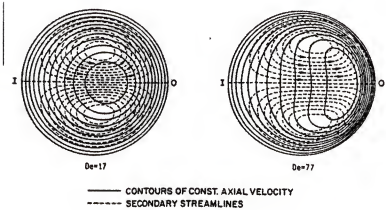

Figure 3-21. Radial iso-velocity contours and secondary streamlines for increasing Dean number (118)

The procedure established to solve the problem of aerosol deposition onto pipe bends showed that the solution is unique for a set of Dean-Reynolds number. In the previous paragraphs, it was shown that solutions could be grouped into small and intermediate Dean numbers. Hence, a solution for each group can be applied, considering different Reynolds numbers. For small Reynolds numbers, Pui et al. (118) had observed that the Cheng and Wang model for the flow field does not result in good agreement with their experimental data. They pointed out that the reason for such disagreement is that the flow-field cannot be characterized by a boundary layer and a core region (Mori and Nakayama). For small Dean numbers, they recommend the use of the Dean's solution. For intermediate and large Dean numbers, good agreement was generally achieved, as shown in Figure 3-22 for the Reynolds number of 1,000.

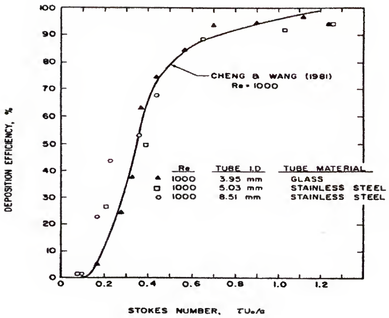

Figure 3-22. Comparison of Cheng and Wang theoretical curves for intermediate Dean numbers and flow Reynolds number of 1,000 and Pui et al experimental data (118)

Since typical small Dean numbers do not make up part of the problem's solution, the procedure is limited to intermediate-to-large Dean numbers. In this case, the Chen and Wang (116) curves are applied. Unfortunately, only theoretical curves for Reynolds numbers of 1,000 and of 100 are available. The curve for the 1000 Reynolds number is used for all Reynolds numbers laminar range, but this procedure does not constitute a good approximation. Nevertheless, we are limited by the available curves. This curve is expressed below, and is expressed in terms of deposition velocity using Equation 3-153.

$\eta_b(r_p) = 2St(r_p) - 0.3$ for 0.15<St<0.25 (Equation 3-165)

$\eta_b(r_p) = 3St(r_p) - 0.55$ for 0.25<St<0.45 (Equation 3-166)

$\eta_b(r_p) = 0.4St(r_p) + 0.62$ for 0.45<St<0.95 (Equation 3-167)

For Stokes numbers less than 0.15, the efficiency is zero, and for Stokes numbers greater than 0.95, an efficiency of one should be assumed.

For turbulent flow conditions, the flow-field characterization is difficult. Pui et al.(118) derived an expression for turbulent flow (Re larger than 5,000) based on their experimental data for Reynolds number of 6,000 and 10,000. This expression is adopted because it is the only expression available in the specialized literature. The expression is presented below

$$\eta_b(r_p) = \left|1 - 10^{0.963 St(r_p)}\right| \qquad \text{(Equation 3-168)}$$

Deposition onto contractions

The deposition onto surfaces of a contraction can be easily understood through the examination of the streamlines in a 90-degrees contraction, as shown in Figure 3-23. The particles closer to the outer edge of the inlet pipe will perform an accentuated curvilinear motion. The particles in this streamline will, consequently, be thrown outside the streamline and possibly can reach the contraction surface.

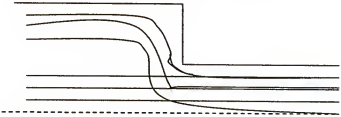

Figure 3-23. Streamlines in a 90-degree contraction

Pitch (122) showed the deposition of aerosol particles in a 90-degrees contraction could be modeled in terms of a Stokes number based on inlet velocity and outlet diameter, the later referred-to Pitch-Stokes number. In the Pitch-Stokes number, the velocity in the numerator is the inlet fluid velocity and the hydraulic-diameter is the outlet diameter. The Pitch model was derived by obtaining an approximate analytical solution for laminar flow in the 90-degree contraction, and then by solving the equations of particle motion using the approximate analytical flow solution to obtain the aerosol losses, resulting in the following expression:

$$\eta_c = \frac{2Z}{1+G} - \frac{Z^2}{(1+G^2)} \qquad \text{(Equation 3-169)}$$

$$Z = 2A + 2A^2\left[e^{(-1/A)} - 1\right] \qquad \text{(Equation 3-170)}$$

$$A = St_{Pitch}\sqrt{G} \qquad \text{(Equation 3-171)}$$

$$G = \frac{\sqrt{\frac{A_o}{A_i}}}{1-\sqrt{\frac{A_o}{A_i}}} \qquad \text{(Equation 3-172)}$$

Where:

St_{Pitch}: Pitch Stokes Number
A_o: Outlet cross-sectional area (m^2)
A_i: Inlet cross-sectional area (m^2)

Ye and Pui (123) observed that the aerosol particle losses in a 90-degree contraction were not only a function of the Pitch-type Stokes number, but also depended on the diameter-contraction ratio. They have also argued that the Reynolds number, for the laminar condition, has no effect in the deposition. A two-dimensional fully developed laminar flow field in cylindrical coordinates was obtained solving the Navier-Stokes equations numerically using a computer program. The deposition efficiency was calculated by tracing the particles trajectories in the flow field, yielding:

$$\eta_b = \left(1 - \frac{A_o}{A_i}\right)\left[1 - e^{(1.721-8.557S+2.227S^2}\right] \qquad \text{(Equation 3-173)}$$

Where:

$$S = \frac{\left(0.5St_{Pitch}\right)^{0.5}}{\left(d_o / d_i\right)^{0.31}}$$ (Equation 3-174)

Where:
d_o: Outlet diameter (m)
d_i: Inlet diameter (m)

Other models were developed, but all of them have the same limitations of the Pitch and Ye and Pui models, that is, they are valid only for a contraction angle and only for laminar flow. For this reason, Muyshondt et al. (124) developed an empirical correlation, valid for different angles and both laminar and turbulent conditions. They used contractions with half-angles of 12, 45 and 90 degrees for area ratios of 0.062, 0.215 and 0.571, with the Reynolds number varying from 1,120 to 58,500. The correlation obtained using the data of these experiments is presented below:

$$\eta_t(r_p) = \frac{1}{1 + \left(\dfrac{X}{3.14e^{-0.0185\theta}}\right)^{-1.24}}$$ (Equation 3-175)

Where:
θ: Contraction half-angle in degrees
$X = St(1 - A_o/A_i)$ (Equation 3-176)

Another issue addressed by researchers is the effect of sudden expansions on the aerosol-deposition processes. Kindler et al. (125) studied analytically the problem and performed experiments. They concluded that sudden expansions do not affect deposition. It is consistent to assume that the Muyshondt model is more appropriate for our purposes due to the completeness of the data used in its derivation and the fact that some of the contractions used in nuclear power plants are not 90-degree contractions, for which the Muyshondt model is more appropriate.

Deposition on separators and driers

Models for aerosol deposition in the up-comer cyclone-type steam separator and steam driers were developed for the RAFT code (20). Since they are the only one available in the literature for these irregularities, they were the models chosen to represent this geometry. Figure 3-24 presents the drawing of this type of steam separator, and Figure 3-25 presents the drawing of the steam drier.

The deposition efficiency in the steam separator is given by the expression:

$$\eta_i = 1 - \frac{R_i^2}{R_s^2} \qquad \text{(Equation 3-177)}$$

In this expression R_s means the radius of the vortex tube, and R_i is defined as the radius within the tube such that a particle originating at R_i will just reach the wall before the end of the vortex tube. The ratio R_i/R_s can be determined from the values of a function of R_i/R_s from a table. The function is defined as:

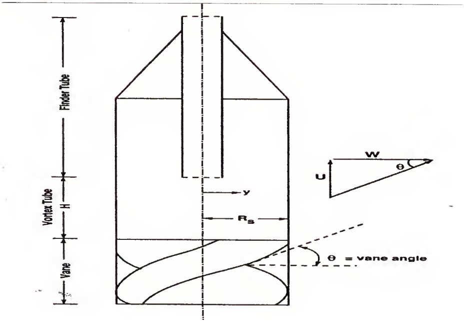

Figure 3-24. Up-comer cyclone-type steam separator (7)

$$f\left[\frac{R_t}{R_s}\right] = 1.29228 St(r_p)\left[\frac{H}{R_s}\right]\cot^2\theta \qquad \text{(Equation 3-178)}$$

Where:
H: Vortex tube length (m)
θ: Vane angle

The RAFT computer model also has an expression used to calculate the expression in steam driers. The drier is modeled as a series of N bends each with a turning angle. The derived efficiency is given by:

$$\eta_t(r_p) = 1 - \lfloor 0.24(5.17 - \cos\psi) - 2.3(1 - \cos\psi) St(r_p) \rfloor \qquad \text{(Equation 3-179)}$$

Where:
ψ: Curvature angle

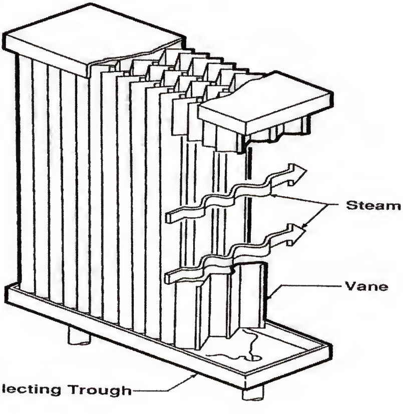

Figure 3-25. Steam drier (7)

Re-suspension

As discussed before, aerosol particles can deposit on the structural surfaces of the primary coolant system. The adhesion forces of these particles are the intermolecular forces, including Van der Walls force. Energy transferred by turbulent flow is capable of re-suspending these deposited aerosols. The energy transfer process is possible due to turbulent bursts that continuously crush the viscous boundary layer like miniature tornados, as shown in Figure 3-26 below (126). Favorable conditions for re-suspension can occur during severe accidents, due to fast gas flows associated with transient events, such as: core quenching due to the delayed intervention of cooling systems; core slump into the water remaining in the lower plenum; fast late depressurization.

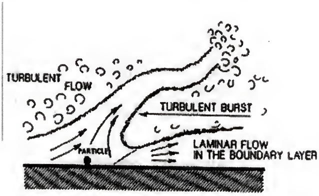

Figure 3-26. Turbulent bursts continuously crushing the boundary layer (126)

Reeks et al. (127) provided the theoretical basis for the re-suspension process, based on the view that an adhering particle is deformed elastically by its surface-adhesive forces. In static equilibrium (no external forces or flow), there is a balance between the adhesive force and an elastic restoring force. However, when a particle is exposed to a turbulent flow, there is a transfer of turbulent energy to the particle, which causes the particle to deform continually about its static equilibrium configuration. Particles in contact with the formed substrate are confined to motion within a surface adhesive-potential wall. The transfer of the energy of the turbulent flow takes place through the agency of aerodynamic lift forces (resultant from the turbulent bursts), where the average component modifies the shape and the height of the adhesive-potential wall, and the random fluctuating component causes the particle and the surface to deform, in a random oscillatory fashion, from their static equilibrium deformation. Eventually, the adhesive potential of the particle becomes unstable, and the particle can be released (re-suspended).

Reeks et al. also realized the existence of two types of re-suspension: the short-term re-suspension occurring earlier than one second after the deposition, and the long-term re-suspension occurring later than a second, which depends on the history of the concentration of surface aerosols. The focus has been directed to the second type.

Reeks used time-constants analysis, statistical tools, and theoretical and experimental approaches to analyze re-suspension. He considered how to estimate the lift forces and the adhesive potential, but did not present any usable expression for re-suspension. Also, he pointed out that adhesive-force potential is very sensitive to the roughness of the surface, and, therefore, can affect the re-suspension rate.

The Aerosol Re-suspension Test (ART) results were used to derive a correlation, based on the dependencies established by Reeks et al. (127). A power law was used by the ORNL researchers to fit the experimental data, leading to the following expression:

$$F = 0.05V_*^2 t^{-1.25} \qquad \text{(Equation 3-180)}$$

Where:
F: Fractional rate of re-suspension (s-1)
t: Time (s)

The time t refers to the time elapsed since the gas flow was initiated in the turbulent condition. In the case of reactor applications, the situation is complicated by the fact that deposition and re-suspension occur simultaneously. Another issue is how to define the composition and the size distribution of the re-suspended aerosol. In order to address these issues, the following assumptions were adopted: (a) all aerosol particles are taken to have the same properties of adhesion to the substrate on which they are deposited and the adhesive force is independent of substrate characteristics; (b) the re-suspended aerosols have the same composition as the deposited aerosol mass; (c) all of the re-suspended mass is allocated in the first section (this assumption is necessary because the size distribution of aerosol on the surfaces is not computed); (d) aerosols are dry.

The last assumption is the most influential over the validity of the theoretical development presented previously and below. As the particle adhesion caused by surface tension of liquids is likely to prevail over whatever aerodynamic force exists in LWR severe accidents (Brockmann, (128)). Whether the nuclear aerosols are dry or not, or the extension that they can be considered dry, are questions difficult to be answered. Aerosol examinations show that they are effectively dry, but the thermal conditions at collection and examination (considerably lower temperatures) are completely different from the severe accident conditions of the deposition. To deal consistently and simply with this issue remains a challenge.

The ORNL model has obvious limitations. It is a very simplistic model, and has no dependency on any quantity related to the adhesive forces. Implicit dependencies on surface characteristics and Reynolds number exist. Other noticeable simplification is the lack of dependency of the re-suspension rate on the particle size. In order to address these simplifications a new theoretical development gained force in the last years, especially after the execution of the STORM experiments (129), which were assessed by this new model and the ORNL model. In this theoretical model, a correlation between the re-suspension rate and the modulus of the resultant force acting was established, based on aerosol re-suspension lab-scale experiments:

$$\Lambda(r_p) = A[F(r_p)]^B \qquad \text{(Equation 3-181)}$$

Where:
$F(r_p)$: Average resultant force (μN)
A and B: Empirical coefficients

Parozzi (126) obtained the coefficients A and B through a curve fitting process, using the experimental results of STORM, Oak Ridge, and Frometin (130) (Wurellingen in Figure 3-27). The process is represented in Figure 3-27 below, and the coefficients are presented in Table 3-11, following the Figure.

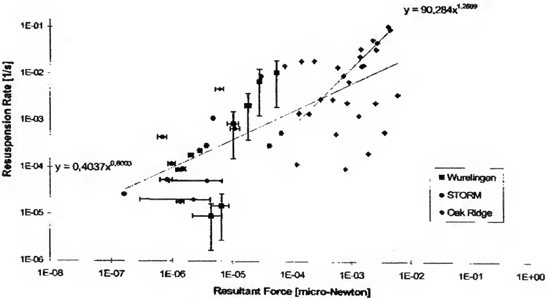

Figure 3-27. Aerosol re-suspension rates obtained from several experiments (126)

Table 3-11. Coefficients of the re-suspension rate (Equation 3-181)

	A	B
$F_R<3.065\times10^{-4}\mu N$	0.4037	0.6003
$F_R>3.065\times10^{-4}\mu N$	90.28	1.269

The average resultant force balances the adhesive forces with the lift-aerodynamic forces' actions on the surface aerosols. The adhesive forces are the gravitational (active for horizontal, bottom surfaces only), and the cohesive forces due to intermolecular attraction, including Van de Walls forces. The aerodynamic forces are drag and lift. Hence, the calculation of the resultant force is accordingly performed through Equation 3-182. Obviously, the force must be positive for re-suspension to occur.

$$F = F_{drag} + F_{burst} - \left(F_{gravit} + F_{cohesive} + F_{frictional}\right) \quad \text{(Equation 3-182)}$$

As the gravitational force is predominant only for particles larger than 50 μm, and few particles are going to reach such size, neglecting the gravitational force is not a harmful procedure in the calculation.

The cohesive force caused by intermolecular attraction, is expressed for a particle having radius r_p according to Brockmann (128):

$$F_{cohesive} = -2Hr_p \quad \text{(Equation 3-183)}$$

Where:

H: Proportionality coefficient (N/m)

The proportionality coefficient is a coefficient depending on the system conditions and material properties. For pure intermolecular forces acting between a perfectly smooth sphere and a plane or between two spheres, Brockmann pointed out that H is on the order of $0.8\text{-}1.2\times10^{-3}$N/m, although these values are likely to be greatly degraded by surface contamination and surface roughness. The same investigator indicated a more realistic value for the coefficient H : 4×10^{-7}N/m. This proportionality coefficient was obtained in the STORM experiment, and its value is in the order of 1×10^{-7}N/m for the first particle layers, while it a rapid increase was detected of H to values of at least 1×10^{-6}N/m after ten layers because of mutual particle interactions.

The dependence of the H factor on the surface roughness was neglected, because it is very difficult to treat this dependency, and the unavailability of models in the literature.

Parozzi (126) proposed an expression for the H coefficient, relating the H coefficient to the number of deposited layers, according to the relation in Equation 3-184. For simplicity, an average H value of 1×10^{-6} N/m was adopted.

$$H = A\sqrt{N} + B \qquad \text{(Equation 3-184)}$$

The sliding and rolling resistance of particles gives rise to the friction force. This is assumed by the model to be proportional to the cohesive force and to the gravitational force. As we are neglecting the gravitational force, the dependency is not shown.

$$F_{frictional} = f\lfloor 2Hr_p \rfloor \qquad \text{(Equation 3-185)}$$

The coefficient f was determined from Brockmann to be in the range of 0.2 to 0.55. The fixed value used was 0.2, because it is the value used in the theoretical predictions of the STORM experiment. The dependence of the friction factor on the deposit shape and the compactness of the substrate are not known.

Aerodynamic forces, responsible for particle re-suspension, can be sub-divided into drag force and lift force. The drag force is due to the particle resistance to the laminar flow of the boundary layer, whereas the lift force is due to turbulent bursts caused by random crushing of the boundary layer.

The drag force can be obtained (126) assuming the profile of fluid velocity begins just at the top of the deposit. Under this condition, the drag force can be conveniently evaluated as the product of the shear stress of the fluid and the particle projected area:

$$F_{drag} = \tau_0 \pi r_p^2 \qquad \text{(Equation 3-186)}$$

Where:

τ_0: Shear Stress (N/m^2), given by:

$$\tau_0 = \left(\frac{f_{Darcy}}{4}\right)\frac{\rho_g V_{fluid}^2}{2} \qquad \text{(Equation 3-187)}$$

Where:

f_{Darcy}: Darcy frictional factor, commonly encountered in fluid mechanics books

The frictional factor has great dependency on the surface roughness. The roughness of the surface depends on the coverage of the surface. If the surface is covered by aerosols, the original roughness of the pipe is completely hidden, and the actual roughness should be related to the average diameter of the aerosol particles. On the other hand, a smooth surface is assumed in the case of liquid deposit. This uncertainty on the actual roughness of the surface constitutes a major uncertainty of the re-suspension model, regarding the drag force calculation.

Aerodynamic drag forces, in a nuclear accident environment are expected to be lower than 10^{-6}-10^{-7}μN for sub-micron particles, but can reach values of 10^{-1}μN for the largest particles (50 μm).

The lift forces associated with "turbulent bursts" are considered the main mechanisms responsible for particle re-suspension. These forces are not constant but oscillatory, as these "turbulent bursts" reach the viscous sub-layer repeatedly. This force is evaluated through the correlation proposed by Frometin (130):

$$F_{burst} = a\rho_g v^2 \mathrm{Re}_{pv}^b \qquad \text{(Equation 3-188)}$$

Where:

$$\mathrm{Re}_{pv} = \frac{2r_p V^*}{\nu} \qquad \text{(Equation 3-189)}$$

The Reynolds number presented in Equation 3-186 is the Reynolds number for a particle deeply submerged in the viscous sub-layer. Different researchers agreed that a has a value of about 10 and b has a value of about 3. Hall (131) obtained the values of a=4.21 and b=2.31 from experimental measurements. These last values were chosen to be used in the model.

The order of magnitude of the lift forces due to turbulent bursts, in a LWR piping under accident conditions, can reach 10^{-5} to 10^{-4} μN for sub-micron particles, and can be of several μN for the largest particles. Therefore, re-suspension will be more active for the largest particles since the adhesive force varies linearly with the particle radius, whereas the lift force varies with a power greater than two.

Many uncertainties affect both the theoretical models available, as well as the re-suspension experiments. In the theoretical models, parameters, which were experimentally obtained, have extremely limited assessment, possibly being off by some significant figure, such as the adhesive force proportional coefficient. Moreover, the coefficients are based on highly scattered data, such as the empirical coefficients of Equation 3-182. Also, assumptions of the theoretical models have no proof of their validity, i.e., the model is over-simplified. In the experimental field, uncertainties also exist regarding actual substrate and particle characteristics. The limited number of experiments is also a constraint of the aerosol re-suspension field. The Oak-Ridge (ART) and Whithfrin Laboratory lab-scale tests and the STORM large-scale tests are the only experiments performed.

Reyes et al. (132) have performed a comparison of several codes' predictions for the STORM experimental results, in the International Standard Problem 40 (ISP-40). Some codes have used the simplified ORNL laboratory model, whereas other codes have used the Parozzi model. They have concluded that the codes using the Parozzi model have considerably better agreement with the experimental data than do the codes using the ORNL model, and the later tends to over predict re-suspension. For this reason, the Parozzi (126) model is chosen to be used.

Since the problem was set in a manner that the aerosol deposited mass is not computed for each aerosol size section, but summed over all sections, the equations equivalent to each section are not available. Two approaches were initially considered. First, it was considered the implementation of the deposited equations for each section, making possible the use of the size-dependent re-suspension rate implementation. Second, a simplified approach, which is capable of representing reasonably well the spectrum of particles over the surface of a volume was considered.

The first option results in an increase in the number of equations calculated of S (number of species) times B (number of bins, or sections). Hence, there is a considerable burden with the benefit of calculating the re-suspension. A more economical and convenient approach is the second, which calculates the average radius of the deposited mass, and use this average radius to calculate the re-suspension rate. This average is achieved by computing the particle density times the re-suspension rates at every time step up to the current time, as represented below: As mentioned earlier, the mass re-suspended is allocated in the first section.

$$r_{apd} = \frac{\sum_{\Delta t_1}^{\Delta t_n} \sum_{B=1}^{B=N} \Lambda(r_p(B),\Delta t) N_B r_p(B)}{\sum_{\Delta t_1}^{\Delta t_n} \sum_{B=1}^{B=N} \Lambda(r_p(B),\Delta t) N_B} \qquad \text{(Equation 3-190)}$$

Where:

r_{apd}: Average particle deposited radius (m)
N: Number of sections
$\Lambda(r_p(B),\Delta t)$: Re-suspension rate for particle radius of section B at time step Δt (s^{-1})
N_B: Particle Number density of section B (particles/m^3)

A simplified Parozzi model was developed to fit the characteristics of the equations previously described. More than ten aerosol layers were assumed so to obtain the coefficient H in the calculation of the adhesive force. Moreover, the gravitational force was neglected. A special treatment was set to avoid the computation of sectional deposited masses.

Agglomeration

The term agglomeration or coagulation is used to describe the process of adhesion or fusion of two particles, which takes place when they touch. Such collisions happen because of the relative velocity between aerosol particles, which can arise from a variety of physical causes. The most commonly known, and effective in our case, are Brownian motion, gravitational settling and turbulence.

The calculation of these processes is achieved by considering the relative motion of two particles and their cross-sectional areas. All processes are difficult to treat for shapes other than spherical, and no current derivations exist for such particles. Therefore, the derivations assume that the particles are spherical and that the agglomerated particle is spherical also, with its volume given by the sum of those of the agglomerated particles. This assumption is consistent, as stressed before. Another assumption of the models is that the sticking coefficient is equal to unity; that is, every particle that encounters another certainly will coagulate.

Brownian agglomeration

Brownian motion is the name given to the irregular movement of small particles suspended in a fluid, due to the random impact of molecules on their surfaces arising from thermal motion. The simultaneous, random 'walk' of such a large number of particles inevitably lead to collisions. As shown earlier, the range of particles considered in our calculation comprises the continuum and the near-continuum regions.

Considering first the continuum region, the derivation of the agglomeration kernel considers the test particle and a calculation of the rate at which other particles diffuse toward this particle. Such motion may be characterized by a diffusion equation of the form:

$$\frac{\partial}{\partial t}C(\vec{r},t) = D\nabla^2 C(\vec{r},t) \qquad \text{(Equation 3-191)}$$

Consider now that the test particle b is the test particle, and particle a is the particle diffusing towards the test particle. To solve Equation 3-191, a polar-coordinate system is set up with the center of particle b at the origin, as shown in Figure 3-28 below.

Since the diffusion process is isotropic, the diffusion equation, given the polar coordinate system of Figure 3-28 reduces to:

$$\frac{\partial}{\partial t}C(r,t) = D_{ab}\left[\frac{\partial^2}{\partial r^2}C(r,t) + \frac{2}{r}\frac{\partial}{\partial r}C(r,t)\right] \qquad \text{(Equation 3-192)}$$

The boundary conditions associated with the problem are (Figure 3-29):

At $r=r_a+r_b$, $C(r_a+r_b,t)=0$ (Spheres are impenetrable)

At $r=\infty$, $C=C_\infty$ (unperturbed uniform concentration distribution far away from the particle)

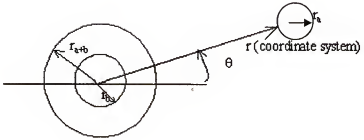

Figure 3-28- Polar-coordinate system for two particle Brownian coagulation

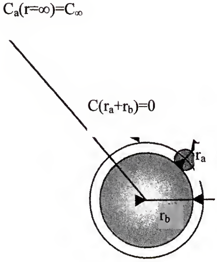

Figure 3-29. Boundary conditions for the Brownian agglomeration calculation

The diffusion coefficient of particle b towards a is proven to be given by the addition of the Brownian diffusion coefficients of each particle (34), thus:

$$D_{ab} = D_a + D_b = kB_{pa}T + kB_{pb}T \qquad \text{(Equation 3-193)}$$

The solution of Equation 3-192 is solved (34), yielding:

$$C(r,t) = C_\infty \left[1 - \frac{r_a + r_b}{r} + \frac{r_a + r_b}{r} erf\left(\frac{r - a - b}{\sqrt{4D_{ab}t}} \right) \right] \quad \text{(Equation 3-194)}$$

The rate at which particles a reach the test particle is given by the net current onto the test particle:

$$J = 4\pi (r_a + r_b)^2 D_{ab} \left. \frac{\partial C}{\partial r} \right|_{r = r_a + r_b} = 4\pi (r_a + r_b)\ D_{ab} C_\infty \left[1 + \frac{r_a + r_b}{\sqrt{\pi D_{ab} t}} \right] \quad \text{(Equation 3-195)}$$

The characteristic time of the Brownian coagulation is, from Equation 3-195, given by:

$$\tau = \frac{(r_a + r_b)^2}{\pi D_{ab}} \quad \text{(Equation 3-196)}$$

For particles in the micron range, and typical thermal-hydraulic conditions of severe accidents, the characteristic time is in the order of 10^{-4} s. Since characteristic times are much larger than time-steps, the last term in Equation 3-195 can be neglected, and the Brownian coagulation kernel (K) expressed as:

$$K_B(r_a + r_b) = \frac{J}{C_\infty} = 4\pi (D_a + D_b)(r_a + r_b) \quad \text{(Equation 3-197)}$$

For the transition region, solving the Boltzmann transport equation is very difficult and laborious, and various approximate techniques have been employed to deal with the near-continuum region. The most-often used and assessed is the Fuchs technique (66) and involves the so-called Fuchs jump distance.

Fuchs assumed that the actual particle is enclosed by a spherical surface at the distance δ from the real surface. The magnitude of δ is dependent upon the particle's radius, and if two particles are involved in a collision each particle has its own δ, and a combined δ_{ab} will exist, representing the coagulated particle.

By making such assumption, Fuchs stipulated that the classical diffusion theory solution is only valid for $r > r_a + r_b + \delta_{ab}$. If the concentration at $r = r_a + r_b + \delta_{ab}$ is C', then the current through the surface $r_a + r_b + \delta_{ab}$ is:

$$J_{diff} = 4\pi(r_a + r_b + \delta_{ab})(D_a + D_b)(C_\infty - C') \quad \text{(Equation 3-198)}$$

Fuchs then assumed that for $r < r_a + r_b + \delta_{ab}$, the particles move according to the kinetic theory of gases as if in a vacuum. In this case, the current of particles is given by:

$$J_{kin} = 4\pi(r_a + r_b)^2 \frac{\overline{V}_{ab}}{4} C' \quad \text{(Equation 3-199)}$$

Where:

$$\overline{V}_{ab} = \left(\overline{V}_a^2 + \overline{V}_b^2\right)^{0.5} \quad \text{(Equation 3-200)}$$

And:

$$\overline{V}_a = \left(\frac{8kT}{\pi m_a}\right)^{0.5} \quad \text{(Equation 3-201)}$$

The term m_a is the mass of particle of radius r_a. The value of C' can be evaluated by making the diffusive particle flux equal to the particle flux obtained through the kinetic theory. Substituting the evaluated C', the agglomeration kernel is obtained:

$$K_G(r_a, r_b) = \frac{4\pi(r_a + r_b)(D_a + D_b)}{\dfrac{r_a + r_b}{r_a + r_b + \delta_{ab}} + \dfrac{4(D_a + D_b)}{(r_a + r_b)\overline{V}_{ab}}} \quad \text{(Equation 3-202)}$$

The Fuchs jump distance was obtained (66) by averaging the distance a particle travel (L), in the normal direction from the sphere surface, after leaving in a random direction. This travel distance is an apparent mean free path for the particle, and was obtained by Fuchs as:

$$L = \frac{8D}{\pi \overline{V}} \qquad \text{(Equation 3-203)}$$

After averaging, Fuchs finds:

$$\delta_a = \frac{1}{6r_a L_a}\left[(2r_a + L_a)^3 - \left(4r_a^2 + L_a^2\right)^{1.5}\right] - 2r_a \qquad \text{(Equation 3-204)}$$

For the combined effect of two spheres of different radii, he assumes that:

$$\delta_{ab} = \left(\delta_a^2 + \delta_b^2\right)^{0.5} \qquad \text{(Equation 3-205)}$$

There is consensus among the researchers that the Fuchs correction factor is the more consistent procedure to correct the continuum diffusive Kernel. Therefore, there is no doubt that Equation 3-202 is the best analytical model for Brownian coagulation.

Gravitational agglomeration

As shown before, particles of different sizes and mass will have different settling velocities, and so there will be velocity differentials among the particles. If two particles are within a certain distance of each other, the faster one might collide with the slower one; if it does, they will coagulate. The calculation of the coagulation kernel for this problem is rather difficult, but an elementary derivation is available which shows the general principles. The simple derivation is performed first, and then the deviations from this elementary derivation are considered. The process is shown in Figure 3-30 below.

Assume a spherical test particle of radius r_a moving with velocity v_a. Then assume a cloud of other particles of radius r_b, velocity v_b and concentration C_∞. The number of collisions per unit of time (J) will be equal to the product of the effective area, the relative velocity and the concentration, as Shown in Figure 3-31. The coagulation kernel is obtained from the flux of particles:

$$J = \pi(r_a^2 + r_b^2)\left|V_{g,a} - v_{g,b}\right|C_\infty$$ (Equation 3-206)

$$K_G(r_a, r_b) = \pi(r_a^2 + r_b^2)\left|V_{g,a} - V_{g,b}\right|$$ (Equation 3-207)

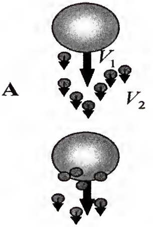

Figure 3-30. Agglomeration process due to different gravitational deposition velocities

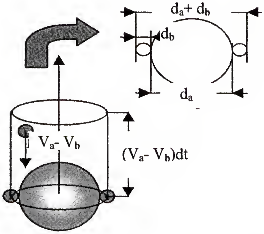

Figure 3-31. Simplified model for differential-gravitational deposition model

This formula suffers from a severe limitation: it ignores the fact that an intra-particle force exists, which can lead to the particles' not colliding, although they would seem to be able to do so on purely geometric grounds. Another way to understand it is to consider the streamlines surrounding the test particle. These streamlines tend to follow the particle curvature near the particle, affecting the particle trajectory, which was previously assumed as straight, as shown in Figure 3-32 (a). The particle trajectories can deviate a putative colliding particle from the colliding trajectory and prohibit it from colliding.

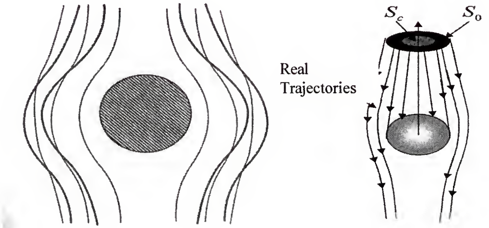

(a) (b)

Figure 3-32. Realistic model for differential-gravitational model: (a) streamlines and particle trajectories; (b) impaction area

Figure 3-32 (b) shows that, because of the realistic particle trajectories, only particles inside the impaction area are going to interact with the test particle, as opposed to the projected area assumed in the simplified model. Hence, the simplified model must be corrected by a parameter called collision efficiency, ε, which is the relation between the impaction area and the projected area. Defining the radius of the impaction area as the impact parameter, y_c, the collision efficiency is defined as:

$$\varepsilon = \left(\frac{y_c}{r_a + r_b} \right)^2 \qquad \text{(Equation 3-208)}$$

In order to calculate the effect of the trajectory, it is necessary to solve the associated equation of the motion of the particles. However, the Stokes stream function can be applied if one assumes that the smaller particle is so small compared with the larger one that it does not appreciably perturb the fluid about the larger particle. The problem is that, considering the range of particle size chosen and a typical number of sections of 20, and assuming as ten times a relation between particles radius where this assumption is good, the condition will be reached only by particles in seven or eight sections of difference. For instance, a particle of the first section can be considered small only for particles above section 7. Hence, this issue remains not completely resolved, since it is not guaranteed that the assumption is good. The extent of the accuracy of this method for particles that are not small compared to the test particle is not known. The procedure to obtain the collision efficiency can be followed in Morlock (133), and is summarized below.

Morlock assumed that the large particle a̲ is at rest and that the fluid is moving over it with an upstream unperturbed velocity U (V_b-V_a). The Stokes stream function then determines the flow field about the sphere and the small particle is assumed to be frozen into that flow field. If the flow is directed in the positive z-direction, and considering the coordinate system in Figure 3-33, the Stokes stream function takes the form:

$$\psi(\rho,\theta) = -0.5U\rho^2 \sin^2\theta\left[1-\frac{3a}{2\rho}+\frac{a^3}{2\rho^3}\right] \quad \text{(Equation 3-209)}$$

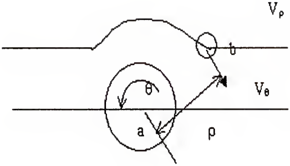

Figure 3-33. Coordinate system for the Stokes flow field

The stream function is symmetric in θ about θ=π/2 and therefore its distance of closest approach to the sphere is at θ=π/2. Murlock defines a critical streamline, y_c, as one that leads to a grazing collision between the sphere a and b in the equatorial plane, thus:

$$\psi\big((r_a+r_b),\pi/2\big) = -0.5U(r_a+r_b)^2\left[1-\frac{3}{2(1+\kappa)}+0.5\left(\frac{1}{1+\kappa}\right)^3\right] \quad \text{(Equation 3-210)}$$

In Equation 3-210, the parameter κ is provided by the relation b/a, and the term between brackets is conveniently referred as f(κ). Now, following Morlock, the impact parameter y_c, is obtained as ρ goes to infinity and θ goes to zero, such that ρsinθ = y_c. Thus:

$$\psi = -0.5Uy_c^2 \qquad \text{(Equation 3-211)}$$

Since the stream function is constant, it is possible to infer that ε=f(κ), and expanding f(κ) for small κ (recall κ<<<1), the collision efficiency can be expressed as:

$$\varepsilon_M = \frac{3}{2}\left(\frac{\kappa}{1+\kappa}\right)^2 \qquad \text{(Equation 3-212)}$$

A different approach to this problem has been followed by Pruppacher and Klett (134). These researchers have correctly noted that the above formula assumes that the particles settle with a relative speed V_b- V_a, throughout the motion. This, however, is not the case, because, as they pass near each other, the velocity is no longer in the downward direction but perturbed by the streamline motion. Hence, the velocity due to gravitational settling must be corrected in its direction. Proceeding similarly to the procedure described, they arrived at the following expression:

$$\varepsilon_{PK} = \frac{1}{2}\left(\frac{\kappa}{1+\kappa}\right)^2 \qquad \text{(Equation 2-213)}$$

Obviously, the Prupacher and Klett collision efficiency is more consistent with the physical behavior of the particles. Therefore, the chosen expression to model the gravitational agglomeration is the simplified expression, corrected by the Prupacher and Klett collision efficiency. The limitation of the assumption of one particle smaller than the test particle remains an issue to be addressed. The used expression is presented below:

$$K_G(r_a, r_b) = \varepsilon_{PK} \pi (r_a^2 + r_b^2) \left| V_{g,a} - V_{g,b} \right| \qquad \text{(Equation 3-214)}$$

Turbulent agglomeration

In our problem, the flow can be turbulent, that is, the fluid is in a state of random motion containing eddies of varying sizes and is moving in an approximately isotropic manner. The frequency of collisions of particles entrained in such a flow will be increased substantially above that of those in a quiescent flow.

The increase in collisions due to a turbulent fluid may be caused by two independent and essentially different mechanisms. One of these mechanisms is called turbulent inertial effect, and is due to large differences in the densities of the particles and the fluid. Because of this density differential, the particles are not fully entrained by the turbulent eddies, and an inertial effect forces particles out of one eddy and into another.

The second mechanism is called turbulent diffusion, and is restricted to particles whose sizes are smaller, by at least an order of magnitude, than the length-scale of small eddies in the turbulence, and, as pointed out in the turbulent deposition section, is the case for the chosen particle size range. Hence, specifically in this case the inertia effect can be neglected.

There are two seemingly unrelated methods for calculating the collision rate for the turbulent agglomeration kernel. One depends on the use of a turbulent diffusion coefficient, which was derived by Lifshitz (62). The other one uses statistically averaged fluid velocities, derived by Saffman and Turner (135).

The Lifshitz derivation is based upon classical diffusion concepts, or the solution of the steady-state diffusion equation in spherical coordinates:

$$\frac{1}{r^2}\frac{d}{dr}\left(r^2 D(r)\frac{d}{dr}C(r)\right)=0 \qquad \text{(Equation 3-215)}$$

In this case, the diffusion coefficient, D(r), is written:

$$D(r) = D_B + D_T(r) \qquad \text{(Equation 3-216)}$$

In Equation 3-216, the Brownian diffusion coefficient is, as pointed out earlier, the addition of the diffusion coefficient of each particle (D_a+ D_b). The turbulent diffusion coefficient can be shown, by means of mixing length theory, to depend on the distance from solid wall or, in our case, to depend on the distance between the particles centers (66), as expressed below:

$$D_T(r) = \beta_0 \left(\frac{\varepsilon_T}{\nu} \right)^{0.5} r^2 \qquad \text{(Equation 3-217)}$$

Where:

ε_T: Energy dissipation rate per unit mass fluid (m^2/s^3), given by Delichasios and Probstein (136):

$$\varepsilon_{DP} = \frac{0.03146V^3}{d_h \,\mathrm{Re}^{0.375}} \qquad \text{(Equation 3-218)}$$

According to Lifshitz, $\beta_0 = 0.15$ and r is the distance between particle centers. At very close separations, the net diffusion coefficient approaches $D_B+D_T(r_a+ r_b)$. An explicit expression for the coagulation kernel may be obtained by solving the Equation 3-215. This is a two region problem, r> or $<\lambda_0$, where λ_0 is a measurement of the turbulent micro-scale. Let the C_1 be the solution in $r<\lambda_0$ and C_2 be the solution in $r>\lambda_0$. Then:

$$r^2 D(r) \frac{d}{dr} C(r) = const. \qquad \text{(Equation 3-219)}$$

For $r<\lambda_0$, $D(r)=D_1(r)$, integrating Equation 3-219, and using $C_1(r_a+r_b)=0$:

$$C_1(r) = A_1 \int_{r_a+r_b}^{\lambda_0} \frac{dw}{w^2 D_1(w)} \qquad \text{(Equation 3-220)}$$

In this equation, $w= r_a+ r_b$

Similarly, in the region $r>\lambda_0$:

$$C_2(r) = C_\infty - A_2 \int_{\lambda_0}^{\infty} \frac{dw}{w^2 D_2(w)} \qquad \text{(Equation 3-221)}$$

To find A_1 and A_2, we use the continuity condition:

$$C_1 = C_2 \quad for \quad r = \lambda_0 \qquad \text{(Equation 3-222)}$$

$$D_1 \frac{dC_1}{dr}\bigg|_{r=\lambda_0} = D_2 \frac{dC_2}{dr}\bigg|_{r=\lambda_0} \qquad \text{(Equation 3-223)}$$

By determining these two constants and the particle flux at the combined radius, the agglomeration Kernel can be determined:

$$K_T(r_a, r_B) = 4\pi \left\{ \int_{r_a+r_b}^{\lambda_0} \frac{dw}{w^2 D_1(w)} + \int_{\lambda_0}^{\infty} \frac{dw}{w^2 D_2(w)} \right\}^{-1} \qquad \text{(Equation 3-224)}$$

Since $(r_a + r_b)^3/\lambda_0^3 << 1$, the second term inside the brackets can be neglected, yielding:

$$K_T(r_a, r_B) = 4\pi \left\{ \int_{r_a+r_b}^{\infty} \frac{dw}{w^2 D_1(w)} \right\}^{-1} \qquad \text{(Equation 3-225)}$$

Evaluating the integral, and using the combined diffusion coefficient:

$$K_T(r_a, r_B) = 4\pi D_B (r_a + r_b) g(\chi) \qquad \text{(Equation 3-226)}$$

Where:

$$g(\chi) = \left(1 - \frac{\pi\chi}{2} + \chi \tan^{-1}(\chi)\right)^{-1} \qquad \text{(Equation 3-227)}$$

$$\chi = (r_a + r_b)\left(\frac{k_e}{D_B}\right)^{0.5} \qquad \text{(Equation 3-228)}$$

$$k_e = \beta_0 \left(\frac{\varepsilon_T}{\nu}\right)^{0.5} \qquad \text{(Equation 3-229)}$$

One can observe that for small χ, when Brownian coagulation dominates, the correction factor goes to 1, and the classical Brownian Kernel is regained. On the other hand, when χ goes to infinity, g(χ) goes to 3 χ 2, yielding:

$$K_T(r_a, r_b) = 5.65 (r_a + r_b)^3 \left(\frac{\varepsilon_T}{\nu}\right)^{0.5} \qquad \text{(Equation 3-230)}$$

Saffman and Turner (135) obtained a unique expression for diffusive and inertial turbulence, considering the undisturbed velocity of the fluid, related to the diffusive process and the fluctuations of the fluid velocity, that is, the difference between the instantaneous velocity and the undisturbed velocity. In their calculations they assumed that the relative velocity of two particles, w, is distributed in some fashion, P(w), where P(w)dw is the probability that the relative velocity lies between w and w+dw. Then, the rate of collision between two particles of radii, r_a and r_b, with number densities, N_a and N_b, will be:

$$J = \pi(r_a + r_b)^2 N_a N_b \int wP(w)dw \qquad \text{(Equation 3-231)}$$

This type of averaging is used frequently in the kinetic theory of gases. In the case of turbulent motion, it is valid if the mean velocity of each particle is statistically independent of its relative velocity. Since the mean velocity is controlled by large, energy containing eddies and the relative velocity by small eddies, which are statistically independent for large Reynolds numbers, the condition is met.

Saffman and Turner used the Gaussian distribution function to represent P(w), because leads to a simple integration:

$$P(w) = \left(\frac{\beta}{\pi}\right)^{1.5} \exp(-\beta w^2) \qquad \text{(Equation 3-232)}$$

The parameter β is chosen to be the variance corresponding to the relative velocity of the particles, as expressed below:

$$\mathrm{var}(w) = \mathrm{var}(c_a - c_b) = \mathrm{var}(q_a - q_b) + \mathrm{var}(u_a - u_b) \qquad \text{(Equation 3-233)}$$

Where:
c_n: Instantaneous velocity of particle n (m/s)
q_n: Fluctuation velocity of particle n (m/s)
u_n: Mean velocity of particle n (m/s)

The researchers used several theories to determine such variances. These developments are not presented here, because they involve several theories that are not reached by this research. Nevertheless, they are presented in Saffman and Turner (135). The variances were expressed below:

$$\mathrm{var}(u_a - u_b) = 5(r_a + r_b)^2 \left\langle \left(\frac{du}{dx} \right)^2 \right\rangle \quad \text{(Equation 3-234)}$$

The brackets in Equation 3-234 denote a statistical average over many realizations of the turbulence. According to Taylor (137):

$$\left\langle \left(\frac{du}{dx} \right)^2 \right\rangle = \frac{\varepsilon_T}{15\nu} \quad \text{(Equation 3-235)}$$

Hence:

$$\mathrm{var}(u_a - u_b) = \frac{1}{3}(r_a + r_b)^2 \frac{\varepsilon_T}{\nu} \quad \text{(Equation 3-236)}$$

The variance in the fluctuation velocity is given by:

$$\mathrm{var}(q_a - q_b) = (\tau_a - \tau_b)^2 \left\langle \left(\frac{du}{dt} \right)^2 \right\rangle \quad \text{(Equation 3-237)}$$

According to Batchelor (138):

$$\left\langle \left(\frac{du}{dt} \right)^2 \right\rangle = 3.9 \frac{\varepsilon_T^{3/2}}{\nu^{1/2}} \quad \text{(Equation 3-238)}$$

Hence:

$$\mathrm{var}(q_a - q_b) = 3.9(\tau_a - \tau_b)^2 \frac{\varepsilon_T^{3/2}}{\nu^{1/2}} \quad \text{(Equation 3-239)}$$

Adding Equation 3-239 to Equation 3-236, the variance of the relative velocity can be obtained. The agglomeration kernel can be obtained by calculating the rate of collision of particles (Equation 3-231), and dividing by the particle number concentration, yielding:

$$K_T(r_a,r_b) = 2\sqrt{2\pi}(r_a + r_b)^2 \left[1.3(\tau_a - \tau_b)^2 \frac{\varepsilon_T^{3/2}}{\nu^{1/2}} + \frac{1}{9}(r_a + r_b)^2 \frac{\varepsilon_T}{\nu} \right]^{1/2} \quad \text{(Equation 3-240)}$$

It is not obvious whether the method of Saffmann and Turner is better or worse than that of the diffusion equation. Both techniques have weaknesses. With Saffman and Turner it is the use of a Gaussian distribution, and the diffusion equation is the adequacy of the turbulent diffusion coefficient. However, there is no doubt that the Saffmann and Turner has a more complete approach, because it considers both the diffusive and inertial process, whereas the diffusion approach considers only the diffusive process. As, for typical particle size range adopted in the model inertial effect can be neglected, the diffusive approach seems to be simpler. In addition, the weakness of this approach, which is the non-consideration of inertial effects, becomes not representative. Therefore, the Lifshitz model was chosen.

Agglomeration is not an experimentally assessed phenomenon. The difficulty in the experimental set-up of agglomeration due to the difficulty in the separation of it from other competitive phenomena, and the sampling difficulties are the major reasons for such lack. For this reason, the model selection process, did not present any empirical support.

Vapor Species Properties

During the phenomenological assessment of the vapor processes, the necessity of computing vapor properties has arisen. Because they are dependent upon the species, and are not currently computed in the code, it is necessary to establish models to calculate them. Aerosol's properties, on the contrary, do not depend upon its components and were presented in the phenomenological assessment. Moreover, it is necessary to establish the intensity by which each vapor property affects the solution of the fission products transport, identifying areas where improvements would be welcome. The models used, as well as an evaluation of the impact of the vapor property on the solution, are provided in Appendix A.

Comparison with Other Models

In this section, the developed model is compared to the best of the codes for fission products transport, in order to make the first assessment of the advanced model's performance. The codes that have been constantly updated and assessed throughout the last twenty years are the French Escadre, the Japanese ART, and the NRC codes Victoria and Melcor. The Escadre is the French model for fission products transport, which works coupled with the Cathare thermal-hydraulic code. Similarly, ART is a module of the severe accident Japanese code. Victoria is the NRC fission products code and works de-coupled from a thermal-hydraulic code. Melcor is a best-estimate general code with a module of fission products transport. The comparison is divided into the mathematical development of the model and the phenomenological model. The latter is bifurcated regarding the vapor and the aerosol phenomena. Table 3-12 presents the mathematical development of fission products-transport model, and Tables 3-13 and 3-14 present the phenomenological comparison of vapor and aerosol phenomena, respectively.

Table 3-12 shows that all developers have felt the necessity to decouple the convective term, and only the developed model used the fractional step , rather than simply decoupling the terms. A unique technique was used to numerically treat the aerosol size discretization, developed by Lemmon, and complemented in this research.

Also the package chosen to solve the ODE system is a unique feature of the developed model.

Table 3-12. Comparison of mathematical developments of different codes

	Scdap	Victoria	Melcor	Escadre
Numerical Treat. Aerosol size	Discrete ordinates	Finite element	Finite element	Finite element
Numerical Strategy				
Convective decoupling	Yes, fractional step	Yes	Yes	Yes
ODE system solving method	BDF/ functional iteration	SLATEC	Runge-Kutta/ Explicit Euler	Not available
Constraints	Negative masses	Not available	Not available	Not available

Table 3-13. Comparison of vapor phenomenological treatment of different codes

	Scdap	Victoria	Melcor	Sophie
Structural Condensation	Mass transfer empirical	Diffusion through B. L.	Mass transfer empirical	Mass transfer empirical
Physisorption	Experimental	Experimental	Experimental	Mechanistic
Aerosol Condensation	Continuum and near continuum region	Continuum and near continuum region	Continuum region	Continuum region

Regarding the vapor phenomena, Table 3-13 shows a good uniformity of treatment from the top fission products behavior codes. Some mechanistic approaches exist in the transport to the wall in Victoria, and in the surface layers for chemical interactions in Sophie. Both are expensive procedures and incompatible with the Scdap/Relap approach. The diffusivity calculation of the vapor molecule using the classical Chapmann-Enksog approach was implemented.

The following table shows that the developed model was brought to the same level as the state-of-the-art fission product codes, in terms of phenomenological models, and the treatment is even wider when compared to other codes, due to the consideration, with the better and more efficient models, of all possible phenomena. The developed optimized nucleation model is an example of state-of-the art model designed to be faster than the other mechanistic models. Therefore, it is expected that the advanced model will carry all the experience of these codes through their assessment processes, since these models were considered the more appropriate, when compared to the experiments.

Table 3-14. Comparison of aerosol phenomenological treatment of different codes

	Scdap	Victoria	Melcor	Sophaeros	ART
Treatment	Stokes Near Continuum	Near continuum Continuum	Near contin. Continuum Stokes	Near continuum continuum	Stokes Near continuum .
Assumptions					
Spherical Particles	Yes	Yes	Yes	Yes	Yes
No synergetic	Yes	Yes	Yes	Yes	Yes
Size range	0.5-50 μm	0.5-50 μm	Not available	Not available	0.5-50 μm
Deposition					
Gravitational	Gravitational force times mobility	Gravitational force times mobility	Gravitational force times mobility	Gravitational force times mobility	Gravitational force times mobility
Laminar diffusion	Gormley and Kennedy	Gormley and Kennedy	Not modeled	Gormley and Kennedy	Gormley and Kennedy
Turbulent	Sehmel	Sehmel	Not modeled	Sehmel	Friedlander
Thermophoresis	Brock	Brock	Brock	Brock	Brock
Centrifugal					
Bend	Pui et al.	Pui et al.	Not modeled	Not available	Pui et al
Contractions	Muyshondt	Pui et al.	Not modeled	Not available	Not modeled
Separators	RAFT model	RAFT model	Not modeled	Not modeled	Not modeled
Driers	RAFT model	RAFT model	Not modeled	Not modeled	Not modeled
Re-suspension	Parozzi	ORNL	Not modeled	Parozzi	Parozzi
Aerosol Hom. Nucleation	Optimized Grishick	Approx.	Approx.	Grishick	Not available
Agglomeration					
Brownian diffusion	Mass transport and Fuchs correction	Mass transport and Fuchs correction	Mass transport and Fuchs correction	Mass transport and Fuchs correction	Mass transport and Fuchs correction
Differential Gravitation	Corrected geometrical	Corrected geometrical	Corrected geometrical	Corrected geometrical	Corrected geometrical
Turbulent	Leifshitz	Saffman and Turner	Saffman and Turner	Saffman and Turner	Saffman and Turner

CHAPTER 4
IMPLEMENTATION AND VERIFICATION

The purpose of this chapter is to describe the implementation of the developed model in Scdap/Relap5, as well as present the verification process performed after the implementation. A summarized description of the programming features of Scdap/Relap5 is first presented. Later, the implementation is described, emphasizing the distribution of tasks among the several sub-routines and the structural organization of the module. Then, the verification process is presented, where consistency and operation of the fission products transport module are checked.

Programming Features of Scdap/Relap 5

In Chapter 2, the code was briefly described in terms of the solution's methods and the models available. Detailed information is accessible in the code manuals (references (27) and (40)). In this Section, programming strategy, source features, programming structure, and programming requirements are discussed.

The development of Scdap/Relap5 started in the seventies with the development of the preliminary versions of Relap. In the 1980s, Scdap was incorporated into Relap. Consequently, Scdap/Relap5 was originally written in FORTRAN 77. During the last few years, FORTRAN 90 or FORTRAN 95 has been gradually replacing FORTRAN 77. Since different organizations maintain the code (primarily, the INEEL, ScienTech, a company hired by the NRC, and ISS, a company developing an independent version), different sources are at different stages in this replacement process.

The code development strategy is guided by the following considerations (139): modeling flexibility, user convenience, computer efficiency, and design for future growth. Modeling flexibility is reflected in the generic character of the code. The models developed have the flexibility of use of different materials, as well as different models, geometry and boundary conditions types, which ensure that a wide range of problems can be solved by the code. Also, special models have been developed for several phenomena. The burden of this characteristic is that the user is penalized, having to input information, such as material properties, and to go through a model-selection process. Another consequence of this strategically guided decision is that the code does not afford elaborated methods, that is, since the proposed task is very broad, a composition of elaborated methods would make the code extremely slow, even when running into super-computers. To avoid inaccuracies resulting from this strategy, models are adjusted using experimental programs data or more elaborated tools.

User convenience is achieved through a very extensive checking of the input information. The input/output (I/O) process is performed through I/O files. The input file is large, where the user inputs the space discretization (nodalization), geometrical and material data, boundary conditions, and the models selected. Because of the large amount of information, errors in this input elaboration are almost impossible to avoid. To deal with this problem, and to make the code more user-convenient, the input package has extensive checking. Part of this checking is performed by the package itself, mostly regarding the type of variable selected . The presence of the required information in the correct format is set by the program developer. Other error checks are performed during the input-level routines., i.e., after the reading process has finished. This check is more extensive, and verifies the consistency of the discretization, the continuity of the flow, inconsistency between settings, and the ranges into which settings should fall. When errors are encountered, diagnostic messages are issued, so the user can easily correct his mistakes. Because the input-checking process is normally a maintainer attribution, the input improvements to afford the model's necessity are merely suggested in a typical format, but not implemented. This is a standard procedure of the code development. Hence, user convenience is obtained through an extensive input-checking process. This is an area where there is considerable work to be done. Some attempts have been made to improve the input and output format, making the code user-friendlier, but the work has not progressed considerably.

Computer efficiency is accomplished through a modular organized structure, which allows the identification of repeated activities, centralizing them in only one routine, a package of programming techniques used to increase efficiency, and a bit-packing procedure technique, which places several quantities requiring only one or a few bits into one 64-bit word. The initial choice of data storage had been for dynamic storage. This option remains the best still today, given the code features, e.g., multiple physical models, extensive interactions between models, and current input design. The dynamic storage is managed by the Fortran Tape Buffering (FTB) package, and this optimized management contributes to computer efficiency. Lately, dynamic storage is becoming standard in Fortran, it being convenient to change the coding by using the dynamic storage functions now available.

Preparing for future growth of the code is addressed by including all of the important parameters, which are calculated in common blocks (the so-called include-files). Each common block and a listing and explanation of its variables are presented in the programmer's manual (139). The variables found in these include-files are, therefore, used to pass information from one calculation to another, facilitating explicit couplings. Actually, the model implemented is an expansion of the code's capability. That being said, the first activity in the implementation, as pointed out earlier, is the determination of the available quantities in the common blocks to be used, using the programmer's manual. Scdap has been the first package to take advantage to this feature. Later, the Couple package, a finite-element model used to calculate the temperature behavior for molten pools, was coupled to Scdap/Relap. The fission products-transport package is the third great coupling to be done. In the future, a containment package, having special models to deal with typical containment phenomena, would be a significant improvement.

The base file for source contains only six sub-directories (139): auxx, graphics, envrl, matpro, relap, and scdap; and two files: makerm and makerp. The auxx subdirectory contains the files select.f and cnv32.f, which are the source files for the two pre-compiler steps.

The select utility is applied to source code for all machines, and is intended to activate or deactivate specific sections of coding which are machine or option specified. The cnv32 program applies additional logic prior to compilation, to allow operation of the program on 32-bit machines.

The graphics subdirectory contains source code for plotting subroutines. These are obtained as part of the Fortran compiler package and have been slightly modified for use in Relap5-Scdap.

The envrl, matpro, relap, and scdap sub-directories contain the source files for Scdap/Relap5. The files to be compiled have a ".ff" suffix. The *.ff files may have include statements, which are commands to copy the indicated files into the file to be compiled before the compilation. The files to be included have a ".hh" suffix.

The envrl sub-directory contains the source files for the auxiliary packages, such as the input package and the FTB package. The relap and scdap sub-directories hold the respective sub-routines for thermal-hydraulic calculations and severe accident calculations. The matpro sub-directory contains the material properties calculation sub-routines.

The source is written to be applicable to a variety of computers, but the source in the *.ff and *.hh files are not suitable for any computer. Through the application of the two levels of pre-compilers, the resultant source is suitable for a particular computer. The files resulting from the pre-compilers reside in the same sub-directory and have the same base names as the ".ff" and ".hh" files, but now have ".for" and ".h" suffixes. The include statements referencing the ".h" files, and the ".for" files are submitted to the compiler. The object files resulting from the compilation have the suffix ".obj" for debug compilation and ".o" for optimized compilation and likewise reside in the same directory as the *.ff files. Compilations with both the optimized and debug options can coexist.

The makerm file provides the input for the execution of the make utility. The make utility is used to control and up-dating of Relap-Scdap5, and the makerp file establishes the dependences of the sub-routines for the make utility.

The program is designed using the top-down to bottom-up technique. This means that the design was primarily top-down but also considers existing subroutine packages such as matrix and water property subroutines.

The top level in the Scdap/Relap5 structure is shown below, in Figure 4.1. The first activity executed is the input processing, consisting of three levels. The first level is the reading of data from the input file, checking the basic punctuation of the input, and storing the data into an array from which the data can be randomly retrieved using the line number. This activity is performed by sub-routine inputd. Checking is limited to errors in the data items on each line and the proper entry of line numbers.

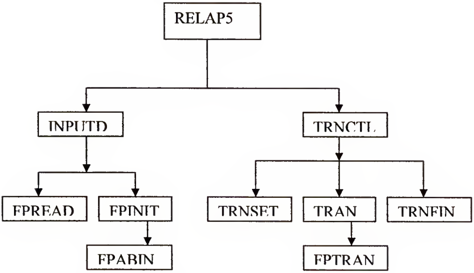

Figure 4-1. Top-level structure for Scdap/Relap5

The next level is called r-level, since this level calls subroutines (mostly having names that begin with r, and managed by rnewp) that reads data from the random storage array, and stores the data into common blocks or creates dynamic blocks and stores the data into them. The data is checked for the proper number of words entered and that the type of the words, integer, real, or alphanumeric, is correct. A check on the range of the input is done. Relap5 data is not checked for reasonableness since the code can be applied over a wide range of simulation conditions. Because of a more limited application, some Scdap values are checked for reasonableness. The r-level is represented, in Figure 4-1, by the fission products-transport routine fpread. Checking on relationships between data items in each subroutine is limited to data being read by that subroutine.

When all r-level subroutines have been executed, a check is done to determine whether all lines in the random array have been processed. The i-level processing calls subroutines that perform initializing calculations. One example is obtaining the initial conditions of pressure and phasic internal energies of hydrodynamic volumes. For user convenience, several options are allowed for the initial conditions of volumes. Using the equation of state, the required conditions are computed from the input conditions.

Error checking continues. For example, the equation of state conditions of volumes are checked to ensure they are within the range of the thermal property package. Relationships can now be checked. During r-level processing, the junction to and from volumes could not be checked because the components defining those volumes may not have been processed. The time-dependent portion of source for heat structures could not be checked because the reactor kinetics input may not have been processed. But at i-level, all input has completed r-level processing and the data has been moved into the database. The i-level is represented by the sub-routine fpinit in Figure 4-1.

Further creation of dynamic blocks and storage into modules are done during i-level processing. Individual r- and i-level subroutines are called from rnewp.

For most cases, the r-level subroutines can be called in any order, since each routine processes only data in the dynamic blocks and modules constructed by those routines.

Care must be used in locating i-level subroutines, since information from dynamic blocks and module data defined during i-level processing may be used. The current order of calls to i-level subroutines is related to the order of processing during time advancement.

At the end of input processing control is returned to the main program, relap5. If a set of input has been processed with no user errors, relap5 calls the trnctl subroutine.

Subroutine trnctl calls three subroutines, trnset, tran, and trnfin. Subroutine trnset completes linking of references of sections of the database, builds list vectors, sets up matrix information (and, in older versions, released unused memory space), and prints a summary of the dynamic file information.

Subroutine tran is then called to control the time advancements and remains in control until time advancements are terminated. This is by far the routine where the program spends the most time. Tran routine calls several routines to make different computations. In the case of fission products transport, the routine calls the sub-routine fptran, as shown in Figure 4-1. After return from tran, subroutine trnctl calls trnfin, which deletes scratch dynamic blocks or deallocates scratch arrays. Subroutine trnfin returns control to trnctl, which returns control to the main program, relap5. Hence, the implementation must be carried out in three levels, the r-level, the i-level, and the tran level.

The requirements or “rules” needed to be followed for the Scdap/Relap5 developers are listed in the programmer’s manual (139), and are again listed here:(a) do not use implicit typing; (b) use generic function names. For instance, use log, instead of alog, and min instead of min0 or amin1. Most Fortran manuals have tables giving both functions and their generic names; (c) do not use tab character for spacing. Many compilers generate error messages when tabs are encountered; (d) use 'e' rather than 'd' to indicate floating-point constants that need specification of a power of ten. The CNV32 routine will convert them to 'd', if necessary; (e) do not use format information imbedded in the read or write statements, if it includes 'e'-type format specifications. This can confuse the CNV32 sub-routine; (f) Local variables must be recomputed for each call sub-routine. Dynamic allocation, and time step repetition may make the local variable invalid.

Regarding input/output, the following requirements/recommendations are: (a) the use of INP routines (the input package) is mandatory; (b) perform error and range checking; (c) gather input in a logical manner. That is, group related input on the same card; (d) Gather output in a concise and clear manner; (e) use of real-time messages is discouraged; (f) identify significant parameters for major edit printout and less significant parameters for minor edit or plot capability.

Two figures co-exist in the enhancing process of a large scientific code such as Scdap/Relap5. The code developer is the general scientist with reasonable programming knowledge and deeper understanding of the physical-mathematical character of the modeling subject. He is responsible for implementing new models to improve the code capability, respecting the programming requirements. On the other hand, the code maintainer is a professional with more programming experience and deeper program knowledge and is responsible for the maintenance of the source code and checking of the developer's work, regarding his programming. The maintenance comprises the source code optimization, organization and updating, according to the language's evolution. In

Scdap/Relap5, as pointed out earlier, the maintainer also normally implements the r-level and the i-level, given the complexity of the INP package and the necessity of good practice in checking the input and issuing error messages.

Implementation

The implementation of the model is divided into I/O design, and the implementation of the solution of the problem, which have their procedure following described. In Chapter 3, it was seen that the ODE system is set by volume and the structural surfaces surrounding this volume. Examination of the phenomenological-modeling equations chosen, listed in Table 4-1, shows several quantities are needed for the computation to be performed. These quantities here are called auxiliary quantities, since they are used to obtain the main quantities that are the coefficients of the differential equations.

These auxiliary quantities can be code-, user- or developer-supplied. The first step in the design of the input is to list all quantities and define the supplier. The following methodology applies: (a) First, eliminate the code supplied, i.e., the quantities available in the common blocks already available (the already code calculated quantities). (b) Second, ask whether the quantity is related to the solution or to the specific problem. If related to the solution, it should be developer-calculated or -supplied. Otherwise, it should be user-supplied. The quantities needed in the computation are supplied in Table 4-2, together with their type and the methodology used to obtain the quantity.

Table 4-1. Phenomenological chosen equations

Phenomenon	Equation	Dependencies
I. Vapor Phenomena		
Condensation on Structural Surface	3-72	Vapor diffusivity, equilibrium concentration, Reynolds, Schimidt numbers, deposition area, gas pressure and temperature
Adsorption	3-69	Deposition area, surface material, gas temperature
II. Vapor-aerosol		
Condensation onto aerosol surface	3-102	Vapor diffusivity, equilibrium concentration, particle area, gas pressure and temperature, Knudsen number
Homogeneous nucleation	3-92	Molecular weight, equilibrium concentration, surface tension
III. Aerosol deposition		
Gravitational	3-117	Particle mobility, particle mass
Thermophoresis	3-146	Surface and gas temperatures, thermal boundary layer thickness, particle and gas thermal conductivities, Particle Knudsen number
Turbulent	3-128	Hydraulic diameter, particle radius, Reynolds and frictional velocity
Laminar diffusion	3-120/3-119	Particle diffusivity, fluid velocity, hydraulic diameter
Singularities	3-165/3-173/3-168	Bend angle, Stokes number, Dean number, bend curvature, contraction angle, area reduction ratio
IV. Aerosol re-suspension	3-181	Frictional velocity, particle size, Burst Reynolds number
V. Aerosol agglomeration		
Brownian	3-202	Particles' diffusivities, particles' radii
Gravitational	3-214	Particles' gravitational deposition velocities, particles' radii
Turbulent	3-240	Particles' gravitational deposition velocities, particles' radii, energy dissipation rate, kinematics gas viscosity

Table 4-2 shows that several auxiliary quantities are available in the voldat and htsrcm include-files. Hence, these files are included in the fission products routines. In addition, the include-files ufiles, cons, fast, comctl, and contrl are also included. The ufiles include-file contains the files where the quantities are to be written, Cons defines the constants to be used throughout the code, such as $\underline{\pi}$. The fast routine defines the storage pool in the computer memory, and comctl file contains information on the dynamic storage and reading/writing of restart blocks. The contrl file has the time advancement control quantities, such as time step size and time history.

Table 4-2. Auxiliary quantities of the fission product transport

Quantity	Type	Method
1. Fluid velocity, density	code	Available in Voldat.hh
2. Fluid dynamic viscosity	code	Available in Voldat.hh
3. Fluid temperature	code	Available in Voldat.hh
4. System pressure	code	Available in Voldat.hh
5. Gas non-cond. fraction	code	Available in Voldat.hh
6. Gas thermal conductivity	code	Available in Voldat.hh
7. Volume of the volume	code	Available in Voldat.hh
8. Area of the volume	code	Available in Voldat.hh
9. Hydraulic diameter	code	Available in Voldat.hh
10. Surface area	code	Available in Htsrcm.hh
11. Surface angle	user	Input quantity
12. Surface temperature	code	Available in Htsrcm.hh
13. Surface material	user	Input quantity
14. Reynolds number	code	Equation 3-53 in Fptran.ff
15. Vapor diffusivity in gas	developer	Chapmann-Enksog method/Fpvdif.ff routine/depend on Lenard-Jones parameters and molecular weight defined/ Fptrmod.hh
16. Specie equilibrium concentration	developer	Routine fpvceq.ff/coefficients of equations defined in fptrmod.ff
17. Surface tension	developer	Defined in fptrmod.hh
18. Singularities data*	user	Input
19. Particle size spectrum	developer	0.5-100 μm (diameter) in Fpinit.ff
20. Thermal BL thickness	developer	Equation 3-147 in Fpkdep.ff
21. Frictional velocity	code	Available in Voldat.hh
22. Particle size/volume	developer	Routine Fpabin.ff
23. Total bin part. volume	developer	Routine Fpvbin.ff
24. Total bin part. mass	developer	Routine Fpmbin.ff
25. Particle number conc.	developer	Routine. Fpconc.ff
26. Particle Mobility, diffusivity, density	developer	Equations 3-115,3-114, total mass/total volume per particle in Fpmdlk.ff
27. Particle and viscous layer Reynolds, MFP	developer	Equations 3-110, 3-189,3-112 in Fpmdlk.ff
28. Solution quantities**	Developer/user	Set in routine Fptran.ff

* Singularities data refers to the presence of singularities in a volume (bend, contraction, separator or drier).

** Solution quantities: Absolute and relative tolerances, minimum time step and maximum number of iterations, and number of bins (user supplied).

Input/Output Design

The input is designed to use the source from the release model, or user-supplied source. The species to be tracked are also defined in the input. In addition, it could be seen from Table 4-2 that the number of sections, the singularities data, and some undefined quantities in the calculation, such as surface material and angle, are user-defined. Table 4-3 shows a more detailed description of the quantities to be user-input. They are divided into system quantities, which represents quantities related to the hydrodynamics systems, singularities data, source and species data and solution settings. Regarding the last one, the adopted logic is that mathematical settings are too detailed to be user-selected. Consequently, the mathematical settings of the mathematical package to solve the ODE system are set by the developer. The setting was performed during the verification process. Therefore, the iteration technique, number of iterations, tolerances and minimum time-step size were defined during the verification process, leaving only the number of sections to be defined by the user.

The input should contain the information in Table 4-3. The input design is suggested below in Table 4-4. The model input is set in the cards of the family 2070XXXX, according to the input manual (42). The cards are designed toward making the input simple and efficient.

The r-level and i-level processes of the information in the input (Table 4-4) are performed by fpread and fpinit routines. Moreover, in fpinit the following activities are performed: the output is initialized, and important quantities that need be set to zero or whose values need be defined, are set accordingly. The masses in each state, for instance, are set to zero or obtained from the input information. This routine is also the best opportunity to perform calculations that are fixed throughout the transient, optimizing the calculation. In the case of fission-products transport, the only computation having this characteristic is the determination of the discrete size distribution. Hence, as pointed out in Figure 4.1, the routine fpinit calls the routine fpabin, which performs the size distribution, as a function of the limits of the spectrum and the number of sections.

Table 4-3. Input quantities of fission product transport module

Type of Quantity	Quantity
I. Solution	Number of bins (1 to 50)
II. System	Hydrodynamic systems specification
	Surfaces where special settings are needed
Special settings	Structural surface angle (not horizontal)
	Structural material (zircaloy)
III. Source and species	
	Species to be tracked
	Flag to define user or code source
	Release mass rate (in case of user defined)
	Volumes where the source are released
IV. Singularities data	Volume where the singularity exists
	Type of singularity
If contraction	Contraction angle, contraction ratio
If bend	
If separator	Vortex tube length, vane angle
If drier	Curvature angle

The output design of any module in Scdap/Relap must obey the principle that only quantities of interest must be printed out, given the enormous amount of quantities computed. Following this principle, the quantities selected to be part of the output are the masses in all the states. These quantities are related to the volume or heat structure, and are also dependent on the species and the section in the case of bin quantities. The surface quantities are the condensed mass, the adsorbed mass, and the mass plated out (aerosol-deposited) for each species. The volume quantities are the mass of vapor and aerosol in each bin, for each species.

Table 4-4. Input cards of fission product transport module

Card Number	Card Word	Meaning
20700000	W1(I)	Number of bins (sections)
20700001 to 05	W1(I)	Hydrodynamic system specification, through definition of one volume of the system
20700010 to 19	W1....(A)	Species selection cards, through setting of species alphanumeric symbols
20700020 to 29		Special settings for structural surface
	W1(I)	Structural surface number
	W2(I)	Flag: 0 structural angle; 1 material (zircaloy); 2 material (stainless steel) 3,4 both
	W3(R)	Structural angle (rad)
20700030 to 39		Singularities data
	W1(I)	Flag: 0 bend; 1 contraction; 2 separator; 3 drier
	W2....W4(R)	Required quantities
20700040 to 207nnn0		User defined source (last digit should be zero)
	W1(I)	Initial volume number
	W2(I)	Final volume number
207nnn1 to nnn9		Release rates in vol. defined in 207nnn0 (4<nnn<999)
	W1(A)	Species alphanumeric symbol
	W2 (R)....	Mass in liquid, vapor and section in crescent order

Calculation Implementation

The calculation implementation is executed into a level below Fptran, by three different routines, fpgedr, fpmdlk and fptmix. Fptran is the controller of the computation, performing the integration over one time step for all the volumes. This integration is achieved performing first the advection of the volume masses, between all volumes in the hydrodynamic system, using fptmix routine. The fptmix is a donor-cell convection routine, which swaps the entire hydrodynamic system. After the convection, a swap over the volumes is performed. During the swap, the source term is added, and the masses are re-sized (changing from a three-dimensional to two-dimensional array) and renamed, to be worked by the other routines. Moreover, the code-supplied quantities are taken from the include-files, and made available for the calculation. Then, the coefficients of the equations are calculated in the routine fpmdlk, and, following, the process of solving the ODE system is managed by fpgedr. The first level in the fptran is represented in Figure 4-2.

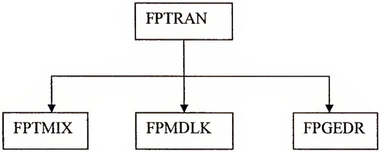

Figure 4-2. First level below fptran

The fpmdlk routine performs its purpose in a two-step process. First, it calculates or obtains all the quantities used in the coefficients calculations, and then calculates the coefficients calling other routines for the coefficients calculation. Several auxiliary routines are used to determine vapor and aerosol quantities. The routines below the fpmdlk routine are represented in Figure 4-3 below.

The function of the routines shown above is described next, in Table 4-5. The quantities first calculated, before the coefficients' calculation, are: Reynolds number, frictional velocity, particle mass, mobility, diffusivity, gravitational settling velocity, density, thermal conductivity and vapor diffusivity. Some of these quantities are directly obtained from the subroutines, such as vapor diffusivity, whereas other quantities, such as particle densities, are calculated in fpmdlk.

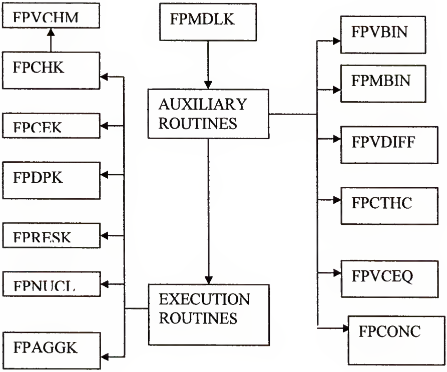

Figure 4-3. The fpmdlk routine and its sub-routines

Table 4-5. Function of sub-routines called by fpmdlk

Sub-routine	Function
Fpvbin	Calculates the total volume of particles in a bin
Fpmbin	Calculates the total mass of particles in a bin
Fpvdiff	Calculates species vapor diffusivities
Fpvceq	Calculates equilibrium concentration for the chosen species
Fpcthc	Calculates the particle thermal conductivity
Fpvchm	Calculates the adsorption constants
Fpchk	Calculates the adsorption coefficients
Fpcek	Calculates vapor condensation coefficients
Fpdpk	Calculates aerosol deposition coefficients
Fpaggk	Calculates aerosol agglomeration coefficients
Fpresk	Calculates re-suspension coefficients
Fpnucl	Calculates aerosol homogeneous nucleation rates
Fpconc	Calculates the concentration of particles in a bin

The fpgedr routine is the routine that manages the solution of the ODE system, working in the same level as the fpmdlk routine. To better understand the function of each subroutine, the major activities in the process of the solution are arranged in the flow chart presented in Figure 4-4 below. This figure shows that the process can be broken into several activities, in accordance with the modular philosophy of the code.

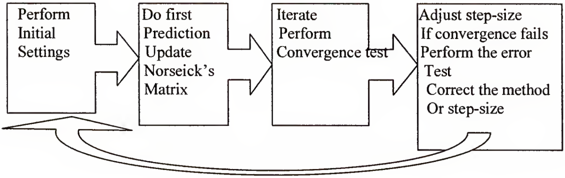

Figure 4-4. Solution process for the ODE system in Hindmarsh package

The two most important routines of the ODE system calculation package are fpgedr and fpgeci. They are here considered due to their multiple functions. Fpgedr is the process manager, but it is responsible also for the settings during a first call process, checking the consistency of these entries. It also calculates common quantities for the execution routines, such as the weighting vector. After performing these preparatory activities, fpgedr calls the fpgeci routine, which is the execution's manager. Fpgeci performs the adjustment settings during one iteration, resultant from convergence or error test. After performing the settings, fpgeci performs the step-size reduction, if the convergence test fails successively (convergence test is performed in fpgepc), and performs the error test, adjusting the step-size or method order and re-doing the computation. The overall structure of the ODE system package solver is shown below in Figure 4-5. The function of each routine, except fpgedr and fpgeci is presented in Table 4-6. The routines were divided into preparatory routines, which prepare the data for the solution, and execution routines, which execute the computation.

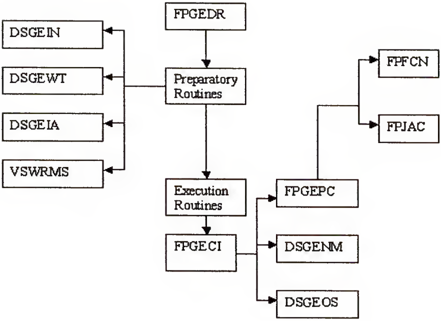

Figure 4-5. Fpgedr sub-routines structure

Table 4-6. Function of sub-routines called in Fpgedr structure

Sub-routine	Function
Dsgewt	Updates the weighting vector (Equation 3-39)
Dsgeia	Adjusts the initial step size
Dsgein	Interpolates the derivative after overshooting
Vswrms	Finds a weighted Euclidean norm of a real vector (Equations 3-37 and 3-42)
Fpgepc	Performs one iteration and the convergence test
Dsgeos	Computes step size ratios to adjust method order or step-size
Dsgenm	Updates the Nordsheick's history matrix
Fpfcn	Calculates the derivatives for vapor equations
Fpjac	Calculates the Jacobian for vapor equations

An include-file is set to store temporarily the quantities that are shared by several routines. This routine also contains all species data to calculate vapor and aerosol properties, such as molecular weight, densities and surface tensions. In this routine, the dynamic storage quantities are allocated. These quantities are the masses in each state, for each species in each volume, and storage parameters, such as offsets and skip factors. This routine is named fptrmod. Fptrmod, therefore, is the fission products-transport include-file, having the functions of storing shared quantities (such as the equation coefficients and the fixed species properties) and managing the dynamic storage allocation.

Figure 4-6 below provides a general picture of the transient calculation in the fptran module. Only the most important routines (execution routines) are presented, but the reader can draw a general picture of the problem breakdown, examining this picture and the function of each sub-routine.

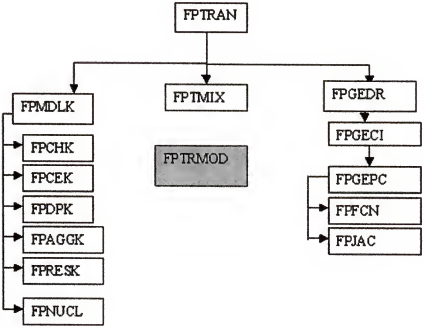

Figure 4-6. Simplified scheme of fission product transport modular organization

The fission products-transport model is described in terms of the programming structure in this section. In accordance with the code programming structure, the activities are broken in the input reading and initialization process, and the advancement of the problem solution. It is suggested an input capable to provide the necessary information to the code execution. Regarding the calculation, the activity is broken in three major activities, the calculation of the equation coefficients, the convection, and the solution of the ODE system. Further task division occurs in these activities. This division of activities, as well as the sub-routines responsible for each task is also described.

Verification

Verification, in the context of this research, means the execution of all necessary tests to evaluate the performance of the model, except for accuracy. In this research, the accuracy of the model is evaluated in the assessment. Verification, therefore, should comprise all the evaluations necessary for the solution aspects, except for accuracy.

The verification process is divided into two phases. In the first phase, the following checking is performed: (a) Accuracy of the mathematical solver; (b) Conservation of mass in a time-step; (c) Non-negativity of masses; (d) Robustness of the model; (e) Order of magnitude of the more important quantities. In the second phase, the global mass conservation is tested, that is, the input source integration over the transient time must be shared over all the defined states. In addition, sensitive studies of the phenomenological importance, according to the thermal-hydraulic conditions, are performed. The stability of the solution is also tested by performing re-nodalization and varying the number of sections used.

The mathematical solver was tested by setting three ODE systems, of which the solution is known. The use of the mathematical solver to calculate these problems proved that the package was correctly implemented, once the calculated results match the known exact results. Since the problems were simple problems, the results matched in a very accurate form.

The remaining checks are performed through the settings of two models. The fist one is a simplified two-channel core model, and the second is a typical LWR primary-circuit pipe with typical severe accident thermal-hydraulic conditions, and typical fission product source. Because two models are used in this chapter, and one is used in the next chapter, a brief understanding of the input settings is necessary, providing the basis for the understanding of the input descriptions later given.

Input File Description

The input requirements could be divided into initial settings, related to special models, and elements, which can be special or basic elements. This section focuses, primarily, on the basic elements and initial settings because they are used in the modeling.

The basic elements in Relap5 are the basic hydrodynamic volumes, the hydrodynamic junctions to connect the volumes, time-dependent volume and junctions to establish the boundary conditions and the heat structures, representing the solid materials surrounding the flow such as pipes and rods. The time-dependent volume adds input of equation of state as a function of time or other variables, whereas the time-dependent junction adds input of velocities as a function of time or other variables.

The basic hydrodynamics elements are the single volume, single junction, pipe and branch. The single volume is the basic building block for a hydro system, while the single junction is the basic connection. A pipe is a string of volumes with interior connecting junctions and a branch is one single volume with no junctions or with as many as nine.

Special hydrodynamic volumes are present in the code to model certain components of the plant. They are the separator, valve, pump, accumulator, annulus, prizer, jetmixer, turbine, eccmix. The annulus is a pipe with special flow-regime considerations. The other elements are branch or single volume elements with special features and models to simulate the component behavior. The prizer simulates the pressurizer, the jetmix simulates jet pumps, and eccmix the ECCS (emergency core cooling systems). The others are related to the component with the same name.

There is only one type of heat structure, used to model fuel pins, pipes or plates with or without nuclear or electrical power. The user should define different heat structures for each element. Different heat structures are distinguishable in geometry, boundary conditions and composition (material). For simulation of fuel rods, separate elements should be defined, because additional settings should be supplied.

The initial setting information required is: (a) type of problem (transient or steady-state/new or restart); (b) major and minor edits in the output and its print frequencies; (c) initial time step; (d) non-condensable gases and their fractions; and (e) solution scheme selection (semi-implicit or nearly implicit).

The information required for all types of volumes is: (a) the volume flow area; (b) volume length; (c) volume of the volume; (d) azimuthal angle; (e) inclination angle; (f) elevation change; (g) wall roughness; (h) hydraulic diameter; (i) initial conditions; and (j) name and type of element. The volume should be the product of the flow area and the length. Other requirements are that the azimuthal angle should be between zero and 360 degrees and the inclination angle should be between zero and 90 degrees, being the horizontal inclination considered zero by the code. There is an implicit coordinate system in each hydrodynamic volume, in which the x axe represents the fluid direction. A set of examples is presented in Figure 4-7 (a) as well as the face nomenclature used by the code in Figure 4-7 (b). The hydraulic diameter is given by:

$$D_h = 4\text{x}\left(\frac{\text{Flow Area}}{\text{Wetted Perimeter}}\right) \qquad \text{(Equation 4.1)}$$

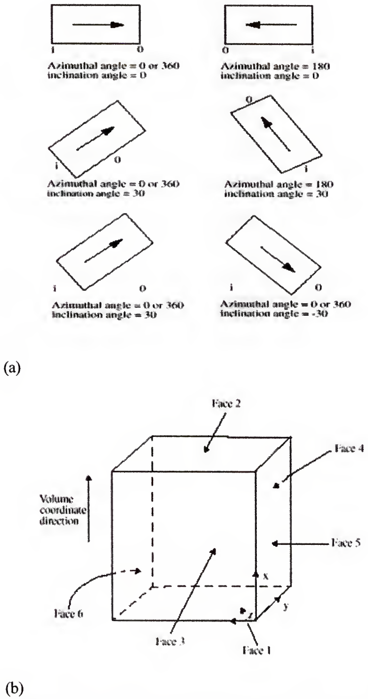

Figure 4-7.Geometrical settings of Relap (a) references for azimuthal and inclination angle; (b) volume face numbers (42)

The initial conditions are the fluid type and its initial state, represented by two of the three variables defining a fluid state (pressure, temperature or quality).

The junction's required information is: (a) the volume from which the junction coordinate direction coordinates (entrance); (b) the volume to which the junction is connected (exit); (c) the junction area; (d) Reynolds-number independent forward-flow energy-loss coefficient; (e) Reynolds-number independent reverse-flow energy-loss coefficient; (f) initial conditions. The initial conditions are the initial liquid or vapor velocity or mass flow rate.

For the pipe/annulus element the number of single volumes composing the pipe should be supplied and all the above-listed information for each volume and junction connecting the volumes must be supplied. For this type of element the sequential expanded format, described in (42) is very useful. For the branch element, the number of junctions should be supplied, establishing all junction settings for each one.

The boundary conditions elements (time-dependent volume and time-dependent junction) have the same requirement of a simple junction or volume. Nevertheless, the variation of the temperature, pressure and/or quality, for the time-dependent volume, and of the velocity or mass flow rate, for the time-dependent junction, with time should be set, instead of as in the initial conditions.

Heat structures information required is: (a) geometry of the heat structure; (b) dimensions; (c) mesh points; (d) boundary volumes; (e) number of axial heat structures with this geometry; (f) material type; (g) material properties (thermal conductivity and volumetric heat capacity); (h) initial temperatures; (i) boundary conditions; and (j) time dependence of heat source. The geometry types allowed are rectangular, cylindrical and spherical. There are built-in properties for common materials and they can be supplied too. Mesh points can be set with different mesh spacing, or both. Spatial dependence of internal heat source may vary for each mesh interval.

The boundary conditions could be: (a) symmetry or insulated condition; (b) tables of surface temperature or heat transfer versus time; and (c) convective correlation package. When the convective-boundary condition is activated, which is a common situation in reactor analysis, additional information must be supplied. The power could be set through tables, the kinetics module or control systems. For the radiative heat transfer, the user should supply the view factors.

The additional information is: (a) heat-transfer hydraulic diameter; and (b) information for critical heat flux (CHF) calculations, described in (42). The heat transfer hydraulic diameter is given by the equation:

$$D_h = 4x \left(\frac{\text{Flow Area}}{\text{Heated Perimeter}} \right) \qquad \text{(Equation 4.2)}$$

Code options could be set through flags in the elements cards or optional special cards. Normally, they are defined when writing the input for the elements of the model. Therefore, this section is organized in accordance with the Relap element. Special elements could have options not mentioned here, because, again, they are not used in the model.

For the basic volumes (single volume, pipe and branch), the code options are: (a) thermal stratification model activation; (b) mixture level tracking model activation; (c) water packing scheme; (d) vertical stratification model; (e) non-equilibrium or equilibrium model selection; (f) inter-phase friction model selection; (g) boron presence activation; (h) non–condensable gases presence activation; (i) cross-flow modeling; and

(j) additional wall friction model. The vertical stratification and water packing scheme are typically used when modeling pressurizers.

The activation options are executed through flags in the elements' definition cards. The cross-flow is modeled defining lateral volumes and junctions. The available inter-phase friction models are the rod bundle, pipe and ORNL ANS narrow plate. Coefficients to the wall friction correlation can be furnished in an optional card.

The junction options are: (a) countercurrent fluid level model activation; (b) horizontal stratification model activation;(b) chocked flow model activation; (c) abrupt area change model activation; and (d) homogeneous or non-homogeneous model selection. The activation of the abrupt area change necessitates additional information, detailed in (42).

The heat structures options are: (a) gap-conductance model activation; (b) reflood model; (c) metal-water reaction model; and (d) fuel-cladding deformation model. All these models are activated through special cards, requiring additional input requirements. The gap-conductance model must be activated when modeling fuel pins, and the geometry of the heat structure must be cylindrical.

As mentioned previously, special elements, special models, reactor kinetics, trip and control systems have their own input requirements and options, which are not here detailed. Information about these settings is available in the Input Manual (42).

The input file is set through cards, which provide the information to the code. A good practice is to limit the data to 72 characters per line. A RELAP5 problem input deck consists of at least one title card, comment cards, data card and a terminator card. The title card must be supplied and is identified by an equal sign (=). The comment cards are optional and an asterisk or a dollar sign should appear as the first nonblank character and the terminator card is defined by a slash (/) or a period (.) as a nonblank character. Continuation cards are identified by a plus sign (+) as the first nonblank character.

Data cards may contain varying number of fields, called words, that may be an integer, real (floating point), or alphanumeric. Blanks preceding or following fields are ignored, meaning that at least one blank space should separate the words. In the data cards, the user supplies all the input requirements and makes all the code options. Code options could be activated through special cards or flags in some cards. The data cards could be required or optional.

Cards 100 through 199 are used for the problem definition. The user selects the type of problem (transient or steady-state) and whether the problem is a new or a restart problem. The non-condensable species present, as well as the correspondent mass fraction, are also specified in these cards.

The cards of the 200 family are used to define the numerical scheme to be used (semi-implicit or nearly implicit), the initial time step, and the minor and major edit print frequencies overall transient period. Major edits are variables (temperatures, pressure, void fraction, for instance), which are given automatically, without the necessity of requesting them. Minor edits are calculated variables, but only available when requested through cards 300 to 399.

Cards 400 to 799 or 2060000 to 2062000 are used to set trip input data, whereas cards 205CCNN are used to set control variables. CC is the variable number and NN the variable type definition. Cards 1001 to 1999 are for strip request data, used to extract specific information. Reactor kinetics inputs are set using cards 30000000 to 39999999.

Hydrodynamic element specification has the format CCCXXXX, where CCC is the number of the element and XXXX are the settings. Heat structures numeration follows almost the same pattern. Its form is 1CCCgXXXX, where g is the geometry type and the other symbols are the same as for the hydrodynamic element.

Furthermore, thermal properties are input through cards 201MMMXX, where MMM is the material number and XX are settings, specified in (19). General tables use cards 202TTTNN. TTT is the table number and NN is the table row.

The Scdap input is composed of a general input part, where the user provides general parameters of the system being modeled and important settings of the core - amage progression (cards 4000XXXX) and a second part, where the elements (cards 40CCXXXX) and special models are defined. CC defines the component number and XXXX the settings.

The SCDAP elements are: (a) fuel-rod element; (b) simulator element; (c) PWR control-rod element; (d) BWR control-rod element; and (e) shroud component. The special models are: (a) upper plenum structure model (cards 48CCXXXX); (b) Couple model (cards 50CCXXXX); and (c) Radiation Heat Transfer Model (cards 49CCXXXX). In this section, the fuel rod, simulator and shroud elements, and the radiation heat transfer model are focused on, because they are used in the developed input file.

The general input requirements are: (a) length, height and number of axial nodes; (b) reactor environment (PWR, BWR, or electrically heated); (c) power history; (d) grid spacer description; (e) control volumes which will receive slumped material; and (f) material properties from the code or user-defined properties.

The fuel rod element requirements are: (a) number of rods; (b) power profile; (c) pin geometry (plenum length and void volumes); (d) fuel rod dimensions (pellet radius, inner and outer cladding radius); (e) upper and lower hydrodynamic volumes; (f) radial mesh spacing; (g) Initial temperatures; (h) material specification; (i) theoretical fuel density; and (j) gas internal pressure.

The information required by the simulator rod element and the shroud element are the same. The only difference is the geometry. The simulator requires the radius of tungsten filament, whereas the shroud element requires the perimeter of the inner shroud surface and the shroud flow area thickness. In the surface radiation model the user should provide the view factors between the elements and the path lengths.

The overall options of the Scdap input are related to user-supplied limits, parameters and selections related to the damage progression. The general input options are the debris bed characteristics, oxide shattering trip or control variable, metallic meltdown parameters, core fragmentation parameters and oxide-shell stability parameters of the molten pool. Furthermore, the cladding-rupture strain and transition strain could be supplied by the user. In the fuel rod and simulator elements, the code options are previous power history, fission products release model, and gap conductance. In the shroud elements, the user can supply the interface with molten pools.

First Verification

The first verification is done with a simplified two-channel vessel model. The geometry is typical of a PWR, and Scdap fuel elements were used to represent the fuel, with control rod elements set to represent the control rods. Since this is the first one to be tested, an accelerated degradation was set, using the knowledge obtained from the experimental program Severe Fuel Damage (SFD). This experimental program aided the selection of the boundary conditions needed for this accelerated degradation to happen. So, core degradation starts after 46 seconds of the transient, and the transient is finished at 150 seconds (a very rapid transient). The degradation was accelerated so to reduce the running time, so errors can be rapidly identified and corrected. The nodalization diagram of the model is shown in Figure 4-8. The Figure only shows the Relap elements. Scdap fuel elements and control rods elements are placed in the pressure vessel control volumes (100 and 101) to represent them.

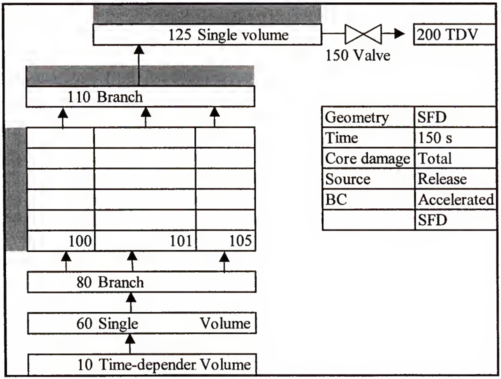

Geometry	SFD
Time	150 s
Core damage	Total
Source	Release
BC	Accelerated
	SFD

Figure 4-8. Nodalization diagram for the firs model used in the verification

The initial conditions assumed are an initial core temperature of typical operational conditions. The flow boundary conditions are set initially without forced flow for up to 76 seconds of the transient, at which time water is injected, simulating the high-pressure injection system, with typical fluid temperature and mass flow rates. The flow boundary conditions are set through the time-dependent volume (010 in Figure 4-8), and the respective time-dependent junction (050 in Figure 4-8). The system pressure is set at 7 MPa.

The 060 volume simulates the lower plenum, which connects to the core through the branch element 080. The hydraulic diameter of the pressure vessel is of 3.5 m. The core has a heated length of about 3.6 m, and is divided into two channels, represented by the pipe elements 100 and 101. The core by-pass is represented by the pipe element 105. The upper plenum is represented by the branch element 110, which is connected to the 125 pipe, representing a part of the primary circuit. The circuit is closed by a time-dependent volume (200) and a valve (150). The valve remains open from the beginning of the transient up to 70 seconds, when it is closed, remaining so until the end of the transient (150 seconds).

Three heat structures are set, to verify the level of the temperatures at the pressure vessel at the core region, upper plenum, and in the primary circuit. These heat structures are attached to the components 100, 110, and 125 respectively. The pressure vessel thickness used are roughly 15 cm for the pressure vessel, and 2 cm for the pipe wall. The set boundary conditions are the hydrodynamic volumes on one side, and adiabatic conditions on the other side. This setting contributes to the rapid onset of core damage, which is desired, as pointed out earlier.

Scdap fuel elements are used to represent the fuel. About 18,000 fuel elements and 118 PWR control rod elements are set in control volumes 100 and 105. The geometry of the problem, and initial conditions are presented in Table 4-7.

Table 4-7. Major settings of the first verification model: (a) initial conditions; (b) geometric settings

(a)

Parameter	
Pressure	7.0 MPa
Quality in the core	1.0
Quality in the lower plenum (060)	0.02
Mass flow rate	0.0
Fuel temperature	900 K
Structures temperatures	560 K
Fuel pin internal pressure	5.8 MPa
Fill gas	He

(b)

Parameter	
Heated length	3.6 m
Pressure vessel diameter	3.5 m
Pressure vessel thickness	15 cm
Pellet radius	4.699 mm
Rod internal radius	4.788 mm
Rod outside radius	5.461 mm
Pipe wall thicness	2 cm
Pipe diameter	20 cm
Pitch	14.427 mm

Figure 4-9 presents the time history of the most important thermal-hydraulic parameters for the fission-products transport: the system pressure, maximum fluid temperature, and velocity of the fluid in the exit pipe (volume 125).

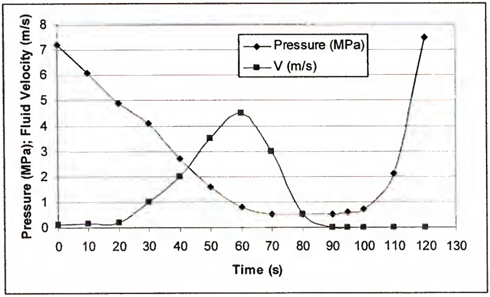

(a)

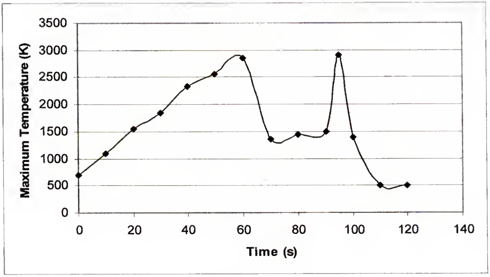

(b)

Figure 4-9. Thermal-hydraulic parameters for the first verification model: (a) fluid velocity and system pressure; (b) maximum fluid temperature

In the first phase of the transient (up to 76 seconds, when the valve is closed), despite the initial absence of flow, a natural circulation occurs due to the temperature differences of the upper and lower parts of the circuit. As a consequence, steam circulates from the lower to the upper part of the circuit. As long as the gas temperature increases, resulting from the energy balance of decay power and circulating fluid, the fluid velocity increases. The first peak in the temperature occurs at about 60 seconds of transient time, and constitutes the first oxidation peak. The fluid velocity is resultant of the temperature gradient, and is affected by the fluid density and flow area. Consequently, as shown in Figure 4-9 (a), the velocity reaches its maximum at the same time of that of the gas temperature. Since the fluid inventory is under reduction, the system pressure reduces, reaching about 0.5 MPa at 75 seconds of transient time (Figure 4-9 (a)).

In the second phase of the transient, the valve is closed, and water is injected from the bottom. With the injection of the water and valve action, the system pressure starts to increase. The fluid velocities decrease to nearly zero, and the volumes start to fill with water, as long as the structures are cooled down. A significant increase in the liquid volumetric fraction occurs after the onset of this phase. At 95 transient seconds, the liquid fraction suffers oscillations. These oscillations are the reflex of the slump of a molten pool into the lower plenum, resulting in very strong and rapid vaporization of the water. The effect of this occurrence is also felt in the fluid velocity at the lower plenum, which present a small peak at the same time. At 110 transient seconds, the water level reaches a height of 2.4 m in the core.

The transient selected, therefore, joins together desired qualities in order to fulfill the purposes of the first verification. It contains a great variety of thermal-hydraulic and fission-products source conditions, which are important for testing the robustness of the model; and it is a very rapid transient, which is good for the "debugging" of this model. This first model is used to debug all the written and changed routines. Hence, it is important to have a rapid transient. The fission-products source used came from the release module in the code, which released masses differ by four to five orders of magnitude.

In order to achieve the goals of this phase, a debug file is set to be printed when a flag is set in card 20700000. This debug printout prints all the important thermal-hydraulic quantities, the masses of all states before and after the vapor or the aerosol calculation, and the deposition and agglomeration coefficients.

The robustness, non-negativity of the masses, order of magnitude of the more important quantities, and conservation of mass in a time-step are tested, by running the model and printing all the information. The results for all the volumes are checked, regarding these subjects for 10 periods of one second each, randomly chosen in the transient period of time after the first release (34 seconds of transient time). After extensive work in the coding, all the programming errors detected were corrected. Applying, then, the analysis criterion (choose ten random periods of one second), the following observations are performed: (a) No negative masses are observed; (b) Mass, in a time step, is conserved for all cases; (c) The mathematical package is capable of handling all cases; (d) No abnormalities in the order of magnitude of the coefficients of the equations are found.

Therefore, the analysis of this model shows that the developed fission products-transport package is capable of handling properly the analyzed problem. Since it is a demanding problem, the developed package seems ready to be used, considering the analyzed aspects. Obviously, this analysis does not include the full spectrum of possibilities of phenomena and thermal-hydraulic parameters. For this reason, the analysis here performed continues in the subsequent models studied.

Second Verification

As mentioned earlier, in this phase the global mass balance, stability, and sensitive studies are performed. The first two activities are performed using the basic model (the first one developed for this verification), and the last one is performed varying the flow conditions of the basic problem. A survey of the impact of the model in the CPU time is presented, as well as the selection of the best iterative technique.

The model used intends to represent a more realistic problem of transport into the pipes of the primary-circuit system. Typical measures of primary-circuit systems are used in an 8 m stainless steel tube, having one 90-degree bend, half of its length in the vertical direction, and the other half in the horizontal direction, as shown in Figure 4-10 (nodalization diagram). The pipe diameter is 0.7 m, and the thickness of the pipe wall is 2.5 cm. The geometry, therefore, is easily set.

Nevertheless, thermal-hydraulic conditions during a severe accident vary widely. In addition, the released fission products masses have a time-dependent behavior. Consequently, under these circumstances, the selection of thermal-hydraulic conditions would be accidental. In order to have more control of the thermal-hydraulic conditions, allowing easier interpretation of the results, as well as facilitating the verification process, a special procedure is set. The initial conditions for the pipe temperature and the wall heat-transfer coefficients are selected from typical steady-state nuclear power plant calculations. The pipe wall temperature is set to 560 K, and the heat transfer coefficient to 2.0 W/m^2K.

Once the pipe wall initial temperature and boundary condition are set, the inlet fluid conditions are chosen, namely, pressure, temperature and fluid velocity. The initial conditions along the volumes are guessed, and a steady-state problem is solved (running a steady-state problem in the code) to obtain the steady initial conditions. The input is reset with the initial conditions obtained in this calculation. Five species are used in the problem. The release rates for these species are obtained considering the importance study in Chapter 2. Some rates are increased to allow saturation conditions to occur. Constant release rates are set so to simplify the problem. This source is far from representative of the actual condition, but allows an easy physical interpretation. Moreover, the aerosol agglomeration and deposition coefficients have weak dependence on the composition, but strong dependence on particle size and flow conditions. For this reason, the sensitive studies, which are focused on the aerosol coefficients, are not significantly affected by the speciation and release rates. Figure 4-10 contains the species and release rates used in the model. The inlet initial conditions chosen are pressure of 0.2 MPa, fluid temperature of 1500 K, and flow velocity of 0.5 m/s.

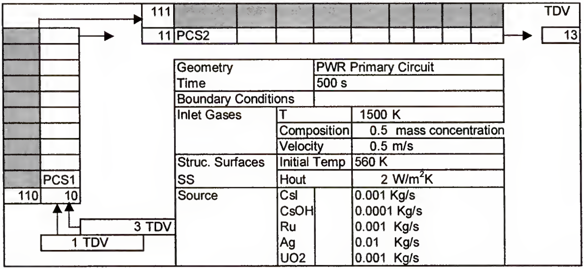

Geometry	PWR Primary Circuit	
Time	500 s	
Boundary Conditions		
Inlet Gases	T	1500 K
	Composition	0.5 mass concentration
	Velocity	0.5 m/s
Struc. Surfaces	Initial Temp	560 K
SS	Hout	2 W/m^2K
Source	CsI	0.001 Kg/s
	CsOH	0.0001 Kg/s
	Ru	0.001 Kg/s
	Ag	0.01 Kg/s
	UO2	0.001 Kg/s

Figure 4-10. Nodalization diagram of the second verification model

The inlet conditions are introduced using two sets of time-dependent volume and junctions, time-dependent volumes 001 and 003 and time-dependent junctions 002 and 004. The first set is used to input the steam inlet conditions, whereas the second one is used to set the hydrogen inlet conditions. The vertical pipe is represented by the pipe element 010, and the horizontal pipe is represented by the pipe element 011. The pipe wall is represented by the heat structure 110 and 110, respectively attached to the pipes 010 and 011.

Global mass error

This model was used to verify the global mass error. The procedure for such verification is to set a control variable that adds the condensed, deposited and adsorbed mass for all the heat structures in the problem for each species. Another control variable integrates the source for each species. The integral of the convected masses in the volume states (vapor and section masses) are not computed normally. Since these masses are needed to perform the global mass error check, new variables and computations are set in the source code to calculate the time-integrated mass convected out of the last volume (the pipe volume 011-10), and they are made available in the output. The verification is performed by comparing the integral source to the addition of the deposited mass and the mass convected out from the last volume in the hydrodynamic system, as expressed in Equation 4-3 below.

$$\sum_{v=1}^{V}\int_{0}^{t} Source_{i,v}dt = \sum_{s=1}^{S}\sum_{v=1}^{V} C_{i,s,v} + \sum_{s=1}^{S}\sum_{v=1}^{V} D_{i,s,v} + \sum_{s=1}^{S}\sum_{v=1}^{V} A_{i,s,v} + \sum_{vst=1}^{VST}\sum_{\Delta t=1}^{nstep} m_{i,vst,\Delta t}^{last} \qquad \text{(Equation 4-3)}$$

Where:
$Source_i$: Mass source rate for species i into volume v (kg/s);
$C_{i,s,v}$: Condensed mass for species i, onto surface s of volume v (Kg);
$D_{i,s,v}$: Deposited (aerosol) mass for species i, onto surface s of volume v (Kg);
$A_{i,s,v}$: Adsorbed mass for species i, onto surface s of volume v (Kg);
$m_{i,vst,\Delta t}$: Mass for species i, in the volume state vst, in time step Δt convected out from the last volume in the hydrodynamic system (Kg).

The error for all the species considered in the problem oscillates from 10^{-5} to 10^{-9}. This error is acceptable and its occurrence is attributed to the accumulation of mass neglected due to its small value (imposed constraint described in Chapter 3) and to numerical errors, i.e., round off and truncation errors. Hence the verification showed that the model is conserving acceptably the global mass.

Stability

The stability of the model is tested regarding the sectional discretization and spatial discretization (re-nodalization). Regarding the sectional discretization, the analysis is performed comparing the sectional distribution of masses and the number of particles for several numbers of sections. Also, the convergence of the result with the increase in the number of sections is analyzed. Regarding the spatial discretization, the model is tested comparing the results for the basic model, which has 20 volumes, to a re-nodalized model with 40 volumes.

Sectional analysis is performed by observing the sectional distribution of the number of particles as a function of the size distribution of these particles and the total number of particles as a function of the number of sections. These two graphs are plotted for three volumes at 496.5 transient seconds (close to the end of the transient). The volumes are chosen close to the release site (volume 010-01), in the middle of the model (volume 011-01), and at the end of the model (volume 011-10). The results are presented in Figures 4-11, 4-12 and 4-13. These pictures present the location of the volume in the pipe, the sectional-size distribution of the number of particles, as well as the behavior of the total number of particles, as the number of sections continuously increases.

In the sectional level, a model can be considered stable if the particle distribution, for a varied number of sections, does not oscillate, having the expected log-normal shape distribution. The model is also considered stable if, for an increasing number of sections, masses in the bins and the number of particles converge. The quantity chosen to be examined is the total number of particles, i.e., the addition of the number of particles in all the sections.

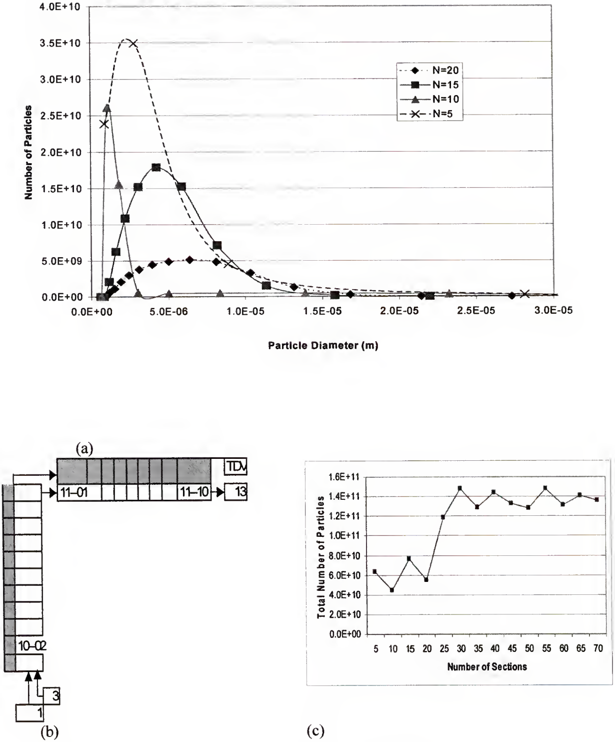

Figure 4-11. Sectional analysis for control volume 10-02: (a) number of particles distribution for diferent number of sections; (b) location of the volume 10-02; (c) total number of particles for different number of sections

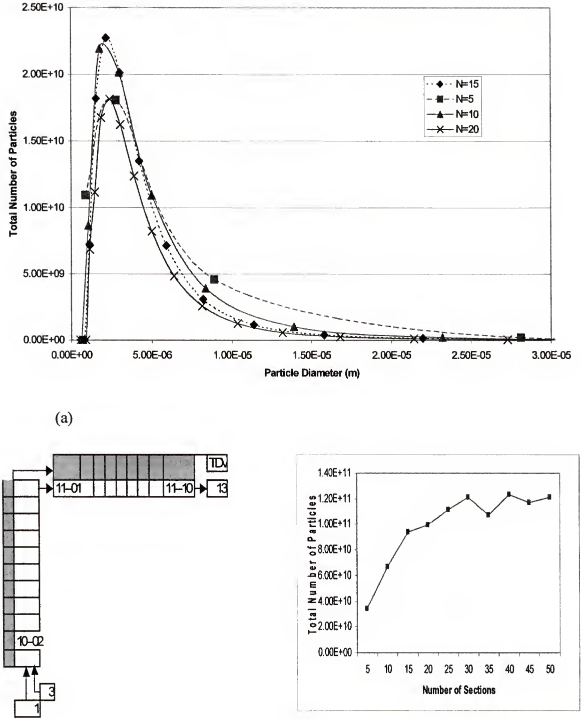

(a)

(b) (c)

Figure 4-12. Sectional analysis for control volume 11-01: (a) number of particles distribution for diferent number of sections; (b) location of the volume 11-01; (c) total number of particles for different number of sections

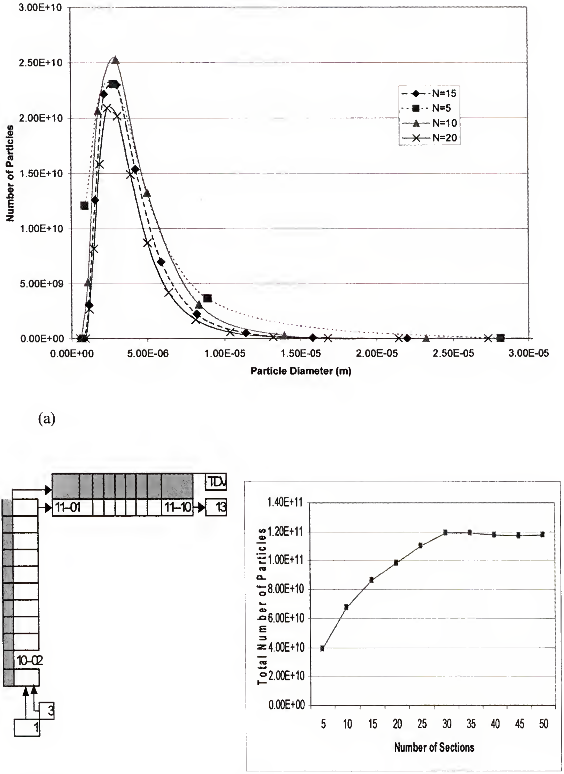

(a)

(b) (c)

Figure 4-13. Sectional analysis for control volume 11-10: (a) number of particles distribution for diferent number of sections; (b) location of the volume 11-10; (c) total number of particles for different number of sections

The above Figures show that, in general, the model is stable. The distribution of the number of particles, as a function of the size distribution, for the three volumes does not present any deviation from the expected behavior (a log-normal distribution). The volume 10-02 is the one that presents the major discrepancies. It can be seen in Figure 4-11 (a) that differences exist in the distribution for several numbers of the sections considered. The differences are in the mean diameter of the distributions, their correspondent number of particles, and the variance of these distributions. The difficulties in the stability are confirmed in Figure 4-11 (c), where the convergence of the total number of particles has some oscillation, but still presenting a convergent behavior. These discrepancies occur given the proximity of this volume to the release site, where the phenomena tend to occur intensely.

As long as the discussion moves to volumes farther from the release site, the number of particles distribution differences and the convergence of the total number of particles become more noticeable, as can be seen in Figures 4-12 and 4-13 (a) and (c). Figure (a) shows a very good agreement in terms of mean diameter and variance. Figure (c) shows that the convergence becomes smoother as long as the volume is located away from the release site.

The only unusual behavior is the fact that the total number of particles is lower when the calculation uses lower number of sections. The explanation for such behavior comes from the manner the mean diameter of each section is calculated. For lower number of sections, the mean diameter of the first section is higher. As the particles are released in the first section, lower number of section yields lower number of particles. Nevertheless, there are easy remedies for this flaw, such as change the mean diameters, fixing the first section size, or adopting a minimum of 30 sections, because after this number of sections, the differences in the first section becomes negligible, which is confirmed by the stability after this number of sections, as can be seen in the last plot (letter (c)) of Figures 4-11, 4-12, and 2-13.

Therefore, the model can be considered stable for the studied parameter. The calculated quantities near the release site have a more oscillatory nature, but did not diverge. As long as the analysis moves away from the release site, convergence is smoother and more rapid.

The stability of the model considering the spatial discretization is evaluated by comparing the result of the basic model (20 volumes) to the result of a re-nodalized model (40 volumes), in which the volumes of the basic volume are divided into two volumes. The comparison is performed by adding the masses of the two volumes in the re-nodalized model, and comparing it with the masses in the equivalent volume of the basic model.

Obviously differences are expected, but the results should be similar. Otherwise, significant differences mean that the accuracy of the model will be highly dependent on the discretization. The model must be consistent with the code general guides of spatial discretization, and is not desirable that the fission products-transport package requires a special nodalization. Besides the transiting masses, the error was calculated also for the deposited mass of the surface for the several species. This comparison showed not convenient for some sectional masses given the small values that they can reach, sometimes yielding an elevated relative error, but nevertheless an insignificant absolute error. This procedure was repeated for the three volumes (10-02,11-01,11-10), but only the results for the 11-10 volume are here presented, because the conclusions are similar. Figure 4-14 presents a comparison of the masses for this volume, at transient time 496.5 seconds, for silver, which is the predominant species. The graph is presented in a logarithmic scale, given the variation of the masses in orders of magnitude.

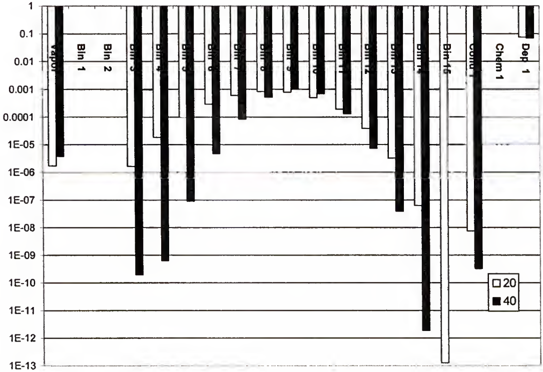

Figure 4-14. Comparison of silver mass distribution (Kg) for the 20 and 40 volumes models in volume 11-10 and 496.5 seconds transient time of the basic model (logarithmic scale)

One should be aware that Figure 4-14 is in a logarithmic scale. Consequently, the smaller columns represent larger masses. The first observation is that the differences, for the states where there are greater masses (vapor, deposited, and bins 8, 9 and 10 are reasonable, even though they can lead to a considerable difference in the overall estimation of deposited mass, which is the ultimate purpose of the model. The relative error of the deposited mass (deposited mass refers to mass deposited in the aerosol form) is of 7%. Regarding the other states, the relative error can be large, but their absolute values have no significant impact in the problem.

In order to better address the issue of the overall impact in the deposited mass of the re-nodalization, the overall deposited mass was compared for the re-nodalized and the basic model. For all the species, the re-nodalized model deposits (the addition of condensed, adsorbed, and aerosol plated masses) less mass. The differences range from 0.5 % for the least-deposited species (CsOH) to 5 % for the most-deposited (Ag).

The stability studies showed that the model is stable, in the sense that sectional discretization or spatial discretization is not capable of causing divergence of the solution. On the other hand, a flaw in the first section size setting was detected, and the problem showed sensitive to spatial discretization, indicating the necessity of further investigation, and elaboration of guidelines, in a similar procedure that resulted in the publication of the user's guide manual (42), which contains the accumulated experience of the users regarding discretization and settings. Similarly, a body of recommendations needs to be developed, created mainly from the comparison of the code's performance with known results.

Sensitivity studies

Sensitivity studies are done by varying the inlet thermal hydraulic conditions, as well as the fission products conditions (release rates and number of sections), from the basic model. The objectives of the performed studies are: (a) Determination of order of magnitude of the phenomenological time constants; (b) Determination of the better iterative method; (c) Determination of the impact of the model in terms of computer time; and (d) Determination of synergies of the aerosol deposition and agglomeration.

The thermal-hydraulic conditions calculated are the conditions used in the basic model, varying the inlet gas temperature, pressure and fluid velocity. The values used for these boundary conditions are presented in Table 4-8. A total of six different sets are used, combining different conditions.

Table 4-8. Flow inlet conditions for the sets used in the sensitivity studies

Set	P_{sys} (MPa)	T_{gas}(K)	V_{gas}(m/s)	Reynolds	Observation
1	0.2	1500	0.2	500	Number of sections varyied
2	0.2	1000	0.5	5,800	
3	0.2	600	0.8	78,000	
4	1.0	700	0.5	13,000	
5	0.2	600	0.05	1,200	
6	0.2	800	0.2	1,800	

The first study is performed to obtain typical numbers and the range of the reciprocal time constants of the several phenomena modeled in the fission products-transport package. Table 4-9 contains the range of this value and typical values. These data come from the observation of the coefficients for the several cases calculated, including the first verification and second verification. Typical values are chosen considering average thermal-hydraulic conditions in an accident and the mean diameter of the particle encountered in the Phebus-FP-01 experiment, presented in the next chapter. Table 4-9 is presented in a simplified version in Chapter 3. In Chapter 3, this information is used to consider the problem stiffness. The agglomeration and condensation processes depend on the number of particles. The considered range of the number of particles is from 10^6 to 10^{12} particles, obtained from the studied cases.

Table 4-9 ratifies some of the observations made about the behavior of the retention of fission products in the piping walls and the agglomeration process. The aerosol growth is dominated by condensation, when there is significant amount of aerosol, or when there are no walls for condensation. This observed feature is confirmed by the analysis of time constants, which shows that typical reciprocal time constants are significantly greater for condensation than agglomeration.

Table 4-9. Ranges and typical values of the reciprocal time-constants for fission-products transport phenomena

Phenomenon	Range (s^{-1})	Typical (s^{-1})
1. Adsorption	10^{-6}-10^{-1}	10^{-4}
2. Condensation on structural surfaces	10^{-1}-10^{-3}	10^{-1}
3. Condensation onto aerosol surface	10^{-5}-10^{3}	10^{-1}
4. Aerosol Deposition	10^{-6}-10^{0}	10^{-2}
5. Aerosol agglomeration	10^{-6}-10^{0}	10^{-3}

Vapor condensation onto structural surfaces is comparable with aerosol condensation for typically 10^{10} particles number concentration. Above that condensation onto aerosol will prevail. Adsorption is normally not an important process.

The comparison of the iterative methods is performed running the first verification model and the second verification basic model, for 15 sections for both methods (functional and Jacobian). The result is presented in Figure 4-15. This Figure shows that the functional iteration is considerably more rapid than the Jacobian. Noticing that the time-steps taken by the code are, for most of the computations, smaller than the small time-constant of the several phenomena, one can conclude that the convergence will be, most of the time, faster for the simpler method. This means that less iteration is needed for the convergence, benefiting the simpler method.

This figure shows that the fission products-transport package results in an increase in the CPU time of 16% for the first verification input deck, and 73% for the second verification input deck, for the functional iteration method using five species. Actually, the relative increase should be somewhere between these two values. The first verification input deck is a harsh severe accident. Because several calculations are simultaneously performed, the weight of the fission products package is small in this input deck. On the other hand, in the second verification, the major calculation is the fission products transport, and the weight of this package is larger.

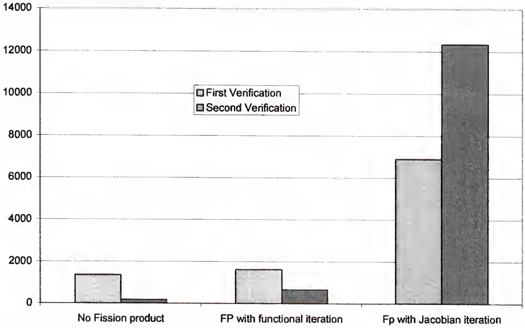

Figure 4-15. Comparative CPU times for different iterative methods with the case of no fission product for the input decks of the first and second verification, using a 1.2 GHz CPU, an 256 Mbytes of RAM.

The computer time variation with the number of sections is obtained varying the number of sections of the basic model of the second verification input deck. Figure 4-16 shows the evolution of the computer time as the number of sections is increased. The number of sections starts at five and is increased by increments of five.

The expression in Figure 4-16 (b) shows that the CPU time has a mild quadratic dependence on the number of sections, and a strong linear dependence. Considering that the computation time normally varies approximately with the square of the number of equations, the result is consistent with the fact that there are other, simultaneous computations under execution, which tends to deviate the dependence from the quadratic expected behavior. A calculation of 50 sections is approximately four times slower than a standard 20 sections calculation.

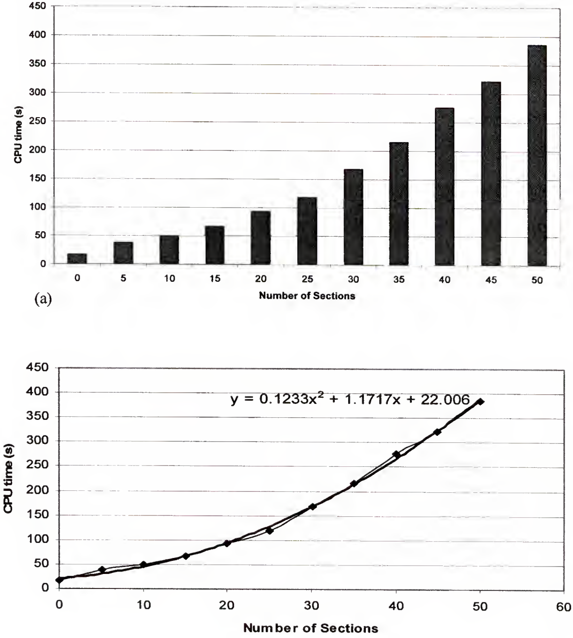

Figure 4-16. Variation of CPU time with the number of sections for second verification model: (a) bars representations; (b) best-fit expression for the variation

A comparison is also established of the basic model of second verification (20 volumes) with the re-nodalized model (40 volumes) for a 15-sections calculation. The result is presented in Figure 4-17. This Figure shows that the CPU time of the re-nodalized model is roughly two times the CPU time of the basic model.

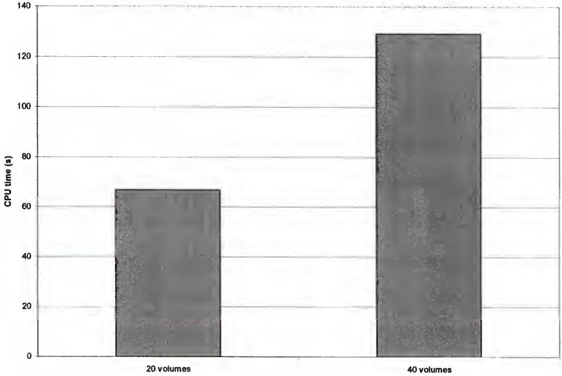

Figure 4-17. Comparison of the CPU time of the basic model (20 volumes) and the Re-nodalized model (40 volumes)

The last purpose of the sensitive studies is the identification of synergisms among the several aerosol phenomena for deposition and agglomeration. To perform this activity, the equations' coefficients are pulled out of the output and compared. A criterion for the synergism to occur is established: the phenomenon must be in the order of at least one percent of the total coefficient. Three volumes of six sets of different thermal-hydraulic conditions are analyzed, in a total of 18 analyzed cases.

The result is presented in the form of phenomenological maps. The maps are presented for horizontal and vertical tubes for deposition (gravitational settling plays a major role in the horizontal case), and turbulent and laminar conditions for both deposition and agglomeration. These maps contain the predominant phenomena for each particle size, according to the geometric and thermal-hydraulic conditions. In the x- and y-axes, the spectrum of particle sizes is divided into 15 sections, according to the calculation performed with 15 sections. These diameters are presented in microns.

The maps for the agglomeration process, for the laminar and turbulent cases, are given first, as presented in Figure 4-18. The result for the turbulent condition is presented for a low-turbulent Reynolds number (about 5000), and high-turbulent Reynolds number (about 80,000) to observe the differences in the influence of the turbulent agglomeration as the Reynolds number increases.

Figure 4-18 (a) shows, for the laminar flow condition, given interactions of particles up to 3.05 μm with all the spectrum of particle sizes, that diffusive and gravitational agglomerations kernels are comparable. For the diagonal interactions, diffusive agglomeration prevails, as a result of the fact that gravitational is zero for this case. For interactions between large particles, the gravitational agglomeration alone prevails.

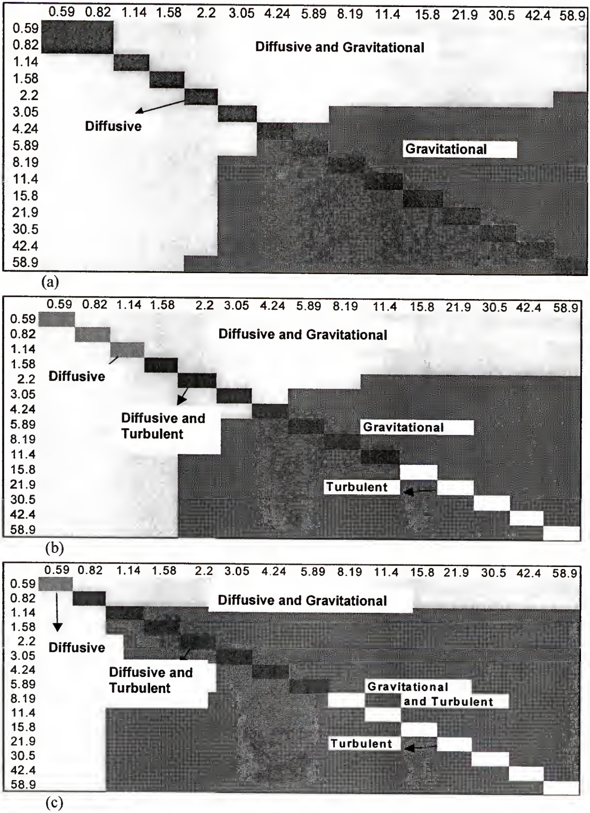

Figure 4-18. Agglomeration phenomenological maps: (a) laminar; (b) turbulent (Re=5869); (c) turbulent (Re=79,550)

Regarding the turbulent flow conditions, for a low Reynolds number, the scenario is not much different from the laminar flow conditions. The differences appear in the diagonal interactions where the prevailing interaction starts with the diffusive, goes into a region where diffusive and turbulent are comparable (particles between 1.58 and 15.8 μm) , and finally arrives in a region where turbulent agglomeration alone prevails, for particles larger than 15.8 μm.

For highly turbulent conditions, the turbulent agglomeration grows in importance, as Figure 4-18 (b) shows for interacting particles larger than 4.24 μm, where gravitational and turbulent exist. In addition, the diagonal interactions for the regions mentioned above are altered, concerning their beginning and ending particle sizes. The influence of the turbulent agglomeration is felt earlier, as long as the Reynolds number increases.

Considering that the great majority of the particles have less than 4 μm of diameter (data from in-pile experiments), the more important synergy to be considered is Brownian diffusion and gravitational settling. The gravitational and turbulent synergy can be thought to be important also, from Figure 4-18 (c). Nevertheless, this is important only for very high Reynolds numbers. Therefore, an optimized agglomeration synergetic model preferably would include a synergetic model for Brownian diffusion and agglomeration model.

Figure 4-19 presents the phenomenological maps for the deposition process. For the deposition process, as mentioned before, the aspects of surface angle and flow conditions were considered. A considerable variation in the phenomenological maps is found for the turbulent conditions for crescent Reynolds numbers.

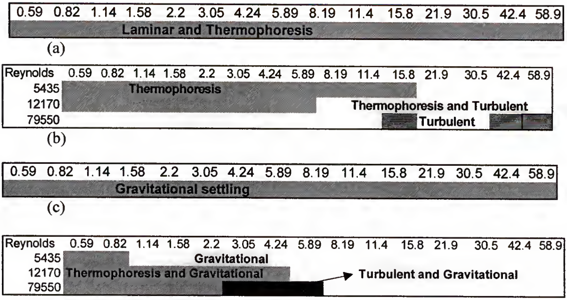

(a)

(b)

(c)

(d)

Figure 4-19. Deposition phenomenological maps: (a) vertical and laminar conditions; (b) vertical and turbulent conditions; (c) horizontal and laminar conditions; (d) horizontal and turbulent conditions

For laminar conditions, in the vertical pipe, the laminar and thermophoretic deposition velocities are comparable, whereas for the horizontal tube, gravitational settling prevails. These conclusions are drawn based on Figures 4-19 (a) and (c). Concerning the turbulent condition, for vertical pipes, thermophoresis prevails for small particles, and then thermophoresis and turbulent prevail. The transition particle diameter gradually decreases as the Reynolds number increases. In the limiting cases of high Reynolds numbers, the only thermophoresis region vanishes, and the thermophoresis-turbulent region prevails up to a certain size, when turbulent alone is dominant, as shown in Figure 4-19 (b). For horizontal pipes, thermophoresis and gravitational prevail for small particles, and gravitational prevails after a certain diameter. The transition diameter shifts increasingly, as the Reynolds number increases. For high Reynolds numbers, a region of turbulent and gravitational exists between the two regions.

Both the agglomeration and deposition processes have some regions where synergy actually exists. Hence, a synergetic model can somehow increase the accuracy of the code's predictions. In order to have an optimized synergetic model, the fact that the predominant number of particles observed, for typical in-pile experiments, is below 5 μm, can be used. Restrictions on the maximum Reynolds number, based on observations of these numbers from a typical severe accident, can also be used to simplify and to optimize the model.

Parameters other than the Reynolds number, such as gas temperature and flow velocity, are capable of altering the boundaries of the regions for both agglomeration and deposition (but more intensely for deposition). However, the derivation of expressions for these boundaries is very complex and laborious. A synergetic model that can be applied to the entire range of particles is, therefore, more convenient, instead of a selective model, according to the particle's size.

Using the principles delineated in the last two paragraphs above, aspects of the synergetic relations are presented here, and the development of an optimized model for those synergisms is presented in Appendix B. In the next chapter, an evaluation of the gains in the use of such a model is presented.

The inertial form of deposition was verified in this last verification not to be an important deposition mechanism for particles less than 20 μm. Since the typical particle diameter in the primary cooling system is in the order of 1.5 μm, there is no need to make advanced study of this mechanism, since it does not significantly impact in the deposition.

During this chapter, the implementation of the fission products-transport module in Scdap/Relap5 was described, and it was proven that it is consistent with the Scdap/Relap programming philosophy and recommendations. The module is composed of 40 sub-routines. Five of them are related to the reading, checking and management of the calculation. The calculation is divided into three major activities, managed by three routines, the convection of the fission products, the calculation of the coefficients of the ODE system, and the solution of the ODE system. The calculation of the coefficients uses 13 sub-routines, and the solution of the ODE system takes 11 sub-routines. Additionally, there are 3 debugging routines, and 5 routines to work indexes.

The model was verified, regarding the operation of the math solver, the possibility of affecting other code modules, and stability of the calculations for different spatial and aerosol size discretizations. The math solver proved to be working properly. In the performed test, there was no impact of the transport calculation in other modules. The model showed to be consistent for more than 30 sections.

Sensitivity studies were performed to provide some insight about the most important deposition mechanisms, and possible aerosol synergisms. Condensation onto structural surfaces is considerably more rapid than adsorption reactions. The inertial aerosol deposition mechanism showed to be not important. The most important synergism for the agglomeration process is the diffusive-gravitational agglomeration, and for the deposition, synergy exists, for horizontal pipes between gravitational settling and thermophoresis for small Reynolds, and between turbulent and gravitational settling, for higher Reynolds.

CHAPTER 5
PRELIMINARY ASSESSMENT

This chapter presents the description of a preliminary assessment of the code's performance. A preliminary assessment comprises a first evaluation of the code's capability to predict the attenuation of fission products release to the containment by the primary-circuit piping, and the aerosol characterization. Given the body of assumptions made and the simplifications performed in the development, the performance evaluation is not the main purpose of the assessment, but rather the identification of possible programming errors and weaknesses of the model. This chapter begins with the survey of the experimental programs performed that could be used to adjust and validate the model, as well as consolidate a body of guidelines for the model's usage. Then, one is selected, modeled and assessed. The chosen experiment is described and modeled, and its results compared with the experimental data.

Adjustment and Validation Matrix

The overall strategy in studying the fission products-behavior in primary circuits, delineated after a TMI accident, was to address separate effects and simultaneous effects both theoretically and experimentally, as pointed out earlier. From the point of view of the developed model, it is of interest that the experiments that have simultaneity of effects, and, preferably, severe accident thermal-hydraulic conditions and fission products species. Experiments considering simultaneity of effects are the Markiven Test, the Aerosol Containment Experiment (LACE), the Aerosol Transport Test (ATT), the Power Burst Facility (PBF), the Loss of Fluid Test (LOFT) and the Phebus experiment. In the following paragraphs, these experiments are briefly described and summarized in Table 5-1.

The Makiven-V Aerosol Transport tests were conducted between 1983 and 1985 to study the transport and attenuation of aerosols and volatile fission products and aerosols through a large-scale reactor system with steam atmosphere. The fission products vapors consisted of cesium iodide and cesium hydroxide, and the aerosols consisted of silver and magnese oxide.

The test facility consisted of an aerosol generation system, reactor vessel with simulated LWR internals, pressurizer, relief tank and filter. Five main tests of increasing complexity were conducted. Although a number of problems were experienced with these tests, notably in meeting the aerosol input specification and closing the mass balance, this program represents a valuable source of data on aerosol transport for code assessment. Moreover, the experimental results of these experiments are not available in the open literature.

The LACE program was established to study aerosol behavior in the containment and pipework of a LWR under severe accident conditions. The experiments were conducted between 1985 and 1987. Although the main interest was in aerosol behavior within the containment, two tests focused on containment by-pass sequences. These tests involved passing a simulant aerosol mixture (soluble cesium hydroxide and insoluble magnese oxide) along a complex test pipe of 63 mm in diameter and 27 m long with five 90-degree bends, four horizontal sections, and two vertical sections.

The inconveniences of the test are, first, its primary focus is the containment behavior, and second, the gas velocities are in the order of 100 m/s. Under these velocities, the assumed Stokesian flow is not true for a considerable fraction of the particle spectrum. Hence, most of the aerosol models used can have their validity questioned.

A series of experiments was performed at Oak Ridge National Laboratory between 1985 and 1987 to provide data to validate aerosol models within the TRAPMELT code. Aerosol transport tests were set to investigate aerosol wall plated-out in a vertical pipe geometry, simulating conditions in the upper plenum of the reactor vessel. The range of phenomena covered by these experiments is limited, given the orientation and length of the tube.

In-pile tests conducted at INEEL in the 1980s contributed to the understanding of fission products-release and -transport behavior. The programs were the Severe Fuel Damage experiments 1.1 and 1.4 conducted at the Power Burst Facility and the two fission product experiments (LP-FP-1 and 2) conducted as part of the Organization for Economical Cooperation and Development (OECD) Loss-of-Fluid Tests (LOFT) program.

These tests focused primarily on the understanding of the fuel and primary-circuit thermal-hydraulic behavior under accident conditions. The fission products studies were a secondary purpose, and, consequently, had a limited set of instrumentation to investigate fission products phenomena.

The most significant experimental program in the fission products behavior field is the Phebus program. This program was initiated in 1988 and is under conduction. The primary purpose is to understand fission products behavior in the primary circuit and containment under severe accidents, as well as investigate severe accident phenomena.

The program is being executed in Cadarache, France, and takes advantage of the knowledge of fission products behavior progressively acquired after the 1980s. The high level of investment and the use of a scale reactor resulted in a very elaborated experiment, yielding extensive experimental data and important conclusions.

Because of the degree of elaboration, the fact that they are in-pile, and the carefulness of its conduction, the Phebus experiments are ideal for assessing the transport model. The only inconvenience is that, since the chemistry and release were not considered in the development, a procedure needs to be set to overcome this limitation of the model. Moreover, the Phebus experiment is a typical experiment to test a fission product-thermal hydraulic coupled code, such as Scdap/Relap. Therefore, the Phebus FPT-01 experiment is chosen to be modeled. In the following sections, this experiment and the procedure to overcome the limitation of the model are described.

Table 5-1. Fission-products integral effects experiments

Experiment	Type	Purpose	Observation
Markiven (Sweden) 1985-1987	Out-of-pile	Investigate Vapor/ aerosol interactions in primary circuit/containment	CsI/CsOH/Te vapor Ag_2O, MnO aerosol Reliability of the data
LACE (ORNL) 1985-1987	Out-of-pile	Investigate aerosol interactions in containment	$Al(OH)_3$, CsOH aerosol in steam
SFD,LOFT 1983-1985	In-pile	Investigate severe accident phenomena	Limited fission product data
Phebus 1988-2003	In-pile	Investigate Vapor/ aerosol interactions in primary circuit/containment	Well designed, instrumented and analyzed

Phebus Experimental Program

The PHEBUS FP program is a Light Water Reactor (LWR) source term research program, undertaken by the "Institut de Protection et de Sûreté Nucléaire" (IPSN) of the "Commissariat à l'Energie Atomique" (CEA) and the Joint Research Centre (JRC) of the

Commission of theEuropean Communities (CEC) in collaboration with the United States, Canada, Japan, Korea and Switzerland.

The aim of the experimental program is to study the release, transport and behavior of fission products , structure and control rod materials, from the core of a LWR under severe accident conditions, in a scaled reactor circuit and containment building, in order to verify the validity of, or to improve, the analytical models developed on the basis of separate effects test results. The reduced volumetric scale factor compared to a Pressurized Water Reactor (PWR) 900 MW is approximately 1/5000. A further important objective is the study of core degradation phenomena, especially during the late phase of the process.

The program consists of six integral in-pile tests, varying the type of fuel (fresh, irradiated or debris), the thermal-hydraulic conditions, and the physical-chemical environment of the fuel, as well as the configuration of the experimental circuit components and the thermal-hydraulic conditions in the containment.

The first two tests were carried out in order to study the release of fission products and their subsequent transport and deposition in the primary circuit and in the containment of a Pressurized Water Reactor (PWR) under low-pressure oxidizing or "steam-rich" conditions. The first test (FPT0) was performed in December 1993 using a test bundle of fresh fuel rods. The second test (FPT1) was conducted in July 1996 under similar experimental conditions but using irradiated fuel.

In this research, the Phebus FPT-01 experiment is presented because there is extensive availability of data, once it is being used in the International Standard Problem

(ISP-46). In the subsequent sections are presented the Phebus test facility, the test conduction, and the important lessons learned from the Phebus series of experiments.

Phebus Test Facility

The Phebus experimental facility is briefly described in this Section. The facility mainly consists of: (1) a driver core and its cooling circuit, (2) a pressurized water loop (PWL), (3) a bundle of fuel rods, (4) an injection loop, (5) an experimental fission product (FP) circuit including a horizontal line and a steam generator, and (6) a containment vessel. Figures 5-1 present a simplified diagram of the Phebus fission products circuits.

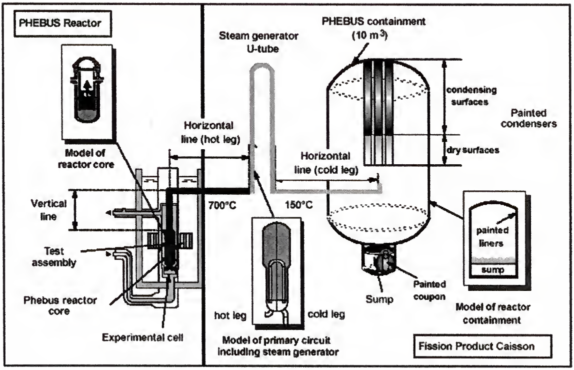

Figure 5-1. Phebus experimental facility (48)

Geometry and material

The Phebus driver core includes PWR type fuel rods of 800 mm fissile length. The core is cooled by a forced water flow at atmospheric pressure and at room temperature.

The maximum nuclear power of the reactor is 40 MW, but limited to 23 MW for the Phebus program. The pressurized water loop crosses the reactor through a cavity made in the central part of the driver core. A schematic of the fission products driver core is shown in Figure 5-2.

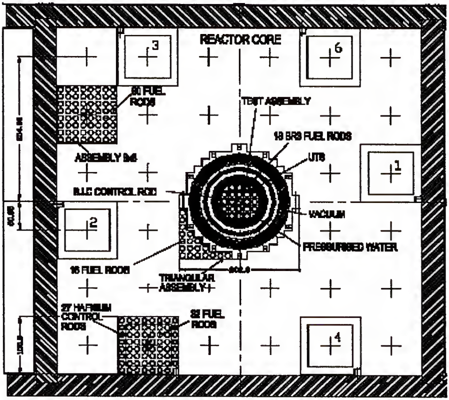

Figure 5-2. Driver core of Phebus Test Facility (48)

The pressurized water loop (Figure 5-3) is an independent pressurized cooling circuit (2.5 MPa, 165°C) containing the test train. The test bundle is housed in the in-pile part of the PWL. The PWL mainly acts as a cooling circuit for the test section. During the irradiation period of the experiment a fraction of the water flow is bypassed inside the test bundle (entering at the bottom of the test train through a valve) so as to cool the fuel rods. For the transient phase of the test, the valve is closed in order to dry the fuel rods and to fill the bundle with steam using the injection circuit. From the point of view of this research, the PWL is not important. For this reason, it is not here shown.

The injection loop (seen in Figure 5-1) allows the reproduction of the thermal-hydraulic conditions for the experimental period of the test by supplying steam flow (or gas such as helium, argon or hydrogen) to the bundle. The injected water is heated on its way through the test train by the PWL (165°C). At the bundle inlet, the steam temperature is 165°C at 0.2 MPa.

The conditions of the postulated severe accident are applied to a bundle of representative PWR fuel rods contained inside the test train. The heat-up of the fuel bundle is obtained by fission reactions produced by the neutronic flux generated in the driver core. Meanwhile, the steam flow rate at the bundle inlet is adjusted to the prescribed values. The fuel bundle is surrounded by a thoria layer, a ceramic low porosity ZrO_2 layer, and an outer dense zirconia coating on the Inconel pressure tube. Heated metallic sleeves are added above the fuel bundle region in order to maintain outlet gas temperatures at about 700°C (973 K).

The FPT1 test bundle contains 18 fuel rods (UO_2) previously irradiated in the Belgian BR3 reactor, where they attained a rod average burn-up of ~23.4 GWd/tU. Two fresh-instrumented fuel rods were also introduced into the bundle as well as an Ag, In, Cd (AIC) absorber control rod (containing 80 wt.% silver, 15 wt.% indium and 5 wt.% cadmium).

The irradiated fuel rods consist of a stack of fuel pellets housed in a zircaloy (Zry) cladding. The enriched UO_2 column is 1 m in length and the cladding is closed at the top by a Zry welded plug. The lower end of the irradiated fuel rods is composed of a blanket of 3 UO_2 pellets (36 mm length). The instrumented rods are slightly shorter, without the blanket of UO_2 pellets in the lower part.

The AIC control rod is composed of a stainless steel cladding housed in a zircaloy guide-tube. The spacing between the fuel rods and the control rod in the test assembly is maintained by two zircaloy spacer-grids 43 mm in height located at the 240 and 760 mm elevations. The zircaloy grids also include small inconel springs in contact with the external surface of the fuel rods. In addition, the test bundle contains four zircaloy stiffeners (U tube), located close to the inner surface of the shroud, designed to strengthen the structure of the rod assembly.

The fuel rod bundle is housed in an insulating shroud to limit the radial heat losses. The shroud is composed of a 2.5 mm thick thoria inner layer, an 8 mm thick insulated region of porous zirconia (20YSZ) and a 6 mm thick inconel-625 pressure tube, flame-spray coated with a 2 mm thick high-density zirconia (8YSZ) layer on its inner surface. There are two 0.5 mm gaps inside the shroud at room temperature; the first one is located between the thoria and the zirconia sleeves (inner gap), the second one between the porous zirconia insulator and the ZrO_2 spray coating of the pressure tube (outer gap).

Table 5-2 contains the more important geometrical parameters for the bundle, whereas Figure 5-3 contains the radial cross-sections of the test bundle, and Figure5-4 contains the axial cross-section of the test bundle.

Table 5-2. Fuel bundle geometrical parameters (48)

Irradiated Fuel	number of rods : 18 fuel material : UO_2	
	Initial values	After pre-irradiation in BR3 reactor
	pellet enrichment (U^{235}) : ~6.85 % porosity : ~5.67 % fuel pellet OD : 8.04 mm length of the fissile zone : 1000 mm cladding material : Zry-4 cladding ID : 8.24 mm cladding OD : 9.489 mm type of filling gas : He Volume Upper/Lower plenum : 2331/0 mm^3 Pressure of filling gas : 2.36 MPa at R.T.	pellet enrichment (U^{235}) : ~3.75 % porosity : ~3.1 % mean burn-up : 23.4 GWd/tU fuel pellet OD : 8.11 mm cladding material : Zry-4 cladding ID : 8.208 mm cladding OD : 9.484 mm
Fresh Fuel	number of rods : 2 fuel material : UO_2 pellet enrichment (U^{235}) : ~3.5 % porosity : 4.18 % cladding material : Zry-4 fuel pellet OD : 8.19 mm cladding ID : 8.3575 mm cladding OD : 9.4975 mm type of filling : He Pressure of filling gas : 2.4 MPa at R.T.	
Control Rod	number of rod : 1 absorber material : 80 wt.% silver, 15 wt.% indium, 5 wt.% cadmium cladding material : steel (304L) guide-tube material : Zry-4 Ag-In-Cd length : 1000 mm (+plugs) absorber OD : 8.66 mm cladding ID : 8.75 mm cladding OD : 9.70 mm cladding material : stainless steel (304L) guide-tube ID : 11.3 mm guide-tube OD : 12.1 mm guide tube material : Zry-4 type of filling : Air Pressure of filling gas : 0.15 MPa at R.T.	
Shroud	thoria sleeve ID : 73 mm thoria sleeve OD : 78 mm zirconia sleeve ID : 79 mm zirconia sleeve OD : 95 mm spray coating of dense zirconia ID : 96 mm pressure tube ID : 100 mm pressure tube OD : 112 mm	

The gases and aerosols released from the fuel bundle during the degradation phase are conveyed through experimental lines up to the Phebus containment (see Figure 5-1). The experimental lines are composed successively of: (a) A vertical line directly above the test bundle, leading to a horizontal line (seen in Figure 5-4); (b) A horizontal pipe, simulating conditions in the hot leg of a PWR primary circuit; (c) a U tube simulating a PWR steam generator; (d) A horizontal line, simulating conditions in the cold leg of a PWR primary circuit, leading to the containment.

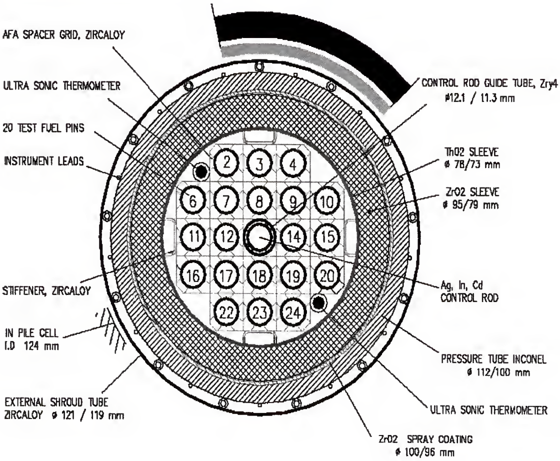

Figure 5-3. Radial Cross Section of the test bundle (48)

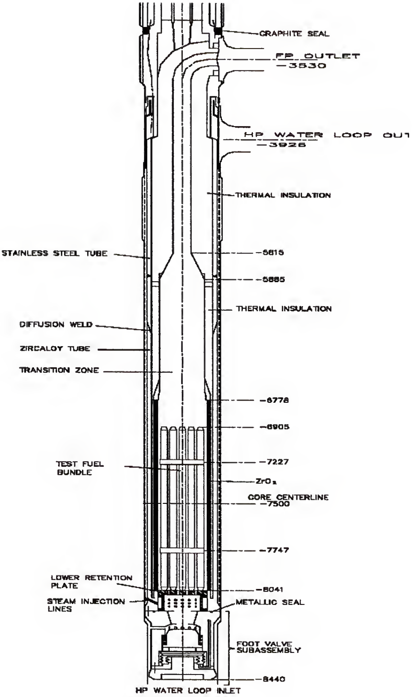

Figure 5-4. Axial cross-section of the test bundle (48)

The vertical line is composed of the upper plenum and the riser. The bottom (0.2 m length) of the upper plenum is unheated and the remainder of the vertical line is regulated to a temperature of 700°C. In FPT1, a section of the liner in the temperature-controlled part of the vertical line was made of stainless steel, allowing the differences in deposition on this material and on inconel, which was used elsewhere in the circuit to be studied. The horizontal line simulating conditions in the hot leg is made of inconel-600 and its temperature is regulated to 700°C. The steam generator U-tube is made of inconel-600, its downward walls were maintained at 150°C during the test, i.e., above the conditions for steam saturation for the considered pressure. The outlet of the U tube and the horizontal line, simulating conditions in the cold leg, are made of stainless-steel (AISI 304L) and are maintained at 150°C. The diameters and lengths of the experimental circuit lines, as well as materials of which they are made, are presented in Table 5-3.

Table 5-3. Geometrical characteristics of the experimental circuit

	Hydraulic Diameter (m)	Length (m)	Material
Vertical liner	0.07	0.249	Inconel 600
	0.048	1.6055	
	0.03	1.44	
Hot leg	0.029	5.273	Inconel 600
	0.03	3.875	
Steam Generator	0.02	4.2775	Inconel 600
	0.02	2.3	
	0.02	3.64	
Cold Leg	0.03	3.438	Stainless Steel

Instrumentation

The instrumentation used in the experimental program is divided into nuclear instrumentation, thermal-hydraulic instrumentation, and fission products instrumentation. The nuclear instrumentation is used to obtain the neutron flux in the test train, and, consequently, the power. The thermal-hydraulic instrumentation is used in the core and circuits measuring thermal-hydraulic parameters. These parameters measurement devices are thermocouples, flow meters and manometers. The fission products instrumentation is used to measure fission products-related parameters, such as aerosol size, composition and mass retained. They are better described later. In the following sections, this instrumentation is detailed, considering the level of knowledge necessary to perform the tasks of this chapter, which are the modeling of the experiment and the understanding of its operation. This section is limited to the instrumentation of the bundle, injection circuit, and primary circuit; that is, the containment is excluded because it is not of the interest of this research.

Nuclear instrumentation

The total nuclear power generated in the fuel assembly is deduced from the core power measurement (ionization chambers calibrated by thermal balance) divided by the coupling factor. The coupling factor is the ratio between the nuclear power of the driver core and the nuclear power actually produced in the test bundle.

Four U_{235} fission chambers were installed outside the test train but close to the pressure tube surface, to detect movements of the fuel or the control rod material (or both). The fission chambers were 60 mm long, and had 0.225 mg of U_{235}. They were located at the elevations of 400, 600, 700 and 800 mm. These elevations are measured from the bottom of the fissile column (BFC).

Thermal-hydraulic instrumentation

Thermal-hydraulic instrumentation can be divided into core and circuit instruments. In the core region, the temperature is the parameter measured, whereas other quantities, such as pressure and flow rates, are measured outside the core region.

The two fresh fuel rods, the control rod, the stiffeners, and the shroud were equipped with different types of thermocouples (TCs) at various elevations and radial positions to control the thermal behavior of the test bundle during the experiment.

The fresh fuel rods were instrumented with six W-Re thermocouples located inside the fuel and outside the Zry cladding. The control rod was equipped with four W-Re thermocouples located at the outer surface of the guide tube and two Cr/Al thermocouples positioned in the absorber material (AIC). Three temperature measurements were also located on the stiffeners (W-Re TCs). The shroud is instrumented with 29 thermocouples located inside (five Pt/Pt Rh plus 11 Cr/Al at D = 90 mm) and outside (11 Cr/Al at D = 95 mm) the porous zirconia layer.

The W-Re thermocouples are made with a hafnia insulator (HfO_2) and rhenium sheaths, coated by a layer of rhenium silicide (TC Re/Si_2) or iridium (TC Re/Ir). The Pt/Pt Rh thermocouples are insulated with alumina (Al_2O_3) and the sheath is made of Pt/Pt Rh (S-type). The Cr/Al thermocouples (K type) use alumina insulator and stainless steel sheaths.

A melt-through detector was specially designed to identify local hot spots in the shroud. This detector uses two thermocouples at the bottom of the shroud and two additional, insulated wires of the thermocouple. The wires are wrapped around the outer surface of the porous zirconia insulator over an axial zone spanned between 0 and 0.36 m elevations. Rupture of the wires could be interpreted as the result of fuel accumulation and localized melt progression inside the shroud.

Two Ultrasonic Thermometer Sensors (UTS) were introduced into the fluid channel for high-temperature measurements. The ultrasonic thermometry technique exploits the temperature dependence of the speed of sound in a thin wire sensor. Short acoustic pulses are injected into the sensor. Each sensor contains eight discontinuities (radial grooves) producing echoes. The time interval between partial echoes from these discontinuities can be converted to an "average" temperature over the corresponding section after a preceding calibration in an environment with a known temperature profile. Figure 5-5 presents the radial and axial position of the thermocouples in the bundle. In this figure the K type thermocouple is represented by a TC symbol, whereas the Re-W thermocouple is represented by a TCW symbol.

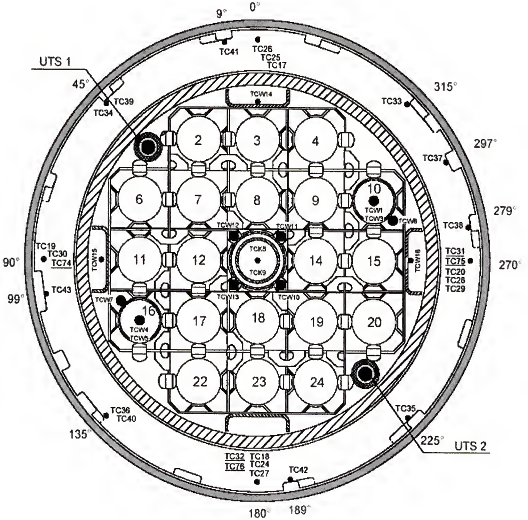

(a)

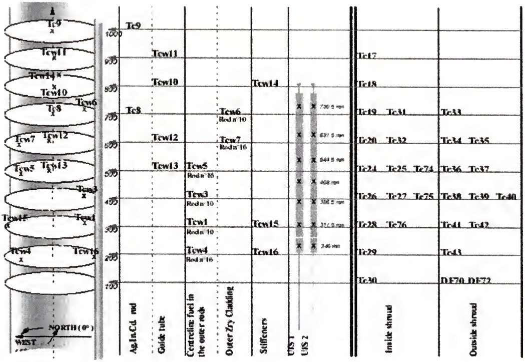

(b)

Figure 5-5. Location of thermocouples in the bundle: (a) radial; (b) axial (48)

Liquid water at room temperature and 0.2 MPa is introduced by the injection circuit into a steam generator located in the bottom part of the test bundle. This steam generator is heated by the pressurized water circuit at 165°C (438 K). The steam pressure of the bundle is controlled by regulating the temperature of the containment tank. The steam mass flow rate is measured by weighing the mass of the feed water tank. The steam flow rate injected in the test bundle is then deduced by the decrease of the water mass in the tank over time (the tank and steam generator are not shown here because they do not make part of the model).

Several pressure transducers are located on the steam outlet circuit and in the containment. A differential pressure transducer (Voituriez type), measuring the difference of the pressure between the inlet (at the level of 108 mm from BFC) and the outlet (1252 mm from BFC) was used to detect a possible blockage of the fluid through the bundle.

Other on-line data measurements concern the monitoring of thermal-hydraulic parameters exist in the circuit. These include, at different locations in the circuit, K-type thermocouples measuring both fluid and wall temperatures together with pressure sensors. The concentrations of hydrogen and oxygen were measured at the circuit's cold leg during the test transient.

After the test, the fuel bundle was transferred to the PEC facility ("Poste d'Examen et de Contrôle") in order to perform non-destructive post-test examinations: (1) axial γ-scanning, (2) numerical radiographs, (3) transmission tomograms, and, for the first time in the Phebus FP program, (4) emission tomograms. Combination of the results gained in these examinations gave a very good overview of the radial and axial degradation state of the bundle after the transient as well as the axial and radial position of the various fission products that remained in the melt or in the fuel rods. In association with image analysis, the tomograms also provided a quantitative estimate of the mass of relocated material. After the non-destructive examinations, the bundle was enclosed in epoxy resin to keep the degradation state of the bundle intact during the subsequent handling and transportation. The bundle was sent to the Institute for Transuranium Elements (ITU), Karlsruhe,Germany, for sectioning in hot cells.

The test assembly was sawed for further examinations: macrographs using an optical microscope, γ-scanning, metallographs, electronic micro-probe analysis (EPMA), X-ray diffraction, X-ray imaging, and measurement of the melting temperature of the corium. Samples were also transported to PSI (the Paul Scherrer Institute, Villigen, Switzerland) for additional examinations (ceramography and EPMA).

Described below are the test instrumentation, the post-test analyses, and the objectives of the various measurements devoted to the determination of the fission products behavior in the circuit.

Many data measurement devices were operated during the test. They include on-line γ-spectrometers, which were installed at specific locations in the circuit, as well as instruments devoted to monitoring thermal-hydraulic conditions and aerosol behavior in the circuit.

Two on-line γ-spectrometers were collimated on the hot leg of the horizontal line (700°C) and one on the cold leg of the horizontal line (150°C) to follow the γ-emitter activity at these locations. An additional γ-spectrometer station was devoted to the same kind of measurement in the steam generator tube. This station was placed on a lift-system, designed to scan both the cold and the hot legs of the steam generator tube at different elevations (six positions for the cold leg and seven positions for the hot). The objectives of these measurements were to follow on-line the release of γ-emitters from the fuel bundle and their transport through the circuit during degradation, and to determine the amounts deposited in the circuit at the end of the test transient to help establish the mass balance at the end of the test.

Specific devices are devoted to the on-line determination of aerosol concentration in the circuit hot leg :on-line aerosol monitor(OLAM). This apparatus is a photometer that measures the light extinction produced by the aerosols (the higher the aerosol concentration, the greater the light extinction).

In the test, sampling of released material was performed by instrumentation placed in furnaces at specific points on the experimental line at 700°C (point C) and at 150°C (point G). All sampling instruments and sections of the main circuit were recovered by remote handling as soon as the experimental installation was back to atmospheric pressure and room temperature. They were transferred to a special device, named the CECILE hot cell, where several measurements were performed. In the CECILE hot cell, the first inspections and γ-scans were carried out. Then, disassembly, weighing, and quantitative γ-spectrometry of all samples were performed in the CECILE cell. The cell was also used for temporary storage. At this level, a selection of samples to be dispatched to other laboratories for post-test analyses was performed.

Aerosols in the circuit were collected on impactors and filters. The objective of these samples was to contribute to the determination of the aerosol mass, inlet flow and size during the test transient in the circuit. Gas capsules located downstream of filters and impactors were used to collect gas in the cold leg of the circuit at point G. The main objective of these samples was to collect gaseous iodine fractions that were still present in the cold leg of the circuit. Thermal gradient tubes were used in the hot leg of the circuit at point C to determine the condensation temperatures of vapor species to gain insight on chemical speciation in the circuit's hot leg.

Combined with on-line γ-spectrometry data and post-test γ-counting of parts of the circuits, CECILE data analysis of sequential samples provided a mass balance for the main γ-emitters (Ru_{103}, Ag_{110m}, Sb_{125}, Te_{129m}/Te_{132}, I_{131}, Cs_{134}, Cs_{136}, Cs_{137}, $Ba_{140}(La_{140})$) in the circuit.

After the test, the evaluation of the amount of fission products and activation products still present in the fuel region or deposited in the vertical channel was obtained by quantitative γ-spectrometry of the test. These measurements concerned the isotopes

Zr_{95}-Nb_{95}, Mo_{99}, Ru_{103}, Ag_{110m}, Te_{129m}/Te_{132}, I_{131}, Cs_{136}, Cs_{137}, and Ba_{140}(La_{140}). The results were used to establish the circuit mass balance for γ-emitters at the end of the test. This evaluation was performed in the PEC facility.

The steam generator U-tube was cut into several sections. Each section was transferred to the CECILE hot cell for γ-counting. Deposition profiles of the main γ-emitters (Ru_{103}, Ag_{110m}, Sb_{125},Te_{129m}, I_{131}, Cs_{134}, Cs_{136}, Cs_{137}, Ba_{140}(La_{140})) in the hot leg and the cold leg of the steam generator could be established. The results were used to gain insight into the γ-emitter deposition mechanisms (thermophoretic aerosol deposition or vapor species condensation) and to determine the circuit's mass balance at the end of the test.

Some of the experimental circuit parts were further examined by post-test analyses (analyses of non γ-emitters). Many Phebus program partners' laboratories were involved in the FPT1 Post Test Analysis (PTA) campaign which lasted from early 1997 until the end of 1999: ITU (Karlsruhe), COGEMA (Marcoule), CEA/Cadarache, CEA/Grenoble, CEA/Saclay, AEAT (Winfrith), and Siemens/KWU. The main objectives of the PTA were to: (a) Establish a mass balance for the different elements collected on sequential samplings (first priority); (b) Determine the chemical species of the collected material; and (c) Gather information about the aerosol size, morphology, composition and species distribution as a function of depth in the aerosol particle.

Many elements of interest were not measurable at all or measurable accurately by γ-spectrometry methods. These elements include fission products (Sr, Y, Rb, Tc, Nb, Eu, Ce, Pr), and material from the fuel bundle (U, Pu, Am, Cm), the control rod (Ag, In, Cd), the structures (Zr,Sn, Fe, Ni, Cr), and the instrumentation (Re, W). These elements represented most of the aerosol mass. Mass determination on the samples required the use of quantitative analyses. Besides the γ-spectrometry measurements performed by the laboratories on receipt of the samples, masses were determined via destructive analyses using ICPAES/ICPOES or ICPMS (inductively coupled plasma atomic emission spectroscopy/optical emission spectroscopy or mass spectrometry).

These analyses are destructive in the sense that samples have to be treated in order to be analyzed. The treatment usually involves dissolution of material in solutions of increasing acidic and/or basic strength (starting from water solutions to HNO_3 or NaOH solutions and going to strong acid-mix HNO_3 + HF solutions). The treatment may also involve chemical separation methods, which are essential in some cases for getting accurate data on specific elements (for instance, β-emitters and iodine determination by, respectively, β and γ–spectrometry).

Information on the chemical species present in solid samples can be obtained directly either by X-ray diffraction (XRD) or by X-ray photoelectron spectroscopy (XPS); the latter method provides data on the oxidation state of the measured elements. Indirect information may be obtained by examining the solubilities in water and in acid solutions of the various elements or by interpreting re-volatilization test results (measurements of equilibrium vapor pressures and effusion rates of elements revaporized in Knudsen cells) performed on FPT1 deposited samples (vertical line and steam generator deposits).

Direct and indirect information on the aerosol characteristics (size, morphology and composition) may be obtained by scanning electron microscopy (SEM) examinations of the sample. The SEM technique may be used in various modes: optical microscopy (observation of μm-sized particles); energy dispersive analysis, EDS or EDX (semi-quantitative determination of particle elemental composition); particle recognition and characterization, PRC (particle size determination; when combined with EDS, the method can be used to characterize particles based on size and elemental composition). Sputtering of the samples by using SEM at various accelerating voltages were also performed on FPT1 samples to provide data on the evolution of the elemental composition of the particles by removal of surface layers. In other words, these methods offer the possibility of probing the layered structure of particles.

Post-test analysis results obtained on FPT1 samples are summarized in reference (48). The PTA results constitute a very important database, which provides additional understanding of the fission products behavior in the circuit and in the containment and mass balance data for the non γ-emitter elements. The instrumentation plan, containing the more important instruments, is presented below in Figure 5-6.

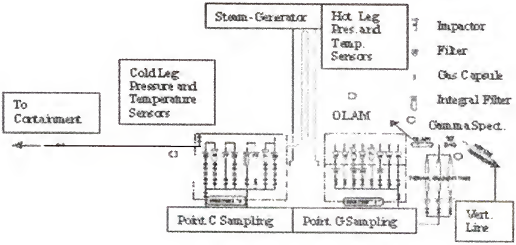

Figure 5-6. Instrumentation in the experimental circuit

Test Conduct and Bundle Degradation

The FPT1 test is devoted to studying the phenomenology of severe accident sequences, under oxidizing conditions without steam starvation at low pressure, for which the fission products flow-path involves a portion of the primary circuit, the steam generator and the reactor containment building. The objectives of the test may be stated separately for the bundle and the experimental circuit.

The objective for the bundle was to obtain a significant degradation of the fuel rods in order to maximize the fission products releases. It was estimated, in the pre-test analyses, that about 2 kg of liquefied fuel was necessary to release 70% to 80% of the fission products. The bundle degradation was obtained by reaching the liquefaction temperature of the fuel. It was expected that interactions between the fuel pellets and the molten cladding or control rod could also contribute to the degradation of the bundle.

Regarding the circuit, the main objectives were to investigate depletion of the fission products within the primary circuit of the reactor at low pressure (around 0.2 MPa) without steam condensation and to provide data on fission products chemistry including interactions of these fission products with pipe walls at high temperature. A secondary objective was to explore phenomena in the section just above the bundle exit where sharp changes of the carrier gas temperature were expected. In the FPT1 test, a section of the liner, in the temperature-controlled part of the vertical line above the bundle, was made of stainless steel, allowing differences in deposition on this material and on inconel, which was used elsewhere in the circuit to be studied.

The Phebus FPT-1 test can be divided into the preparatory phase, the transition phase, and the bundle-degradation phase. Of the interest of this research is only the bundle-degradation phase, once it is correspondent to the modeled transient time. Therefore, the first two phases receive here only a simplified description.

The preparatory phase can be divided into the pre-irradiation phase and the re-irradiation phase. In the pre-irradiation phase, 18 irradiated fuel rods of the FPT1 bundle were previously irradiated in the Belgian BR3 reactor where they attained an average burn-up of ~23.4 GWd/tU.

The test bundle was re-irradiated in the Phebus reactor in order to generate short-lived fission products in the fuel. Short-lived fission products are easily detectable by γ-spectrometry measurements and the activity of the short-lived fission products is necessary to initiate radiolysis phenomena in the containment. The re-irradiation phase lasted 7.4 days with a core power of 15 MW (205 kW produced in the bundle) and a bundle coolant water flow rate of 10 t/h at 60°C under 2.5 MPa. At the end of this phase, the reactor was shutdown for 36 hours. During this period, the fuel bundle was dried out and conditioned in steam, corresponding to the transition phase experiment environmental condition.

The drying of the bundle was done by stopping the coolant water flow through the bundle by closing the inlet valve and drying the test train using nitrogen gas and electrical heaters (in addition to raising the temperature of the pressurized cooling water circuit). The bundle steam pressure was controlled by pressurizing the containment vessel to around 0.2 MPa. The steam injected at the bottom of the bundle in the subsequent phases of the test was heated to 165°C (438 K) by the pressurized water circuit.

The inlet steam temperature and the system pressure were kept constant at these values in the bundle throughout the experiment. The parameters operated during the course of the experiment were the steam inlet mass flow rate and the nuclear power. The nuclear power generated in the bundle during this phase was evaluated using the measured reactor power, and the coupling factor determined previously ($C_{steam} = 155$ in steam with control rod or $C_{steam} = 141$ without control rod) and the residual power estimated at $P_{res} = 330$ W after the re-irradiation. These factors are used to calculate bundle power through the relation below.

$$P_{bundle}^{\deg radation} = \frac{P_{reactor}^{\deg radation}}{C_{steam}} + P_{residual} \qquad \text{(Equation 5-1)}$$

Where:

$P_{bundle}^{\deg radation}$: Power in the bundle during the degradation phase (W)

$P_{reactor}^{\deg radation}$: Power in the reactor during the degradation phase (W)

$P_{residual}$: Residual power during the degradation phase (W)

C_{steam} : Coupling factor during the degradation phase

The bundle degradation phase started on 26 July 1996 at 10 h 15 min (i.e., 35 h 47 min after the end of the re-irradiation phase) and was stopped by reactor shut-down at 14 h 58 min 59 s, after four hours, 43 minutes and 59 seconds of transient. This time period is presented here. The steam injected into the fuel bundle was stopped at 15 h 25 min 17 s and the containment was definitively isolated from the circuit at 15 h 26 min.

The degradation phase of the test was initiated by progressively increasing the nuclear power generated in the fuel rods with a steam flow rate (between 0.5 and 2.2 g/s) injected at the bottom of the bundle under 0.2 MPa. During this phase, lasting 5 hours, the temperatures of the test bundle were continuously controlled so that they followed as closely as possible those foreseen by the pre-test calculations.

At the end of the bundle-degradation phase, the reactor was shut-down and the circuit was isolated from the containment. The long-term experimental phases (aerosol, washing and chemistry) followed. These phases are not here explored, because the model does not calculate them.

The axial power profile for the bundle-degradation phase was estimated using the signals of the fission chambers measured during the FPT1. The axial power profile recommended for the bundle-degradation phase is slightly different from the one considered for the re-irradiation phase due to the relatively low position of the control rods (~370 mm, rather than 550 mm in the re-irradiation phase). The axial power profile during the bundle-degradation phase is presented in Table 5-4.

Table 5-4. Axial power profiles $F_d(z)$ during the bundle degradation phase

Level from BFC (mm)	0	50	150	250	350	450	550	650	750	850	950	1000
Fd (z)	0	0.3	0.92	1.38	1.56	1.56	1.43	1.18	0.86	0.52	0.17	0

The radial power profile in the fuel bundle during the degradation phase is reported in Table 5-5 below, from the experimental report (48):

Table 5-5. Radial power profile during the bundle degradation phase

Rods	With CR*	Without CR
8 irradiated inner rods	0.91	0.95
10 irradiated outer rods	1.11	1.08
2 fresh fuel rods	0.89	0.89

* Control rod

The steam mass flow rate introduced into the bundle was measured by weighing the injected water with an accurate balance (uncertainty of ± 0.04 g/s). The parameters of the injection line (bundle power and injection flow rate) are shown in Figure 5-7 (48).

The bundle degradation phase started on 26 July 1996 at 10 h 15 min., as mentioned before. This time corresponds to the reference time for the FPT1 experiment. The bundle degradation phase spanned the period between the reference time and the reactor shut-down decided by the test director at the end of the heat-up period. The degradation phase of the FPT1 test included: (1) a thermal calibration period, (2) an oxidation period, (3) a power plateau P1, (4) a heat-up period and, (5) a cool-down period. The final high-temperature period of the test was carried out in order to produce fuel rod degradation.

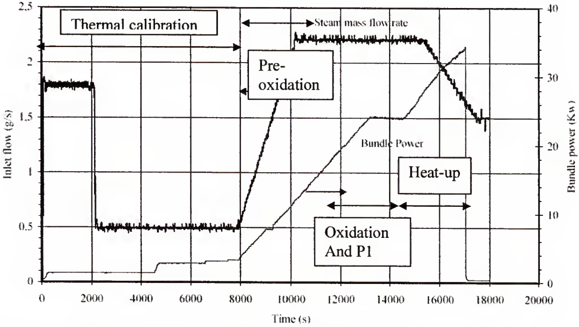

Figure 5-7. Boundary conditions of the FPT-01 experiment (48)

The first part of the experiment addressed the phenomena involved in the so-called early phase of core degradation occurring during postulated severe accidents. In the final period of the test, the bundle experienced late phase conditions with a consequent loss of the rod-like geometry and the formation of a molten pool in the lower part of the bundle. In the following paragraphs, the boundary conditions and main events related to severe accident phenomena and bundle degradation are described.

A preliminary period was devoted to the thermal calibration of the test bundle including three-temperature plateau. The first plateau (500°C) was conducted with a constant bundle power of 1.28 kW and a steam flow rate of 1.8 g/s. At 10 h 50 min, the steam flow rate was decreased to 0.5 g/s with the same bundle power and the second temperature plateau was obtained 2300 seconds later (626°C). The third temperature plateau (920°C) was initiated at 11 h 33 min 20 s with an increase of the bundle power to 3.19 kW. The stabilization of the temperature was obtained after 3600 seconds. The total duration of the calibration phase was 7900 seconds.

Evidence of cladding bursts was first detected at 5678 seconds by an increase of the activity signals (Xe_{135} and Sb_{122}). The cladding ruptures were clearly identified at the beginning of the third temperature plateau of the calibration phase at 5800 seconds by the presence of Xe_{135} and Sb_{122} in the containment in conjunction with a small attenuation of the OLAM signal.

At 7900 seconds in the transient, the pre-oxidation phase started. The nuclear power generated in the bundle was increased at a rate of 318 W/min. At $P_0 = 7.75$ kW (9000 seconds) the nuclear power was stabilized for 5 min (until 9300 seconds). This power plateau corresponds to a maximum measured temperature of 1330°C inside the bundle (the limit of operating temperature for the K-type thermocouples). At 7900 seconds, the steam flow rate was increased from 0.5 g/s to 2.2 g/s in 37 min (until 10,160 seconds), when the pre-oxidation phase was finished. The pre-oxidation period was set to obtain the thermal-hydraulic conditions for the oxidation of the cladding to start to take place significantly, i.e., the onset of temperature escalation in the bundle. The maximum cladding temperature was about 1300 K.

The nuclear power was increased again at 9300 seconds up to $P_1 = 24$ kW (13,200 seconds), characterizing the oxidation period. The steam mass flow rate remained constant at 2.2 Kg/s during this phase.

The temperature escalation started at 11,060 seconds at the 600 mm elevation, as the cladding temperature exceeded 1570°C (1840 K) and lasted for about 5 minutes in the upper part of the bundle. The heating rate reached 15°C/s on (guide-tube) at the 800 mm elevation. The total hydrogen production increased very rapidly after 11,060 seconds; the cumulated mass, at the end of the escalation phase (12,400 seconds), was 70 g.

The increase of the steam flow rate, which carries the fission products, was required to provide oxidizing or "steam-rich" conditions for the fission products chemistry and to avoid steam-starved conditions in the upper part of the bundle. During this oxidation phase, the melting and the relocation of the absorber material of the control rod was detected, as well as the beginning of the aerosol and fission products releases.

The control rod rupture was first detected at 9690 seconds by a steep increase in the temperature under the support plate of the bundle at the -108 mm elevation. At this time, the maximum temperature measured on the guide tube was 1330°C (1600 K) (at the 600 mm elevation).

The power plateau phase started when the power was stabilized at 24kW, and lasted for 23 min (until 14,580 seconds). The steam mass flow rated remained constant at 2.2 m/s until the end of this phase. This power plateau corresponds to a maximum measured temperature of 1730°C on the thermocouples located inside the test bundle (at the 0.5 m elevation).

During the subsequent period of the test (the heat-up phase), the temperatures were increased up to those of fuel liquefaction in order to produce extensive degradation of the bundle and additional fission products releases. Beyond the P_1 plateau, the nuclear power was increased at a mean rate of 365 W/min. After 16,500 seconds, the power ramp was reduced to 240 W/min. At 15,380 seconds, the steam flow rate was decreased to 1.5 g/s in 37 min and kept constant until the end of the test.

The criteria to terminate the test when reaching the mass of liquefied or molten fuel of 2 kg were determined by pre-test calculations using computer codes. These calculations defined the following conditions to be met for the reactor shut down: (a) In the lower part of the bundle (200 mm to 400 mm), detection of a temperature higher than the average temperature for different levels in the upper part (500 mm, 600 mm, 700 mm), to bring this type of condition correspondent to a progressive downward relocation; (b) Decrease of the temperature in the upper part of the bundle for an axial level between 500 mm and 800 mm (this type of condition corresponds to a rapid solid fuel-rod slumping situation); (c) Heat-up rate in the lower part of the bundle between the elevations 200 mm and 400 mm (this type of condition also corresponds to a solid fuel-rod slumping situation). The numerical values of these criteria depend on the axial elevation of the assumed relocation and also on the power level at which the relocation occurs, and are not here defined.

The first possible fuel movements were identified shortly after 15,380 seconds (heat-up of UTS at the 245 mm and 311 mm elevations). Evidence of fuel relocation was clearly detected at 16,000 seconds with a rapid increase in the temperature at the lower levels of the shroud and cooling in the upper part (the OLAM signal also decreased from this time onward). Material movements were also confirmed by the analysis of the OLAM signal indicating the release of significant quantities of aerosols after 15,380 seconds.

However, the criteria for test termination were not met and a second rapid heat-up of the bottom of the shroud (and cooling in the upper part) was detected at 16,900 seconds (second fuel relocation). This second temperature peak in the lower part of the shroud triggered reactor shutdown and the end of the test at 17,039 seconds. At this time, the maximum nuclear power generated in the bundle was 34.4 kW. Figure 5-8 contains the more important events in terms of severe accident phenomena, as well as the temperatures in the gas outlet and cladding, and the hydrogen production rate.

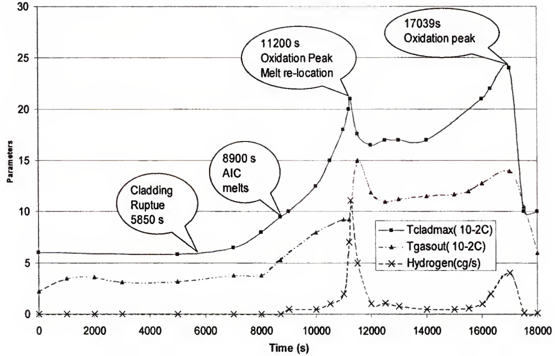

Figure 5-8. Phebus FPT-01 parameters and major events

Lessons Learned from Phebus FPT-01 Experiment

The purposes of the experimental program were both to validate current models for fission products behavior, as well as to better understand some phenomena and gain empirical knowledge to employ in the modeling activity. The knowledge gained in aerosol shape and composition has already been used in the aerosol nucleation model developed in Chapter 3. Besides the acquired knowledge used in Chapter 3, the following important conclusions were drawn from the experimental and post-test analysis: (a) Material release was not simply linked to the temperature levels reached in the fuel, but it was strongly correlated with the bundle degradation events and the configuration of the degraded fuel; (b) Circuit chemistry was found to be complex, probably involving ternary or more complex substances, rather than simple gases or condensed substances of the type MxOy (where M is a metal).

Remarks on the Fission Product Results of Phebus FPT-01 Experiment

The release and transport of material through the primary circuit during the FPT1 test transient were strongly correlated with bundle degradation events. In this chapter the quantitative and qualitative remarks on the fission products behavior in the experiment are identified, in order to aid the model elaboration as well as the comparison of calculated and experimental behavior. Three main release phases could be identified. The first release phase corresponds to the first main zircaloy oxidation phase (phase I), comprising the period of time from 10,960 to 11,800 transient seconds, the second release phase to the beginning of the fuel-melt progression phase (phase II), lasting from 11,800 to 15,300 transient seconds, and the third phase to the hot material relocation in the lower part of the test bundle (phase III), from 15,300 seconds to the transient's end.

Materials can be classified according to their major release period: (a) Cd, In and Sn were mostly released during phase I; (b) Noble gases, such as Kr and Xe, and volatile fission products, such as I, Te, Cs and Mo/Tc, were mostly released during phase II and to a lesser extent during phases I and III. (Sb behaved differently from the other volatile fission products in that it was released more extensively during phase III); (c) Low volatile fission products, such as Ru, Ba(La), Zr-Nb and Sr-Y, fuel material, such as U and Np, Ag arising from the relocated control rod material, thermocouple material, such as Re and W, and other material, such as Pb, were mostly released during phase III. Ag and Re were released, at some extent in phases I and II, during the failure of the control rod guide tube and subsequent re-location. Except for Ag, Re, and U, which have large initial inventories, an extremely low percent of the low volatile fission products was released in the containment.

Regarding the release fractions, the elements may be classified depending on their overall release: (a) Strongly released elements (80% to 85% of the initial bundle inventory), composed of the noble gases Xe and Kr and the highly volatile fission products Te, I, Cs, and Rb. Cadmium, originating from the control rod, may also be classified in this first series with a release fraction higher than 65%. (b) Elements with an intermediate fractional release (20% to 60% of the bundle inventory) composed of volatile fission products such as Mo, Tc and Sb, and Sn arising from structure material. (c) Elements with a low fractional release (5% to 15%), composed of Ag and In from the control rod and Re from the thermocouples. (d) Elements with a very low fractional release (of the order of 1% of the bundle inventory or much less), composed of low volatility fission products, such as Ba(La), Ru, Sr, Zr-Nb, Nd and Sm, fuel material U, Pu and Np, and Zr arising from the structures.

Regarding the transport of fission products, a significant amount of vapor condensation occurred on the walls of the upper plenum and vertical liner, which was more or less intense according to the volatility of the element. In the rest of the circuit, transport was dominated by aerosol phenomena, except for the most volatile species, such as I and Cd.

Aerosol samplings performed in the hot leg (point C, 700°C) indicate that most elements, except iodine and cadmium, were already in a condensed form in this part of the circuit. The behavior of Cs (and the chemically similar Rb) was more complex than expected with possibly a significant fraction of Cs transported as a vapor species (most probably Cs hydroxides or oxides) and another fraction transported as a condensed species (Cs_2MoO_4 is the most probable candidate, but no experimental evidence could confirm its existence). Other elements could have been present partly in a vapor form in the hot leg of the circuit. Material that was transported in a vapor form in the circuit's hot leg condensed in the steam generator tube, so that all material, with the exception of iodine, was in a condensed form in the cold leg of the circuit.

Condensed material was transported in the circuit's hot leg and cold leg as mixed aerosols whose masses were dominated by control rod, structure and fuel bundle material. X-ray photoelectron sputtering studies suggest, more volatile compounds, such as In, Sn, Cd, and volatile fission products probably condensed on the already-condensed material following the order of their condensing temperatures. For Cs (and Rb), condensation may have been followed by inward diffusion and chemical reaction with low volatility material, confirming the reactive nature of cesium with the surface materials. This process can explain the aerosol structure presented in Chapter 3 (Figure 3-6).

Cesium movement was registered after the reactor shutdown. This phenomenon was explained by the reactive nature of this element, which probably reacts with surface materials, resulting in new chemical composition and desorption. Certainly, the behavior of cesium over the structural and aerosol surfaces (re-vaporization) is a phenomenon that is not considered in the developed model. However, the knowledge about the chemistry and kinetics of these reactions is very limited, and it is not possible to model such behavior. This is an important area for research for the future.

The aerosol composition was shown from impactor data to be rather homogeneous for a given sample and independent of the particle size. The size distribution was log-normal in the circuit's cold leg with a characteristic AMMD of 1.6 µm and a standard deviation of 1.45 µm. In the circuit's hot leg, the distribution could be described approximately by a log-normal distribution with an AMMD of 1.4 µm and a standard deviation of 0.98 µm. These results are explained by ongoing agglomeration processes in the circuit's hot leg.

The overall mass composition of material transiting through the circuit's hot leg (point C, 700°C) and the cold leg (point G, 150°C) of the circuit during the whole test transient may be approximated by the following remarks (there are variations of the aerosol composition, according to the phase). The major contributors to the aerosol mass are Ag and Re, each representing about 20% of the aerosol mass. These elements, together with U, represent more than half of the aerosol mass that transited through the circuit during the FPT1 test transient. The mass flow rate curves of Ag, Re and U at point G indicate that these three elements are mostly transported through the circuit during the late oxidation phase. Thus, the measured aerosol mass concentrations in the circuit peaked during the late phase of the experiment when hot material relocated at the bottom of the test bundle. This statement can be confirmed by the OLAM signal presented in Figure 5-9 below. The OLAM signal is lower when the aerosol concentration is greater. Because the OLAM value was lower at the end of this transient, it is proved that the aerosol concentration was greater at this period.

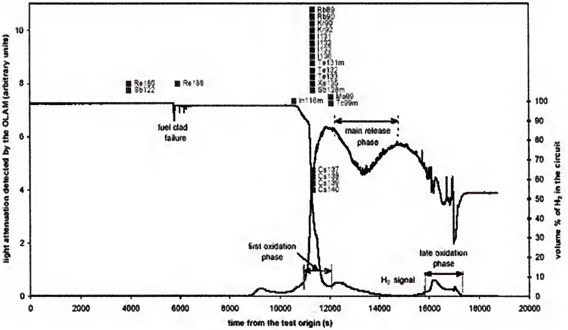

Figure 5-9. On-line aerosol monitor signal for Phebus FPT-01 experiment (48)

The second class of elements which contributes significantly to the aerosol mass conveyed through the experimental circuit is that which was released early during the test transient, from the Ag-In-Cd control rod rupture event or during the first main oxidation phase: Cd and Sn each represents about 10% of the total aerosol mass and In about 5%. Globally, Cd, Sn and In represent about a quarter of the aerosol mass, this mass being mostly conveyed through the circuit during the early phases of the test (from the control rod rupture event and during the first oxidation phase for Cd and mostly during the first oxidation phase for In and Sn).

The third class of elements that represents a significant fraction of the total aerosol mass is the class of volatile fissions products, with the following approximate relative contributions: Cs 5.8%, Mo 4%, Te 1%, Rb 1%, and I 0.6%. As mentioned earlier in this section, these elements are mostly released before the onset of the formation of the molten pool. During this phase, bundle, structure and control rod materials are released less than during the other experimental phases, inducing larger contributions of the volatile fission products to the total aerosol weight transiting through the circuit.

Several different compositions were encountered, using different procedures, for the aerosols, in different transient times, at the cold and the hot leg. Examples of such compositions for the cold leg are presented in Figure 5-10. For the purpose of comparison, is more appropriate to use the general description presented in the paragraphs above, given the high degree of variation of the compositions obtained.

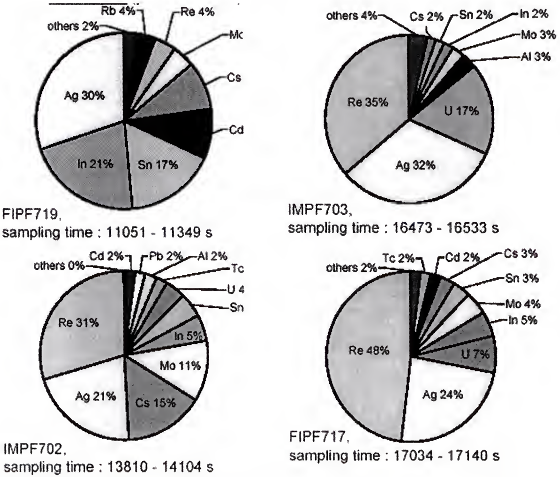

FIPF719,
sampling time : 11051 - 11349 s

IMPF703,
sampling time : 16473 - 16533 s

IMPF702,
sampling time : 13810 - 14104 s

FIPF717,
sampling time : 17034 - 17140 s

Figure 5-10. Aerosol composition for several transient times for the cold leg (48)

The walls of the steam generator tube were maintained at the approximately temperature of 450°C the up section, and of 150°C in the down section. When material conveyed in a fluid at 700°C entered the tube, the following behavior was observed: (a)

Species in a vapor form (essentially I and Cd) condensed either on the tube walls (essentially at the entrance) or on the aerosols; (b) Species in an aerosol form deposited on the tube walls under the effect of the temperature gradient between the fluid and the walls (thermophoresis) (c) Iodine and cadmium deposition, mainly by vapor condensation, was greater than aerosol deposition and represented about 25 % of the mass entering the steam generator tube. The deposition profile for iodine can be represented by two successive exponential decays. The deposition in the hot leg of the steam generator was higher than for aerosols and represents more than 90 % of the total amount of deposited iodine.

The deposition of aerosols in the steam generator was essentially by thermophoresis. The deposition profile for aerosols can be represented by a simple exponential decay profile. Most of the deposition (85 % of it) occurred in the hot leg of the steam generator.

The mass balance for the several species in the transport process is important for the comparison experimental-calculated data, as well as the released mass for the input setting of the Phebus Relap/Scdap model. The Table 5-6 below presents these data, obtained from the experiment report (48). The percentiles are related to the initial inventory. Most of the data was obtained by a combination of procedures involving on-line measurements and PTA.

Table 5-6. Global mass balance for Phebus FPT-01 experiment (% of initial inventory)

Elem.	Initial Inventory (mg)	Released Mass (%)			Deposition (%)	Steam	Generator
			Vertical line	Hot Leg	Cold Leg	Hot Leg	Cold Leg
I	1.12	87±4	5.3±0.7	0.2	0.7	17.45	1.75
Cs/Rb	15.86/2.53	84±1	25.7±0.7	3.5	0.6	10	1.4
Mo	20.17	56±4	22.0±2	NA	0.5	5.8	1.0
Te	2.54	83±1	26.0±1.6	1.7	0.5	7.73	1.38
Ag	478.31	15.5±2	7.5±0.5	0.2	0.7	0.81	0.12
Re	482.2	15.5±2	7.5±0.5	NA	0.1	1.1*	NA
U	9163	0.14	NA	NA	Negligible	0.021*	
Ru		1±0.4	0.59	NA	Negligible	0.09	
In	89.68	9.0**	NA	NA	0.7	1.2*	
Cd	29.3	66.7**	NA	NA	0.8	13.78	2.42
Sn	49.48	38.4**	NA	NA	0.5	5.4*	
Sb		30.8**	NA	NA	0.5	4.6*	

* Total

**Released in the hot leg (deposition in the vertical line already accounted for)

NA: Not available

Other information of interest about the fission products behavior for the development of an experiment model is the release-time profile, i.e., the amount of material released in each phase of the transport period (from 10,960 to 17,039 seconds). To be more specific, it is important to know the percent released in each phase. Unfortunately, this information is not available, leading to the necessity of establishing an approximate procedure to obtain these values.

This procedure was to separate the released material into groups, according to the release behavior previously commented, and to give each group the appropriate treatment. The selected groups, the characteristic behavior, and the evidence that leads to the commented behavior are presented in Table 5-7 below.

Table 5-7 shows that the first two groups have not much dependence on the OLAM signal, whereas the last two have high dependence on the OLAM signal. Another important aspect of the release is the percent of release of each experimental phase, if a constant release rate was considered. In this case, the relative release fractions would be 0.13, 0.55, and 0.32 for each phase, respectively. A combination of the information in Table 5-7, and the relative fractions under constant release, is used to establish the fraction released in each phase.

Table 5-7. Release time characteristics for the several release groups

Group	Elements	Characteristic	Evidence
1. High Volatile	Cd, I, Sn, In	Higher relative release in the phase I	High relative presence of Cd, Sn and In in the aerosol; high vapor pressure of Cd, In
2. Volatile	Cs,Rb,Mo Sb,Te	Higher relative release in the phase II	High relative presence of Cs and Mo in aerosol; intermediate vapor pressure
3. Ag/Re		Higher relative release in phases II and III	Dependence on OLAM signal; Low vapor pressure
4. U		Release only on phase III	Presence only in this phase; Very low vapor pressure

The relative fractional release, according to the OLAM signal is obtained by integrating the inverse of the signal's function. The inverse signal function was built as a discrete function, in which the time was discretized in 200-seconds intervals from 10,600 to 17,000 seconds. The value of the "OLAM signal function" was obtained by measuring the OLAM signal in Figure 5-9, and decreasing it from a reference value of 7.2. This procedure originated the OLAM signal function in Figure 5-11.

The values of the fractional releases from the OLAM signal are 0.15, 0.51 and 0.34, in phases I, II and III respectively. The information in Table 5-7 and the relative fractional releases, according to the even assumption and the OLAM signal, were used to determine the relative releases of the four main groups in Table 5-8. These relative releases are shown in Table 5-8.

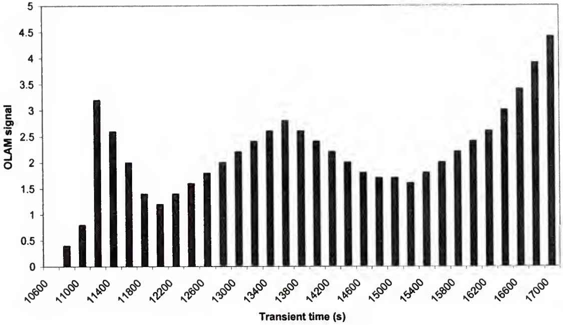

Figure 5-11. On-Line Monitor signal function for Phebus experiment

Table 5-8. Relative releases for the fission product groups

	Phase I	Phase II	Phase III
1. High Volatile	0.30	0.50	0.20
2. Volatile	0.14	0.61	0.25
3. Ag/Re	0.13	0.62	0.25
4. U	0.0	0.0	1.0

Modeling the Phebus Experiment with Relap/Scdap

In this section all the procedures used to set the input file of the Phebus experiment are described. The section follows the logic sequence necessary to build Relap/Scdap models. Initially, the nodalization diagram is built and afterwards the input requirements and code options are set.

Elaboration of Nodalization Diagram

As pointed out in Chapter 2, a nodalization diagram is a sketch of the spatial discretization adopted to model a system. Creating the nodalization diagram involves the following steps: (a) definition of model boundaries; (b) axial and radial discretization; (c) definition of the type of elements and their geometries; and (d) setting the boundary conditions of the problem.

In the case of the Phebus experiments, there is information about the inlet flow conditions and the power in the test bundle, as well as, in the radial direction, exist thermal information in the physical boundaries of the test bundle through thermocouples. Therefore, in the core region, the model is limited to the test bundle, and, since the inlet conditions are known, the injection circuit need not be modeled.

The main goal of this model is to calculate the effect of the experimental circuit in the transport of fission products. Hence, the experimental circuit obviously needs to be modeled. The containment is modeled as a time-dependent volume, since the phenomenological behavior in its interior is not of interest.

The next step is the determination of the spatial discretization. The spatial discretization determines the location and size of each element in the model. Two aspects are considered in the spatial discretization. First, and more important, is the recommendations of the user's guideline (34). The other factor is the geometry of the problem, i.e., there should exist discretization changes every time the geometry varies. The combination of these two factors led to the nodalization diagram represented in Figure 5-12 below.

Figure 5-12 (a) shows the discretization in the test bundle. The test bundle includes the bundle, injection circuits, and the pressurized water loop, which cools down externally the test bundle. The elements in the test bundle, discriminating their type, function, and main characteristics, in terms of geometry and settings, are presented in Table 5-9. The geometric parameters were obtained from Table 5-6, using Equations 4-1 and 4-2. The flow boundary conditions were obtained from Figure 5-7. Other data were retrieved from the ISP 46 specification (48).

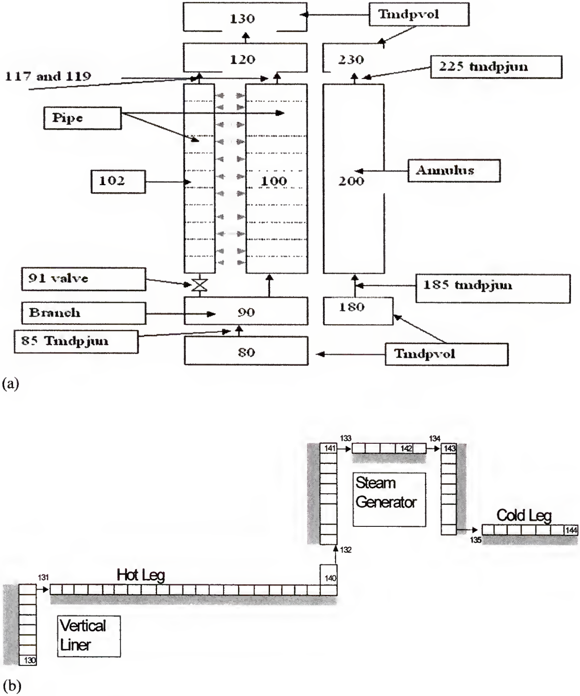

Figure 5-12. Nodalization diagram: (a) test bundle region; (b) experimental circuit

Table 5-9. Elements of the core region in Phebus test train

Element	Type	Function	Characteristics
080	tmdpvol	Establish the flow inlet BC	P= 0.22 MPa; T=438 K
085	tmdpjun	Establish the flow inlet BC	Mass flow rate history from (48)
090	branch	Represents the volume below the fuel stack (lower plenum)	L=0.0825m; d_h=0.018 m Receive the BC flow elements
091	valve	By-pass during the flow blockage	Dummy structure to simulate flow conditions after blockage. Valve is opened at 1 MPa pressure
100	pipe	Represent the bundle region	20 elements of 0.05 m length d_h=0.018 m. Grid loss coefficient for spacer grids (0.5)
102	pipe	Represent the effect of the flow blockage	20 elements of 0.05 m length d_h=0.018 m. Loss coefficients for all junctions (200). Cross-flow linked with element 100
115	sngljun	Connects the bundle with the region above the fuel stack	
117	sngljun	Connects the by-pass with the region above the fuel stack	
120	snglvol	Volume above the fuel stack	L=0.0825m; d_h=0.018 m Receive the pipe elements; initial condition from thermocouple
180	tmdpvol	Establish the flow inlet BC for the pressurized water loop (PWL)	P= 8.0 MPa; T=438 K PWL cools down the bundle externally; d_h=0.018 m
185	tmdpjun	Establish the flow inlet BC for the pressurized water loop (PWL)	Mass flow rate of 10 Kg/s throughout the transient
200	annulus	Represent the PWL, which is the cooling device of the test bundle, externally	L=1.0825m; d_h=0.00906 m
225	sngljun	Connects the PWL with its BC volume 230	
230	tmdvol	Establish the top BC of the PWL	P= 8.0 MPa; T=383 K

The abbreviators used in Table 5-10 have the following meaning:

BC: Boundary condition
Tmdpvol: time-dependent volume element
Tmdpjun: time-dependent junction element
Snglvol: Single volume element

Sngljun: Single junction element
Annulus: Annular element
Valve: Valve element
Pipe: Pipe element

The nodalization of the test bundle region followed the common sense of the user's practice, established in the code user's guideline (34). The unconventionality in this model is the by-pass set of elements established to be used when the flow blockage occurs. Actually, this procedure was performed to overcome a code deficiency. The modeling of the flow representation under blockage conditions becomes severely prejudiced. Hence, this procedure of bypassing the flow, establishing a large value friction factor, was established. To arrive at the desired result, there was a matching procedure for the important flow parameters.

Figure 5-12 (b) shows the nodalization of the primary circuit, which was divided into vertical line, hot leg, cold leg, steam-generator in its up, top, and down sections, and the containment. The containment was modeled as a time-dependent volume, as pointed out earlier. Table 5-10 below contains the same information as of Table 5-9 for the experimental circuit elements. The discretization process in the experimental circuit followed again the guidelines, adding to the needed discretization when geometrical parameters changed.

The most important information about the elements in the experimental circuit is presented in Table 5-10. First, the initial conditions were obtained from the instrumentation. The temperatures were obtained from the thermocouples. The nodalization was set in a manner to provide volumes with approximately the same length. The hydraulic diameter was obtained from Table 5-3.

Table 5-10. Elements of the experimental circuit in the Phebus FPT1 experiment

Element	Type	Function	Characteristics
130	pipe	Represents the vertical liner	IC: P= 0.22 MPa; m = 1.78 g/s 8 nodes: 1 L = 0.249m d_h=0.073m; 4 L=0.400m d_h=0.048m(T=803K) 3 L =0.404m d_h=0.073m(T=976K)
131	sngljun	Connects the vertical liner with the hot leg	
140	pipe	Represents the hot leg	IC: P= 0.22 MPa; m = 1.78 g/s 21 nodes:11 L=0.408m d_h=0.073m 8 L=0.430m d_h=0.030m(T=976K) 1 L =0.6375m d_h=0.02m(T=976K)
132	sngljun	Connects the hot leg to the steam generator	
141	pipe	Represents the steam generator in the up direction	IC: P= 0.22 MPa; m = 1.78 g/s 9 nodes:11 L=0.404m d_h=0.02m (T=750K)
133	sngljun	Connects the steam generator up section to the top section	
142	pipe	Represents the steam generator in the top section	IC: P= 0.22 MPa; m = 1.78 g/s 5 nodes: L=0.460m d_h=0.02m (T=750K)
134	sngljun	Connects the top section to the down section	
143	pipe	Represents the steam generator in the down section	IC: P= 0.22 MPa; m = 1.78 g/s 8 nodes: L=0.455m d_h=0.02m (T=550K)
135	sngljun	Connects the down section to the cold leg	
144	pipe	Represents the cold leg	IC: P= 0.22 MPa; m = 1.78 g/s 8 nodes: L=0.42795m d_h=0.02m (T=423K)
136	sngljun	Connects the cold leg to the containment	
150	tmdvol	Represents the containment	P= 0.22 MPa; T=383 K

In Figure 5-12 (b), the gray lines surrounding the pipes are representative of the pipes, and are modeled as heat structures. The major settings in this heat structures are its discretization and boundary conditions. They were defined as cylindrical, with a thickness of 5 mm. The materials (important in setting the thermal properties) are presented in Table 5-3. The thermal properties used were those recommended in the ISP-

46 specification (48). The boundary conditions of the heat structures are the hydrodynamic volumes in one side and the temperature time-history in the other side, obtained from thermocouples information.

The physical elements in the core region, that is, the fuel and control rod elements, as well as the shroud, were modeled as Scdap elements. The Scdap input is composed of a general part, where parameters used in the severe accident models are defined, and a second part, where the element settings and special models settings are executed.

In the general input cards, the number of axial nodes is defined (twenty 0.05m axial nodes, as the bundle discretization). Parameters for the cladding deformation and ballooning are also defined. These parameters were set as the defaults, with some minor changes to better match the results. The properties of the spacer grids, such as weight, material and length, were obtained from the specification report. Moreover, the power time-history is defined, which was performed through a table derived from Figure 5-7.

The fuel elements were divided into three Scdap fuel elements, the inner ring, the outer ring, and the fresh fuel. The inner ring element is composed of the eight elements closer to the central rod (control rod). The outer ring element is composed of ten of the twelve elements closer to the shroud inner liner. In addition, the two fresh elements were modeled as another fuel element, because of their different burn-up. The control rod was modeled as a Scdap control rod element, whereas the shroud was modeled as a shroud element. In the following paragraphs, the major settings of these elements are described, and the procedure used to obtain those settings defined.

The major settings of a fuel element are the number of elements, its geometry and the radial and axial discretization, axial and radial power profile, initial temperatures, and burn-up. In the fission products field, the pre-irradiation history is necessary for the code to estimate the fission product's initial inventory. However, in our case, this information is not necessary, since the released inventory is used directly.

The first fuel element defined represents the inner ring elements (element 01). The necessary geometrical information is the radii of the fuel pellet and the inner and the outer cladding, and the pitch. This information is furnished in Table 5-3. Furthermore, the volume of the lower and upper plenum was obtained from reference (48). The set fuel burn-up was 23.4 MWd/MTU, as pointed out earlier. The axial discretization followed the core hydrodynamic volumes, i.e., 20 axial nodes equally 0.05 m in length.

The radial discretization employed three equally-spaced intervals in the fuel region, one interval in the gap region, and one in the cladding region. This is a simple discretization, which is appropriate to the purpose of the model of the estimation of fission products-transport behavior. If this model is capable of predicting reasonably well the gas and structural behavior, as well as the gas composition, further computational effort should not be wasted in the conduction equation solution. This arrangement was found to attend to this trade-off. The initial temperatures profile was obtained from the thermocouple's information. The same profile is assumed for all elements.

The power was distributed among the three fuel elements (inner, outer ring and fresh fuel), according to the number of rods of each element. The axial power profile followed the recommended curve, in Figure 5-13, from the ISP-46 specification. The last information provided in the inner ring set-up is the helium inventory in the fuel rod (to compose the fluid in the case of release) and the fuel density, which were set as 1.95e-5 Kg and as 94.3325%.

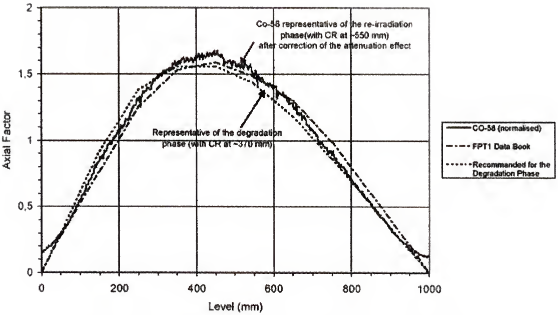

Figure 5-13. Recommended axial power profile for Phebus experiment (48)

The outer ring element (element 03) was set to allow a better representation of the radiation heat transfer, through the establishment of appropriate view factors and path lengths. Radiation heat transfer has a crescent importance as a severe accident progresses. Hence, a more detailed radiation model exists in Scdap, where these important parameters are defined. Thus, the settings are the same as of the inner ring, except for the number of rods (10) and the power multiplier (0.5506).

The fresh fuel element (element 04) is defined because it has a different burn-up from the others. Therefore, its settings are equal to the inner ring settings, except for the number of rods (2), the power multiplier (0.0836), and the burn-up (0.0).

The control rod Scdap element is used to represent the central control rod (Scdap element 02). The geometry settings in the control rod element are the radius of the absorber, the cladding, and the guide tube. These measurements were obtained from Table 5-3. The radial and axial discretizations are the same as that used in the other elements, and the power multiplier is zero. The only additional necessary information is the mass of tin and silver, which are presented in Table 5-7.

The shroud is composed of a zircaloy inner layer, followed by a thoria and a zirconia layer. Next in the sequence there is a spray coating of dense zirconia and an inconel pressure tube. Between the inconel pressure tube and the spray coating there is a gap filled with helium. The geometry of these layers is presented in Table 5-2, and the materials' thermal properties set came from the ISP specification (48).

The axial nodalization of the shroud followed the overall discretizaton adopted in the hydrodynamic volumes and in the other elements. The radial nodalization used 18 radial nodes, with a crescent spatial distance as one walks in the direction of the pressure tube. In other words, the discretization is more intense close to the zircaloy liner and becomes less intense while moving outward.

In the Scdap usage is important and necessary to establish the radiation heat transfer parameters, view factors and mean path lengths. The view factors used came from the Honaiser master's thesis (144), in which was used the Jull (145) method to obtain the view factors for the Quench experiment test bundle. Since both (Phebus and Quench) have the same geometry, the same view factors can be used.

Mean path length is defined as a fictitious length (i.e., the radius of a gas hemisphere) such that the radiation heat flux to the center of its base is equal to the average radiation flux exchange by the gas and two surface areas containing the actual volume of gas.

Mean path length between two rods is calculated by the approximated formula:

$L_{ij} = P_{ij} - \pi/2\,(R_i + R_j)$ (Equation 5.2)

Where:
P_{ij}: Center-to-center distance of rods i and j;
R_i: Radius of rod i.

To calculate the average path length between two component groups, the path length is weighted by the corresponding view factor, originating the formulation:

$$L_{ij} = \frac{\sum_{i=1}^{N_i}\sum_{j=1}^{N_j} F_{ij} L_{ij}}{\sum_{i=1}^{N_i}\sum_{j=1}^{N_j} F_{ij}} .$$

(Equation 5.3)

In Equation 5.3, the F_{ij} is the view factor of rod i to rod j. Honaiser (144) calculated these path lengths for the Quench bundle, which has geometrical similarity with that of the Phebus. Consequently, these path lengths can be used in the Phebus model.

Great importance must be given to the fission products input. The fission products input in the Scdap code is composed of the release and the transport settings. The release settings are composed of the initial inventory and the release method choice. The initial inventory can be calculated by the pre-irradiation history or by user-input initial masses. For the release method, the user should specify the species to be tracked and the method to release them. The user can choose between the Paragrass and the CORSOR methods. Since the focus of this research is the transport, and the fission products-release models were not benchmarked, the estimated released inventories were directly released in the experimental circuit in the volume just above the bundle. Then, the two issues that pose more difficulty and uncertainty are treated. First, the species under which each element must be transported is defined, and then the release time profile is established.

As detected earlier, the chemistry of the fission products, or their speciation, is the most challenging issue of the fission products-behavior study. Speciation has great dependence on the environmental conditions and the time evolution of the environment. A fixed speciation treatment can only be justified by extensive empirical evidence. However, a more mechanistic approach faces the problem of data availability and computational feasibility. Consequently, the uncertainty of chemistry is a difficulty that all codes share. Since there is no chemistry calculation in the code, a fixed structure is assumed, with the selection of the species occurring based on the described behavior of each species.

Additional complications arise from the experimental scenario. The most important, and that considered, is the presence of Re and W in the experimental circuit. Rhenium and tungsten are thermocouple materials, which, in a severe accident condition, are not present in the primary circuit, and, hence, do not make up part of the thermochemical database of the code. The effect of tungsten is neglected in the calculation, since its impact in the kinetics of the fission products behavior is not significant, given its volatility and small initial inventory. Rhenium, on the other hand, has a significant impact in the fission products behavior, constituting one of the major components of the aerosol. The behavior of rhenium is similar to silver's, in terms of vapor pressure. Therefore, silver properties was adopted, when the rhenium property was not available.

The selection of the elements to be tracked was based on two criteria. First, the element must have a significant release in the containment. This criterion eliminates from the selection the low volatility elements. The second criterion is the importance of the element. Every element having effect in the composition of the aerosol is considered important. Hence, the elements present in Figure 5-10 are tracked. Since no thermochemical data for technetium exist in the code, and given its similarity with molybdenum, this element is treated as molybdenum. Antimony (Sb) is not treated given the difficulty of experimentally measuring it. Rubidium is treated as cesium, given that their chemical behavior is known to be similar. The selection of the species to be used was based on the assumption that most of the elements are transported in the oxide form. The assumed speciation is based on the current knowledge of the most probable species for each element, considering the known oxidizing conditions. The speciation is presented in Table 5-11.

This procedure is a very simplistic procedure, even considering a fixed structure, but it is used here merely to provide a first-order idea of the code's performance. Actually, the back-end procedure would be rather interesting in obtaining the speciation. What is suggested for future work is the whole set of experimental results of the Phebus experiments can be used to establish fictitious species for each important element, that is, species of which the molecular form is not of interest, but whose properties (vapor pressure, diffusivity and density) are capable of providing good agreement between calculations and experimental results. In other words, what is being proposed is to use the experimental results to obtain vapor pressures, diffusivities and densities for each elemental species. This could be a simple and very efficient manner to address the chemistry issue. The elements and correspondent species considered are presented in Table 5-11.

Regarding the release time-profile, a constant release rate was assumed, considering the relative releases in Table 5-8. The released inventories (the product of the first two columns in Table 5-6) are divided into the phase released masses by multiplying the relative release to the total released. Then, these masses by phase are divided by the total time of each phase, yielding the release rates. The results of these operations are presented in Table 5.12.

Table 5-11. Speciation used in the Phebus FPT-01 Relap/Scdap experiment model

Elements	Species
1. Cs/Rb	CsOH/CsI
2. I	CsI
3. Mo/Tc	Mo
4. Te	Te
5. Ag/Re	Ag
6. U	UO_2
7. Cd	Cd
8. In	In
9. Sn	Sn

Table 5-12. Release rates for element considered in the modeling of FPT-1 experiment

Elem.	Initial Invent. (mg)	Released Mass(%)	Total Released (mg)	Phase I Released (mg)	Rate (Kg/s)	Phase II Released (mg)	Rate (Kg/s)	Phase III Released (mg)	Rate (Kg/s)
I	1.12	0.87	0.9744	0.29232	3.5E-10	0.4872	1.39E-10	0.19488	1.299E-10
In	89.68	0.09	8.0712	2.42136	2.9E-09	4.0356	1.15E-09	1.61424	1.076E-09
Cd	29.3	0.667	19.5431	5.86293	7E-09	9.77155	2.79E-09	3.90862	2.606E-09
Sn	49.48	0.38	18.8024	5.64072	6.7E-09	9.4012	2.69E-09	3.76048	2.507E-09
Cs/Rb	17.27	0.84	14.5068	2.03095	2.4E-09	8.849148	2.53E-09	3.6267	2.418E-09
Mo	20.17	0.56	11.2952	1.69428	2E-09	6.890072	1.97E-09	2.8238	1.883E-09
Te	2.54	0.83	2.1082	0.31623	3.8E-10	1.286002	3.67E-10	0.52705	3.514E-10
Ag/Re	960.51	0.1 55	148.879	17.8655	2.1E-08	93.793802	2.68E-08	37.2198	2.481E-08
U	9163	0.0014	12.8282	0	0		0	12.8282	8.552E-09

Some species (Cd, Sn, and In) do not have the release fractions available, but the hot leg transported fractions. Cadmium and tin were released with the released rates of cesium, and indium was released as molybdenum. This assumption was based on the observation of similarity of vapor pressures of these elements.

Defined the treatment strategy to the release in the experimental circuit, in which the fission products are directly released, in conformity with the release rates in Table 5-12, the next step would be the determination of the transport settings. The transport settings are composed of the number of sections, the species to be tracked, and special settings to consider the singularities and other parameters to be defined, such as surface angle and material. The number of sections chosen was 30, since Chapter 4 shows that, for more than 30 sections there is oscillations of the calculated quantities.

Regarding the bends and contractions, the parameters of these singularities, as well as the settings used, are presented in Table 5-13 below. This Table contains, for each of the elements, the volume inside the hydrodynamic system, and the singularity and its settings.

Table 5-13. Singularities in the Phebus experimental circuit

Element	Volume	Singularity	Parameter
SG* top	142-01; 142-05	2 bends	90°
Vertical liner	130-01	1 contraction	**CA=45°,CR=0.66
Vertical liner	130-08	1 bend	90°
Hot leg	140-21	1 bend	90°
Cold leg	145-01	1 bend	90°

* Steam-generator

** CA: Contraction angle; CR: Contraction ratio

Because the suggested input in Chapter 4 was not implemented, the information in Table 5-13 was hard-wired in the code. Same procedure was adopted in the case of the release; the release rates were programmed directly in the source code, according to the time interval and species.

Comparison of Experimental and Calculated Results

Once both the experiment and the Scdap model were developed, the calculation can be performed, and the outcome compared with the experimental results. This comparison was performed in two phases. In the first phase, the model is tested concerning its thermal-hydraulic performance, and, in a second phase, the most important parameters of the fission products are compared.

Thermal-hydraulic conditions dictate the fission products' behavior. Hence, a good prediction of the thermal-hydraulic conditions is fundamental for a good fission products prediction. This relation forces the necessity first to verify and to obtain good results of the thermal-hydraulic condition, so to be able to make any judgment about the fission products mode performance. Moreover, the conditions in the entrance of the experimental circuit are not known, forcing the necessity to obtain these conditions.

The most important thermal- hydraulic parameters affecting the fission products transport are the gas temperature, pressure, and composition. The system pressure remains roughly the same throughout the transient. The gas composition is affected by the hydrogen production. The hydrogen production is also an indication whether the temperatures prediction is good since it is highly dependent on the cladding temperature. Hence, the figures below show the maximum cladding temperature, the gas temperature in the hot and cold legs, and the hydrogen production rate and the total accumulated.

Figure 5-14 shows the maximum cladding temperature for the fuel rods, or the hot spot, which occurred in the fresh fuel rod at the axial height of 650 mm. This Figure shows a very good agreement between experimental and calculated data up to the first oxidation peak. After that, the calculated temperature is greater than the experimental by roughly 100 K. The thermocouple failed at about 16,000 seconds. The figure also shows that, at the hot spot, there was an advancement of the calculated temperature in relation to the experimental value in the first oxidation peak of 204 seconds.

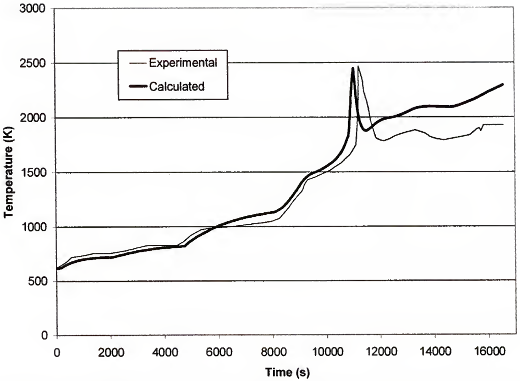

Figure 5-14. Comparison of outside cladding temperature at the fresh fuel, at 650 mm elevation

Figure 5-15 shows the hydrogen production rate and the total hydrogen produced. The agreement is good, and there was a delay in the first hydrogen peak of the calculated value in relation to the experimental value. The behavior is contrary to that presented in the hot-spot temperature behavior. This discrepancy is explained by the fact that, on average, the delayed behavior is superior to the advanced one, considering all the spots where the oxidation peak occurred. The difference between the calculated and the experimental amounts of total hydrogen produced is close to 11 grams (negative). This difference is a little higher than the uncertainty level of these measurements, which is 5 grams (48).

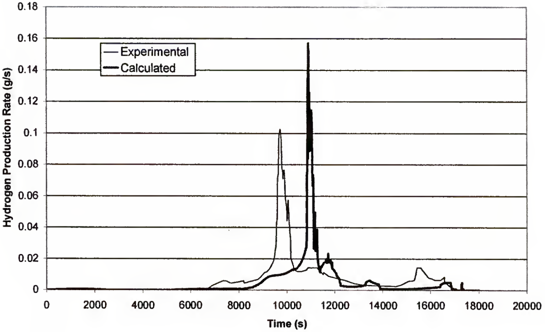

(a)

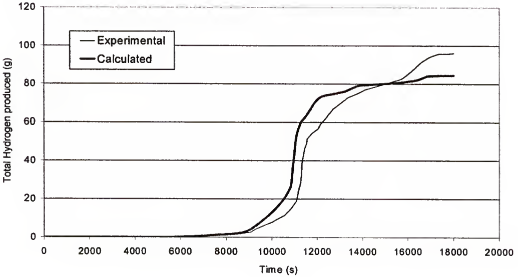

(b)

Figure 5-15. Hydrogen parameters: (a) production rate; (b) total hydrogen produced

The experimental production of hydrogen was greater after the first oxidation peak than the calculated prediction. This is an indication that, on average, the cladding temperatures were at some extent lower in the predictions than those observed in the experiment. For this reason, the total hydrogen produced was slightly lower than the experimental observation. However, it could be said that the production of hydrogen and the consequent gas composition were satisfactorily predicted by the code.

The most important parameter for the fission products behavior is the gas and structural surface temperatures. The surface temperature is a supplied boundary condition, and certainly its value is accurate. The gas temperature was compared with the experimental temperature in the hot leg (point C) and in the cold leg (point G). The results are presented in Figure 5-16. These figures show a very good agreement for the cold leg, and a good agreement for the hot leg, where the calculated value stayed above the experimental temperature by 30-40 K.

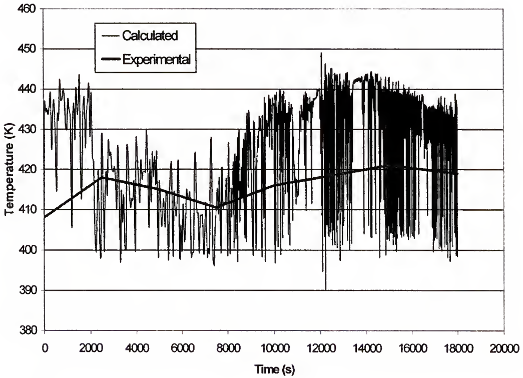

(a)

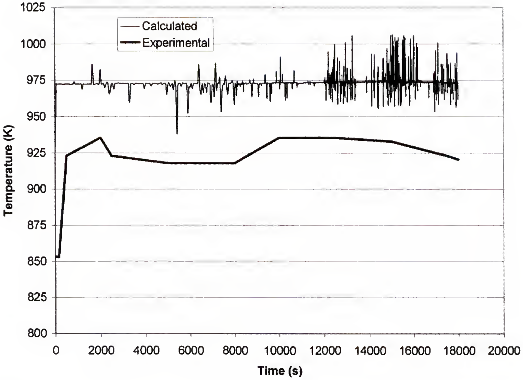

(b)
Figure 5-16. Comparison of experimental circuit temperatures: (a) cold leg; (b) hot leg

Verified that the Relap/Scdap model is capable of providing a good prediction of the more important severe accident and thermal-hydraulic parameters, the fission product transport model is assessed. Good thermal-hydraulic and severe accident predictions are the warranty that inaccuracies presented in the fission product transport predictions are not caused by the thermal-hydraulic and severe-accident calculation. Obviously, the prediction is not completely accurate, but they are acceptable for best-estimate codes. Furthermore, the model must not be much sensitive to typical thermal-hydraulic errors of best-estimate codes. Otherwise, it cannot assure always-acceptable results.

In this second phase of the comparison, the mass balance for the calculated elements, aerosol size and composition were contrasted with experimental data. In addition, consistency analysis is performed for the deposition profiles onto the several sections of the experimental circuit.

Preliminary runs' results showed two major problems: (a) Aerosol nucleation was over predicted, detected by the low condensation of Ag in the vertical liner, and high deposition in the steam generator; (b) Some elements did not condense in the vertical liner in the calculation, oppose to the experimental evidence in Table 5-7, notably Cesium, Iodine, Cadmium and Tellurium.

Sensitivity analysis of the nucleation rate used, Equation 3-83, showed that the nucleation rate is extremely sensitive to the dimensionless surface tension, Θ, expressed by Equation 3-85, due to the third power dependence of the exponential term. It was observed that small variations in this term affect the nucleation rate by orders of magnitude. Since the dimensionless surface tension has dependencies on the surface tension, speciation (molecular weight and species density), and gas temperature, and these quantities are not completely accurate, acceptable predictions are very difficult to obtain, given that: (a) Surface tension for most of the species, and its variation with temperature, are not well known; (b) The correct speciation for the nucleating species is not known, and is not the scope of this research; (c) The gas temperature predictions are just reasonably accurate, given the best-estimate nature of the code.

Therefore, an acceptable prediction of nucleating rate is not guaranteed by the adopted procedure, and constitutes a great challenge for future work, involving a speciation study for the nucleating particles and a survey and acquisition of surface tension for this species. Even with these actions, the uncertainty of the gas temperature remains.

This issue is extremely important because it impacts decisively the deposition kinetics, since vapor and aerosol have different deposition kinetics. Said that, a consistent model should be based on the definition of the speciation of mainly Ag and U, and the usage of accurate material properties. This can be achieved by using a pool of experimental data, experimenting different species to match experimental results. It can be said that most of the aerosol nucleation predictions of other codes fail due to a simplistic approach to deal with aerosol nucleation.

For the simulation, artificial density for Ag, Re and U were set, in order to match the experimentally observed nucleation, by accomplishing a reasonable agreement of the condensation of these species in the vertical liner. A value of 13,500 Kg/m^3 was hard-wired in the nucleation routine (fpnucl). This procedure was done to allow the analysis of the other calculations of the code, once the over predicted nucleation affects all the other calculations. Notice that this value is not completely inconsistent, since the value is between the Silver and Rhenium value of density, which is an indication that the Girshik model used can be used, since adjusted.

The non-condensation of some species in the vertical liner is more straightforward. It is known that these species are transported in other species than its elemental form, and specifically in the Phebus FPT-1 experiment species are in oxide form, or in more complex forms (ternary and quaternary). These species have lower saturation concentrations, and will condense in the vertical liner.

The procedure adopted to deal with this problem was to transport fraction of the mass as an oxide or a ternary form. This procedure was performed for Cesium, Cadmium, and Molybdenum. For Iodine, its mass was transported as Cesium Iodide (CsI), and

Tellurium was transported in its elemental form. Iodine and Tellurium were kept in its original form to highlight the importance of speciation in the fission product transport. The experimental results showed that the original assumption that Iodine is transported as CsI is not good, needing a re-evaluation. The tellurium predictions, because it was transported in elemental form, also have shown a completely different behavior of the experimental data.

Cesium was transported as CsI. The remaining mass was transported in a mass fraction of 0.7 in the form of Cesium Molybdate (Cs_2MoO_4), and the remaining as Cesium Hydroxide (CsOH). This selection was based on indications of the experiment (48) that Cesium Molybdate is a possible transport species, and the previous common sense that Cesium Hydroxide is a transported species.

Cadmium was transported in the form of Cadmium oxide (CdO) in the mass fraction of 0.5, and the remaining as elemental Cadmium. Molybdenum was transported as Cesium Molybdate and in its elemental form, as consequence of the Cesium speciation (the chemical behavior of the elemental form and Cesium Molybdate is similar).

This re-alignment of the speciation led to the necessity to re-establish the release rates, in accordance with the new species and the mass fractions above mentioned. These new release rates are presented in Table 5-14, which replaces the original Table 5-12.

The mass balance comparison is performed for each element, using the experimental data available, presented in Table 5-7. The comparison is established for total mass deposited. Details about the process that led to the deposition are presented in the analysis of deposition profile. The comparison with the experimental data is performed for the vertical line, hot leg, steam generator, and cold leg. The steam generator is treated as a whole, because, for some elements, there is only information about the total. Uranium was not compared given the not availability of most important data.

Table 5-14. Release rates and speciation after preliminary run analysis

Species	Initial Invent. (mg)	Releas. Fraction	Total Releas (mg)	Phase I rel. (mg)	Rate I (Kg/s)	Phase II rel. (mg)	Rate II (Kg/s)	Phase III rel. (mg)	Rate III (Kg/s)
CsI	1.12	0.87	2.15	0.615	7.7e-10	1.07	3.07e-10	0.43	2.87e-10
In	89.68	0.20	17.94	5.38	6.41e-09	8.97	2.95e-09	3.59	2.39e-09
Cd	29.3	0.87	15.29	4.59	5.16e-09	7.65	2.18e-09	3.06	2.04e-09
Sn	48.48	0.55	27.21	8.16	9.72e-09	13.6	3.89e-09	5.44	3.63e-09
CsOH	17.27	0.84	5.27	0.74	8.78e-10	3.21	9.18e-10	1.32	8.78e-10
Mo	20.17	0.56	8.33	1.17	1.39e-09	5.08	1.45e-09	2.08	1.39e-09
Te	2.54	0.83	2.11	0.295	3.51e-10	1.29	3.67e-10	0.53	3.51e-10
Ag	478.31	0.155	74.14	8.90	1.06e-08	46.7	1.33e-08	18.5	1.24e-08
Re	482.2	0.155	74.74	8.97	1.07e-08	47.1	1.35e-08	18.7	1.25e-08
U	9163.0	0.0014	12.83	0.0	0.0	0.0	0.0	12.8	8.55e-09
CdO	29.3	0.87	11.65	3.5	4.16e-09	5.83	1.66e-09	2.33	1.55e-09
Cs_2MoO_4	17.27	0.84	13.23	1.85	2.2e-09	8.07	2.31e-09	3.31	2.20e-09

Several observations can be drawn from Table 5-7. First, the percentiles are related to the initial inventory. Second, the deposition occurred mostly in the vertical line and steam generator, with small fractions depositing in the hot and cold leg. Third, the uncertainties presented for deposition are experimental uncertainties (result of measurement methods uncertainty), i.e., the release uncertainties, which sometimes, as for Ag, is large were not carried to the deposited uncertainties.

Using these observations, the fractions were corrected to be expressed as function of the released masses, and a procedure was set to correctly consider the uncertainty. The uncertainty correction was just applied to the steam generator and vertical line, because they constitute the bulk of the deposition. The new uncertainties were obtained considering the range of variation of the released masses and depositions that means, the upper limit of the released fraction with the lower limit of the deposition fraction to obtain the lower limit of the deposition fraction. The opposite operation was performed to obtain the upper limit of the deposition fraction. For the steam generator, the deposition uncertainty was the same relative uncertainty of the vertical line.

As mentioned earlier, for some species (Cd, Sn, and In), the release fraction is not available, and release rates of similar elements (established by vapor pressures comparison) were assumed. The vertical line deposition fraction was calculated using the assumed release fractions and the known hot leg transported fractions. The result of these assumptions and operations is presented in Table 5-15.

Table 5.15- Experimental fractional deposition (% of released mass)

	Vertical Line	**Steam Generator**	**Hot Leg**	**Cold Leg**
Cs/Rb	30.6±2.6	13.5±0.6	4.16	0.71
I	6.1±1.2	22±4	0.23	0.89
Re	48.4±8.4	12.5±3.2	1.30	3.60
Ag	48.4±8.5	12.5±3.3	1.30	3.60
In	55±5	9.5±0.9	NA	3.00
Cd	23±3	18±1.7	NA	0.90
Te	31.3±2	11.4±1.3	2.10	0.60
Mo	39.9±5	12.3±1.9	NA	0.90
Sn	48.4±4.1	10±1.1	NA	0.9

The presentation of the comparison of the mass balance for the considered elements is divided into four major groups, because of the different behavior and importance of these groups. The nucleating group (Ag and Re) includes the species that nucleate aerosols. The structural materials group includes materials from control rod and cladding (Sn, In and Cd). The fission product species (Cs, Mo, I and Te) are divided into the group that speciation was pre-defined (Cs and Mo) and the group that speciation was not worked (I and Te).

Figure 5-17 presents the results for Ag and Re, the nucleation species. For these species, the results were very good, being in accordance with the experimental data. Part of this good performance is due to the procedure of changing the nucleating species density to match the condensation on the vertical line, but a good agreement was also encountered in the other sections of the experimental circuit, especially on the steam generator, which is the second more important section, in terms of deposition. Hence, some credit must be attributed to the code performance.

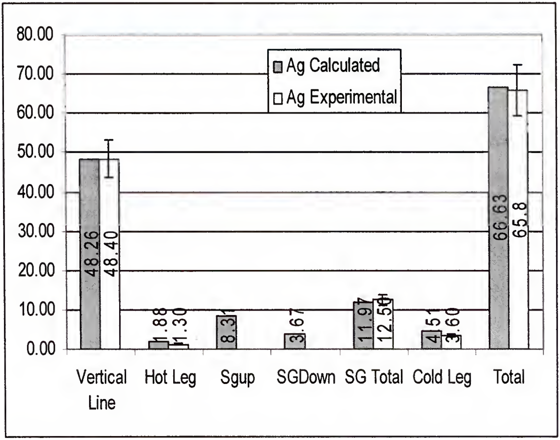

(a)

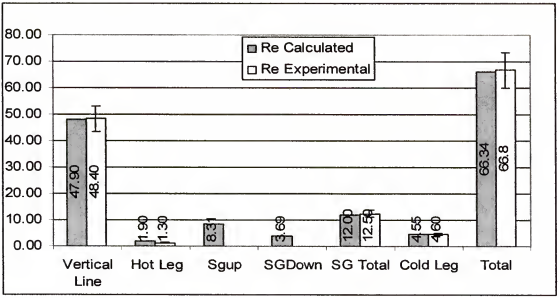

(b)

Figure 5-17. Comparison of predicted and experimental deposition fractions (%) for the nucleating group along the experimental circuit: (a) silver; (b) rhenium

In the vertical line most of the deposition occurred by condensation on the structural surface (more than 95%). In the other sections of the experimental circuit, deposition occurred basically in the aerosol form. Great amount of deposition occurred on the steam generator up section (8.31 %), due to thermophoresis, as expected (reported in the Phebus ISP-46 report). Considerable deposition was also registered both in the experimental data and in the calculation on the cold leg. All the calculated values are matching the experimental data, within the range of experimental uncertainty.

The deposition fractions for the structural species are presented in Figure 5-18. As a general conclusion of the predictions of the structural materials, it can be observed that condensation onto structural surface of the vertical line was over-predicted by the code, meaning that the problem is caused by the wrong speciation or the kinetics of the structural condensation. Since Sn and In have saturation concentrations similar to their oxide form, it is more likely that the kinetics of the condensation onto structural surface needs some reduction to match the experimental data. Both laminar and turbulent regimes occur in the vertical line, but most of the condensation occurred under the laminar regime. In addition, condensation was predicted higher in other sections where turbulent regime prevails. Hence, it is not possible to determine under which regime over prediction occurred, but the most likely answer is both.

Once it is most likely that the over prediction occur in both regimes, the problem probably is not in the models, but in the vapor diffusivity in the bulk gas. Another indication that this could be a source of the problem is the small-to-medium difference encountered, meaning that variations in the diffusivity can lead to this over-prediction. Once the diffusivity depends on the speciation, as they depend on the Lennard-Jones parameters, wrong speciation can affect both directly (more volatile species do not condense) and indirectly (through the vapor diffusivities) the condensation kinetics. In addition, because the most of the Lennard-Jones for oxide species, are not available, the diffusivity was calculated with the elemental Lennard-Jones parameters.

Investigation of this small-to-medium deviation from the experimental prediction needs to be addressed with a thermo-chemical database and experimental observations, to evaluate the most probable species, a Lennard-Jones database to obtain the correct diffusivities, and a consistent experimental database to evaluate the several possibilities. In this way, it can be better understood the reason for this deviation, and a consistent correction procedure can be set. As mentioned earlier, speciation is not part of this work, but has intimate relationship with the results. Therefore, it is the most important work to be done in the maturing process of the developed fission product model.

The indium mass balance, Figure 5-18 (a), shows that the code calculated that about 62 % of the released mass condensed on the vertical line. In the steam-generator, almost 12% deposited on the steam generator up section, some of them by condensation (3%). In the steam generator down section about 2% deposited by aerosol deposition, adding up 14% in the steam generator, which agrees with the experimental data. A good agreement was also encountered in the cold leg aerosol deposition. Therefore, the total deposition predicted is about 10% higher than the mean experimental value and 3% higher than the upper limit of the experimental range of values. Notice that less deposition on the steam generator, would be expected, because more mass condensed on the vertical line, and less mass was left over to deposit on the other sections, but as the condensation kinetics seems to be faster in the calculation, there is a compensation.

Tin (Figure 5-18(c)) has the same behavior of indium, but with a larger difference of the experimental and calculated values, being the difference of about 18%. On the steam generator up section, about 8% of the released mass deposited, being half of this under condensation. Two percent deposition was calculated on the steam generator down section yielding a good agreement with the experimental data for the steam generator. Another two percent deposited on the cold leg, according to the prediction. The difference in the vertical line is transferred to the total deposited, resulting in a total difference of about 20 % positive from the calculated to the experimental data.

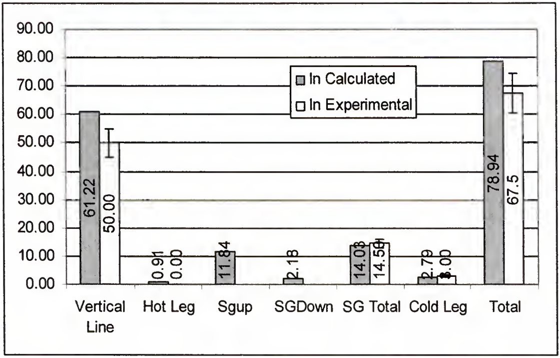
90.00
80.00
70.00
60.00
50.00
40.00
30.00
20.00
10.00
0.00
▨ In Calculated
☐ In Experimental
61.22
50.00
0.91
0.00
11.84
2.18
14.03
14.50
2.79
3.00
78.94
67.5
Vertical Line
Hot Leg
Sgup
SGDown
SG Total
Cold Leg
Total

(a)

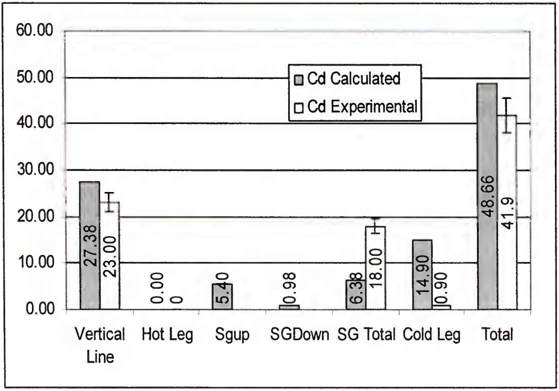
60.00
50.00
40.00
30.00
20.00
10.00
0.00
▨ Cd Calculated
☐ Cd Experimental
27.38
23.00
0.00
0
5.40
0.98
6.38
18.00
14.90
0.90
48.66
41.9
Vertical Line
Hot Leg
Sgup
SGDown
SG Total
Cold Leg
Total

(b)

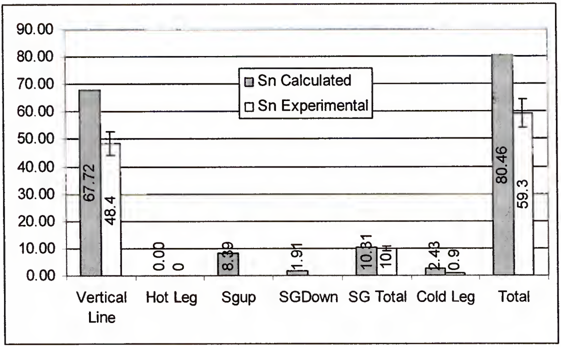

(c)
Figure 5-18. Comparison of calculated and experimental deposition fractions (%) for the structural materials group along the experimental circuit: (a) indium; (b) cadmium; (c) tin

Cadmium was transported part in the oxide form, and part in the elemental form (half-to-half), having a different dynamics from tin and indium. The cadmium oxide condensed on the vertical leg (about 60%) resulting in a deposition fraction of 28 %, a little higher than the experimental data. In the steam generator, there was deposition of 6% of the cadmium-released mass on the steam generator. Five percent deposited on the steam generator up section (75% in the condensed form), and close to one percent deposited in aerosol form on the steam generator down section. This steam generator total is well below the experimental value.

An explanation can be encountered in the observation of the cold leg deposit. Strong deposition occurred on the cold leg (14 %), corresponding to the condensation of elemental cadmium. Adding up the steam generator depositions with the cold leg deposition, the prediction becomes within the experimental uncertainty width. What probably occurred is that the cadmium actually condensed in the steam generator, but in the calculation, because of errors in the surface temperature or saturation concentration, the condensation was only predicted in the cold leg. The total calculated is a little higher than the experimental data (about 6 %).

Figure 5-19 contains the mass balance for the fission products cesium and Molybdenum, the fission products that incorporated some knowledge about speciation. Cesium was transported as cesium iodide, cesium molybdate (70% of the remaining mass of cesium iodide) and cesium hydroxide. Molybdenum was transported as cesium molybdate and elemental molybdenum.

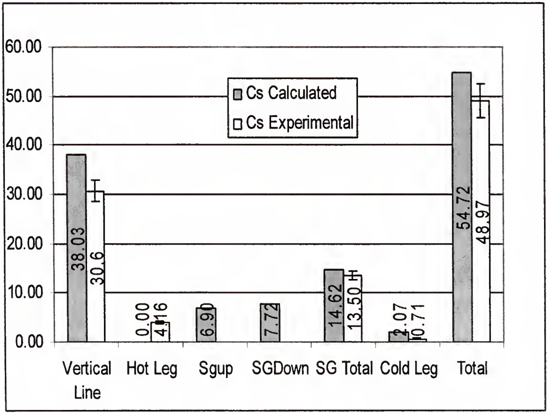

(a)

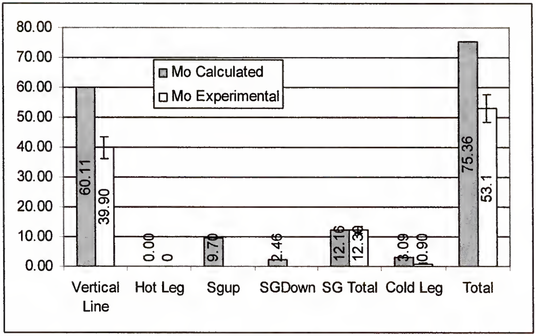

(b)
Figure 5-19. Comparison of calculated and experimental deposition fractions (%) for the first fission product group along the experimental circuit: (a) cesium; (b) molybdenum

Cesium, in the form of cesium molybdate condensed on the vertical line, resulting in a condensation fraction of about 38 % for the element. In the steam generator up section, there was a deposition of cesium molybdate through condensation (about 60 % of the deposited mass) and aerosol deposition, adding up the deposition of 6.9% of the released mass. Differently from the species so far presented, there was more deposition on the steam generator down section than on the up section. This occurred because Cesium Iodide condensed on the structural surfaces of this section, resulting in an elemental deposition of 7.7%. In this way, the total predicted mass for cesium in the steam generator has good agreement with the experimental data.

Differently from the calculation prediction, Table 5-7 shows that more deposition occurred on the steam generator up section. It is not possible to determine the exact reason for this discrepancy. It can be originated from a wrong speciation, or a late prediction of Cesium iodide condensation in the calculation, due to errors in the saturation concentration expression or in the structural surface temperatures. However, for Cesium, clear evidences that the speciation is consistent exist. Hence, the second hypothesis is more likely.

In the cold leg, the prediction was little above the experimental data. Adding together all the depositions along the experimental circuit, the prediction of the code stayed 3 to 5 % above the experimental total. Therefore, the prediction for cesium was good.

The predictions for Molybdenum on the vertical line were about 20 % higher than the experimental value. The behavior of molybdenum deposits is very similar to the behavior of tin. Hence, the analysis of the overall mass balance is equivalent to the tin analysis, presented previously. In this analysis, it was shown that speciation or the adopted correlations for the condensation can be the cause, being more likely the speciation, acting directly (through the absence of a more volatile species), or indirectly, through the use of the wrong vapor diffusivity.

For the steam generator good agreement, the same argument used for indium can be used, i.e., the rapid condensation compensates the absence of aerosol deposited mass, leading to a good agreement in the steam generator total deposited mass. Therefore, equally to Tin and Indium, this difference was carried to the total, which stayed roughly 20 % above the experimental data.

Figure 5-20 presents the results for the fission products that were transported without any elaboration, Iodine, transported as Cesium Iodide, and Tellurium, transported in its elemental form. These elements were purposely chosen to be transported under this speciation to show the direct importance of the speciation.

For both there was no condensation on the vertical line, whereas experimental data shows that it happened, which is a clear indication that, at least, fraction of them is transported in a less volatile species.

Tellurium violently condensed on the steam generator up section. This high condensation is an additional indication that the condensation is over predicted. It also occurred because of the length of the steam generator up section, and because the amount of aerosol is reduced by the strong deposition i.e., most of the condensation onto aerosol structure occurred in the hot leg, and, as long as they deposit in the steam generator, the aerosol number of particles is reduced. The dynamics of tellurium predicted were, therefore, completely different from the observed, leading to a very bad prediction.

Similar behavior was predicted for iodine. It also violently condenses, but on the steam generator down section, where the saturation conditions for cesium iodide were reached. The reason is the same described for Tellurium, and also a very bad prediction was performed by the code.

The comparison of calculated and experimental deposition fractions for iodine and tellurium is the proof of the already mentioned importance of speciation in the calculation of fission products deposition. Elements where the speciation was addressed with some consistency had good or reasonable predictions, whereas the prediction was completely wrong for these two species.

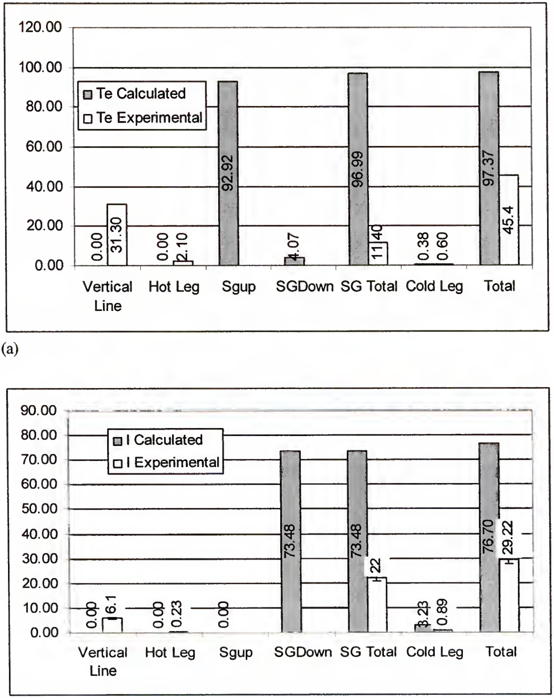

Figure 5-20. Comparison of calculated and experimental deposition fractions (%) for the second fission product group along the experimental circuit: (a) tellurium; (b) iodine

In general, the calculation showed that the developed model has the potential to consistently and reasonably well predict the fission product deposition onto the piping system of the Phebus FPT-01 experimental circuit, since the correct speciation is used. This is particularly true given the approximations and assumptions used in the modeling of the experiment. Very good results were obtained for silver and rhenium. Good results were obtained for indium, cadmium, and cesium, although some questions were raised about the speciation of cadmium and cesium. Reasonable results were obtained for tin and molybdenum, and very bad results were encountered for iodine and tellurium.

Condensation onto structural surfaces was found to be over-predicted. Possible causes were raised: the accuracy of the used correlations, or speciation, through direct actuation, i.e., the definition of correct low volatile and volatile species and mass transported fractions, or indirect actuation, affecting the vapor diffusivity of the element in the bulk gas. Therefore, speciation and an investigation about the cause of the over-prediction of condensation need to be addressed consistently for the completeness of the model.

The nucleation model also showed to be extremely sensitive, especially to the terms in the exponential of Equation 3-85: the surface tension, the monomer surface area, and the gas temperature. Small changes in these properties affect significantly the nucleating rate, affecting the deposition kinetics. More evaluations need to be done to verify the necessity to make adjustments in this model to deal with the uncertainties of the properties above mentioned, specially the surface tension.

The aerosol composition is compared in Figure 5-21. The aerosol composition varies with the transient phase, as shown in Figure 5-10. For simplicity, it was assumed as the average particle composition the approximated description of this chapter section that presents the remarks on the fission product results of the Phebus FPT-01 experiment. The calculated composition is based on the aerosol deposited masses, which is a better representation of the average composition throughout the transient.

The mass composition of the aerosols could be determined from the quantitative chemical analyses of the dissolved aerosol samples, by ICPAES/ICPOES or ICPMS and by qualitative aerosol characterization techniques such as scanning electron microscopy used in the energy dispersive analysis mode (SEM/EDX) for some of the point C and point G sequential samplings. The second method (electron microscopy) is qualitative since, firstly, the analysis was performed on small sub-samples (usually obtained by stubbing) and secondly, it only probes the surface layers of the aerosols and thus may not be representative of the bulk composition.

One should also be aware that the list of elements measured by these two techniques is not complete, and the results obtained by different techniques are not equivalent. The following points should be considered when interpreting the results: (a) In was not measured accurately by ICPMS (filter results); (b) Cs could not be determined by ICPMS, Cs results were deduced from Cs_{137} γ-spectrometry measurements of the samplings; (c) U/Cd separation using SEM/EDX is rather difficult and may produce inaccurate results for these elements; (d) Determinations of elements such as Zr, I, Pu, Pb, Tc, Rb, Te, W and Al which represent a few % of the weight are often close to or under the detection limits of the methods; (e) O, which may represent a significant fraction of the mass (oxidized material), cannot be measured by the methods used.

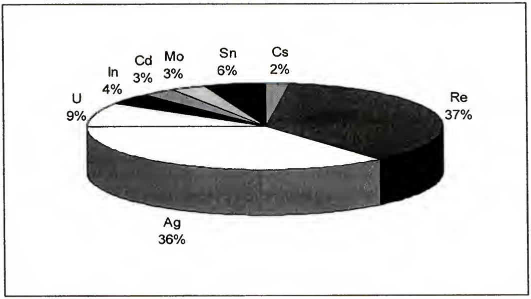

(a)

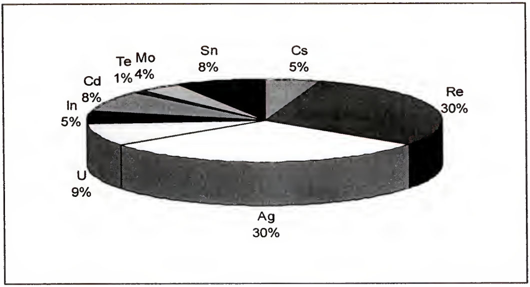

(b)

Figure 5-21. Aerosol composition: (a) calculated; (b) experimental

Figure 5-21 shows that the aerosol calculated and experimental composition are distinguished by the greater amount of nucleating species in the calculated aerosol composition than in the assumed approximated composition. This greater presence naturally reduced the amount of other species for the calculated composition. Given the high degree of approximation for the assumed experimental composition, and the uncertainties of the experimental result, the code predictions did not present any significant anomaly that deserves analysis. Cadmium and cesium were the species that present the greater difference, but the origin of this difference could be attributed to the degree of approximation, especially given the difficulties in the measurement of these elements above described.

Aerosol size distribution experimental data was collected during the experiment in the hot leg, cold leg and the containment. These collections were possible through the use of inertial impactors, which collect different size particles on different target plates.

These impactors results in the circuit provide, in principle, by the measured collected mass distribution on the various impactor target plates, a mean of determining the AMMD and the standard deviation of the distribution. An accurate determination is, however, only possible if the aerosol carrier gas flow rate entering the impactor apparatus is well controlled and if the mass distribution results are not biased by over-loading of the plates. The impactor functioning in the FPT1 circuits was not optimal with respect to those two conditions. Steam condensation in the sampling lines, downstream of the impactor, leading to the flow meter resulted in unstable mass flow rates, and aerosol mass concentrations transported through the experimental circuits over-loaded the plates.

Despite these drawbacks, the obtained data were analyzed assuming that the aerosol particles were homogeneous in composition, in shape and that they followed a uni-modal log-normal mass distribution. Under these assumptions, it was shown that the aerosol AMMD was between 1.3 and 2.0 μm, varying with the transient time in the hot leg of the circuit (point C impactors) and was of the order of 1.4-2.5 μm in the cold leg of the circuit; the standard deviation of the log-normal distribution was close to $\sigma_g \approx 1.5$ μm.

The assumption of log-normality for the aerosol mass distribution was examined in more detail for the less loaded impactors, i.e., at point C and at point G. The masses collected on the impactor plates calculated from the log-normal mass distribution fit are compared with the experimental data of the plates. The agreement is quite satisfactory for the point G impactor, but is less satisfactory for the point C impactor.

This result is not surprising since, in the circuit hot leg, the characteristics of the aerosol population are probably complex as a result of on-going particle agglomeration processes and on-going condensation of species which are still partly under a vapor form at this location in the circuit. Also, it cannot be excluded that the actual population of aerosols could deviate from the log-normal description or could be multi-modal, i.e. the superposition of two or more populations. Vapor species may also react chemically with metal components of the impactor plates.

Therefore, for several reasons, the experimental data cannot be used to do an extensive and profound analysis. The data of the hot and cold leg was used here just to provide an idea of the code performance, referring to the aerosol growing processes, the agglomeration and condensation of vapors on aerosol surface.

Two comparisons were performed, the first one for the hot leg, corresponding to the sampling time between 13,809 and 14,101 transient seconds, and the second one for the cold leg, during the late oxidation phase (after 16,000 seconds). The comparisons were performed using the mass of Ag distribution into the sections of the calculations, and the mass of Ag deposited in the plates of the experimental data. The procedure was to calculate the AMMD and the variance of the density function of the distribution of the weight fraction of Ag as function of the particle diameter.

Equations 5-3 and 5-4 were used to calculate, respectively, the AMMD and variance of the experimental and calculation distributions. These expressions correspond to the formulas used in discrete distribution functions to obtain these parameters. After calculating them, the density function of the distribution was calculated for several particle diameters, using Equation 5-5. The distribution function was obtained for several sections of the particle diameter spectrum, from 0.5 to 5 μm.

$$AMMD = \frac{\sum_{i=1}^{N} w_i d_{p,i}}{\sum_{i=1}^{N} w_i} \qquad \text{(Equation 5-3)}$$

$$\sigma^2 = \sum w_i \left(d_{p,i} - AMMD\right)^2 \qquad \text{(Equation 5-4)}$$

$$f(d_p) = \frac{1}{\sqrt{2\pi}\ln(\sigma)} \exp\left(-\frac{\left[\ln(d_p) - \ln(AMMD)\right]^2}{2\left[\ln(\sigma)\right]^2} \right) \qquad \text{(Equation 5-5)}$$

Table 5-16 presents the AMMD and the standard deviation for the calculation without synergetic model, the calculation with the synergetic model activated, and for the experimental data. Figure 5-22 presents the Ag weight distribution function for these three cases for particles from 0.5 to 5μm in the hot leg.

Table 5-16 shows some important observations. First, the code under-predicted the aerosol growth, especially in the cold leg. It is not possible to precise the extent of this under-prediction because of the uncertainty of the experimental data, notably in the cold leg where the sampling flow rate of the first impactor, was very irregular (probably as a result of steam condensation in the sampling line) and some of the impactor stages proved to be overloaded (48). Since the major difference was encountered in the cold leg, it is difficult to precise the extent that the calculation is under predicted. However, a biased behavior was identified, which is probably an indication of the growth processes (condensation and agglomeration) models performance. Furthermore, it should be noted that the discretization level of the experimental data is very low (5 nodes), whereas the size spectrum of the impactor was calculated for 30 sections.

Table 5-16. Comparison of log-normal distribution parameters from predicted and experimental data for Ag weight as function of particle diameter

	Hot Leg			Cold Leg		
	Calc. without synergy	**Calc. with synergy**	**Experimental**	**Calc. without synergy**	**Calc. with synergy**	**Experimental**
AMMD	0.956	1.098	1.376	0.59	0.675	1.57
σ	0.231	0.365	0.975	0.241	0.258	1.45

The usage of the synergetic model was important, once it approximated the predicted value to the experimental data. Nevertheless, it was not enough to match the experimental data. Innumerous causes can be speculated for this under prediction, but it is very difficult to determine it, since in could be caused by both the condensation and/or the agglomeration model. In addition, external parameters like the total number of particles, and minimum particle size can affect the calculation.

One of the possible causes of this under-prediction is the fact that some important aerosol components (Sn, In) were transported in its elemental form. Since the oxide form has a considerable lower density than its elemental form, the volume would be greater, if they were transported in the oxide form. Hence, speciation also impacts in the aerosol size.

The study of this discrepancy should not be a priority, because the encountered difference level has a very small impact in the deposition, that means, the difference in the deposition velocities for these two AMMD (for calculated and experimental) is small. Nevertheless, it can be listed as a fine tune-up activity for the model.

Figure 5-22 illustrates how these distributions are. It can be noticed that the experimental data has a considerable larger standard deviation, which is consequence of the small amount of experimental data available to determine the distribution.

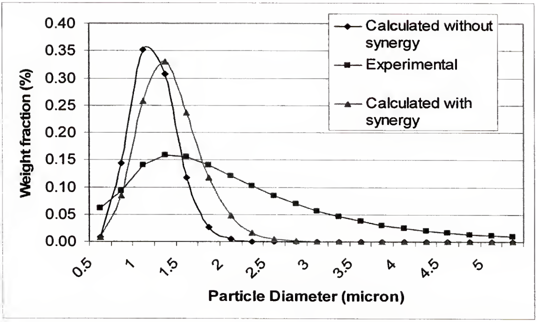

Figure 5-22. Silver weight distribution function comparison of calculated and experimental data

The dynamics of the deposition was analyzed plotting the deposited masses (mg) as function of the position in the experimental circuit. One species of each group (nucleating species, structural materials, and the two fission product groups) was chosen to represent the group behavior. This spatial dependent profile is presented in Figure 5-23.

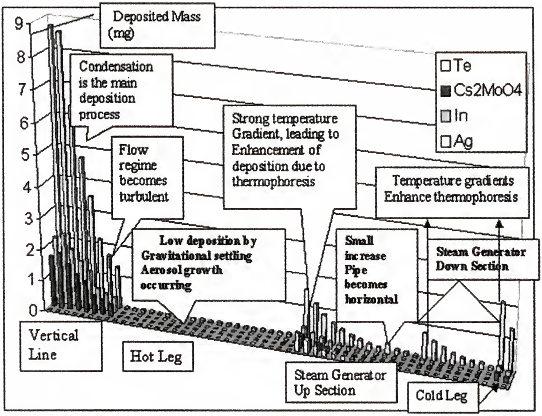

Figure 5-23. Dynamics of the deposition in the experimental circuit for several species

Figure 5-23 provides a general view of the main deposition characteristics of each section. First, the silver behavior is explained and then difference for other species are highlighted and explained. The bulk of the deposition, as mentioned before, occurred on the vertical line through condensation onto the piping structure. The condensation occurred violently in the first two cells of the vertical line, which, in the model, corresponds to the upper plenum, agreeing with the experimental observed behavior. Then, in the following cells, the deposition reduces significantly. When the last two cells are reached, the flow regime changes from laminar to turbulent. As consequence, the condensation deposition velocity has an increase. However, there already was, at this location, considerable mass depletion. Consequently, this increase in the deposition velocity could not be felt in terms of absolute masses. Nevertheless, the relative decrease in the deposition masses was less in these two last cells. The instrumentation apparatus of the vertical line, as shown in Figure 5-24 (48), registered this behavior. The figure shows the activity of Ag^{110m} in the vertical line, obtained by γ spectroscopy.

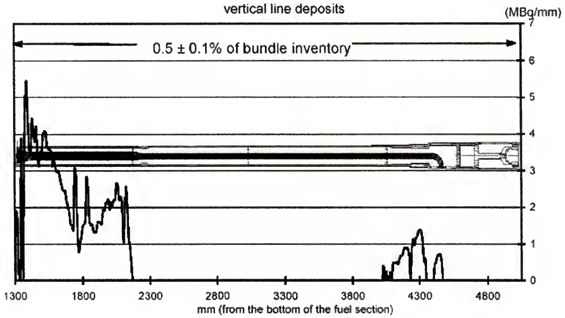

Figure 5-24. Activity of Ag^{110m}, obtained by γ spectroscopy

In the hot leg, the deposition was quite low due to, mainly, aerosol gravitational settling. Condensation and thermophoresis did not occur due to the high temperature of the hot leg piping. During the hot leg transport, aerosol growth by both condensation and agglomeration dominated.

When the steam generator up section is reached, the piping temperature reduces significantly, causing the deposition by thermophoresis to be triggered. This deposition mechanism is higher than the other mechanisms, which agrees with the behavior described previously. As the temperature of the gas and the mass of aerosol available decreases, as long as the gas-aerosol mixture flows through the steam generator up section, the amount of deposition decreases significantly. A small increase is registered in Figure 5-23. This increase occurred because it corresponds to the steam generator section that is in the horizontal orientation. The horizontal orientation leads to an enhancement of the aerosol deposition due to gravitational settling.

In the steam generator down section, and cold leg, the same dynamics of the steam generator up section occurred, i.e., by entering these sections, the gas-aerosol mixture encounters lower piping temperatures, enhancing the thermophoretic deposition, resulting in a relative (to the previous cell) increase in the deposited mass. Following the entrance, the deposited mass gradually reduces due to decrease in the thermal gradient and mass depletion.

The experimental observation that approximately 85% of the aerosol deposition occurred in the steam generation up section was well predicted by the calculation. The relative amount of aerosol deposited can be estimated observing the percentiles of mass deposition on the steam generator up and down sections of the elements most presents in the aerosol composition (Ag,Cd,In,Sn). These elements results indicates that approximately 83 % of the aerosol mass was deposited on the up section.

Cesium molybdate and indium followed the silver behavior. The only noticeable difference is that the reduction in the deposited mass is not steep as for Silver for the vertical line. This is expected since the diffusivities of Indium and Cesium Molybdate are lower than the Silver diffusivity. Consequently, the deposition is slower, remaining more mass to deposit in the next cell. Tellurium has a completely different dynamics due to its assumed erratic speciation. The deposition occurs in the steam generator up section, by condensation, similarly to the Silver behavior in the vertical line.

The predicted dynamics of the considered species is completely consistent with the experimental observations for the species that the predictions are reasonable (not the case of iodine and tellurium). This is an additional indication that the code performance is good, since the major deposition mechanisms were correctly predicted, as well as the spatial profile of the deposition.

In this chapter, it was seen that several experiments can be used in the process of adjustment and validation of the model developed. The Phebus FPT-01 experiment was chosen to be used in a preliminary assessment due to its degree of elaboration, and the great amount of experimental information available.

A Scdap/Relap model for the experiment was developed, applying several simplifications and assumptions, notably in the fission product release process representation. This model presented a good performance in predicting severe accident parameters. The most important, regarding the fission product transport, are the gas temperature in the cold and hot leg, and the hydrogen generation resulted from zirconium oxidation.

In general terms, the fission product predictions can be considered rather satisfactory, in terms of mass balance, for the elements that received a speciation treatment, given the approximations of the model developed.

The results showed two major discrepancies in the comparison of predicted and experimental data. First, the nucleation calculation showed to be a very sensitive calculation. However, it was possible to obtain a very good prediction of the nucleation (indicated by the correct prediction of the vertical line condensation of the nucleating species), by setting the density of the nucleating species to an intermediate value between the Silver and Rhenium densities. A consistent procedure, possibly adjusting the model, as done in this model, needs to be set. The whole set of six experiments of the Phebus program can be used, but the Phebus experiments have the inconvenient of the rhenium presence.

The second discrepancy is an indication that condensation is over-estimated, particularly for some species. An investigation needs to be set, to determine whether this discrepancy is caused by erratic-used speciation, resulting in wrong saturation concentration or wrong vapor diffusivities, or is result of deviations in the used models. Then, the cause of the problem needs to be consistently addressed, through adjustments or replacements of the wrong assumptions or models.

Regarding aerosol composition, some deviations, notably in the under-predicted cesium and cadmium contents were encountered. These deviations cannot be attributed to deviations in the aerosol condensation model, once there is a high degree of uncertainty in the experimental data, and the comparison is based on coarse approximations.

The aerosol sizing analysis showed that probably the predictions are little lower than the experimental data. However, the aerosol size distribution is less important for the mass deposition prediction. Certainly, the encountered level of deviation (Table 5-17) does not affect the aerosol deposition significantly. The synergetic model contributed significantly bringing the prediction closer to the experimental data. The synergetic deposition model could not be evaluated, given that most of the deposition occurred in the vertical sections of the steam generator.

The purpose of the chapter to define a body of experiments that could be used to adjust and validate the developed model, and perform a preliminary evaluation of the model was achieved. More important than the quantitative results obtained are the conclusions that can be drawn from the chapter, which are following enumerated: (a) There is a considerable amount of experimental data that can be used to adjust and validate the code; (b) Speciation is a key issue for the good performance of the code; (c) The program has the potential, if adjusted (adjustment would involve speciation definition and model adjustment), to predict consistently and satisfactorily, depositions in the primary coolant system, and the fission product states (vapor or aerosol), as well as aerosol characteristics (size and composition); (d) The aerosol nucleation model needs to be adjusted, through experimental data, given its high sensibility to the exponential term of Equation 3-51; (e) Condensation on structural surfaces possibly is being over-predicted by a small extent, needing an extensive and profound analysis, that would involve speciation, thermo-chemical database, and the models used.

CHAPTER 6
CONCLUSIONS

Scdap/Relap5 is the most world-widely used best-estimate code in the nuclear community. The development of the code started in the seventies, with the purpose of providing a best tool to estimate thermal-hydraulic parameters for design-basis accidents of LWRs. After the events of Chernobyl and TMI-2 accidents, there was a mobilization of the nuclear community to enhance the knowledge and tools to predict the behavior of nuclear power plants under severe accident conditions, especially the core degradation and radioactive materials release, including the fission products. As part of this effort, Scdap was coupled to the Relap code, providing additional capabilities to the code, including the zircaloy oxidation model, the modeling of the dynamics of the debris and molten material formed, and the pressure vessel failure. An attempt was made to model the fission product behavior, which has failed.

The fission product behavior, as seen in Chapter 1, is divided into three major fields, the release from the fuel, the transport in the primary coolant system, and the chemistry of the several elements present in the reactor, in the fuel and primary coolant system.

This research reassesses the issue of the fission product transport, to incorporate this module to Scdap, enhancing the code capability. Since the code is the most widely used, having several experiments and nuclear power plants being modeled, it has the ideal conditions to augment the incorporated model through extensive usage, feedback, and improvements by the several users throughout the world.

Considerable contributions to the nuclear community can derive from this developed tool. Among these contributions, is the capability of the improvement of the quality and accuracy of the containment source term in severe accidents, increasing the reliability of probabilistic safety assessment level two (PSA level 2), which estimates the severe-accident external source term. In addition, the developed tool can be used to improve and develop severe accident mitigating devices. The severe-accident management procedures can also be improved, through the execution of simulations of different management procedures, and comparison of the results, to verify which one yields a smaller source term.

Although mechanistic models of fission products behavior in the core and in the primary coolant system have been developed, regulatory source terms to the containment used in various countries are still based upon simplistic assumptions. For instance, the fission products are assumed to be released in the form of aerosol, but no information about the size of the aerosol is provided. In addition, these source terms are fixed, but not dependent on the accident scenario. A comparison is established of the containment source terms in various countries and the experimental and code calculated source terms for the Phebus FPT-01 experiment. The source terms were obtained from survey made by a NRC established team (146). To the comparison is added the alternative source term, NUREG-1465 (147). This alternative source term is based upon the results of several simulations of different NPPs in the United States, using mechanistic procedures. The NUREG-1465 is a more elaborated containment source term, because it is based on mechanistic simulations, but still does not depend on the accident scenario. The result of this comparison is presented in Figure 6-1.

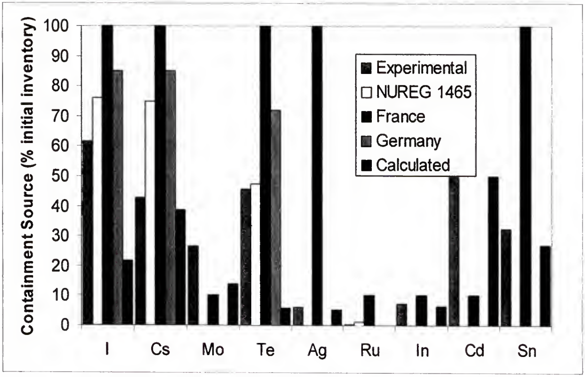

Figure 6-1. Comparison of different regulatory containment source terms with the experimental data and calculated values for the Phebus FPT-01 experiment

The United States, Japan, and Sweden do not have containment source terms, but only environmental source terms (the amount released from the containment to the environment). Several observations can be drawn from Figure 6-1. First, France and Germany have very conservative source terms. The NUREG-1465 term can be considered more realistic, when compared to the experimental results, reflecting the higher degree of elaboration of this method.

Regarding the performance of the developed model predictions, the predicted values were closer to the experimental values than any other source term. In general, a little under-prediction of the experimental values was observed. As pointed out in Chapter 5, this is result of the small over-prediction of structural-vapor condensation. The exceptions are iodine and tellurium, which were left with a poor speciation treatment to show the importance of speciation for the fission product behavior. Therefore, their result can be disregarded.

The usage of a mechanistic tool to predict the containment source term has the potential to provide much more accurate results. Furthermore, additional information, such as aerosol composition, and size distribution are available using this type of tool.

The development of the fission-products transport model was consistently achieved, through the accomplishment of the following steps: (a) Historic survey of the developed models, methods and techniques in the fission-products behavior field; (b) Definition of the mathematical model that represents the fission products transport; (c) Selection and development of models to represent the several phenomena affecting the fission products; (d) Implementation of the model in the code; and (e) Preliminary assessment of the code, through the modeling of the Phebus FPT-01 experiment.

The strategy adopted by the nuclear-scientific community to enhance the knowledge and prediction capability of the fission products behavior in severe accidents, is presented in Chapter 1. Progression occurred separately in each separate discipline, which are coupled as shown in Figure 2-1. In the fission products-transport field, important developments occurred in the area of the mathematical setting of the problem, and in the phenomenological modeling.

The major issues in the mathematical modeling of the problem are the aerosol agglomeration and condensation of vapors onto its surface. They imply an additional discretization, the aerosol size, since these processes are dependent on this parameter. To concatenate aerosol growth by these processes can be troublesome. Some models were developed, based on different techniques. CHARM (21) and MAEROS (22) are finite-element methods, used, respectively in Victoria and Melcor codes. Lemmon and Marwill (23) developed a discrete-ordinate model, which was used in this development.

In the phenomenological modeling activity, two early fission-products transport phenomenological packages were used as base for current codes. Trapmelt (15) was sponsored by the United States NRC, whereas RAFT (16) was sponsored by the EPRI.

Most of the models from these packages were improved or new models were developed afterwards, notably in the aerosol phenomena area, which has a wide range of applications, other than nuclear-engineering oriented. An assessment of the available models for all considered phenomena was performed in Chapter 3, and the best-fit selection was performed. New models were also presented.

Before start the development of the model, it was important to characterize the problem being modeled. The problem can be defined as a transport problem of multi-component vapor and aerosols mixed to a bulk gas, composed mostly of steam and hydrogen, through a piping system, surrounded by typical light-water-reactors geometry and materials, and under severe-accident thermal hydraulic conditions.

The geometry and structural material composition was obtained in Chapter 2, when light water reactors were described in terms of composition and dimensions, and were presented in Table 2-1 for a BWR, and in Table 2-2 for a PWR.

The more important thermal-hydraulic parameters for the fission-products transport are the flow regime, fluid velocity, fluid temperatures, structural surface temperatures, and the transient time. These parameters were obtained defining the most probable severe accident scenarios, and the variation of the thermal-hydraulic parameters during these scenarios. The information was collected from several published plant simulations of severe accidents, and was presented in Tables 2-3 and 2-4.

Another important information for the model development is typical calculation parameters. Since Scdap/Relap5 is a code used to solve thermal-hydraulic transients, the discretization of the problem being solved in space and time is governed by this solution. Hence, typical node sizes and time-steps are committed to the methods of solution of the thermal-hydraulic equations. Typical node sizes were obtained from the Scdap/Relap5 user's guide (42), and typical time-steps were obtained from code simulations. A summary of the more important parameters for the model development is presented in Table 2-6.

An overall picture of the fission product behavior is presented in Chapter 2. Departing from the fission process, it was shown how the fission products accumulate and behave in the fuel region up to the release instant. The release process was quickly described, stressing the most important release mechanisms, according to the fuel state. The release model constitutes the source for the transport calculation. The importance of the structural materials release in the transport was shown to be related to the formation of aerosols, which provides area for fission products condensation.

The importance of the chemistry of the fission products and structural materials among themselves, among them, and with bulk gas components, commonly referred in the field as speciation, was emphasized. The correct speciation of the elements in the problem is fundamental to provide the correct properties, such as vapor pressures, vapor diffusivities, surface tension and densities. Hence, it is a key issue, as became clear in Chapter 5, when elements that were calculated with poorly worked speciation had a bad performance when predicted results were compared to experimental data. A distinguishable attribute of the chemistry is that it should occur both in the fuel and transport zones. Therefore, the treatment should be consistent in the two zones.

Explaining the other two fields, it was possible to separate the phenomena that embody the fission product transport model, and what is the linkage with the release and chemistry. Figure 2-12 shows the inter-linkages of the fission products behavior disciplines, and their linkage with the calculations in Relap and in Scdap. Table 2-7 contains the phenomena that make part of the fission product transport model, the condensation and adsorption of vapors on structural and aerosol surfaces, the aerosol nucleation, agglomeration and deposition.

The fission products transport is modeled by defining a set of first-order differential equations that represent the several phenomena occurring in the transport process. For this purpose, states wherein the mass can exist are defined, and an equation for each state is derived, representing all processes that can add or remove mass of that state. These states are defined in the volume, or on the surfaces surrounding the volume. The volume states are the vapor, and aerosol in each of the sections defined by the aerosol discretization level. The surface states are vapor mass adsorbed, condensed, and mass deposited in the aerosol form. This set of equations is defined for each species, in each volume.

The vapor mass (state) in the volume, for instance, can be reduced by condensation on aerosol and structural surface, adsorption, and nucleation of aerosols. They can be added or reduced by convection, according to the rate that the mass enter and leave the volume. Proceeding the same way, it was shown that the volume states yield partial differential equations, due to the convective term, whereas the surface states yield ordinary differential equations. Therefore, the problem was defined, in Chapter 3, as a system of equations, involving partial and ordinary differential equations. The system is solved in each volume, and the number of equations depends on the number of sections and number of surfaces surrounding the volume.

The strategy adopted to solve this system was to separate the spatial dependent term (convection term), and to solve the problem using the fractional-steps method (Yanenko (54)). The discrete-ordinates method (Lenon and Marwill (23)) was used to treat the aerosol-size dependent terms. Thus, the problem was transformed into a system of ordinary differential equations, presented in Equations 3-15 through 3-19. The convection was performed separately, using a donored-cell technique. The nature of the system was studied, determining that the problem can, occasionally, be stiff. The backwards-differentiating method (Gear (56)) was chosen to solve the ODE system, because it is recommended for stiff problems, and the Hindmarsh (57) package was implemented to solve the ODE systems. The system solution was bounded by some constraints. The masses' non-negativity constraint is the most important.

An assessment was performed in Chapter 3 to determine the best models to be used for each of the phenomena involved in the equations, having as selection criteria the performance of the model in the range of thermal hydraulics parameters defined for the problem, and the adequacy to the equations and code philosophy and methods. Regarding the vapor phenomena, condensation onto structural surfaces was modeled using boundary-layer theory for the laminar-flow regime, and similarity with heat-transfer for turbulent-flow regime. The adsorption was modeled using empirical correlations. The condensation onto aerosol surfaces was modeled using diffusion theory, and near-continuum correction for the cases when diffusion theory is not perfectly valid.

Aerosol nucleation was modeled using the Girshick model (74), which showed more theoretical consistency, and present better performance, when compared with more elaborate methods results. A specific model was developed, surveying the most likely species that nucleate aerosols, and empirical evidence. Empirical evidence of the Phebus FPT-01 experiment and SFD experiments, showed a pattern in which the particles have as seed particles Ag and U. This information was used to calculate the nucleation only for these species. This model has limitation to PWR cases. In the future, an alternative model for BWR aerosol nucleation needs to be developed.

During the preliminary analysis of the Phebus FPT-01 model results, it was detected that the Girshick model is very sensitive to the dimensionless surface tension, which depends on the species density, surface tension, and gas temperature. Because of this hypersensitivity, the model should be more studied against experimental data, and the exact speciation of the nucleation species became very important, as well as accurate values of surface tensions. In a future work, improvements in the speciation and properties need to occur, and a deeper analysis of the impact of this hypersensitivity is necessary, searching for remedies for this problem. A very good prediction of nucleation was possible by performing a small adjustment in the nucleating species density.

The range of particles size was determined to be between 0.5 μm and 50 μm. The lower limit is associated to the minimum stable droplet diameter for Ag and U, under typical gas temperature of severe accidents. This approximate size was confirmed by empirical evidences of the SFD and Withfrin Laboratories experiments. To be more precise, this nucleating size would be represented by a log-normal distribution function, but a simplified procedure was adopted. The upper limit was chosen, because particles reaching that size will rapidly deposit, because their gravitational settling velocity becomes comparable with the fluid velocity.

Two major assumptions were used in the aerosol phenomena modeling. First, the aerosol was assumed as spherical. Although some empirical evidence exists, from the SFD and Phebus experiments that nuclear aerosols in primary coolant systems have a shape close to spherical, this issue remains uncertain, mainly because these evidences came from aerosol filters analysis, through SEM, and the effect of the flow on the aerosol shape could not be observed. The second assumption is the additive assumption, which states that the steady-state mass flux equation can be solved separately for each phenomenon, and the deposition velocity, or the agglomeration kernel can then be added. In Chapter 4, this assumption was verified not to be always true, and an optimized model was derived in Appendix B to treat the mode important synergetic mechanisms. The considered synergisms were the synergy of the Brownian diffusion and differential gravitational for the agglomeration processes, and the synergy between gravitational settling with thermophoresis and turbulent deposition mechanisms in a horizontal pipe. The synergetic model proved to be helpful in the Phebus prediction-experimental data comparison for the agglomeration case.

Deposition of aerosols onto primary circuit pipe walls was identified as possibly occurring by gravitational settling, thermophoresis, turbulence, inertial and diffusion. Diffusion was considered together with the laminar or turbulent model. Gormley and Kennedy (65) have obtained the exact solution of the steady-state mass conservation equation, which is employed in the model. For the turbulence model, in the non-synergetic model, the semi-empirical Sehmel model was selected, given its good performance, when compared to experimental data. For the synergetic model, the Crump and Seinfeld (139) model was used (Equation B-26). Thermophoresis was modeled using the Brock (103) expression, using Talbot (105) coefficients. The gravitational settling deposition velocity was obtained using the concept of particle mobility. Models were selected to calculate the deposition on bends contractions, separators, and driers.

The most important aerosol agglomeration mechanisms considered were the Brownian diffusion, the turbulent, and the differential gravitational. For the Brownian diffusion agglomeration kernel, the classical diffusion coefficient expression was used, corrected by the Fuchs and Stugin (69) factor for near continuum region. For the differential gravitational kernel, the differential gravitational velocity was used corrected by the Pruppacher and Klett (134) correction factor, to take into account intra-particle forces. The turbulent agglomeration kernel was modeled using the Lifschitz (62) method, based on eddy diffusivity theory. A re-suspension model, similar to the Parozzi (126) model, was implemented; even tough the model was derived for dry aerosols, which is not always true in severe accident depositions.

The developed model was compared with other fission products transport models in other codes. Table 3-11, which present the major features, in the mathematical solution of the problem, showed that the developed model is the only one using the discrete-ordinate method in the aerosol-size treatment. In addition, the developed model is also the only one that considers the fractional-step method when treating the convective term, i.e., other models simply decouple the convective term, although no justification was presented in their manuals for such procedure.

Table 2-13 and 2-14 present the comparison of the phenomenological modeling of the several models existent. This comparison shows that the developed model is the most complete model, having models for all the phenomena considered. Additionally, it is the only model that has a synergetic model, and, together with the Sophaeros is the only code that considers aerosol nucleation mechanistically.

The optimized-nucleation mechanistic model, and the aerosol optimized-synergetic model are special and unique models developed for best-estimate codes. Thus, they can be applied to other best-estimate codes, and constitute contributions to the field of fission products transport in nuclear power plants.

All the described models were implemented in Scdap/Relap5, obeying the programming principles and recommendations delineated in the programmer's manual (140). Three routines were used to read, initialize, and manage the whole calculation. The calculation was divided in three major activities, the solution of the ODE system, the convection of the masses, and the calculation of the coefficients of the system, being managed by three different sub-routines. A total of 29 sub-routines were used in the model.

The developed model was tested against two problems. During these tests, several verifications were done. First, the model does not affect other calculations of Relap and Scdap. Second, functional iteration proved to be more efficient than the Newton-Raphson iterative method for typical problems. Third, inertial deposition is not an important deposition mechanism for typical primary circuit geometries.

Sensitivity studies were also executed to determine the behavior of the model response to variations in the aerosol size- and spatial-discretization levels. The responses, at different sites of a typical LWR primary-coolant system model, were compared for different number of sections. The study showed that the response became stable faster for volumes far from the release sites. It was verified that satisfactory convergence occurred for 30 sections discretization level. One of the models was tested using a 20 and 40 cells discretization. It was estimated that the difference could reach five percent, for deposition masses, which is a significant difference. The results of these sensitive studies emphasize the necessity of elaboration of a guideline manual for the usage of the model that should join all the modeling-acquired knowledge about the model, as long as several users use it. The difference encountered in the re-nodalization study deserves deeper investigation.

An assessment was made, in Chapter 5, to identify the experiments that can be used to adjust and validate the model. These experiments were presented in Table 5-1. Phebus FT-1 experiment was chosen to perform a preliminary assessment of the developed model, because of the high degree of elaboration and great amount of information that the experiment offers.

A model was developed that predicts satisfactorily correct and consistently the experimental thermal-hydraulic parameters. The fission product transport was, then, incorporated to the model. In general terms, the performance of the code was good, not presenting any great discrepancy, caused by programming errors. The model predicted very well the dynamics of the deposition, and reasonably well the aerosol composition, and aerosol mass mean diameter. Some differences were obtained in the mass balance comparison, but the exact cause could not be determined, although there are indications that speciation can be the cause of such deviations, through direct or indirect actuation.

The results of the calculation cannot be interpreted as conclusive, given the approximations and simplifications used in the model, especially the way the release was modeled, the simplistic approach used in the speciation, and the experimental uncertainties. The results of the comparison are, hence, classified as indications.

The result of these preliminary runs present strong indications that the condensation is being little over-estimated by the model, and that nucleation is a very sensitive model. Therefore, studies are necessary, in the future, to determine the exact cause of the over-prediction, and establish a procedure that makes the nucleation model less sensitive. At first glance, the cause of the condensation wrong prediction is related to the speciation, but further analysis is necessary.

Several approximations, assumptions and simplifications were made throughout the model development. Adding up to the uncertainties resultant from the assumptions and simplifications, the uncertainties of the phenomenological chosen models, it becomes understandable that the process of augmentation of the model is a long-lasting continuous process, needing adjustment. The model needs, therefore, to be continuously up-dated, as it is used. Some important initial works were identified throughout the research. These future works are related specifically to the transport, and related to the fission product behavior implementation in the code. These initially identified future works are presented in Tables 5-1 and 5-2.

Table 6-1. Future-work matrix for the fission products-transport model

Priority	Activity	Observation
1.	Develop a model for speciation, with a consistent thermo-chemical database	Consistency with the release model
2.	Gain robustness of the nucleation model	
3.	Study of the structural condensation models	
4.	Implement the input as suggested	
5.	Start the validation process	
6.	Elaboration of the guidelines for the code usage	

Table 6-2. Future-work matrix for the fission products-behavior model

Priority	Activity	Observation
1.	Develop a model for speciation, with a consistent thermo-chemical database	Consistency with the transport model
2.	Review and improve the release model	
3.	Adjust and gradually validate the release model	
4.	Elaboration of the guidelines for the code usage	

APPENDIX A
FISSION PRODUCTS-VAPOR PROPERTIES

Several vapor properties of fission products appear in the development of the models used to represent the vapor phenomena in Chapter 3, namely:(a) Bulk gas dynamic viscosity;(b) Bulk gas thermal conductivity (c) Fission product molecular diffusion coefficient in the bulk gas; (d) Equilibrium or saturation concentration of vapor. The bulk-gas viscosity and thermal conductivity are already calculated in the code. Consequently, the following assessment is limited to the two last properties.

The most used method to determine the vapor diffusivity is to use the Chapman-Enksog theory to determine binary diffusivity of vapor A in the bulk gas specie B, expressed by the equation below (66):

$$D_{AB} = 0.0018583 \frac{\sqrt{T^3\left(\frac{1}{M_A} + \frac{1}{M_B}\right)}}{p\sigma_{AB}{}^2\Omega_{D,AB}} \qquad \text{(Equation A-1)}$$

Where:

$$\sigma_{AB} = \frac{1}{2}(\sigma_A + \sigma_B) \qquad \text{(Equation A-2)}$$

$$\varepsilon_{AB} = \sqrt{\varepsilon_A \varepsilon_B} \qquad \text{(Equation A-3)}$$

D_{AB}: Diffusivity of vapor A in bulk gas B (m^2/s)
σ_{AB}: Leonard Jones collision integral (Angstrom)
$\Omega_{D,AB}$: Diffusivity collision integral (dimensionless), tabulated as function of ε_{AB}
T: Gas temperature (K)
P: Gas pressure (atm)

Once determined the binary diffusivity of the vapor A in specie B, the mass diffusivity of the vapor in the bulk gas is determined by the equation presented by Welty et al. (67):

$$D_{k,g} = \frac{1 - y_A}{\sum_n (y_n / D_{An})} \qquad \text{(Equation A-4)}$$

Where:
y_A: mole fraction of vapor A
y_n: mole fraction of bulk gas n
$D_{A,n}$: Diffusivity of vapor A in bulk gas n (m^2/s)

The Lennard Jones parameters are used to calculate the dynamic viscosity, thermal conductivity and binary vapor diffusivity for gases. These parameters were found empirically by Lennard-Jones to define the potential energy of interaction between a pair of mono-atomic gas molecules, opening the possibility to use the Chapman-Enskog theory for mono-atomic low-density gases transport properties calculation. Later, this theory showed also to be appropriate for poly-atomic gases. Hence, once these parameters are known for the species component, the vapor diffusivity can be calculate by the Welty formulation.

The parameter σ is the characteristic diameter of the molecule (the “collision diameter”), whereas the ε parameter is a characteristic energy of interaction between the molecules (the maximum energy of attraction between a pair of molecules). Hence, it is necessary to know the Lennard-Jones parameters to calculate several transport properties.

The bulk species are steam and hydrogen. Therefore, the knowledge of the Lennard-Jones parameters for the modeled species and the two bulk species is necessary to determine gases transport properties, once using the Chapman-Enksog approach. Data for the species modeled in Scdap are provided in Table A-1.

The Chapman-Enksog theory with support of Lennard-Jones parameters is proved to be effective for pressures up to 10 atm (about 1 MPa). The uncertainty in the diffusivity calculation was estimated as 6% (67).

Table A-1. Lennard-Jones parameters for more important species

Specie	σ (Å)	ε/κ (K)
CsI	4.7	1786
CsOH	4.08	1046
Cs	5.06	1188
BaO	3.6	4220
Ba	4.15	2080
H_2O	2.47	776
H_2	2.92	38
SrO	3.27	5640
Te	3.35	1387
TeO	3.58	500
Sn	2.95	3330
Cd	2.887	1195
CdO	3.92	2035
In	2.92	2695
H_2Te	4.3	530
Ag	2.65	2590
I	4.61	316
I_2	4.98	550
HI	4.12	324

It is important to provide some parametric analysis and determine some figures for the vapor diffusivity. As pointed out by the formulations, they are dependent on the bulk gas composition. A calculation of these parameters was performed, assuming a bulk gas composed only by steam and hydrogen, with equal molar concentrations. The result of the calculation is shown in Figure A-1 below.

Typical diffusivities, in the range of temperatures in the bulk region, are of the order of cm^2/s. Diffusivities are higher for species such as tellurium and lower for cesium iodide, but the variation is relatively small (not orders of magnitude), especially in the temperatures which condensation is more likely (450-750 K). The diffusivity increases with the temperature and with the hydrogen concentration.

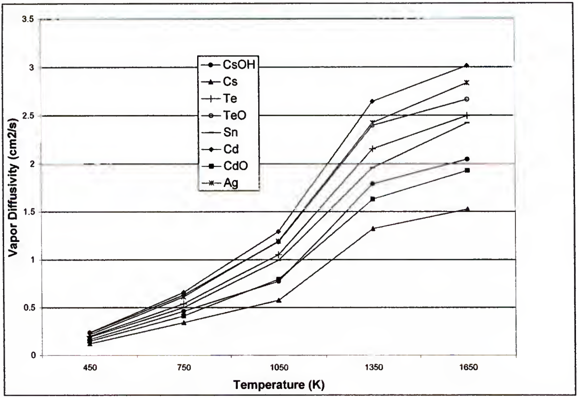

Figure A-1. Typical vapor diffusivities

The other species property used in the calculation is the equilibrium concentration. The property of liquid-vapor phase equilibrium is actually measured in pressure units. Hence, is necessary to change from vapor pressure to equilibrium vapor concentration. Along the progression of the fission products modeling, significant effort was done to obtain reliable data of vapor pressure for the more important species. The data for vapor pressure used in the implementation is from references (50) to (53), in the form of temperature dependent equations. The standard deviation for the used data range from 0.1 to 5%.

Two approaches are used to transform the vapor pressure to vapor equilibrium concentration. The first one is to assume ideal gas behavior and obtain the concentration by applying the ideal gas law:

$$C_{eq} = \frac{1.332x10^2 M_i P_{v,i}(T)}{RT} \qquad \text{(Equation A-5)}$$

Where P_v is given by the following expression:

$$\log_{10}(P_{v,i}) = -A_i / T + B_i + C_i \log_{10}(T) \qquad \text{(Equation A-6)}$$

Where:
P_v: Vapor Pressure of species i (mmHg)
A_i,B_i,C_i: Constants species dependent
T: Temperature (K)

The numerical factor in Equation A-5 is applied to convert the pressure units. The second approach is to apply the equation of state. Scdap applies the Van der Walls equation, which yields:

$$C_{eq,i} = \frac{M_i}{RT + b_i P_{sys}} \exp\left\{2.3026\left[A_i / T + B_i + C_i \log_{10}(T)\right] + \frac{b_i}{RT}(P_{sys} - P_{atm})\right\} \qquad \text{(Equation A-7)}$$

Where:
P_{sys}: System pressure (Pa)
P_{atm}: Atmospheric pressure (101.3kPa)

Melcor code applies the first approach, whereas Scdap adopts the second one. In order to evaluate the validity of the application of the gas Law, the equilibrium concentrations were calculated using the two approaches, named Scdap and Melcor approaches in Table A-2, for the system pressures of 0.2 MPa and 2 MPa.

The following table shows that for low pressures, the concentration equilibrium calculated by ideal gas law (Melcor) is within the uncertainty range (±5%), when compared to the equation of state approach. Nevertheless, higher differences arise when the pressure is 2MPa for high temperatures. Therefore, the ideal gas approach holds up for low pressures, but for higher pressures, the Scdap approach is the only one recommendable. In order to provide an idea of the range of values of concentrations and the behavior of the curves, the concentrations are plotted as function of the temperature.

Table A-2. Concentration equilibrium for CsI

	P=0.2 MPa			P=2MPa		
T (K)	Scdap	Melcor	Difference	Scdap	Melcor	Difference
450	2.968E-14	3.1528E-14	0.062373	2.98E-14	3.153E-14	0.0589167
550	2.156E-10	2.2827E-10	0.058757	2.16E-10	2.283E-10	0.0559958
650	9.073E-08	9.5826E-08	0.056212	9.09E-08	9.583E-08	0.0539145
750	7.016E-06	7.3975E-06	0.054314	7.03E-06	7.397E-06	0.0523473
850	0.0001831	0.00019279	0.052837	0.000183	0.0001928	0.0511185
950	0.0019404	0.00208533	0.074669	0.002291	0.0020853	- 0.089831
1050	0.0115417	0.0123861	0.07316	0.016993	0.0123861	- 0.271109
1150	0.0484929	0.05198125	0.071935	0.086035	0.0519812	- 0.395813
1250	0.1569141	0.16804278	0.070922	0.326752	0.1680428	- 0.485718
1350	0.4153764	0.4444834 5	0.070074	0.994378	0.4444835	- 0.553004
1450	0.9394315	1.0045857	0.069355	2.542697	1.0045857	- 0.604913
1550	1.8741795	2.00300888	0.068739	5.657894	2.0030089	- 0.64598
1650	3.3784359	3.60886923	0.068207	11.24819	3.6088692	- 0.67916
1750	5.6049051	5.984604 08	0.067744	20.38716	5.9846041	- 0.706452
1850	8.6812746	9.26585617	0.067338	34.22285	9.2658562	- 0.729249
1950	12.695894	13.5462708	0.06698	53.87198	13.546271	- 0.748547

Differently from the diffusivity, equilibrium concentration is a very sensitive property, especially to temperature, as shown in Figure A-2. Its value affects condensation over structural and aerosol surfaces, besides aerosol homogeneous nucleation. Therefore, it is a very important and sensible property. Hence, an improvement in the equations used is very welcome, because accuracy in this property is fundamental to obtain accuracy in the fission product transport calculation. The molecular diffusivity into the gas is also very important because of the linear variation of the deposition velocity with this property, affecting the condensation on structural surfaces and on aerosol surfaces.

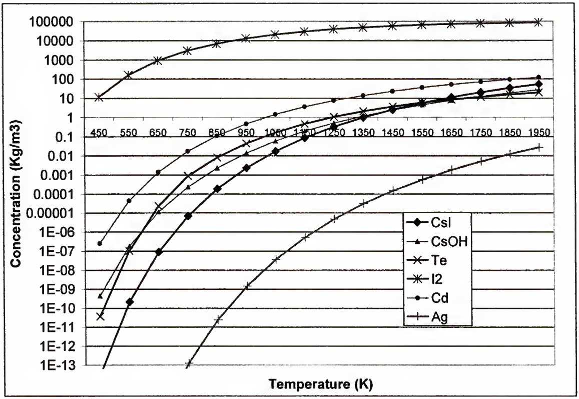

Figure A-2. Equilibrium concentrations using Scdap approach

APPENDIX B
SYNERGISMS OF AEROSOL INTERACTIONS IN SEVERE-ACCIDENT ENVIRONMENTS FOR LIGHT WATER REACTORS

In Chapter 4, several cases of typical thermal-hydraulic conditions of severe-accidents in light water reactors were evaluated, resulting in the phenomenological maps presented in Figures 4-18 and 4-19. These maps showed that the additive assumption is not always true for those conditions. Thus, a more elaborated approach is more convenient to treat these phenomena.

These new approaches must be consistent with the code philosophy and model assumptions, that is, must be optimized and consider the model methods and approach. Considering the optimization requirement, it was seen in Chapter 5 that typical aerosol particles in primary coolant systems have mean diameter of the order of 1-3 µm. This information is used to limit the considered synergisms to those ones that are within the range from the considered lower limit (0.5µm) to 4 µm. Considering this range of particle's sizes, the phenomena that have more representative mathematical interaction (the additive assumption is not valid) are presented in the Table A-1 below, according to the flow regime and pipe orientation. Recalling that the boundaries of the regions in the map have some mobility, according to different thermal hydraulic conditions (fluid and structural temperatures and Reynolds number), the models to be adopted should not be driven by the particle size, and, therefore, need to be valid for all particle sizes.

In general, Brownian diffusive and the differential gravitational settling coagulation kernels are in the same order of magnitude, as shown in Figures 4-18 (a), (b) and (c), for the considered particle size range.

Table A-1. Most significant phenomena synergisms for different particle interactions

Interaction	Phenomena
Agglomeration	Brownian diffusive and gravitational
Deposition	
Horizontal pipe	Thermophoresis and Gravitational
Turbulent condition	Turbulent and gravitational

At some extent, diffusive and turbulent kernels are close in some diagonal terms, since the differential gravitational is null at this site. Considering that the a few particle interactions will occur in this particle size combination, and that actually the observation shows that, in most of the situations, one of the kernels is one order of magnitude higher than the other (recall that the criterion for synergy established in Chapter 4 considered two orders of magnitude as minimum condition), the few occurrences of this synergy were neglected to optimize the model.

At very high Reynolds number, gravitational and turbulent agglomeration kernels become close, at some extent in the range region. Since the occurrence of this high Reynolds is not common in severe accident conditions, this effect was neglected.

Hence, in terms of agglomeration process, the synergy that can generate the most significant contribution for the model is the interaction of differential gravitational settling and Brownian diffusive agglomeration processes.

Regarding the aerosol deposition process, the phenomenological maps shown that for vertical pipes, the thermophoretic process dominates, whereas gravitational settling dominates for horizontal tubes. For the vertical turbulent pipe, thermophoresis dominates for small particles, and the turbulent process importance grows only for larger particles, which sizes are difficultly reached in primary cooling systems.

For the horizontal turbulent case, more synergisms exist. For small particles and Reynolds number, gravitational and thermophoresis are comparable, and for high Reynolds number thermophoresis gives place to the turbulent process, resulting in the gravitational and turbulence combination. In the next sections, an optimized model is selected or developed for the most significant synergies.

Agglomeration

A synergetic expression for the Brownian diffusive agglomeration and the gravitational settling was derived by Loyalka (34). This model assumes that there are no intra-particle and hydrodynamic forces, which is consistent with the assumption of the purely gravitational model derived in Chapter 3. Loyalka (34) conveniently has chosen the spherical polar coordinates in Figure A-1.

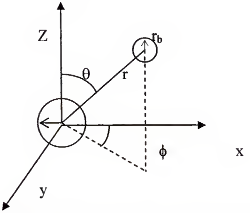

Figure B-1. Spherical polar coordinate system adopted

The sphere of radius r_a is the test particle and is located at the origin. The sphere of radius r_b has its center at the point (r,θ). The problem is azimuthally symmetric, and so the angle ϕ can be integrated out from the equations. In Equation B-1, the effects of

Brownian motion are incorporated via D, and gravitational settling via the relative velocity of the particles V (the absolute value of V_{ga}-V_{gb}).

$$D_{ab}\nabla^2 c(r) - \vec{V}\nabla c(r) = 0 \qquad \text{(Equation B-1)}$$

In this coordinate system, the relative velocity has the z direction, and the vector composition in k (z) direction is obtained by the following equation:

$$\vec{k}\nabla c = \cos\theta\frac{\partial c}{\partial r} - \frac{\sin\theta}{r}\frac{\partial c}{\partial \theta} \qquad \text{(Equation B-2)}$$

Applying the spherical coordinates definition of the first term in Equation B-1, and using the expression in Equation B-2 to the second term, Equation B-1 is re-expressed as:

$$\frac{D_{ab}}{r^2}\frac{\partial}{\partial r}\left(r^2\frac{\partial c}{\partial r}\right) + \frac{D_{ab}}{r^2\sin\theta}\frac{\partial}{\partial\theta}\left(\sin\theta\frac{\partial}{\partial\theta}\right) + V\cos\theta\frac{\partial c}{\partial r} - \frac{V\sin\theta}{r}\frac{\partial c}{\partial\theta} = 0 \quad \text{(Equation B-3)}$$

The problem is completed by the definition of the generalized agglomeration kernel, obtained by Loyalka (34), removing the ϕ dependent term:

$$K(a,b) = \frac{J}{c_\infty} = 2\pi(r_a^2 + r_b^2)D_{ab}\int_0^\pi d\theta\sin\theta\left.\frac{\partial c}{\partial r}\right|_{r=r_a+r_b} \qquad \text{(Equation B-4)}$$

The boundary conditions on Equation B-3 are:

At $r=\infty$, $c=c_\infty$ where c_∞ is the number density of b particles in the absence of agglomeration.

At $r = r_a + r_b$, $c=0$. This is because no b particles can have centers inside the sphere.

Before solving Equation B-3, the notation is simplified by setting $x=r/(r_a+r_b)$, $m(x,\theta)=c(r,\theta)/c_\infty$, and:

$$\beta = \frac{(r_a + r_b)V}{D_{ab}} = \frac{4\pi\rho g r_a r_b}{3KT}\left|r_a^2 - r_b^2\right| \qquad \text{(Equation B-5)}$$

Then, Equation B-3 becomes:

$$\frac{1}{x^2}\frac{\partial}{\partial x}\left(x^2\frac{\partial m}{\partial x}\right)+\frac{1}{x^2\sin\theta}\frac{\partial}{\partial\theta}\left(\sin\theta\frac{\partial m}{\partial\theta}\right)+\beta\cos\theta\frac{\partial m}{\partial x}-\frac{\beta\sin\theta}{x}\frac{\partial m}{\partial\theta}=0 \quad \text{(Equation B-6)}$$

and:

$$K_{BG}^{*}(a,b)=2\pi(r_a+r_b)D_{ab}\int_0^{\pi}d\theta\sin\theta\left.\frac{\partial m}{\partial x}\right|_{x=1} \quad \text{(Equation B-7)}$$

In Equation B-7, K_{BG}^{*} is the synergetic kernel for Brownian diffusion and gravitational processes. As a measure of accuracy of the sum kernel, the following ratio is established:

$$\gamma=\frac{K_{BG}^{*}}{K_{BG}}=\frac{2}{4+\beta}\int_0^{\pi}\left.\frac{\partial m}{\partial x}\right|_{x=1}\sin\theta d\theta \quad \text{(Equation B-8)}$$

Performing other variable transformation, $\mu=\cos\theta$, and:

$$m(x,\mu)=g(x,\mu)\exp(-0.5\beta x\mu) \quad \text{(Equation B-9)}$$

Whereby the equation for g becomes:

$$\frac{1}{x^2}\frac{\partial}{\partial x}\left(x^2\frac{\partial g}{\partial x}\right)+\frac{1}{x^2}\frac{\partial}{\partial\mu}(1-\mu^2)\frac{\partial g}{\partial\mu}-\frac{1}{4}\beta^2 g=0 \quad \text{(Equation B-10)}$$

subject to the boundary conditions:

$$g(1,\mu)=0$$

and:

$$\lim_{x\to\infty}[g(x,\mu)]=\exp(0.5\beta x\mu)$$

Loyalka (34) solved Equation B-10 applying a separation of variables technique, obtaining the $g(x,\mu)$:

$$g(x,\mu)=\left(\frac{2\pi}{\beta x}\right)^{1/2}\sum_{n=0}^{\infty}\left[A_n K_{n+1/2}\left(\frac{\beta x}{2}\right)+B_n I_{n+1/2}\left(\frac{\beta x}{2}\right)\right]P_n(\mu) \quad \text{(Equation B-11)}$$

In Equation B-11, I and K are the modified Bessel functions of half-integer order and $P_n(\mu)$ are Legendre polynomials.

Using $g(1,\mu)$ and the relationship:

$$\exp\left(\frac{\beta x\mu}{2}\right)=\left(\frac{\pi}{\beta x}\right)^{1/2}\sum_{n=0}^{\infty}(2n+1)I_{n+1/2}\left(\frac{\beta x}{2}\right)P_n(\mu) \quad \text{(Equation B-12)}$$

We see that the solution can be written:

$$m(x,\theta)=1-\exp\left(-\frac{\beta x\mu}{2}\right)\left(\frac{\pi}{\beta x}\right)^{1/2}\sum_{n=0}^{\infty}(2n+1)\frac{I_{n+1/2}(\beta/2)}{K_{n+1/2}(\beta/2)}K_{n+1/2}\left(\frac{\beta x}{2}\right)P_n(\mu) \quad \text{(Equation B-13)}$$

Noting that:

$$\left.\frac{\partial m}{\partial x}\right|_{x=1}=\left(\frac{\pi}{\beta}\right)^{1/2}\exp\left(-\frac{\beta\mu}{2}\right)\sum_{n=0}^{\infty}(2n+1)\frac{P_n(\mu)}{K_{n+1/2}(\beta/2)} \quad \text{(Equation B-14)}$$

and using the integral:

$$\int_{-1}^{1}d\mu P_n(\mu)\exp\left(-\frac{\beta\mu}{2}\right)=2(-1)^n\left(\frac{\pi}{\beta}\right)^{1/2}I_{n+1/2}(\beta/2) \quad \text{(Equation B-15)}$$

one finds:

$$\gamma=\frac{4}{4+\beta}\frac{1}{\beta}\sum_{n=0}^{\infty}(-1)^n(2n+1)\frac{I_{n+1/2}(\beta/2)}{K_{n+1/2}(\beta/2)} \quad \text{(Equation B-16)}$$

Loyalka (34) calculated this sum for several β values, when he made some observations. First, the sum in Equation B-16 is always convergent. Second, γ is always greater than one, indicating that the additive assumption underestimates the total kernel. The values of the relative increase in the agglomeration kernel (γ-1) are presented in Figure B-2. The graph extends from values of gravitational-to-diffusive ratios from zero to 60. This graph shows that the maximum relative increase occurred at ratios between 3 and 6, and a steep ramp exists up to 5, and then a smooth decrease occurred.

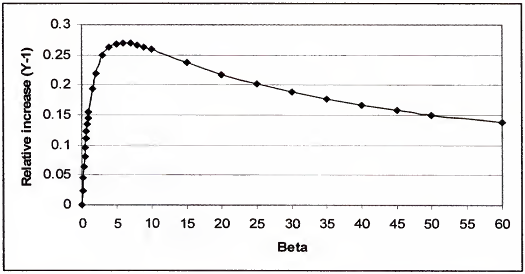

Figure B-2. Relative increase of agglomeration kernel for gravitational-diffusive synergy

The procedure adopted to account for this synergy was to correct the added value by this increase in the range of ratios from 0.01 to 100. To proceed in such manner, the curve in Figure B-1 was divided in several sections, and, for each section, the curve was approximated by an expression, presenting a maximum error of 2%. This package of equations is presented below.

$(\gamma-1)=\kappa=-0.0329\beta^2+0.1758\beta+0.0133$ for $0.01<\beta<3.0$

$(\gamma-1)=\kappa=0.25$ for $3.0\leq\beta<6.0$

$(\gamma-1)=\kappa=3E-05\beta^2-0.0047\beta+0.3009$ for $6.0\leq\beta<60.0$

$(\gamma-1)=\kappa=0.1269-0.317(\beta-60)$ for $6.0\leq\beta<60.0$ (Equation B-17)

The fact that the synergy is always additive can encounter a physical explanation (34). Consider the deposition of small particles onto a large particle. In the conventional calculation of Brownian coagulation, the diffusion equation describes the depletion of small particle distribution in the neighborhood of a large particle due to the diffusive flow of small particles onto the large particles. If the large particle is falling through the small particles, then, apart from those with which it directly collides and coagulates, there will also be an additional flux of small particles into the region of around the large particle which will partly offset the depletion in that region due to the diffusive flux above mentioned. This, in turn, will increase the diffusive flux of small particles onto the large one.

The procedure adopted to consider this synergy was, therefore, to correct the addition of the Brownian diffusive kernel to the gravitational, and correct this term by the κ factor, as shown in Equation B-18 below.

$$K_T = (1+\kappa)(K_B + K_G) + K_T \qquad \text{(Equation B-18)}$$

Deposition

As shown in Chapter 4, possible significant synergies, for typical primary-coolant system thermal-hydraulic conditions, in the range of typical circulating-particle sizes, would occur in horizontal tubes, for turbulent flows. For this case, gravitational and thermophoretic, or gravitational and turbulent depositions can occur in the same order of magnitude. Thus, a model that includes these three effects would be ideal.

Studies for investigating the combination for different deposition mechanisms for several applications include Crump and Seinfeld (140), and Gentry et al. (141). The works of Crump and Seinfeld (140) and Gentry et al. (141) considered the coupled effect of sedimentation (gravitational settling) and diffusion (Brownian and turbulent). Some published experimental work had been done in the area of thermophoretic deposition under turbulent flow. Romay et al. (142) and Nishio et al. (143) presented empirical evidence that the thermophoretic deposition is enhanced by a turbulent flow, but no theoretical expression have been derived.

Therefore, no models were developed for thermophoresis and gravitational coupling, and Crump and Seinfield (140) developed a model for turbulence and gravitational settling. Since the synergy occurs not simultaneously, but of gravitational settling with turbulence and thermophoresis separately, and the nature of the Crump and Seinfield solution, the procedure here developed consider first the coupling of thermophoresis and gravitational settling, and then the application of this composed deposition velocity to the Crump and Seinfield expression. In this way, a unique expression can be obtained, considering the couplings two-by two.

Obtain a synergetic expression for the coupling of thermophoresis and gravitational settling on the mathematical basis is difficult, given that the mathematical incorporation of the eddy diffusive mass transport term into the mass conservation equation of the Brock equations makes the solution not possible to be obtained analitically. Nevertheless, a straightforward model, based on the observation of the direction of the velocity terms, can be obtained. Consider a horizontal pipe, and two particles, one in the upper half of the pipe, and one in the lower half, as shown in Figure B-2. For the upper half particle, the thermophoresis component is towards the upper surface of the pipe, and the gravitational settling component is towards the lower surface of the pipe. Hence, they need to be subtracted. For lower half particles, the two velocities are in the same direction, and need to be added.

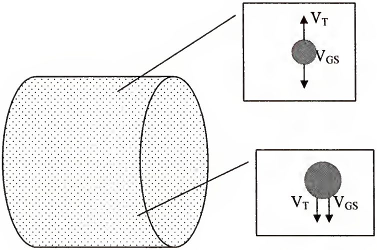

Figure B-3. Directions of the themphoretic and gravitational deposition velocities in a horizontal pipe, according to the particle position

A composite model for the synergetic deposition velocity can be easily obtained, considering the directions in Figure B-3. The expression for the model is presented in Equation B-19:

$$V_{TGS} = f_{lower}(V_T + V_{GS}) + f_{upper}\left|V_T - V_{GS}\right| \qquad \text{(Equation B-19)}$$

Where:
$f_{upper/lower}$: Fraction of the particles in the upper/lower part of the pipe
V_T: Thermophoretic deposition velocity (m/s)
V_{GS}: Gravitational settling deposition velocity (m/s)
V_{TGS}: Synergetic deposition velocity for thermophoresis and gravitational settling (m/s)

The fraction of particles in the upper or lower part of the pipe is assumed to be 0.5 both, to be consistent with the well-mixed assumption used throughout the code development.

The convective-diffusive including the sedimentation current of particles is expressed by:

$$J = -(D + D_e)\nabla c - V_{GS}\vec{k}c \qquad \text{(Equation B-20)}$$

Where:
D: Brownian aerosol diffusivity (m^2/s);
D_e: Eddy diffusivity (m^2/s), given by: $k_e x^2$, where x is the distance to the wall (R), and k_e can be considered the turbulent decay constant (s^{-1}). As mentioned in Chapter 5, the eddy diffusivity was obtained by Lin et al. (92)
c : Particle concentration (# particles/m^3)
V_{GS}: Gravitational settling deposition velocity (m/s)

Now, considering the steady-state assumption, the mass transfer equation ($\nabla J = 0$) becomes:

$$-\nabla\left[(D+D_e)\nabla c\right]-V_{GS}\vec{k}\nabla c=0 \quad \text{(Equation B-21)}$$

The proposed model substitutes the gravitational settling velocity by the gravitational-thermoporetic synergetic velocity, obtained previously. This is a valid procedure since the synergy of thermophoresis and turbulence is not important for this case. Equation B-21 can be re-expressed as:

$$-\nabla\left[(D+D_e)\nabla c\right]-V_{GTh}\vec{k}\nabla c=0 \quad \text{(Equation B-22)}$$

Crump and Seinfeld (140) solved Equation B-22 using boundary layer theory and obtained a particle deposition rate on a surface of an arbitrary geometry given by:

$$J_{wall}=\frac{1}{V}\int_S \frac{V_{GTh}\vec{n}\vec{k}dA}{\exp\left[\frac{\pi V_{GTh}\vec{n}\vec{k}}{2\sqrt{k_e D}}\right]-1} \quad \text{(Equation B-23)}$$

Where:
V: Cell volume (m^3);
dA: Surface element ($d\vec{s}=\vec{n}dA$);
$\vec{n}$: Vector normal to the depositing surface with unitary length

Considering the cylindrical geometry, with its axis in the horizontal direction, and the curvilinear surface of the cylinder, i.e., the deposition surface, the infinitesimal surface area and the scalar product in Equation B-23 are given by:

$dA = Rd\theta L$ (Equation B-24)

$\vec{n}\vec{k} = \cos\theta$ (Equation B-25)

Where:
R: Cell radius (m)
L: Cell length (m)

Applying Equation B-24 and B-25 to Equation B-23, a solution for the rate of deposition, for the horizontal cylinder surfaces can be obtained:

$$J_{hcyl} = \frac{V_{GTh}}{\pi R}\int_0^{2\pi}\frac{\cos\theta d\theta}{\exp\left[\dfrac{\pi V_{GTh}\cos\theta}{2\sqrt{k_e D}}\right]-1} \quad \text{(Equation B-26)}$$

Where the integral needs to be solved numerically. An optimized and consistent model to consider the aerosol synergies under typical severe accident conditions was selected and developed. The performance of this model must now be evaluated, and compared to the model used with the additive assumption, to verify the improvement potential of the developed model.

LIST OF REFERENCES

(1) J.J. Di Nunno, "Calculation of Distance Factors for Power and Test Reactor Sites," TID-14844 Report, U.S. Atomic Energy Commission, Washington, DC 1962.

(2) U. S. Nuclear Regulatory Commission, "The Reactor Safety Study: An Assessment of Accident Risk in U. S. Commercial Nuclear Power Plants," USNRC Report NUREG 75/014 (WASH-1400), Washington, DC, 1975.

(3) U. S. Nuclear Regulatory Commission, "Primary System Fission Product Release and Transport," USNRC Report NUREG/CR-6193, Washington, DC, 1994.

(4) Battele Memorial Laboratories, "Radionuclide Release under Specific LWR Accident Conditions," BMI-2104 Reports, Vols. I to VII, Columbus, Ohio, 1983.

(5) Booth, A. H.,"A Method of Calculating Fission Gas Diffusion from UO_2 Fuel and its Application to the X-2-f Loop Test," Chalk River Report CRDC-721, AECL, Chalk River, Ontario, Canada, 1957.

(6) Ranamurthi, M. and Kuhlman, M. R., "Final Report on Refinement of CORSOR-An Empirical In Vessel Fission Product Release Model," Columbus, Ohio, 1990.

(7) U. S. Nuclear Regulatory Commission, "FASTGRASS: A Mechanistic Model for Prediction of Xe, I, Cs, Te, Ba and Sr Release from Nuclear Fuel under Normal and Severe Accident Conditions," USNRC Report NUREG 5585, Argonne, Illinois, 1992.

(8) Schuster, E., Morell, and W., Kuhnlein, W., "Experiment Analysis Summary Report of OECD LOFT LP-FP-1, Volume 4, Fission Product Behavior," USNRC Report NUREG/CR5130, Idaho Falls, Idaho, 1989.

(9) U. S. Nuclear Regulatory Commission, "Summary of Important Results and SCDAP/RELAP Analysis of OECD LOFT Experiment LP-FP-2,"USNRC Report NUREG/CR 6160, Idaho Falls, Idaho, 1994.

(10) Osborne, M. F., Collins, J. L and Lorenz, R. A., "Experimental Studies of Fission Product Release from Commercial Light Water Reactor Fuel under Accident Conditions," Nuclear Technology, 78, pp157, 1987.

(11) U. S. Nuclear Regulatory Commission, “Data Report on for Fission Product Release Test VI-5,” USNRC Report NUREG/CR-5668, Oak Ridge, Tennessee, 1991.

(12) Petti, D. A., “Results from the Power Burst Facility (SFD) Severe Fuel Damage Test 1-4: A Simulated Fuel Damage Accident with Irradiate Fuel Rods and Control Rods,” Nuclear Technology, 94, pp313, 1991.

(13) U. S. Nuclear Regulatory Commission, “Fission Product Release and Fuel Behavior of Irradiated Light Water Reactor Fuel under Severe Accident Conditions, the ACRR ST-1 Experiment,” USNRC Report NUREG/CR-5445, Albuquerque, New Mexico, 1991.

(14) Im, K. H., “The RAFT Computer Code for Calculating Aerosol Formation and Transport in Severe LWR Accidents,” EPRI Report, NR-5287-CCM, Palo Alto, California, 1987.

(15) U. S. Nuclear Regulatory Commission, “TRAPMELT2 User’s Manual,” USNRC Report NUREG/CR-4205, Columbus, Ohio, 1985.

(16) Leuthrot, C., “SOPHIE: A Computer Code for the Prediction of the Transport and Deposition of Fission Product Vapors in a PWR Primary Circuit during a Severe Core Damage Accident,” Proceedings of the Seminar on Fission Product Transport Processes in Reactor Accidents, Chicago, Illinois, 1990.

(17) Gauvain, J. and Lhiaubet, G., “AEROSOL B2 Reference Document,” Commissariat a l’Energie Átomique, SEAC/91-02, Institut de Protection et de Surele Nucleaire Report, Cadache, France, 1991.

(18) Missirlian, M., Kissane, M. P.and Schimitz, B. M., “Sophaeros: Development and Validation of the ISPN Reactor Coolant System Code for Fission Product Transport,” Instiute de Protection et de Surete Nucleaire, Cadarache, France, 2002.

(19) Wright, A. L., Collen, J. and Rahn, F. J., “Aerosol Behavior Experiments on Light Water Reactors Primary Systems,” Nuclear Technology, 81, pp158, 1988.

(20) Hardt, P. Von and Tattegrain, A., “The Phebus Fission Product Project,” Journal of Nuclear Materials, 188, pp115, 1992.

(21) U. S. Nuclear Regulatory Commission, “CHARM: a Model for Aerosol Behavior in Time Varying Thermal Hydraulic Conditions,” USNRC Report NUREG/CR-5162, Albuquerque, New Mexico, 1988.

(22) U. S. Nuclear Regulatory Commission, “MAEROS User’s Manual,” USNRC Report NUREG/CR-1391, Argonne, Illinois, 1982.

(23) Lemmon, E. C., Marwill, E. S., "Aerosol Simulation Including Chemical and Nuclear Reactions," Proceedings of the Society for Computer Simulation, Chicago, Illinois, 1985.

(24) U. S. Nuclear Regulatory Commission, "STPC User's Guide," USNRC Report NUREG/CR-4587, Columbus, Ohio, 1986.

(25) U. S. Nuclear Regulatory Commission, "VICTORIA: A Mechanistic Model of Radionuclide Behavior in the Reactor Coolant System under Severe Accident Conditions," USNRC Report NUREG/CR-5545, Argonne, Illinois, 1992.

(26) U. S. Nuclear Regulatory Commission, "MELCOR Radionuclide (RN) Package Reference Manual", USNRC Report NUREG/CR-6119, Albuquerque, New Mexico, 1995.

(27) U. S. Nuclear Regulatory Commission,"SCDAP/RELAP5/MOD 3.2- Code Manual Volume I-Code Structure, System Models, and Solution Methods," NUREG-CR/6150, Idaho Falls, Idaho, 1995.

(28) Henry, R. E. and Plys, M. G., "MAAP 3.0B Computer Code Manual," Electric Power Research Institute Report NP-7071-CCML, Palo Alto, California, 1990.

(29) Gonzalez, R., Chatelard, P. and Jacques, F., "ICHARE 2 Version 2 MOD 0 and MOD 0.1, Description of Physical Models," Report DRS/SEMAR 92/94, Institut de Protection et de Surete Nucleaire, Cadarache, France, 1992.

(30) Sehgal, B. R.and Ritzman, R. L., "Fission Product Transport during In-vessel Progression of PWR Severe Accidents," Proceedings of the Seminar on Fission Product Transport Processes in Reactor Accidents, Chicago, Illinois, 1990.

(31) U. S. Nuclear Regulatory Commission, "QUICK User's Manual," USNRC Report NUREG/CR-2105, Palo Alto, California, 1981.

(32) Jones, O. C., *Nuclear Reactor Safety Heat Transfer*, McGraw-Hill International Book Company, New York, 1983.

(33) Todreas, N. E.and Kazimi, M. S., *Nuclear Systems I*, Hemisphere Publishing Corporation, New York, 1990.

(34) Williams, M. M. R. and Loyalka, S. K., *Aerosol Science Theory and Practice with Special Applications to the Nuclear Industry*, Pergamon Press, Elmsford, New York, 1991.

(35) Gieseke, J. A., Cybulskis, P., Denning, S., Kuhlman, M. R. and Chen, H., "Radionuclide Release under Specific Accident Conditions," Vols. I to V, Battele Memorial Institute Reports, Columbus,Ohio, 1984.

(36) U. S. Nuclear Regulatory Commission, "Severe Accident Risks: An Assessment for Five Nuclear Power Plants," USNRC Report NUREG-1150, Washington, DC, 1989.

(37) Hodge, S. A., "Thermal-Hydraulic Processes in the Reactor Coolant System of a BWR under Severe Accident Conditions," Proceedings of the Seminar on Fission Product Transport Processes in Reactor Accidents, Chicago, Illinois, 1990.

(38) U. S. Nuclear Regulatory Commission, "Analysis of Core Damage Frequency: Peach Bottom, Unit 2 Internal Events," USNRC Report NUREG/CR-4550, Washington, DC, 1987.

(39) Warman, E. P. and Donahue, M., "Fission Product Transport in the Reactor Coolant System for a Spectrum of Interfacing System LOCA Scenarios", Proceedings of the Seminar on Fission Product Transport Processes in Reactor Accidents, Chicago, Illinois, 1990.

(40) U. S. Nuclear Regulatory Commission, "SCDAP/RELAP5/MOD3.2 Damage Progression Theory, Code Manual Volume II," USNRC Report NUREG/CR – 6150, Idaho Falls, Idaho, 1995.

(41) Hill, M., *Lange's Handbook of Chemistry*, Mcgraw Hill Book Co., London, 1973.

(42) U. S. Nuclear Regulatory Commission, "SCDAP/RELAP5/MOD 3.2- Code Manual Volume III: User's Guide and Input Manual," USNRC Report NUREG-CR/6150, Idaho Falls, Idaho, 1995.

(43) Olander, D. R., "Fundamental Aspects of Nuclear Reactor Fuel Elements," TID-26711-P1, U.S Technical Information Center Report, Springfield, Virginia, 1976.

(44) U. S. Nuclear Regulatory Commission, "Relative Importance of Individual Elements to Reactor Accident Consequences Assuming Equal Release Fractions," USNRC Report NUREG/CR-4467, Washington, DC, 1986.

(45) U. S. Nuclear Regulatory Commission, "SANDIA-ORIGEN User's Manual," USNRC Report NUREG/CR-0987, Albuquerque, New Mexico,1997.

(46) General Electric Nuclear Energy, "Nuclides and Isotopes- Chart of Nuclides," Fifteenth Edition, General Electric Report, San Jose, California, 1996.

(47) U. S. Nuclear Regulatory Commission, “Technical Bases for Estimating Fission Product Behavior during LWR Accidents,” USNRC Report NUREG-0772, Washington, DC, 1981.

(48) Instiute de Protection et de Surete Nucleaire, “Phebus FPT-01 Final Report,” CEA Report, Cadarache, France, 2002.

(49) Smith, W. R. and R. W. Missen, *Chemical Equilibrium Analysis: Theory and Algorithms*, John Wiley and Sons,New York, 1982.

(50) Barin, I. and O. Kancke, *Thermochemical Properties of Inorganic Substances*, Springer-Verlag, New York, 1977.

(51) Chase, M. W. Jr, Davies C. A., D. J. Frump, R. A. McDonald, and A. N. Syverud, “JANAF Thermochemical Tables,” Third Edition, Parts I and II, 14, 1985.

(52) Ball, R. G., Mignanelli, M. A.and Yates, A. D., “Extension of the Thermodynamic Database in the VICTORIA Code,” AEA-RS-2168 Report, AEA Reactor Services, Harwell, United Kingdom, 1992.

(53) Powers, D., “Supplemental Thermodynamic Data Base for the VICTORIA Code,” Sandia National Laboratories Report, Albuquerque, New Mexico, 1991.

(54) Yanenko, J., *Fractional Step Method for Solving Numerical Systems*, Springer Verlag, New York, 1975.

(55) Chapra, C. and Canale, R., *Numerical Methods for Engineers*, Third Edition, Mac Graw-Hill, New York, 1988.

(56) Gear, C. W., *Numerical Initial-Value Problems in Ordinary Differential Equations*, Prentice-Hall, Englewood Cliffs, New Jersey, 1971.

(57) Hindmarch, A. and Radhakrishnan, K., “Description and Use of LSODE, the Livermore Solver for Ordinary Differential Equations,” Nasa Reference Publication 1327, San Jose, California, 1993.

(58) Nordsieck, A., “On the Numerical Integration of Ordinary Differential Equations,” Mathematical Computation, 16, pp 22-49, 1962.

(59) Lifshitz, M. and Landau, L. *Physicochemical Hydrodynamics*, Pergamon Press, London, United Kingdom, 1962.

(60) U. S. Nuclear Regulatory Commission, “Reactions between some Cesium Iodide Compounds and the Reactor Materials 304 Stainless Steel, Inconel 600 and Silver,” USNRC Report NUREG-CR-3197/1,2 of 3, Albuquerque, New Mexico, 1984.

(61) U. S. Nuclear Regulatory Commission, "Chemical Interactions of Tellurium Vapors with Reactor Materials," USNRC Report NUREG-CR-2921, Albuquerque, New Mexico, 1984.

(62) Bowsher, B. R., and Jenkins, R. "High Temperature Studies of Simulant Fission Products: Part V, Temperature-Dependent Interaction of Tellurium Vapor with Zircaloy," AEEN-R1915 Report, UKAEA, Winfrith, United Kingdom, 1991.

(63) Le Marois, G. and Megnin, M., "Assessment of Fission Product Deposits in Reactor Coolant Systems: the DEVAP Program," Nuclear Safety, 35, pp 213-222, 1994.

(64) Alonso, A. and Gonzallez, C., "The Kinetics of the Reaction of Tellurium with Stainless Steel Surfaces and Aerosols," Nuclear Engineering and Design, 180, pp 1-27, 1998.

(65) Gormley, P. G. and Kennedy, M., "Diffusion from a Stream Flowing Through a Cylindrical Tube," Proceedings of Royal Irish Academy, A52, pp 163-169, 1949.

(66) Gilliland, E. R., "Diffusion Coefficients in Gaseous Systems," Industrial Engineering Chemistry, 26, pp 681, 1934.

(67) Welty, J. R., Wicks, C. E., and Wilson, R. E., *Fundamentals of Momentum, Heat and Mass Transfer*, John Wiley and Sons, New York, 1984.

(68) Hinds, W. C., *Aerosol Technology*, Second Edition, John Wiley and Sons, New York, 1995.

(69) Fuchs, N. A., *The Mechanics of Aerosols*, Pergamon Press, Elmsted, New York, 1964.

(70) Petti, D. A., "Silver-Indium-Cadmium Control Rod Behavior and Aerosol Formation in Severe Reactor Accidents," USNRC Report NUREG-0896, Idaho Falls, 1987.

(71) Bowsher, B. R., Jenkins, R. A., Nichols, N. A. and Simpson, J. A., "Silver-Indium-Cadmium Control Rod Behavior during a Severe Accident," UKAEA Report, Winfrith, United Kingdom, 1986.

(72) Friedlander, S. K., *Smoke, Dust and Haze: Fundamentals of Aerosol Behavior,* Wiley, New York, 1977.

(73) Katz, J. L. and Donohiue, M., "Homogeneous Nucleation Kinetic Theory Model", Advanced Chemistry Physics, 40, pp 137-155, 1979.

(74) Girshick, L. S., Chiu, C. P.and McMurry, P. H., "Time-Dependent Aerosol Models and Homogeneous Nucleation Rates," Aerosol Science and Technology, 13, pp 465-477, 1990.

(75) Chalmers, B.," Condensation and Evaporation," Progress in Material Sciences, 11, pp 1-40, 1963.

(76) Martin, F., "La Nucleation Homogene: Etude de Interactions Vapeurs-Aerosols dans le Circuite Primaire d'un Reacteur Nucleaire lors d'un Accident Grave," Doctoral Thesis, University of Provence, Aix-Marseille, France, 1997.

(77) Seinfeld, J. H., *Atmospheric Chemistry and Physics of Air Pollution*, Wiley, New York, NY, 1986.

(78) Park, S. H. and Lee, K. W., "Condensational Growth of Polydisperse Aerosol from Entire Particle Size Range," Aerosol Science and Technology, 33, pp 222-227, 2000.

(79) Fuchs, N. A. and Sutugin, A. G., *Highly Dispersed Aerosols*, Ann Arbor Science Publication, Ann Harbor, Michigan, 1970.

(80) Kress, T. S., Weber, C. F. and Parker, G. W., "Fission Product Transport Behavior," Nuclear Technology, 101, pp 262-269, 1993.

(81) Gelbard, F., "Modeling Multi-component Aerosol Particle Growth by Vapor Condensation," Aerosol Science and Technology, 12, pp 399-412, 1990.

(82) Payne, L. E. and Pell, W., "The Stokes Flow Problem for a Class of Axially Symmetric Bodies," Journal of Fluid Mechanics, 7, pp 529-534, 1960.

(83) O'Neil, M. E., "On Asymmetrical Slow Viscous Caused by the Motion of Two Equal Spheres Almost in Contact," Proceedings of Cambridge Philosophy Society, 65,pp 543-548, 1969.

(84) Williams, M. R., "Neutron Diffusion in Spheroidal, bispherical and Tortoroidal Systems," Nuclear Science and Engineering, 94, pp 875-882, 1986.

(85) Booth, F., "The Coagulation of Non-Spherical Particles," Faraday Society Discussions, 18, pp 104-111, 1959.

(86) Fernandes, A. "Deposição de Aerossóis em Acidentes Postulados em Reatores Nucleares," Doctoral Thesis, University of São Paulo, São Paulo, Brazil, 1996.

(87) Stokes, G., "On the Theories of the Internal Friction of Fluids in Motion and Equilibrium and motion of Elastic Solids," Proceedings of Cambridge Philosophy Society, 1, pp 16-25, 1845.

(88) Cunningham, E., "On the Velocity of Steady Fall of Spherical Particles through Fluid Medium," Proceedings of Royal Society, A83, pp357, 1910.

(89) Millikan, R. A., "The General Law of a Small Spherical Body through a Gas and its Bearing upon the Nature of Molecular Reflection from Surfaces," Physical Review, 22, pp 1-16, 1923.

(90) Davies, C. N., *Aerosol Science*, Academic Press, London, United Kingdom, 1966.

(91) Einstein, A., *Investigation on the Theory of Brownian Motion*, Dover, New York, 1956.

(92) Tandom, P. and Adewumi, M., "Particle Deposition from Turbulent Flow in a Pipe," Journal of Aerosol Science, 29, pp 141-156, 1998.

(93) Lin, C. S., Moulton, R. W. and Putnam, G., "Mass Transfer between Solid Walls and Fluid Streams," Industrial Chemical Engineering, 45, pp 636-640, 1953.

(94) Sehmel, G. A., "Particle Deposition from Turbulent Air Flow," Journal of Geophysical Research, 75, pp 1766-1782, 1970.

(95) Friedlander, S. K., and Johnstone, H. F., "Deposition of Suspended Particles fro Turbulent Gas Streams," Industrial Engineering Chemistry, 49, pp 1151-1156, 1957.

(96) Davies, C. N., "Deposition of Aerosols from Turbulent Flow Through Pipes," Proceedings of Royal Society London, 289, 235-246, 1966.

(97) Laufer, J. "The structure of Turbulence in Fully Developed Pipe Flow," National Advisory Committee for Aeronautics Research Report 1174, National Bureau of Standards, Washington, DC, 1954.

(98) Beal, S., "Turbulent Deposition of Aerosols," Nuclear Science Engineering, 40, pp 134-137, 1970.

(99) Blackburn, P. E. and Johnson, C., "Light Water Reactor Fission Data Assessment," Argonne National Laboratory Report, Argonne, Illinois, 1982.

(100) Muyshondt, A., Anand, N. K. and McFarland, A. R., "Turbulent Deposition of Aerosol Particles in Large Transport Tubes," Aerosol Technology, 24, pp 107-116, 1996.

(101) Chiang, H. W., Mulpuru, S. R. and Berkis, C. J., "Analysis of Models for Turbulent Deposition of Aerosols," Journal of Aerosol Science, 27, pp 5455-5456, 1996.

(102) Epstein, P. S., "Thermal Force on Spherical Particle in the Slip-Flow Regime," Z. Physics, 54, pp 537, 1929.

(103) Brock, J. R., "On the Theory of Thermal Forces Acting on Aerosol Particles," Journal of Colloid Science, 17, pp 768-780, 1962.

(104) Schadt, C. F. and Cadle, R. D., "Sodium Chloride Aerosol Thermophoretic Deposition onto Vertical Tube," Journal of Physical Chemistry, 65, pp 1689, 1961.

(105) Talbot, L., Cheng, R. K., Schefer, R. W. and Willis, D. R., "Termophoresis of Particles in a Heated Boundary Layer," Journal of Fluid Mechanics, 101, pp 737-758, 1980.

(106) Springer, G. S., "Thermal Force on Particle in the Transition Regime," Journal of Colloid and Interface Science, 2, pp 215-222, 1979.

(107) Waldmann, L., *Rarefied Gas Dynamics*, Academic Press, London, United Kingdom, 1961.

(108) Montassier, N., Bouland D. and Fissan, D., "Comparison between Experimental Study and Theoretical Model of Thermophoretic Particle Deposition in Laminar Flow Tube," Journal of Aerosol Science, 21, pp S85-S88, 1990.

(109) Shimada, M., Seto, T. and Okyuama, K., "Wall deposition of Ultra-Fine Aerosol Particles by Thermphoresis in Nonisothermal Laminar Pipe Flow of Different Carrier Gas," Journal of Applied Physics, 33, pp 1174-1181, 1994.

(110) Stratmann, F., Otto, E. and Fissan, H., "Thermophoretic and Diffusional Particle Transport in Cooled Laminar Tube Flow," Journal of Aerosol Science, 25, pp 1305-1319, 1994.

(111) Batchelor, G. K. and Chen C., "Thermophoretic Deposition of Particles in Gas Flow over Cold Surfaces," Journal of Colloid Interface Science, 107, pp 21-37, 1985.

(112) Dumaz, P., "Termophoretic Deposition Efficiency in Tube Flow," Journal of Aerosol Science, 25, pp S369-370, 1994.

(113) Dumaz, P. and Albiol, T., "TUBA Experiment," AAAR Meeting, Vienna, Austria, 1990.

(114) Chieng, Y. and Wang, C., "Inertial Deposition of Particles in a Bend," Journal of Aerosol Science, 6, pp 139-145, 1975.

(115) Davies, R. E., "The Visual Examination of Gas Flow Round Pipe Bends Using a New Technique," International Journal of Air and Water Pollution, 8, pp 177-184, 1964.

(116) Chieng, Y. and Wang, C., "Motion of Particles in Bends of Circular Pipes," Atmospheric Environment, 15, pp 301-306, 1981.

(117) Hydaka, A., Shibazaki, H., Yoshino, T. and Sugimoto, "Deposition of Cesium Iodide Particles in Bends and Sections of Vertical Pipe under Severe Accident Conditions," Journal of Aerosol Science, 31, 9, pp 1045-1059, 2000.

(118) Pui, D. Y., Romay-Novas, and Liu, B. "Experimental Study of Particle Deposition in bends of Circular Cross Section," Aerosol Science and Technology, 7, pp 301-315, 1987.

(119) Landahl, H. and Hermann, R., "Sampling of Liquid Aerosol by Wires, Cylinders and Slides and Efficiency of Impaction of Droplets," Journal of Colloid Science, 4, pp 103-136, 1949.

(120) Crane, R. and Evans, L., "Inertial Deposition of Particles in a Bent Pipe," Journal of Aerosol Science, 8, pp 161-170, 1977.

(121) Mori, Y. and Nakayama, W., "Study on Forced Convective Heat Transfer in Curved Pipes: Laminar Region," International Journal of Heat and Mass Transfer, 8, pp 67-82, 1965.

(122) Pitch, J. "Impaction of Particles on the Surface of Membrane Filters," Journal of Aerosol Science, 5, pp 17-24, 1974.

(123) Pui, D. Y. and Ye Y., "Particle Deposition in a Tube with an Abrupt Contraction," Aerosol Science and Technology, 13, pp 29-40, 1990.

(124) Muyshondt, A., McFarland, A.R.and Anand, N. K., "Deposition of Aerosol Particles in Contraction Fittings," Aerosol Science and Technology, 24, pp 205-216, 1996.

(125) Kindler, P., Elliot, M. A., Stepheson, B. K., Matheson, M. J., "Particle Deposition After Crossing a Sudden Expansion," Journal of Aerosol Science, 21, pp 367-374, 1992.

(126) Parozzi, F., "A Fast-Running Model for Physical Aerosol Re-Suspension Accounting Storm Experimental Results," International Meeting on "Best-Estimate" Methods in Nuclear Installation Safety Analysis, Pizza, Italy, 2000.

(127) Reeks, M. W. and Hall, D., "Deposition and Re-suspension of Gas-Borne Particles in Re-circulating Turbulent Flow," Journal of Fluids Engineering, 110, pp 165-171, 1988.

(128) Brockmann, J. E., "Range of Possible Re-Suspension and Re-Entrainment of Fission Products during Containment Depressurization," SANDIA Report SAND84-0410, Vol. 2, Albuquerque, New Mexico, 1985.

(129) Hummel, R. "STORM Aerosol Experiments," Annual Report 1998 of the Institute for Systems, Informatics and Safety," EC-JRC EUR 18721, Geneva, Switzerland, 1999.

(130) Frometin, A., "Dry Re-Suspension: State of the Art Report," Paul Scherrer Institut Report, Geneva, Switzerland, 1987.

(131) Hall, D., "Measurements of the Mean Force on a Particle near a Boundary Layer in Turbulent Flow," Journal of Fluid Mechanics, 187, pp 451-466, 1988.

(132) Reyes, A., Capitao, J. A. and De Santi, G., "International Standard Problem 40- Aerosol Deposition and Re-Suspension- Final Comparison Report," OECD-AEN Report NEA/CSNI, Paris, France, 1999.

(133) Morlock, M., "The Collision Efficiency of Gravitational Coagulation of the Aerosol Particles in the Containment System of Fast Reactors," Report OECD GRS-A-1246, Karlsrhue, Germany, 1986.

(134) Pruppacher, H. R. and Klett, J. D., *Microphysics of Clouds and Precipitation*, Reidel, New York, 1978.

(135) Saffman, P. and Turner, J., "On the Collision of Drops in Turbulent Flows," Journal of Fluid Mechanics, 1, pp 16, 1956.

(136) Delichatsios, M. A. and Probstein, R. F., "Coagulation in Turbulent Flow: Theory and Experiment," Journal of Colloid and Interface Science, 51, 3, pp 394-405, 1975.

(137) Taylor, G., "Statistical Theory of Turbulence," Proceedings of Royal Society, A151, pp 421, 1935.

(138) Batchelor, G., "Pressure Fluctuations in Isotropic Turbulence," Proceedings of Cambridge Philosophical Society, 47, pp 359, 1951.

(139) Crump, J. G. and Seinfeld, J. H., "Turbulent Deposition and Gravitational Sedimentation of an Aerosol in a Vessel of Arbitrary Shape," Journal of Aerosol Science, 12, pp 405-415, 1981.

(140) Wagner, R., Coryell, L. and Siefken, L., "Scdap/Relap5 Programmer's Manual," Idaho National Engineering Laboratory Report, Idaho Falls, Idaho, 1994.

(141) Gentry, J.,Ghebart, J. and Scheuch, G., "A Vector Model for the Total Aerosol Deposition Efficiency under the Simultaneous Action of more than One Mechanisms", Journal of Aerosol Science, 25, pp 315-325, 1994.

(142) Romay, F. J., Takagaki, S., Pui, D. and Liu, B., "Thermophoretic Deposition of Aerosol Particles in Turbulent Pipe Flow," Journal of Aerosol Science, 29, pp 943-959, 1998.

(143) Nishio, G., Kitani, S. and Takahashi, K., "Thermophoretic Deposition of Aerosol Particles in a Heat-Exchanger Pipe," Industrial Engineering Chemistry, 13, pp 408-415, 1974.

(144) Honaiser, E., "Modeling the Quench-06 Experiment using Scdap/Relap5," Master's Thesis, University of Florida, Gainesville, Florida, 2001.

(145) Juul, N. H., "View Factors in Radiation Between two Parallel Oriented Cylinder of Finite Elements," Journal of Heat Transfer, 104, pp 383-384, 1982.

(146) Powers, D. A., Lee, R., Sweet, D. and Soda, K., "A Comparison of World-Wide Uses of Severe Reactor Accident Source Terms," SAND94-2157 Report, Albuquerque, New Mexico, 1994.

(147) Soffer, L., Burson, S. B., Ferrel, C., Lee, R. and Righly, J. N., "Accident Source Terms for Light-Water-Nuclear Power Plants," NUREG-1465, U. S. Nuclear Regulatory Commission, Washington, DC, 1992.

BIOGRAPHICAL SKETCH

Eduardo Henrique Rangel Honaiser was born in Rio de Janeiro, Brazil, on November 1968. He entered the Brazilian Navy in 1986, cursing at the Brazilian Naval Academy, which was finished in 1990. In 1992, still in the Navy, he studied at the Polytechnic School of Engineering of the Sao Paulo University, where he earned his bachelor in Naval Architecture and Marine Engineering, ranking second in his class. In 1996 he worked at the Brazilian Navy Shipyard at Rio de Janeiro as the Structural Fabrication Section head. In 1997, he was transferred to Belem, in the north of Brazil, where he assumed the Naval Structural Division head. In 2001, he obtained the Master's degree in Nuclear and Radiological Engineering at the University of Florida. Currently, he is the technical manager of the pressurized water reactor prototype project of the Brazilian Navy. Lieutenant Honaiser is married and has two sons.

I certify that I have read this study and that in my opinion it conforms to acceptable standards of scholarly presentation and is fully adequate, in scope and quality, as a dissertation for the degree of Doctor of Philosophy.

Samim Anghaie

Samim Anghaie, Chairman
Professor of Nuclear and Radiological
Engineering

I certify that I have read this study and that in my opinion it conforms to acceptable standards of scholarly presentation and is fully adequate, in scope and quality, as a dissertation for the degree of Doctor of Philosophy.

Edward T. Dugan

Edward T. Dugan
Associate Professor of Nuclear and
Radiological Engineering

I certify that I have read this study and that in my opinion it conforms to acceptable standards of scholarly presentation and is fully adequate, in scope and quality, as a dissertation for the degree of Doctor of Philosophy.

William G. Vernetson

William G. Vernetson
Associate Engineer of Nuclear and
Radiological Engineering

I certify that I have read this study and that in my opinion it conforms to acceptable standards of scholarly presentation and is fully adequate, in scope and quality, as a dissertation for the degree of Doctor of Philosophy.

James F. Klausner

James F. Klausner
Professor of Mechanical and Aerospace
Engineering

I certify that I have read this study and that in my opinion it conforms to acceptable standards of scholarly presentation and is fully adequate, in scope and quality, as a dissertation for the degree of Doctor of Philosophy.

William R. Dolbier

William R. Dolbier Jr.
Professor of Chemistry

This dissertation was submitted to the Graduate Faculty of the College of Engineering and to the Graduate School and was accepted as partial fulfillment of the requirements for the degree of Doctor of Philosophy.

December, 2003

Pramod Khargonekar

Pramod P. Khargonekar
Dean, College of Engineering

Winfred M. Phillips
Dean, Graduate School